

Characteristic changes in electrocorticographic power spectra of the
human brain

Kai Joshua Miller

A dissertation submitted in partial fulfillment of
the requirements for the degree of

Doctor of Philosophy

University of Washington

2008

Program Authorized to Offer Degree: Physics

University of Washington
Graduate School

This is to certify that I have examined this copy of a doctoral dissertation by

Kai Joshua Miller

and have found that it is complete and satisfactory in all respects,
and that any and all revisions required by the final
examining committee have been made.

Chair of the Supervisory Committee:

Marcel den Nijs

Reading Committee:

Marcel den Nijs

Larry B. Sorensen

Eberhard E. Fetz

Date: _____

In presenting this dissertation in partial fulfillment of the requirements for the doctoral degree at the University of Washington, I agree that the Library shall make its copies freely available for inspection. I further agree that extensive copying of this dissertation is allowable only for scholarly purposes, consistent with "fair use" as prescribed in the U.S. Copyright Law. Requests for copying or reproduction of this dissertation may be referred to Proquest Information and Learning, 300 North Zeeb Road, Ann Arbor, MI 48106-1346, 1-800-521-0600, to whom the author has granted "the right to reproduce and sell (a) copies of the manuscript in microform and/or (b) printed copies of the manuscript made from microform."

Signature_____

Date_____

University of Washington

Abstract

Characteristic changes in electrocorticographic power spectra of the human brain

Kai Joshua Miller

Chair of the Supervisory Committee:
Professor Marcel den Nijs
Physics

We quantified the character and underlying nature of spectral changes in human brain electric potentials, while working with implanted cortical surface arrays in epileptic patients. In our initial motor movement study, we identified a broadband in the power spectrum at 76-100 Hz, which increased in power in a focal brain region during activity, in stark contrast to well known non-focal power decreases in the α/β rhythms at low frequencies 8-32 Hz. We observed that these changes also happened, albeit not as strongly, during movement imagery, but could be dramatically enhanced when we coupled imagery associated spectral changes to cursor-based feedback (a brain computer interface). We hypothesized that this broad band and the α/β rhythms represent different processes: the peaks originate from synchronous processes over large areas of the brain, while the broadband reveals temporally scale-free (asynchronous) changes associated with local neural computation. We were able to map local function in the brain, in real-time, by capturing broadband power changes in the 76-200 Hz “ χ -band”. After careful hardware characterization, we discovered that the cortical spectrum follows a power law of the form $P \sim f^{-\chi}$, where $\chi = 4.0 \pm 0.1$ between 80-500 Hz. The exponent shifts to $\chi_L = 2.0 \pm 0.4$ over all $10 \leq f \leq 500$ Hz, after dividing out a Lorentzian crossover function ($f_0=70$ Hz). In cortical areas associated with motor movement, a principal component-type decomposition removed the α/β rhythms, and find that only the amplitude of the power law, not the value of χ_L , changes with activity.

Project Summary

For the past 5 years, we have worked with epileptic patients undergoing placement of electrocorticographic (ECoG) arrays on the brain surface for seizure focus localization. Our research project began with the intent of identifying behaviorally-modified features in the power spectrum of the potential measured from these arrays. As an initial inquiry, we looked at changes in two frequency ranges during simple motor movement: a high-frequency band (HFB: 76 -100 Hz) and a low frequency band (LFB: 8 -32 Hz) . We demonstrated that the power in anatomically relevant electrodes consistently decreased in the LFB with movement, whereas the power in the HFB consistently increased. In addition, the HFB changes were spatially much more focal than the LFB changes. Based upon these findings, we postulated that these changes reflected distinct physiologic phenomena, characteristically modulated with behavior: one with characteristic correlations on the 30-100 ms timescale, producing the α and β rhythms; and the other with no characteristic timescale, resulting in a power law broadband shape in the power spectrum. We further postulated that local activity in the brain could be captured by this power law, and that the power law, in turn, could be quantified by high pass filtering the raw potential, at frequencies above the α/β rhythms, and used this to create the first real-time functional electrical mapping device from these signals (a stated goal of other groups for many years).

We also performed motor imagery studies based upon the same HFB/LFB spectral changes, and examined how they changed during feedback. During this imagery, the HFB change was roughly 25% compared to actual movement and the LFB change was of order of 50%.When feedback was provided based on spectral change during motor imagery, these changes increased dramatically and, in most cases, exceeded the strength of changes associated with overt movement.

We succeeded in quantifying the nature of the power law broadband shape by increasing the sampling rate beyond what anyone else in the field had used, by using a pair-wise re-

referencing scheme, by correcting for the amplifier frequency-dependent attenuation, and by addressing the noise floor of the amplifiers. The power spectral density (PSD) follows the power-law form $P(f) \sim Af^{-\chi}$ from 80 to 500Hz in fixation tasks. Moreover, this scaling index $\chi = 4.0 \pm 0.1$ appears universal, across subjects, area in the cortex, and local neural activity levels. We observed a knee in the spectra at 70 Hz, implying the existence of a characteristic time scale $\tau = (2\pi f_0)^{-1} \simeq 2 - 4$ ms. For $f < f_0$, we find evidence for a lower power-law with $\chi_L \simeq 2.0 \pm 0.4$.

A principal component type decomposition of the power law during finger movement provided strong evidence that the behaviorally related increases in the power-law correspond to shifts in the overall amplitude, not in the exponent χ . Moreover, this decomposition demonstrated that the power law is marker of local activity. Time-frequency trade-off estimates of the temporal trace of the power law specifically track local cortical function, revealing a generic correlate of local brain activity.

The results of our investigations represent a marked shift away from the classic “frequency-band” paradigm which has dominated the field for decades, in which distinct physiologic phenomena are interpreted as superpositions of specific rhythms. Instead, changes in a power law provide a succinct, aggregate, measure of cortical activity on the local neuronal population scale, at the timescale of cognition. As an illustration, our results resolved the first somatotopic representation of individual finger movement trajectories in motor cortex.

TABLE OF CONTENTS

	Page
List of Figures	ii
Chapter 1: Introduction	1
1.1 Biology underlying field potentials	2
1.2 Experimental Setting	5
1.2.1 Subjects	5
1.3 Evolving objectives of the research	6
Chapter 2: What we measure	15
2.1 Electrodes	16
2.2 Amplifiers	18
2.2.1 Choice of reference.	21
2.2.2 Sampling Frequency	24
2.2.3 Amplifier frequency-dependent attenuation	24
2.2.4 Amplifier noise floor	25
2.2.5 Potential sources of amplifier noise	25
2.3 Neural Structures that give rise to potentials	28
2.3.1 The current dipole	28
2.3.2 Action potentials, Hodgkin-Huxley and the Squid Giant Axon	30
2.3.3 Leaky Cable Equation	36
2.3.4 The role of active channel dynamics:	37
2.4 Synaptic dipole generation	38
2.4.1 Synaptic transmission	39
2.4.2 The post-synaptic current	39
2.5 Field properties of the superimposed dendritic dipoles	40
2.5.1 From the current dipoles to macroscopic potential	43
2.6 Evaluation of the power spectra	44

2.6.1	Estimation of average spectra using the windowed Fourier Transform .	45
2.6.2	The relationship between the Fourier Transform and the Autocorrelation	46
Chapter 3:	Spectral Changes in Cortical Surface Potentials during Motor Movement	48
3.1	Introduction	48
3.2	Methods	50
3.2.1	Subjects	50
3.2.2	Recordings	51
3.2.3	Tasks	52
3.2.4	Signal Analysis	53
3.2.5	Electrode Localization	57
3.2.6	Template Brain Mapping	58
3.2.7	Cortical stimulation mapping	58
3.3	Results	59
3.4	Discussion	60
3.5	Conclusion	65
3.6	Supplemental Figures	66
Chapter 4:	ECoG observations of power-law scaling in the human cortex	81
4.1	Supplement	91
Chapter 5:	Decoupling the Cortical Power Spectrum Reveals Individual Finger Representation in Humans	107
5.1	Introduction	107
5.2	Method Summary	110
5.3	Results and Discussion	111
5.4	Discussion	117
5.5	Supplemental Methods	118
5.5.1	Experimental Protocol	118
5.5.2	Spectral Decoupling	121
5.5.3	Time-Frequency approximation (Dynamic Spectrum)	124
Chapter 6:	Real-time Functional Brain Mapping using Electroencephalography	143
6.1	Introduction	143
6.2	Methods	144

6.3	Results	146
6.4	Discussion	148
Chapter 7:	Augmentation of Cortical Activity by Motor Imagery-Based Learning	151
7.1	Introduction	151
7.2	Brief Methods	152
7.3	Results	156
7.4	Discussion	157
7.5	Supplemental Methods	159
7.5.1	Subjects	159
7.5.2	Recordings	159
7.5.3	Tasks	160
7.5.4	Signal Analysis	161
7.5.5	Electrode Localization and Template Brain Mapping	161
7.6	Supplemental Figures and Tables	163
Bibliography	181
Appendix A:	A Simple, Spectral-Change Based, Electrographic Brain-Computer Interface	195
A.1	Signal acquisition	196
A.2	Feature Selection	198
A.3	Feedback	200
A.4	Learning	202
A.5	Summary	203
A.6	A step-by-step walkthrough of the BCI process	214
A.6.1	Background:	214
A.6.2	Screening for feature identification.	214
A.6.3	One-dimensional cursor feedback	215
A.6.4	Two-Dimensional Cursor Feedback	216
A.7	End notes	217
Appendix B:	Cortical Electrode Localization from X-Rays and Simple Mapping for Electrographic Research: The “Location On Cortex” (LOC) package for Matlab	221

B.1	Introduction	221
B.2	Methods	223
B.3	Results	224
B.4	Conclusion	226
B.5	End notes	231

LIST OF FIGURES

Figure Number	Page
1.1 Large scale organization of the brain	2
1.2 Ions and the neuronal membrane	4
1.3 Grid placement and representation on a brain template	5
2.1 The clinical environment	15
2.2 Electrode Schematic	17
2.3 ECoG electrode and the neuronal dipole	18
2.4 In situ electrode visualization	19
2.5 Identifying electrodes in standard coordinates	20
2.6 The choice of amplifier reference	22
2.7 Measurement of Frequency-dependent amplifier amplitude attenuation	25
2.8 Amplifier noise floor estimation	26
2.9 The neuronal synapse	29
2.10 The action potential	32
2.11 Sodium channel subunit “m”	34
2.12 Sodium channel subunit “h”	34
2.13 Potassium current subunit “n”	35
2.14 Diffusion distance with potential sensitive channels	38
2.15 The cross section of gray matter of the cortex	40
2.16 Figure from Murakami, 2006	41
2.17 calculation of the power spectral density	46
3.1 Grid placement and representation on a brain template	51
3.2 Characteristic power spectral changes	52
3.3 Power spectral change hypothesis	54
3.4 Spectra superimposed on the brain over each electrode in a single subject	56
3.5 Cortical activation maps for hand movement	68
3.6 Cortical activation maps for tongue movement	69

3.7	Average representation during hand and tongue movement	70
3.8	Spectral change compared with electrical stimulation	71
3.9	Spectral changes during five different movement modalities	72
3.10	Spectral change analysis procedure	74
3.11	Spectral changes during many different types of movement	75
3.12	Spectral changes during finger movement	76
3.13	Characteristic spectral shift	77
3.14	Task-related change in the “resting-spectra.”	78
3.15	Cortical activation maps in 3 spectral ranges for hand movement	79
3.16	Cortical activation maps in 3 spectral ranges for tongue movement	80
4.1	The electrode array locations for the high frequency sampling rate subjects	82
4.2	Correction for roll-off and noise floor	84
4.3	The power law in the cortical spectrum	86
4.4	The conserved shape of the power spectrum with movement	88
4.5	Recording setup	92
4.6	The electrode array locations in situ for the high frequency sampling rate subjects	93
4.7	Power Spectral Density Calculation	94
4.8	Frequency-dependent amplifier amplitude attenuation	95
4.9	Equivalent resistor network during amplifier noise floor estimation	96
4.10	Shift in spectra with re-referencing	97
4.11	Insensitivity to noise floor	98
4.12	Recursive range fitting	99
4.13	Correlation between exponent and low frequency power	101
4.14	Correlation between exponent and fit noise floor	101
4.15	Correlation between fit noise floor and high frequency power	102
4.16	Correlation between low frequency and high frequency power	102
4.17	Low frequency fits for high sampling rate subjects	104
4.18	Low frequency fits for low sampling rate subjects	105
4.19	Low frequency fits for low sampling rate subjects, after correction for Lorentzian form	106
5.1	Representative spectral changes, and decoupled form	109

5.2	Decoupling the spectrum, to reveal individual digit representation in adjacent electrodes	111
5.3	Individual digit representation in 4 subjects	113
5.4	Correlation between 1st PSC (χ) and finger position	114
5.5	Dual amplification schematic	119
5.6	Individual finger movements	120
5.7	Signal processing steps in the decoupling procedure	122
5.8	Individual digit representation for both components, in all subjects	127
5.9	Sparsity in cortical finger representation	130
5.10	Somatotopic cortical tuning for different fingers	131
5.11	Time Frequency Plots for 3 adjacent electrodes and 3 different finger movements	133
5.12	Time Frequency Plots for 3 adjacent electrodes and 3 different finger movements, decoupled	135
5.13	Locations of electrodes on intra-operative surgical photograph	136
5.14	Relation between decoupled representation and clinical stimulation findings .	138
5.15	Hypothetical input - spectral change relation	139
5.16	Correlation between different digit movements	140
5.17	Finger movement, and the event-related potential	141
6.1	Electrocorticographic motor mapping	145
6.2	Offline hand motor area mapping	146
6.3	Real-time identification of sensorimotor cortex	147
6.4	figureS1	149
6.5	Real time mapping and stimulation finding	150
7.1	Spectral Changes in Cortical Surface Potentials during Actual and Imagined Hand Movements	153
7.2	Actual and imagined tongue movement activations for 8 subjects	154
7.3	Changes in cortical activity during imagery-based learning	155
7.4	Augmentation of cortical activity after learning in HFB and LFB	158
7.5	Characteristic changes in the cortical spectrum	165
7.6	Paired comparison of active and rest epochs from an electrode	167
7.7	Characteristic changes, without disappearance of the α and β peaks	168
7.8	Method for calculating and displaying “activation”	169
7.9	Imagined to real ratios in spectral change	172

7.10	Electrode - frequency band combinations for feedback	173
7.11	Validation of imagery, through movement, and EMG	175
7.12	An anomaly of post-movement power increase at high frequencies	177
7.13	Anatomic site of the post-movement power increase	178
7.14	Changes with feedback in a second subject	179
7.15	Spectral changes in ECoG with feedback for subject S1, shrug modality . . .	180
A.1	The BCI experimental setting	204
A.2	Co-registration of electrodes and plotting of data on template cortices. . . .	206
A.3	Identifying areas of activity during simple tasks using cross-correlation	207
A.4	Characteristic changes in the power spectrum with activity.	209
A.5	Schematic representation of the closed-loop brain-computer interface that we use.	211
A.6	Feature reassessment after feedback during a speech imagery task	212
A.7	A single case demonstration of the entire BCI process.	220
B.1	The Talairach coordinate axes	227
B.2	Localization of strip electrodes	228
B.3	Characteristic motor changes	229
B.4	A comparison of the LOC method with intra-operative figures	230

ACKNOWLEDGMENTS

I would like to thank my mentors, the patients who built this with me, and my family. This thesis is for them.

Chapter 1

INTRODUCTION

The research in this thesis aims at building understanding of the human brain by studying the potentials measured from its surface. The study is empirical, involving extensive data collection from human subjects in a clinical setting. It requires the application and development of data analysis tools, and it leads to direct application for the development of computer-brain interfaces and novel brain mapping techniques. The insight gained from the structure of power spectral changes in these potentials furthers the basic understanding about how the human neocortex computes, stores and processes information.

At the coarsest level, electrical activity in the human cortex is easy to observe, and has been so since the early 20th century through electroencephalography (EEG). Activity can be recorded simply by placing two electrodes on the scalp, e.g., one above each ear and recording the electric potential between them. The potential difference between two such electrodes changes with time, and also demonstrates changes with behavior (by closing the eyes or moving a limb). We measure the same type of potential differences, but directly from the surface of the brain, and from a high density electrode array.

In this thesis, we quantify how distinguishable such potential changes are from one another, and demonstrate that they can be associated with particular behavior. This knowledge allows us to map the brain in a novel way, and allows subjects to use the changes in these potentials to directly control devices in the context of a brain computer interface. In this introduction, we first sketch the basic organization of the brain, and then introduce the series of questions that encompass our research. Chapter 2 contains a methodological overview of the measurement technique. Chapters 3-7 represent specific projects as they have been

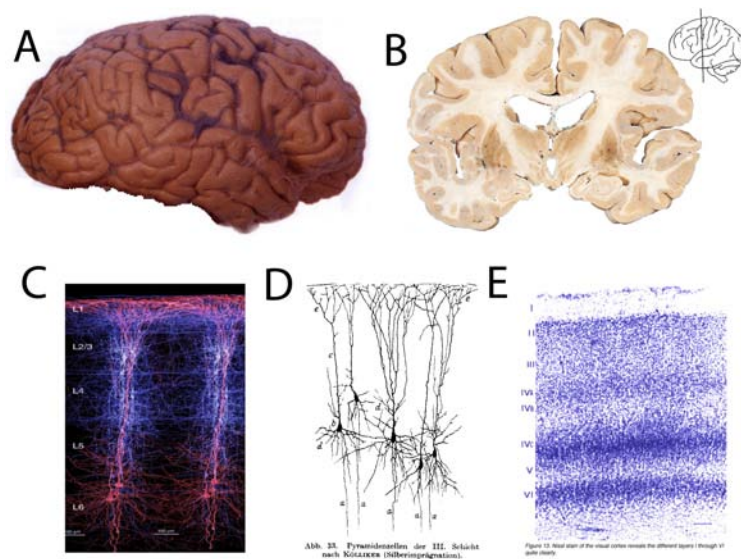


Figure 1.1:

A: Brain removed from skull. Note the folded sheet structure.

B: Cross-section of the brain, illustrating “white” and “grey” matter.

C: Cortical pyramidal neuron from cross-section of grey matter.

D: Many cortical pyramidal neurons, with parallel structure - note net orientation.

E: Stained cross-section of grey matter, showing distinct layers.

(A & B are from: <http://library.thinkquest.org>; C is from the Blue Brain Project; D was produced by Ramon y Cajal; E is from <http://webvision.med.utah.edu/imageswv/nissl2.jpg>)

published.

1.1 Biology underlying field potentials

At its largest scale, the cerebral cortex of the brain is a folded laminar sheet (fig 1.1 A). Unmagnified observation by eye suggests that evolution selected for an overall organization that maximized the two-dimensional area of this tissue. That is, the structure along this surface is mostly translationally invariant (one spot of the cortical surface appears similar to another when viewed with the naked eye). The structure along an orthogonal cut reveals, at the most coarse grained scale, a division into light and dark regions. Inspection of the dark (“gray matter”) portion, at a higher resolution, with the aid of a magnifying glass and ink stain, reveals clear layering within (fig 1.1 C, several lamina - 6 layers in all of cortex

except for limbic lobe (where there are 3-4 layers)). At first glimpse, this suggests that evolutionary selection optimized it to have a massively parallel organization, with some kind of intrinsic hierarchy associated with the layering (fig 1.1 D). A more careful inspection of the lighter, “white matter”, reveals that it is fibrous (and otherwise homogenous), and that these fibers run transverse to the layering of the gray matter.

Further inspection, with the aid of a microscope, reveals that brains are made up of many bag-like objects called cells (new figure 1.2 A). A subset of them, with extensive interconnectedness and dynamic electrical properties (on millisecond timescale), are named neurons. Muscle cells also have electrical properties, but they use the electrical change to trigger physical change (contraction)). Cells have insulating membranes (figure 1.2 B), which isolate an internal conducting bath (ions in solution) from an outer conducting bath (ions in solution). These conducting baths are primarily water and salts, but they also have many different amine based structures (proteins) and hydrocarbon based structures (lipids/hormones). These structures and ion species, have different concentrations inside each neuron, and in the conducting bath that the cells are suspended in. Allowing a substance to selectively cross the neuronal membrane in either direction can be a form of communication, and neurons are optimized to change their global properties based upon either the binding of one protein or lipid to another, or potential changes due to a small change in the concentration of a particular ion.

The different concentration of each ion species inside and outside the neuron establishes battery potentials, which can be exploited for computation and information transfer in the brain. Selective inward and outward current can be turned on and off by opening and closing specialized “channels” which allow only a particular ion species to cross the neuronal membrane. Charge can move passively with the potential gradient, and it can also move against the potential gradient, driven by a chemical gradient of more influence. Some of these selectively open/close when triggered by a specific chemical signal. Others selectively open and close when they have a specific potential across them. The opening and closing properties of these are highly non-linear and allow for soliton-like propagation of electric

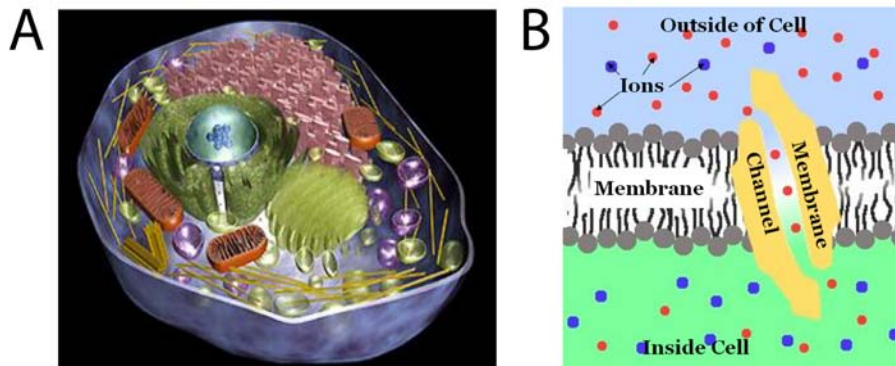


Figure 1.2:
A: Exposed cell, illustrating internal structures, and neuronal membrane.
B: Cross-section of the neuronal membrane - specialized channels allow only specific ion species to cross.
 (Picture in A from: Eukaryotic Cell cross section for Victory Technology)

pulses, which can carry signals to different regions of the neuron, and down tubular neuronal processes.

These tubular processes connect neurons, and this interconnection subserves neural computation. The large scale aggregate of these connective processes are visible to the eye as the white matter of the brain.

The ion pumps and ion channels create the voltages we measure at electrodes directly outside the skull (EEG) and also in our electrocorticographic (ECoG) recordings, where the electrodes are placed immediately on top of the cortex. Cross- and auto-correlations between these electrode voltages reveal spatial and temporal correlations between neuronal activity, and from them we can infer properties of neural computation at the population scale.

As explained in more detail in chapter 2, the predominant current sources that generate ECoG signals are those associated with the post-synaptic potentials at the “synapse”, which is the most common type of interface (the other is the gap junction) between neurons. At each synapse, there is a chemical switch, produced by an input signal from another neuron, where an impulse of net charge is allowed into the connection terminal, setting up

a transient dipole current in the post-synaptic cell. Because of the way that a particular class of neurons (cortical pyramidal neurons), and their processes, are organized, there is a net orientation of current dipoles produced by them. The fields due to these current dipoles, each representing the input from one cell to another, superimpose. By examining the superimposed time signal from large ensembles of neurons, we can infer some general properties of the network of correlated synaptic activity.

1.2 Experimental Setting

1.2.1 Subjects

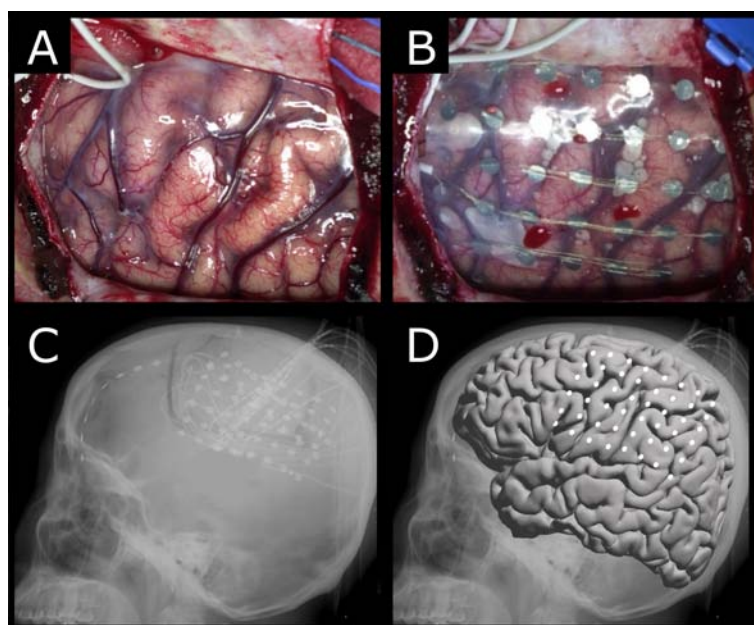


Figure 1.3: Grid placement and representation on a brain template. The brain is exposed (A) and electrodes placed in the subdural space (B) to identify seizure onset and map cortex for clinical purposes prior to resection of epileptic focus. The electrodes are localized with a lateral skull x-ray (C) and positions transformed to a standardized template (D). White dots represent the center of the electrode location in the standardized Talairach coordinate system.

Over the past 4 years, we measured the potential generated by the activity inside the cortex, using platinum electrode arrays on the brain surface. We were able to work with a cohort of subjects who had undergone placement of intracranial electrode arrays to localize seizure foci prior to surgical treatment of medically refractory epilepsy. The arrays were typically placed for 5-7 days with the location of the electrodes and duration of implantation determined independently by clinical criteria alone. Patients underwent craniotomy for electrode placement and were typically studied 4-6 days after electrode placement to allow for recovery from the surgery, as shown in situ in figure B.1. These platinum electrode arrays (Ad-Tech, Racine, WI) were typically configured as linear strips or 8x8 electrode arrays, and we studied those on the lateral part of the brain (frontal, parietal, and temporal cortex). The electrodes had 4mm diameter (2.3mm exposed), 1 cm inter-electrode distance, and were embedded in silastic. The cortical volume directly beneath each electrode contains roughly 5×10^5 neurons, and each such neuron has up to 25,000 synapses.

The organization of the brain is not entirely distributed. Different regions of the brain are specialized to perform specific function. For example, injury to a specific part of the brain might cause a loss of function in language, without damaging memory. The experimental arrays survey large areas of the brain surface, so that in given experiments, we could examine several of these different functions simultaneously (for example, movement of hand and tongue, or individual fingers).

1.3 Evolving objectives of the research

My research in this area started during my second year of medical school, 5 years ago, under supervision/collaboration with Jeffrey Ojemann (Neurosurgery) and Rajesh Rao (Computer Science). When I returned to graduate school, I began work with Marcel den Nijs (Physics), and the methodology rapidly evolved. In the past year, I have also worked with Larry Sorensen (Physics) who has, in addition to added insight and new ideas, helped to make both the experimental and data analysis aspects of the project more fundamentally sound.

In the following, I sketch the fundamental questions and summarize the salient results following the time-line ordering of the research. The subsequent chapters of this thesis are ordered differently, according to significance of the results, from a more intuitive approach to understand the underlying phenomena. Furthermore, the chapters of this thesis represent only a subset of the published work and experimental development (a list of full publications is attached at the end of this introduction). We set out to identify salient aspects of the cortical spectrum for brain mapping and feedback. This evolved as a series of experimental questions, whose answers, in turn, posed new questions. What is the nature of the cortical power spectrum, and how does it change when a particular part of the brain is “used”? That is, what changes in the cortical spectrum can we identify that tell us something about cognition?

“What is the right frequency range in the cortical power spectrum to examine correlations in brain activity?”

We performed a simple movement-based experiment in a large subject cohort which showed that low frequencies (8-32 Hz, in the “classical EEG” range) showed a characteristic decrease in power over a large area with movement. The high frequencies (76-100 Hz, in the so-called “high-gamma” range) showed an increase in power in more focal areas. Both of these findings validated observations from previous studies (Aoki 1999, Crone 1998), involving smaller cohorts, except that a more clearly motor-cortex-specific picture was found across the entire subject population. The increase in power spectral density at higher frequencies appeared to extend to the highest frequencies we could resolve with our sampling rate (Miller 2007). This posed the central question of this thesis:

Is the “high-frequency” range actually indicative of a broad-band feature, rather a characteristic specific frequency, like the famous $\alpha - \beta$ rhythms, but obscured by peaked phenomena at lower frequencies? Furthermore, does this broad band follow a power law form $P \sim f^{-\chi}$, that we can establish quantitatively?

Applications of simple spectral changes and this power law hypothesis

This hypothesis that the power spectrum is a combination of a distinct broad band and specific narrow frequency band peaks, coupled with the knowledge of appropriate frequency range choices to capture each, allowed us to ask further questions about brain activity during movement, movement imagery, and cursor-based feedback (Miller 2008), such that we could segregate the different processes and quantify them independently. It also allowed us to create useful applications for ECoG measurement in both experimental and research settings: a working brain-computer interface (Miller 2008, Schalk 2008, Leuthardt 2006), and a real-time brain mapping technique (Miller 2008) (see chapters 3, 7 and 8).

“What happens to these motor movement associate changes when an individual just imagines the motor activity?”

Motor imagery is associated with a similar spatial distribution, but the change is not as robust as that for actual movement. This suggests that similar populations of neurons are being recruiting during both activities (see chapter 6).

“What happens to these spectral changes when we couple them to feedback that the subject can use to guide behavior?”

During a successful cursor-based feedback task the changes in the signal (both in the high and low frequency bands) were augmented, in many cases beyond what was obtained during actual movement. We hypothesized a potential mechanism for this: Higher brain areas send “top-down” commands to supplemental and primary motor areas during the volitional imagery process (Miller 2008). The populations in these areas have induced activity that mimics task parameters in a “bottom-up” fashion. The intersection of these top-down and bottom-up processes might provide a mechanism for the enhanced activity (and corresponding power spectral change) during feedback-based learning in the task which we observe (see chapter 6, and appendix).

“Is there a power law? If so, over what frequency range does it extend, what is the exponent in the power law, and does it vary with brain region and activity?”

We determined that the broadband in the power spectrum obeys a powerlaw form $P(f) \sim Af^{-\chi}$, with $\chi = 4.0 \pm 0.1$, in the frequency interval $80Hz < f < 300Hz$ and it extends up to $f = 500 Hz$. This was only possible after introduced amplifier frequency-dependent amplifier attenuation and introduced noise floor were accounted for. This scaling index appears universal in all experimental data thus far (and has now become a topic of further study for the experimental group). Below a knee in the power spectrum at $f_0 \simeq 80Hz$, the broad band changes to a less steep power law. The broad band appears to obey the following phenomenological crossover form

$$P(f) \sim A \frac{f^{-\chi_L}}{1 + \left(\frac{f}{f_0}\right)^{\chi_H}}$$

with $\chi_L + \chi_H = 4$. We found $\chi_L = 2.0 \pm 0.4$.

The low frequency spectrum part requires de-convolution of the broad band from the sharp EEG rhythms. In this study, we simply identified electrode pair signals that lack those rhythms. (See chapter 4 for content)

Does this exponent change when the area of cortex beneath it becomes active?

After decoupling the peaked phenomena from the power law, using a principal component type decomposition, we found that the shape of the spectrum is preserved: the exponent doesn't change, but the amplitude does. Full decoupling of the α and β EEG rhythms from the broad band will require the development/application of advanced analysis techniques and empirical studies of more advanced correlations between the electric dipole sources. The results indicate that the overall amplitudes, A , in the power law form increase with local activity, while the exponent indices do not change. (See chapter 5 for a complete discussion)

What does this power law tell us about particular cortical function, and can we examine its dynamics independently?

We were able to demonstrate that changes in amplitude of the power law could differentiate individual fingers from each other. Furthermore, estimation of the changes in amplitude of the power law, as a function of time, tracks the dynamics of behavior so closely, as to suggest that these broadband changes are the correlate of network-level physiological mechanisms.

The interpretation of the values of the critical exponents $\chi_L + \chi_H = 4.0 \pm 0.1$ $\chi_L = 2.0 \pm 0.5$ is open to debate at this point. If it turns out these exponents are integers, it might well be that the power spectra (auto correlation functions) do not reflect the computational complexity, because such power law forms (integer exponents) can be explained by various forms and combinations of uncorrelated or exponential fast decaying correlation functions and with Lorentzian form factors and low pass filtering. Unraveling these types of issues will be at the core of our future research.

List of Publications

- Blakeley*, T., *Miller, K.J.**, Rao, R.P.N., Ojemann, J.G., 2008 **Localization and classification of phonemes using high spatial resolution ECoG grids** (In Submission, * indicates equal contribution)
- Blakeley, T., *Miller, K.J.*, Zanos, S., Rao, R.P.N., Ojemann, J.G., 2008 **Robust long term control of an electrocorticographic brain computer interface with fixed parameters.** (In Submission)
- Crawford, B., *Miller, K.J.*, Shenoy,P., Rao, R.P.N. 2006 **Real-Time Classification of Electromyographic Signals for Robotic Control** Proc. AAAI conference
- Darvas, F., *Miller, K.J.*, Rao, R.P.N., Ojemann, J.G., 2008 **Non-linear phase-phase coupling mediates communication between distant sites in human neocortex** (In Submission)
- Holmes, M.D., Micah Brown, Don M. Tucker, Russell P. Saneto, *Kai J. Miller*, Gagandeep S. Wig, Jeffrey G. Ojemann 2007 **Confirmation of dense array EEG localization of neocortical seizure onset and propagation,** Neurology (currently in submission)
- Kim, W., Miller, J.W., Ojemann, J.G., *Miller, K.J.*, 2008 **Ictal Localization by Invasive Recording of Infralow Activity with DC-Coupled Amplifiers,** (In Submission)
- Leuthardt, E.C., *Miller, K.J.*, Anderson, N., Schalk, G., Dowling, J., Moran, D., Ojemann, J.G., 2007 **Electrocorticographic Frequency Alteration Mapping (EFAM), A Novel Clinical Technique for Mapping Motor Cortex** Neurosurgery 60: ONS-260-ONS-271, 2007 DOI: 10.1227/01.NEU.0000255413.70807.6E
- Leuthardt, E.C., *Miller, K.J.*, Schalk, G., Rao, R.P.N., Ojemann, J.G., 2006 **Electrocorticography-based brain computer interface—the Seattle experience.,** IEEE Trans Neural Syst Rehabil Eng. Jun;14(2):194-8

- **Miller, K.J.**, Leuthardt, E.C., Schalk, G., Anderson, N., Rao, R.P.N., Moran, D., Ojemann, J.G., *2007 Spectral Changes in Cortical Surface Potentials during Motor Movement*, J Neurosci, 27(9):2424-2432

- **Miller, K.J.**, Makeig, S., Hebb, A.O., Rajesh P.N. Rao, R.P.N., denNijs, M., Ojemann, J.G., *2007 Cortical Electrode Localization from X-Rays and Simple Mapping for Electrocorticographic Research: The "Location On Cortex" (LOC) package for Matlab*. J Neurosci Meth, 162; 303-308

- **Miller, K.J.**, Schalk, G., Leuthardt, E.C., Shenoy, P., Rao, R.P.N., Ojemann, J.G. *2007 Correlation in Paired One-Dimensional, Closed Loop, Overt, Motor Controlled BCI* Journal of Technical University of Graz, Special Issue: Brain Computer Interfaces, 2007

- **Miller, K.J.**, denNijs, Marcel, Shenoy, Pradeep, Miller, John W., Rao, Rajesh P.N., Ojemann, Jeffrey G., *2007 Real-time functional brain mapping using electrocorticography*, NeuroImage 37 (2007) 504-507 doi: 10.1016/j.neuroimage.2007.05.029

- **Miller, K.J.**, Rao, R.P.N., and Ojemann, J.G., *2007 The Behavioral Split in the Gamma Band* Neural Engineering, CNE '07. 3rd International IEEE/EMBS Conference on; p 465-468; DOI: 10.1109/CNE.2007.369710

- **Miller, K.J.**; Hebb, A.O.; Ojemann, J.G.; Rao, R.P.N; den Nijs, M, *2007 Task-Related Principal Component Analysis: Formalism and Illustration* IEEE Eng Med Biol Soc. 2007: 5469-72.

- **Miller, K.J.**; Shenoy, P.; den Nijs, M; Sorensen, L.B.; Rao, R.P.N.; Ojemann, J.G., *2008 Beyond the Gamma Band: The Role of High Frequency Features in Movement Classification*, IEEE Trans Biomed Eng. 55(5): p. 1634-1637.

- **Miller, K.J.** and Ojemann, J.G., *2008 A Simple, Spectral-Change Based, Electrocorticographic Brain-Computer Interface* (In Print, Book Chapter)

- **Miller, K.J.**; Shenoy, P.; den Nijs, M; Sorensen, L.B.; Rao, R.P.N.; Ojemann, J.G., *2008 ECoG observations of power-law scaling in the human cortex.* (In Submission, see <http://arxiv.org/abs/0712.0846>)
- **Miller, K.J.**, Schalk, G.S., denNijs, M., Fetz, E.E., Ojemann, J.G., Rao,R.P.N. *2008 Augmentation of Cortical Activity by Motor Imagery-Based Learning,* (In Submission)
- **Miller, K.J.**; Zanos, S.; Fetz, E.E.; den Nijs, M; Ojemann, J.G, *2008 Decoupling the Cortical Power Spectrum Reveals Individual Finger Representation in Humans.* (In Submission)
- **Miller, K.J.**, Blakeley, T., Schalk, G.S., denNijs, M., Ojemann, J.G., Rao, R.P.N., *2008 Three Cases of Feature Correlation in an Electrocorticographic BCI.* (In Submission)
- Ojemann, J.G.; Leuthardt, E.C.; **Miller, K.J.**, *2007 Brain-Machine Interface: Restoring Neurological Function through Bioengineering,* Clin Neurosurg 54; 28 doi:0148-703/07/5401-0001
- Penny, W., Duzel, E., **Miller, K.J.**, Ojemann, J.G., *2008 Testing for Nested Oscillation,* (In Submission)
- Schalk, G., **Miller, K.J.**; N.R. Anderson; J.A. Wilson; M.D. Smyth, J.G. Ojemann; D.W. Moran; J.R. Wolpaw; E.C. Leuthardt, *2008 Two-Dimensional Movement Control Using Electrocorticographic Signals in Humans* J Neural Eng. 5(1): p. 75-84.
- Schalk, G., Leuthardt, E.C., Moran, D., **Miller, K.J.**, Ojemann, J., Wolpaw, J.R. *2006 Towards two-dimensional cursor control using electrocorticographic signals.* Proceedings of the 11th International Conference on Human-Computer Interaction
- Schalk, G., J. Kubanek, **Miller, K.J.**, N. Anderson, E.C. Leuthardt, J.G. Ojemann, D. Limbrick, D. Moran, L.A. Gerhardt, J.R. Wolpaw *2007 Decoding Two-Dimensional Movement Trajectories Using Electrocorticographic Signals in Humans,* J. Neural Eng. 4 264-275 doi:10.1088/1741-2560/4/3/012

- Shenoy, P., *Miller, K.J.*, J.G. Ojemann, R.P.N. Rao *2007 Two class robust classification of ECoG signals during repeated motor movement* Journal of Technical University of Graz, Special Issue: Brain Computer Interfaces, 2007
- Shenoy, P., *Miller, K.J.*, Ojemann, J.G., Schalk, G., Rao, R.P.N. *2007 Generalizable Features for Electrographic BCIs* IEEE Trans Biomed Eng. 55(1): p. 273-80.
- Shenoy, P., *Miller, K.J.*, Crawford, B., Rao, R.P.N. *2008 Online Electromyographic Control of a Robotic Prosthesis* IEEE Trans Biomed Eng. 55(3), 1128-1135
- Shenoy, P.; *Miller, K.J.*; Ojemann, J.G.; Rao, R.P.N., *2007 Finger Movement Classification for an Electrographic BCI*, Neural Engineering, CNE '07. 3rd International IEEE/EMBS Conference on, pp192-195, doi:10.1109/CNE.2007.369644
- Shon, A., *Miller, K.J.*, Ojemann, J.G., Holmes, M.D., Rao, R.P.N. *2007 Predicting Cortical Potentials using Simultaneous Transcranial Recordings*, (In submission)
- Zanos, S, *Miller, K.J.*, Ojemann, J.G., *2008 Electrographic spectral changes associated with ipsilateral individual finger and whole hand movement* (In Submission)

Chapter 2
WHAT WE MEASURE



Figure 2.1: All experiments are done in the clinical environment, where the signal is split and amplified in parallel with the clinical amplification.

In this chapter, we discuss aspects of the brain potentials that we measure: “Hardware considerations” (amplifiers and electrodes), “Wetware considerations” (the biological

processes that create macroscale potentials), and “Software considerations” (spectral calculation and fitting techniques for this type of data.)

2.1 Electrodes

ECoG is available from frequently performed procedures in patients suffering from medically intractable epilepsy (Figure 2.1). Such patients undergo elective placement of electrodes on the surface of the brain when the seizure localization is not evident or sufficiently detailed from non-invasive studies. These electrodes are also placed, in some situations, to localize function such as movement or language prior to a neurosurgical resection. The same electrodes can record ECoG and deliver currents which disrupt the function of the underlying cortex. The implanted electrode arrays are typically only those which would be placed for diagnostic clinical purposes. Most often (as in our case), these are $\sim 2.5\text{mm}$ in diameter with a spacing of 1-cm from center-to-center. While this is somewhat coarse, it is fine enough to resolve individual finger representation and may be sufficient to extract many independent control signals simultaneously [96]. At some institutions, preliminary results are emerging using smaller electrodes and denser arrays [9], and these finer resolution grids may prove to resolve independent function and intention better than the current clinical standard.

The platinum electrode arrays (Ad-Tech, Racine, WI), which we use to measure the potential at the brain surface, were typically configured as linear strips or 8×8 electrode arrays (Figure 2.2). The electrodes had 4mm diameter (2.3mm exposed), 1 cm inter-electrode distance, and were embedded in silastic. In the gray matter beneath the $\sim 5\text{mm}^2$ exposed area of each platinum ($\sigma_{Pt} = 106\text{n}\Omega$ at 20°C) electrode, there were roughly 5×10^5 neurons (Figure 2.1). As discussed below, each electrode measures the potential due to the superposition of dipole producing post-synaptic events in the dendritic trees of each of these neurons. The electrodes are placed directly on the cortical surface, and measure potentials via ohmic contact (Figure 2.1). The change in potential at the interface is

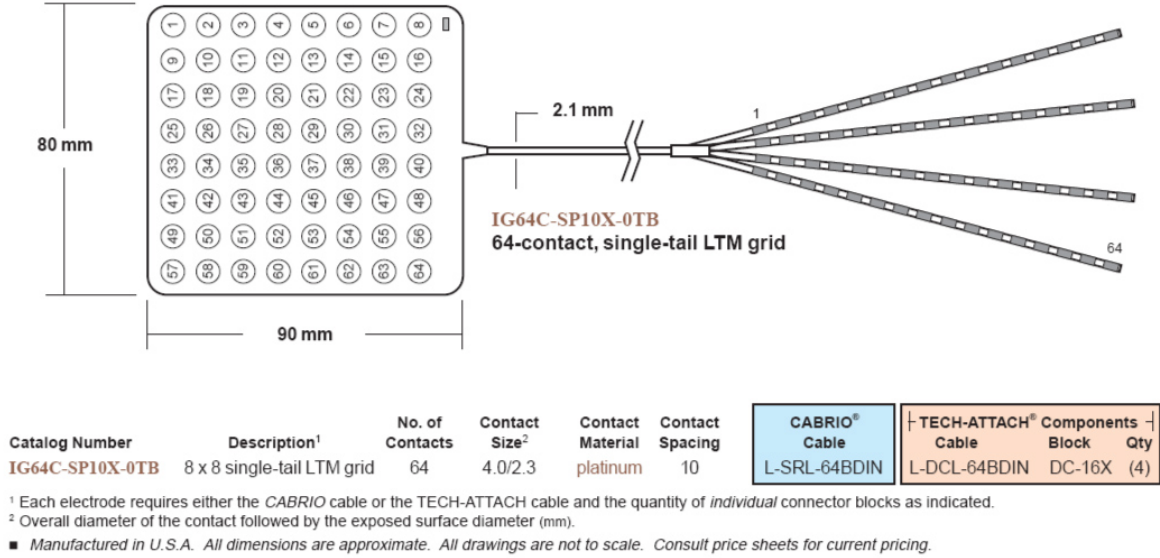


Figure 2.2: Electrode schematic for the standard clinical array used for the experiments in this thesis. From the Ad-Tech 2008 catalog, <http://www.adtechmedical.com/catalog.htm>

$$\Phi^{(electrode)} = \frac{\sigma^{(electrode)}}{\sigma^{(brain)}} \Phi_{\perp}^{(brain)} \quad (2.1)$$

With Φ_{\perp}^{brain} the electric potential of the cortex at the location of the electrode.

It is very helpful to know where each electrode lies in relation to the brain anatomy below it. For example, in our quantitative power spectra studies, [95], electrodes that were above vasculature (blood vessels) were directly rejected because the signal that they measure is strongly attenuated. It can also be extremely useful to know what the relationship is between each electrode and known anatomical landmarks (sulci, gyri, etc) on the brain. Careful comparison of operative photographs taken before and after the array is placed allow one to do this (Figure 2.1).

The electrode positions may also be compared across individuals, by calculating their

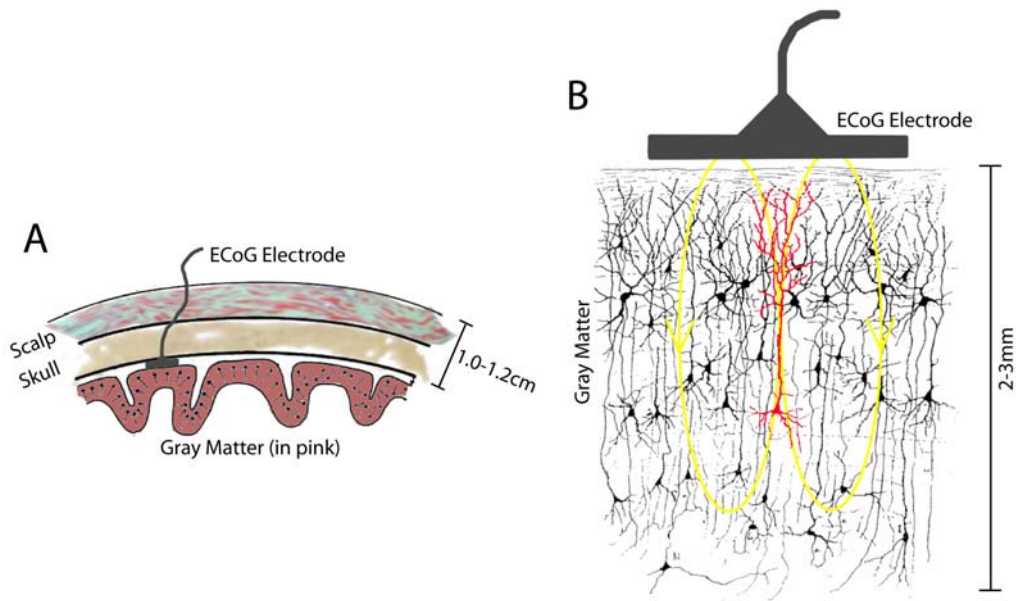


Figure 2.3: Electrode transverse picture (A) The platinum electrodes are placed directly on the brain surface, beneath the skull and scalp. (B) The electrodes are thought to measure primarily potentials due current dipoles in the dendrites of the cortical pyramidal neurons (here, one is shown in red) of the gray matter directly beneath.

positions in a normalized cortical coordinate space. There is a standard convention for three orthogonal axes: The first is given by the left-right symmetry of the head, the second is a line segment which passes through the anterior and posterior commissures, and the third is orthogonal to these two (Figure 2.5). The origin is taken to be the anterior commissure. This reference frame is known as the “Talairach” coordinate system [148].

2.2 Amplifiers

The ECoG recording is, by necessity, in the context of clinical amplification and recording, so the experimental recording must also take place in the context of clinical amplification with commercially available amplifiers (eg, XLTEK, Synamps, GugerTech, Grass). Most clinically relevant EEG features are detected visually. Classically the clinical information

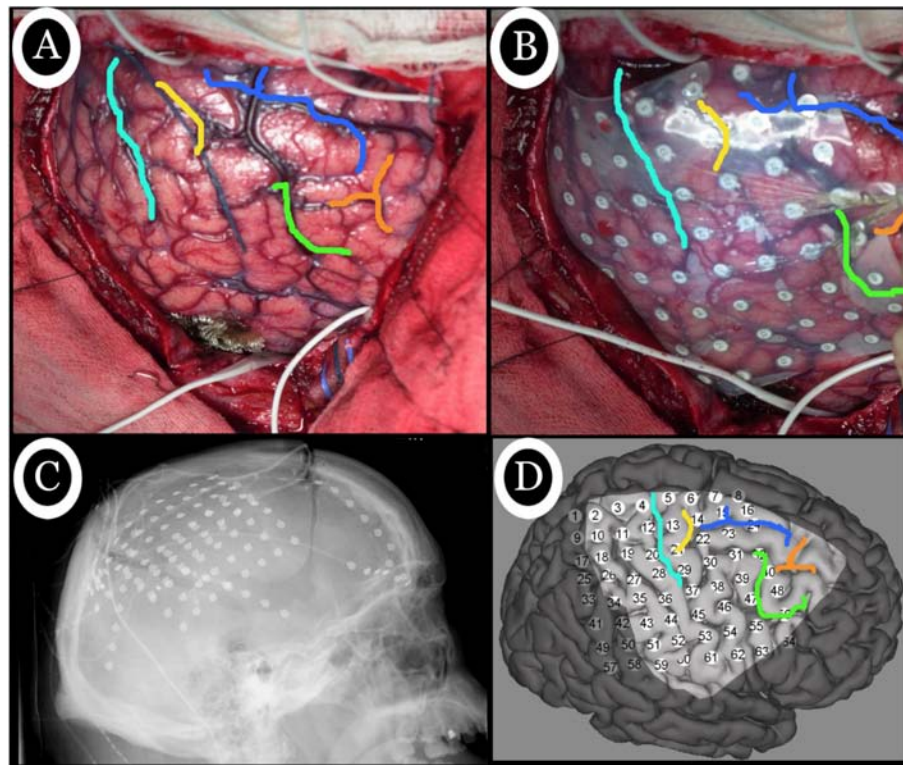


Figure 2.4: (A) A photograph taken before placement of a subdural grid array is used to identify brain sulcal landmarks. (B) The same sulci are identified after electrode placement. (C) The lateral x-ray used to identify the positions of cortical electrodes using the LOC package [91]. (D) The identified electrode positions with the exposed craniotomy unshaded, and the sulci corresponding to those identified in A and B are shown. The cortical schematic in D has been rotated so that its orientation is closer to that of A and B. The figure illustrates how landmarks in the brain can be identified from operative photographs, and both structurally useful landmarks (like gyri, etc), and potentially complicating factors (like vasculature) can be identified and taken into account when assessing the result of analyses.

explored is between 3-40Hz, so the settings on the clinical amplifiers may be adequate for those diagnostic purposes, but they are inadequate for research purposes. Recent advances have suggested that higher frequencies may be clinically relevant so many newer amplifier systems include higher sampling rates (at least 1kHz) as an option to allow for measurement of signals of 200Hz or higher. This varies by institution, and the clinical recording

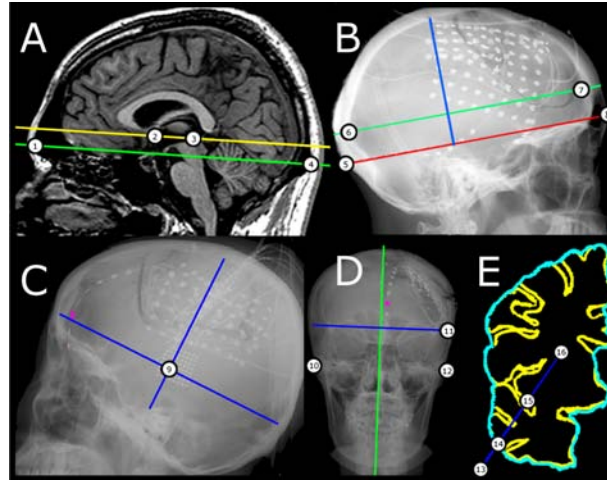


Figure 2.5: Electrode localization in standardized coordinates using the x-ray: (A) The anterior commissure - posterior commissure (AC-PC) line (2 to 3) defines the Talairach y axis, shown in yellow on a patient MRI. The glabella-inion (GI) line (1 to 4) is parallel to AC-PC line and the glabella (1,8) and inion (4,5) are therefore used to approximate the AC-PC line. (B) X-ray image of the same patient. The y-axis (6 to 7, teal) is positioned parallel and superior to the GI line (5 to 8, red), 21% along the length of the longest perpendicular line segment joining the GI line to the skull's inner table (perpendicular line - blue). The distance between posterior and anterior inner tables of the skull (6 to 7) along the y axis is scaled to template dimensions. (C) The y-z origin, the estimated position of the AC, is defined 115 mm anterior of the midpoint (9) of the line segment between the two skull tables. (D) A vertical line segment is drawn that perpendicularly bisects a user-defined line segment joining two symmetric structures (10 and 12). The x,y,z origin is defined as the intersection of this line segment with the y-z origin defined on the lateral projection. The maximal biparietal distance measured on the AP x-ray (11) is scaled to the template brain. (E) Points that do not fall on the cortex after identification using the AP and Lateral x-rays (e.g. 13 and 15) may be projected to the surface of cortex by switching to spherical coordinates, with the center of mass of the surface template (shown in light blue / white in BW figure) as the origin (16). The point on the surface template (14) for this solid angle (dark blue line / white line in BW figure) defines the replacement location, which is converted to standard Talairach coordinates. The process of localizing electrode array positions and plotting data to them is laid out in the supplement [91].

settings will vary even within institutions, depending upon the clinical and technical staff managing the patient. Experimentalists must obtain either the clinically amplified signal,

or split the signal and amplify it separately. Using the clinical signal has the advantage that less hardware is involved, and that there are no potential complications because of the dual-amplification process. Such complications include artifact/noise introduction from one system to the other, or currents between separate grounds if the two do not share a common ground. Splitting the signal has the advantage that the experimentalist can use higher fidelity amplifiers and set the amplification parameters at will, rather than having to use the clinical parameters, which typically sample at a lower frequency than one would like, and often have built in filtering properties which limit the usable frequency range. The ground chosen, which must be the same as the clinical ground to avoid complication, is typically from the surface of the scalp. Most amplifiers have a built-in choice of reference (fig 2.6), which each electrode in the array will be measured with respect to. These may also be from the scalp, as they often are clinically, or they may be from an intra-cranial electrode. Because we needed much higher sampling rates than the clinical recordings obtained, we always split the signal. The institutional constraints of working with humans in the clinical setting required that we use FDA approved, clinically designed, amplifiers. We used Synamps2 amplifiers (Neuroscan, El Paso, TX) in parallel with clinical recording (BMSI or xtek amplifiers for all others). These signals had a system-imposed band-pass filter, but we could characterize and correct for the the higher frequency roll-off from this built-in filter, after the power spectral density was calculated (see below).

2.2.1 Choice of reference.

The subdural electrode array will initially be referenced with respect to an internal (brain surface) electrode, or an external, scalp, electrode by the clinical staff (fig 2.6A). An internal reference electrode may be preferable because its signal and noise properties are more similar to those of the array. We often found it useful to re-reference the electrode array in one of several ways. Each electrode may be re-referenced with respect to a single electrode from within the array, chosen because it is relatively “inactive,” each may be re-referenced to a global linear combination of electrodes from the entire array, or each may be referenced

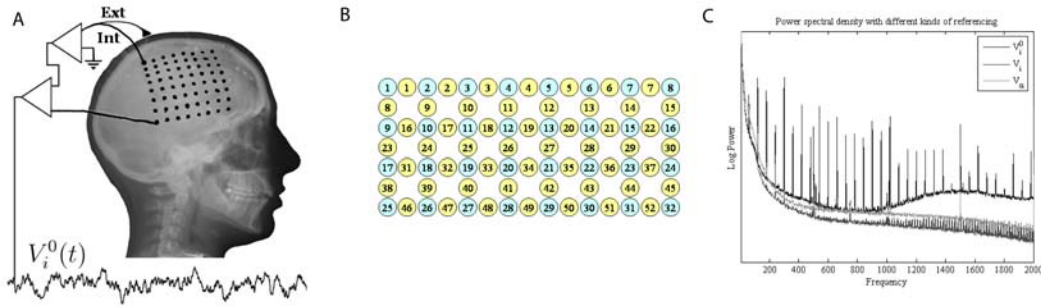


Figure 2.6: Choice of amplifier reference, and re-referencing strategy: (A) Recording scheme, with different initial reference sites: “Int” denotes internal reference, “Ext” denotes external reference. (B) Pair-wise re-referencing scheme for an 8x4 array. Blue dots indicate the original array, and yellow dots indicate pair-wise difference channels. (C) Demonstration of noise rejection by re-referencing. V_i^0 denotes the originally recorded signal. V_i denotes the common-average referenced signal. V_α denotes the pair-wise re-referenced signal.

to one or more nearest neighbors. Re-referencing with respect to a single electrode is useful when the one in the experimental/clinical montage is sub-optimal (noisy, varies with task, etc), but it means that the experimenter has introduced an assumption about which electrode is, in fact, appropriate. The simplest global referencing scheme is a common average re-reference: the average of all electrodes is subtracted from each electrode. The advantage of this is that it is generic (unbiased, not tied to an assumption), and it will get rid of common-mode phenomena. One must be careful that there are not any electrodes that are broken, or have extremely large contamination, or every electrode will be contaminated by the re-referencing process. Local re-referencing may also be performed, such as subtracting the average of nearest-neighbors (Laplacian), which ensures that the potential changes seen in any electrode are spatially localized. One may also re-reference in a pair-wise fashion, producing bipolar channels which are extremely local, but phenomena cannot be tied to a specific electrode from the pair without examination of other, adjacent, pairs. We discuss the 3 basic re-referencing schema in further detail: Common average, pair-wise, and Laplacian. *Common average re-referencing* (CAR) consists of subtracting out the average of the whole array, from each channel, at each point in time. It is useful when there may be common

external contamination to all of the array, but not to the initial reference (or vice-versa), and serves as a generic, unbiased technique. The drawback is that uncorrelated noise is added to every channel. Broken or artifactual channels may potentially contaminate every channel during the re-referencing, and one must be careful to discard them before re-referencing.

$$V_i(t) = V_i^0(t) - \frac{1}{N} \sum_{j=1}^N V_j^0(t) \quad (2.2)$$

Where our scalp or brain surface referenced original signals are $V_j^0(t)$ (j denotes the electrode, and N is the total number of electrodes).

Pair-wise re-referencing is the technique of generating a new set of channels by taking the pair-wise difference between all pairs of adjacent channels, at each point in time, as illustrated in figure 2.6B.

$$V_\alpha(t) = V_i(t) - V_k(t) \quad (2.3)$$

where α labels the channel pair ($i-k$), and typically electrodes i and k are nearest neighbors. This is the most “local” technique - anything surviving subtraction is, by necessity, different on the scale of separation in the grid (in our case, 8mm). In the case of an 8x4 electrode array, there are 52 pair-wise difference channels generated from the 32 electrodes. The results obtained for each channel will be fundamentally ambiguous because there is no way of knowing which of the two electrodes a given phenomena arose from. One must compare different channel pairs to identify which electrode the results came from. This method is the best for eliminating common mode noise while adding the minimal amount of uncorrelated noise.

“Laplacian” re-referencing is a term used generically to mean that each electrode is re-referenced with respect to the electrodes which immediately surround it. There are multiple schema for doing so. The most simple, for a rectilinear array such as ours, is to subtract the mean of the 4 nearest neighbors.

$$V_i(t) = V_i^0(t) - \frac{1}{4} \sum_{j=1}^4 V_j^0(t) \quad (2.4)$$

where j indexes nearest neighbors only (4 total in a rectangular array). This referencing scheme is optimal for the case that the phenomena exists in only one electrode, and none of its neighbors. These “Laplacian” schema are trade-offs between pair-wise approaches and common averaging approaches. The channels are more directly attributable to a single, center, electrode, but are more local than a complete common average reference.

There also are higher order referencing/weighing schema (ICA/PCA/CSP), which require assumptions (pre- or post- measurement) about correlations between different electrode signals and array configurations [135, 51, 63, 53].

2.2.2 Sampling Frequency

Choosing a sampling frequency is important - there is often a trade-off between signal fidelity and the practical issues of manageable data sizes and hardware limitations. Classic studies sampled at low rates ($< 150Hz$) because the focus was on the $\alpha/\beta/\gamma$ rhythms below 40 Hz . We discovered features in the power spectrum all of the way to 300 Hz , and perhaps beyond [95, 94, 96]. Therefore, to properly measure these features, one should be sure to have high signal fidelity up to at least 300 Hz (i.e. sampling rates should be above ~ 750 Hz , and the sampling rate may have to be even higher if the amplifiers used have built-in filtering properties.) At the very least, to capture the spatially focal high frequency change, one must have large bandwidth above a behavioral split at 35-55 Hz [94]. We typically sampled at 1000 Hz . In order to get a good estimate of power law activity, we must sample with the largest feasible bandwidth, and so, in a set of experiments to characterize these spectral phenomena, we sampled the potential at 10 kHz

2.2.3 Amplifier frequency-dependent attenuation

At the 10 kHz sampling rate, the built in amplifier roll-off was measured as a function generator by repeatedly scanning through frequencies at fixed amplitude. This was done for the 10 kHz sampling rate, scanning from 15-4000 Hz , and the 1 kHz sampling rate, scanning from 10 Hz to 300 Hz . This is demonstrated in figure 4.8.

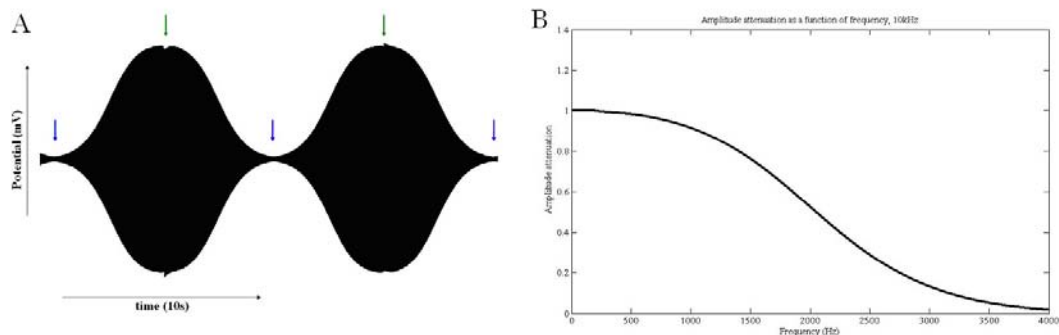


Figure 2.7: **Frequency-dependent amplifier amplitude attenuation:** The frequency-dependent amplifier attenuation could be calculated by using a function generator to scan through frequencies at a constant amplitude. The range shown here is from 15Hz (green arrows in A) to 4000Hz (blue arrows in A). The attenuation as a function of frequency (in B) could be determined directly from the timeseries (in A).

2.2.4 Amplifier noise floor

A distribution of noise floor levels was estimated by recording across an arrangement of resistors (Figure 4.9), chosen to have roughly the same resistance as the brain tissue, in parallel with the clinical amplifiers. Since it is impossible to measure the exact noise in the clinical recording (i.e. the active properties in the brain cannot be turned off in our setting), the noise floor was also fit using a recursive, self-consistent, approach. This is discussed and demonstrated in [95].

2.2.5 Potential sources of amplifier noise

There are intrinsic sources of amplifier noise in electric potential measurement [45]. We will describe two that arise from the fact that current comes from quantized units (electrons). The first of these, “Johnson Noise” (ε_J) comes from electron movement due to thermal kinetic energy in conducting media at finite temperature. The second, “Shot noise,” (ε_S) comes from the fact that a current made up of discrete units will be subject to variation from counting (Poisson) statistics. The last we will consider is “Flicker” (or $1/f$) noise (ε_F),

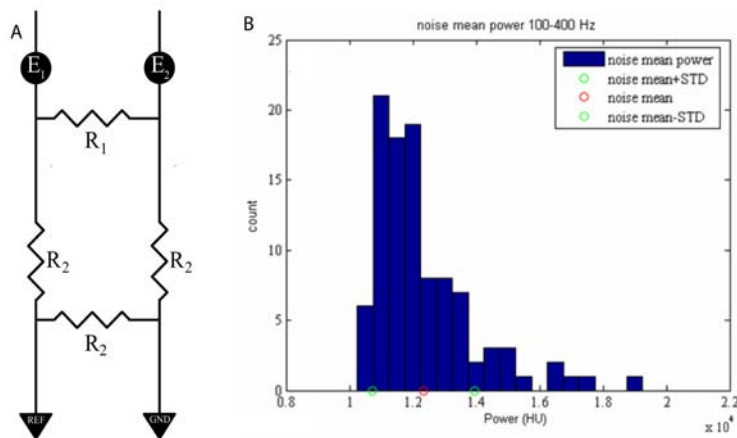


Figure 2.8: **Amplifier Noise Floor Estimation:** The noise floor was estimated experimentally by measuring the potential across an arrangement of resistors (A). The resistance values were based upon electrode-reference impedances that were measured online. Ground floor estimates were made with this configuration of resistors. R2 was set to $10k\Omega$, with R1 set to 0.5Ω (although noise values were robust against R1 changing up to $1k\Omega$). The resistor ensemble was hooked up in parallel with the clinical amplifiers, and a set of noise floors was estimated (B, “HU” denotes amplifier power units before conversion).

due to fabrication details of the electronic components, and have no easy description.

The amplifiers will have many different sources of each kind of noise, and our noise floor measures will represent a superposition of these (e.g. $V_{noise} \sim \varepsilon_J + \varepsilon_S + \varepsilon_F$).

Johnson Noise

Randomized thermal movement of electrons in a conducting medium will produce what is known as Johnson noise (The equivalent of Brownian motion in conductors). Since electrons carry charge, transient currents will produce fluctuations in the potential across the conducting medium. Because the thermally induced velocity is random, the mean current and potential change will be zero, but the mean squared current and potential change will not. Standard kinetic theory tells us that the mean kinetic energy of a point mass is $\frac{1}{2}k_B T$ per degree of freedom ($\frac{3}{2}k_B T$ for 3 translational degrees of freedom, $k_B = 1.38 \times$

10^{-23} Joules/deg denotes Boltzmann's constant). This provides us with the temperature dependence of Johnson noise. Nyquist, in 1928, described the Johnson noise across a resistor of resistance R as producing an EMF, denoted by RMS voltage ε_J , of

$$\varepsilon_J = \langle \varepsilon_{J'}^2 \rangle^{\frac{1}{2}} = \left(4k_B RT \int df (A^2(f)) \right)^{\frac{1}{2}} \quad (2.5)$$

where $A(f)$ is the transfer function of the amplifiers. If the amplifiers are idealized on the interval f_1 to f_2 , and $A^2(f) \rightarrow 1$, then

$$\varepsilon_J = (4k_B RT(f_2 - f_1))^{\frac{1}{2}} \quad (2.6)$$

Shot Noise

“Shot noise” is noise that is present due to fluctuations in the counting statistics of currents. That is, current is made up of moving electrons, and as these electrons come into contact with some surface, there will be fluctuations in the number of electrons per unit time, deviating from the mean current according to Poisson statistics. The Poisson noise distribution will have mean equal to N , the number of electrons producing the current, $I = \frac{Nq_e}{\Delta t}$, where N is the number of electrons making contact with the surface during time Δt , and q_e is the charge of the electron. The variance in electron number, $\langle \sigma_n^2 \rangle$ associated with the measurement process will then also be N , with $\langle \sigma_n^2 \rangle = N = \frac{I\Delta t}{q_e}$. The RMS current associated with this shot noise process is

$$i_S = q_e \frac{\langle \sigma_n^2 \rangle^{\frac{1}{2}}}{\Delta t} = \left(\frac{q_e I}{\Delta t} \right)^{\frac{1}{2}} \quad (2.7)$$

The Δt corresponding to the measurement period of this frequency is half of a complete cycle, or $\Delta t = \frac{1}{2f_s}$, if the measurement device has a maximum sampling frequency, f_s . So,

$$\begin{aligned} i_S &= (2q_e I f_s)^{\frac{1}{2}} \\ \varepsilon_S &= R i_S = R (2q_e I f_s)^{\frac{1}{2}} \end{aligned} \quad (2.8)$$

where R is the resistance across which the noise is measured. In our amplifiers, the signal is often sampled at very high rates (30kHz+), and then digitized at a lower rate (averaging

across samples) so the contribution of shot noise as a function of “sampling frequency” (digitization rate) is not straightforward.

Flicker Noise

Flicker noise can emerge from a variety of sources, including, but not limited to, impurities in the conducting media and generation and recombination noise in a transistor (due to base current) [128]. It is always related to direct current passage through the electronic device. It is also called $1/f$ noise, because it tends to have a $1/f^\alpha$ power spectrum. As such, the “Flicker” EMF can be described by (if $\alpha = 1$)

$$\varepsilon_F = \left(V_F^2 \int_{f_1}^{f_2} df \frac{1}{f} \right)^{\frac{1}{2}} = V_F \left(\ln \left(\frac{f_2}{f_1} \right) \right)^{\frac{1}{2}} \quad (2.9)$$

where V_F is a proportionality constant.

Intrinsic noise, and the experimental noise floor The noise floors we encountered in the clinical amplifiers were much higher than expected from these fundamental processes. This must have to do with the internal make-up of the amplifiers (active feed back etc). Therefore we measured the noise floors directly. The measured floors varied between the channels of the multi-channeled amplifiers and seemed to vary in time (between subjects and sessions). In the end, we had no other option than to treat the noise floor as a dynamic variable in the power spectra (e.g., in fitting of the power law shape), and make sure that the distribution of discovered noise floors were consistent with the offline-measured noise floor distribution [94].

2.3 Neural Structures that give rise to potentials

2.3.1 The current dipole

The basic computational unit of the brain is a cell called the neuron [69, 144]. Neurons differ from other cells in the body because they have the ability to use electric signalling changes to rapidly process a set of inputs, integrate them over time, and send electrical signals over

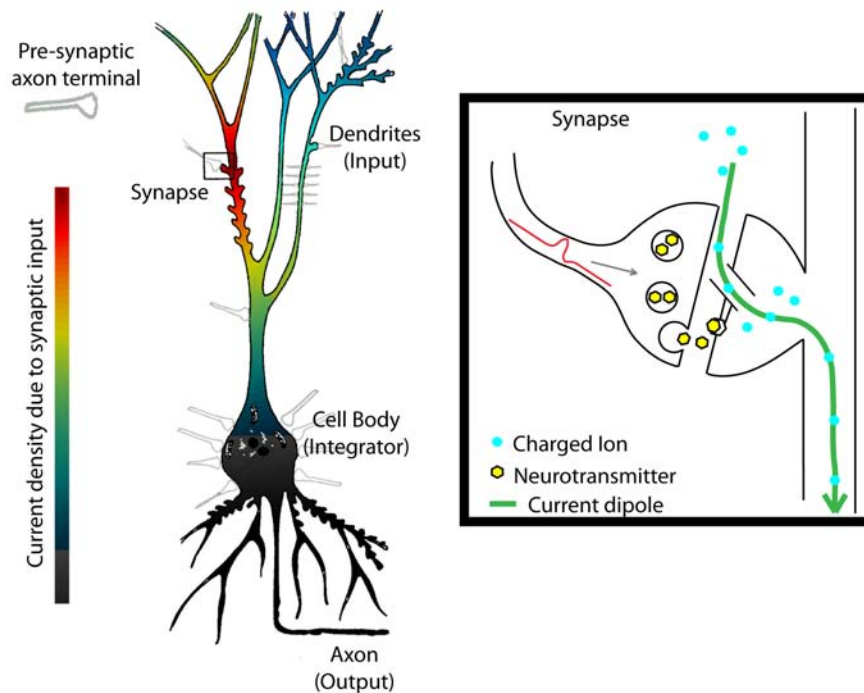


Figure 2.9: The synapse, where one neuron meets another. An action potential arriving from a different neuron via the pre-synaptic axon terminal, triggers the release of a chemical signalling molecule (neurotransmitter), which rapidly diffuses across the space between the pre-synaptic axon and the post-synaptic dendrite (“synaptic cleft”), binding to a receptor on the dendrite side of the synapse. This receptor is coupled to a channel, which opens, selectively allowing a particular species of charged ions to move in or out of the cell, creating a transient current (characterized below). (figure partially modified from [105])

long distances, where they communicate with other neurons. Like neurons, muscle cells have electric behavior, and they electrically conduct as well, but do not differentially process an array of inputs.

At the coarsest level, the neuron may be described as a single central body, called the soma (cell body), with tubular structures protruding from it (Figure 2.9). These tubular structures are generally segregated by their function: dendrites, where input is received and information is carried to the cell body, and axons, which carry information away from

the cell body. The structural and electrical properties of these three types of structures are different. Structurally, the soma is generally spheroidal in shape. The dendrites are a tree-like ensemble of thin tubular structures. The axons are long cables which extend to long distances to connect with other neurons.

The electrical properties of the lipid bilayer membranes of axons and dendrites are different. Axons have high densities of ion-selective channels that open and close in response to specific transmembrane potentials, capable of causing both inward and outward current, against the potential gradient (because of overwhelming concentration gradients). Dendrites have fewer active, potential sensitive membrane channels. Axons also have special wrapping (myelin) that changes the resistance and capacitance between the inside of the neuron (intracellular fluid) and the surrounding bath (extracellular fluid), and regulates the speed of the transmitted signals.

Chemical events at the synapses, interfaces between axons and dendrites, resulting in currents (“post-synaptic” current -PSC) on distal (far from the cell body) sites of the dendrites. These currents flow towards the cell body.

In the axons, signal is propagated by a near charge neutral, soliton-like travelling potential perturbation, called an action potential, which begins at the cell body and travels until it reaches a synapse with another cell, where it triggers a PSC in another neuron.

2.3.2 Action potentials, Hodgkin-Huxley and the Squid Giant Axon

In order to understand how the soliton-like action potentials are maintained in the cylindrical axonal structures, the physiologists Hodgkin and Huxley initially performed experiments in the largest axon they could find in nature: the squid giant axon. By manipulating individual ion concentrations and the potential across the neuronal membrane, they were able to develop a concrete formalism to describe the dynamics of axonal membrane physiology. Their mathematical formalization illustrates how rapid current influx and efflux produces local currents that are opposite in sign, and create a travelling soliton. From the ECoG perspective, their local electric fields cancel out (create only quadripole and higher order

potentials at the electrode). Such fields decay rapidly with distance, and change orientation (at the electrode), with the path of the axon. For these reasons, we expect the axonal action potential currents to be invisible in the large scale electrocortical potential measurements, drowned out by dendritic, post-synaptic, dipole currents. (The action potentials show up in local field potential measurements with extracellular needle electrodes.).

Here, we will briefly follow Hodgkin and Huxley's mathematical description of axonal physiology in order to understand how such action potential phenomena are generated [73, 33]. While axonal action potentials and associated currents are not expected to be visible in ECoG, they serve well to illustrate the important role ionic channels play in neuronal processes. Similar ionic channels at synapses, for example, create the electric dipole currents that are the sources observed in ECoG. In synapses, post-synaptic channel opening is triggered by chemical neurotransmitter signal, rather than characteristic transmembrane potentials. Hodgkin and Huxley modeled the squid giant axon to understand properties of information conductance and ionic behavior in neurons, but the same principles apply to axons in the human brain.

A Step-by-Step Walkthrough of the Hodgkin and Huxley Model

In the following, the model developed by Hodgkin and Huxley is detailed, step by step. All potentials are measured in mV, with respect to resting potential. We will assume that the dynamic range of the potential is bounded by -20 to 120 mV for our estimation of relevant time scales. All of the parameters are for the squid giant axon. A discretized numerical implementation is contained in [97].

Variables and Constants Relevant to the Squid Giant Axon

$$C_m = \text{membrane capacitance } (C_m = 1 \frac{\mu F}{cm^2})$$

$$R_m = \text{membrane resistance } (R_m = 3333 \Omega * cm^2)$$

$$R_l = \text{longitudinal resistance } (R_l = 29.7 \Omega * cm)$$

$$[Na^+]_{out} = \text{extracellular sodium concentration } (491 \text{ mmol} \approx 2.95 * 10^{20} \frac{1}{cm^3})$$

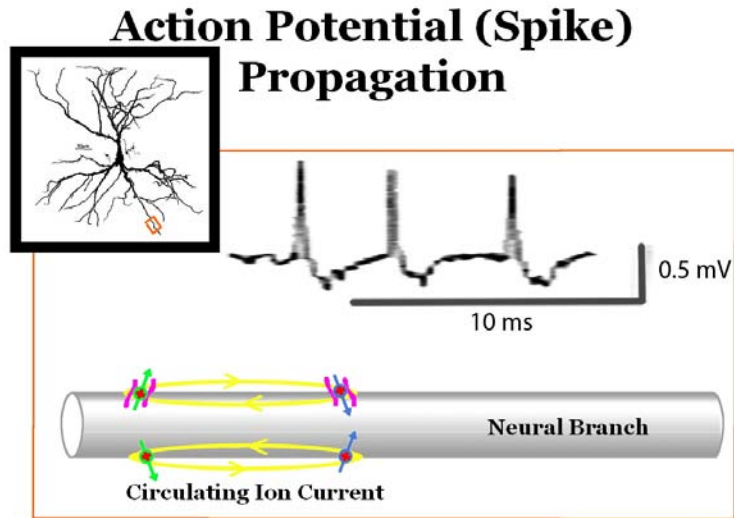


Figure 2.10: An action potential in an axon. Ion specific channels open and close in response to changes in membrane potential, allowing for selective inward or outward current. These currents themselves change the potential, and the net result is the creation and propagation of a soliton-like action potential down the axon. They are initiated in response to a jump in the potential.

$[Na^+]_{in}$ = intracellular sodium concentration ($50 \text{ mmol} \approx 0.30 \cdot 10^{20} \frac{1}{cm^3}$)

$[K^+]_{out}$ = extracellular potassium concentration ($20 \text{ mmol} \approx 0.12 \cdot 10^{20} \frac{1}{cm^3}$)

$[K^+]_{in}$ = intracellular potassium concentration ($400 \text{ mmol} \approx 2.40 \cdot 10^{20} \frac{1}{cm^3}$)

r = axonal radius ($r \approx .05 \text{ cm}$)

V = potential (mV)

Membrane current

Consider a local patch of membrane. It has a capacitance C_m . The potential difference across this capacitor depends on the flow of charge. Currents flow along the axon channel, I_m , and across the membrane, $I_{ion}(x, t)$ in the form of leakage and by means of the highly non-linear potassium and sodium pumps.

$$C_m \frac{dV}{dt} = I_m + I_{ion} \quad (2.10)$$

The active, voltage-dependent, gating elements of the sodium and potassium channels are described by the subunit gating parameters, m , n , and h , which parameterize the overall kinetics of each channel type. They reflect the fact that the ion channels themselves are made up of different subunits (4 each for potassium and sodium). Each has an independent probability of being in its “open” configuration. The channel is open only when all of its subunits are open. Each subunit $\xi = h, m, n$ is characterized by a voltage dependent charging rate $\alpha_\xi(V)$ and discharging rate $\beta_\xi(V)$, and characterized by a voltage-dependent characteristic time scale

$$\tau_\xi(V) \sim \frac{1}{\alpha_\xi + \beta_\xi} \quad (2.11)$$

Sodium Current, Subunit parameters m and h

Sodium channels are composed of three subunits of type “m” and one subunit of type “h”. At rest all three “m” are closed, and “h” is open. Their dynamics are modelled by Hodgkin and Huxley using the following equations.

$$I_{Na} = G_{Na} m^3 h (V - E_{Na}) \quad (2.12)$$

$$\frac{dm}{dt} = \alpha_m(V)(1 - m) - \beta_m(V)m \quad (2.13)$$

$$\alpha_m(V) = \frac{25 - V}{10 \left(e^{\frac{25 - V}{10}} - 1 \right)}; \quad \beta_m(V) = 4e^{-\frac{V}{18}} \quad (2.14)$$

$$\frac{dh}{dt} = \alpha_h(V)(1 - h) - \beta_h(V)h \quad (2.15)$$

$$\alpha_h(V) = 0.07e^{-\frac{V}{20}}; \quad \beta_h(V) = \frac{1}{10 \left(e^{\frac{30 - V}{10}} + 1 \right)} \quad (2.16)$$

The net effect of these are that the “m” subunits open initially at a threshold potential, opening the channel. At a higher characteristic potential, and later in time, the “h” subunit closes, closing the channel. It is important to note that the potential values are all based upon recentering the voltage to -65 mV (resting potential).

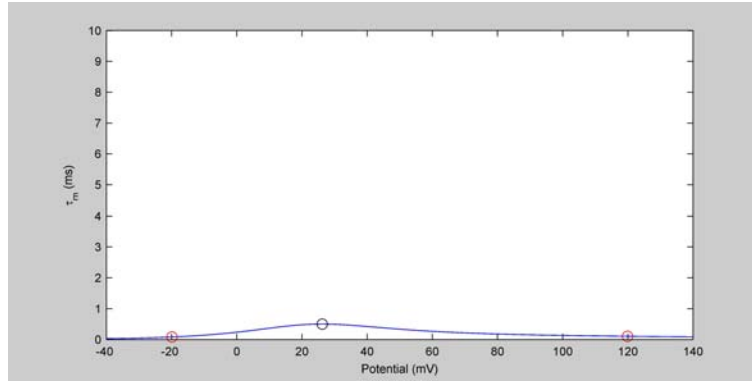


Figure 2.11: Sodium channel subunit m, dictates opening probability, τ_m max is 0.50 ms; τ_m at V_{-20} is 0.08 ms; τ_m at V_{120} is 0.10 ms

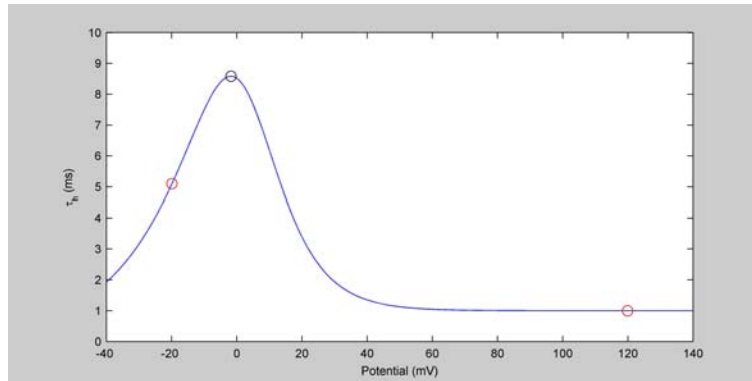


Figure 2.12: Sodium channel subunit h, dictates closing probability, τ_h max: is 8.58 ms; τ_h at V_{-20} is 5.10 ms; τ_h at V_{120} is 1.00 ms

Potassium Current, subunit parameter n

In the case of potassium channels, each of 4 subunits, “n,” are identical, and open and close according to voltage-sensitive rate constants $\alpha_n(V)$ and $\beta_n(V)$, modeled by Hodgkin and Huxley with the following equations.

$$I_K = G_K n^4 (V - E_K) \quad (2.17)$$

$$\frac{dn}{dt} = \alpha_n(V)(1 - n) - \beta_n(V)n \quad (2.18)$$

$$\alpha_n(V) = \frac{10 - V}{100 \left(e^{\frac{10-V}{10}} - 1 \right)}; \quad \beta_n(V) = 0.125e^{-\frac{V}{80}} \quad (2.19)$$

The result of this is that the channel opens above a characteristic voltage, allowing sodium to enter the axon, lowering the potential (Fig 2.13). Thus, after the sodium channels have opened and raised the potential to the characteristic voltage of these “n” subunits, the potassium channels open and return the potential to it’s resting level.

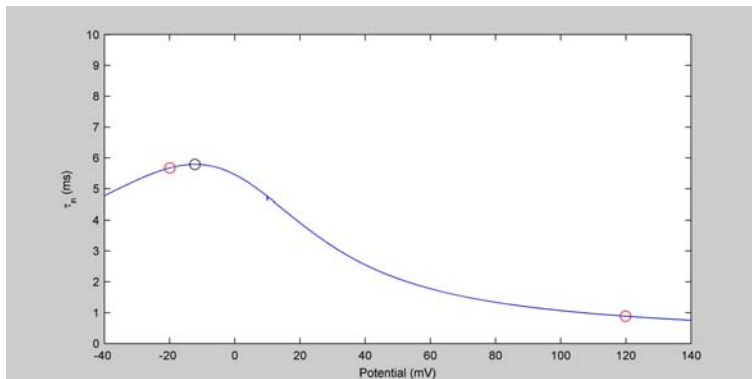


Figure 2.13: Potassium current: τ_n max: is 5.79 ms; τ_n at V_{-20} is 5.68 ms; τ_n at V_{120} is 0.89 ms

Leakage Current

The “leakage” current across the membrane is of the form:

$$I_L = G_L(E_L - V) \quad (2.20)$$

With G_L the passive membrane conductance ($\frac{1}{R_m}$). The time constant associated with this leakage term is the standard passive membrane time constant $\tau_m = R_m C_m = 3.33$ ms.

Diffusive Current

A region of membrane diffusively exchanges charge with spatially adjacent regions.

$$\left(\frac{dV}{dt}\right)_{diff} = D \frac{d^2V}{dx^2} \quad (2.21)$$

With $D = \frac{r}{2R_l C_m} \simeq 840 \frac{s}{cm^2}$, the diffusion constant for the squid giant axon.

Longitudinal diffusion vs. membrane current

Combining the membrane current expressions with the diffusion expression, we obtain the full expression for the dynamics of $V(x, t)$:

$$\frac{dV}{dt} = D \frac{d^2V}{dx^2} + \frac{1}{C_m} \left(G_K n^4 (V - E_K) + G_{Na} m^3 h (V - E_{Na}) - G_L (V - E_L) \right) \quad (2.22)$$

Intuition for the dynamics of the process is obtained by comparing how the first and second terms relate to each other. What looks like a diffusion equation really is not, because the driving terms for inward and outward injected currents have both explicit time dependence and potential dependencies and introduce short term memory effects.

2.3.3 Leaky Cable Equation

In the absence of active channels, equations of type Eq. 2.29 are known as leaky cable equations, first studied by Kelvin around 1900 in the context of engineering underwater telegraph cables across the Atlantic.

$$\frac{dV(x, t)}{dt} = D \frac{d^2V(x, t)}{dx^2} - \frac{1}{\tau_m} V(x, t) \quad (2.23)$$

Where the membrane time constant τ_m is:

$$\tau_m = R_m * C_m = 3.33 * 10^{-3} s \quad (2.24)$$

and the diffusion constant D is:

$$D = \frac{r}{2R_l * C_m} = \frac{5 * 10^{-2} cm}{2 * (29.7 \Omega * cm) * (10^{-6} \frac{F}{cm^2})} = 8.42 * 10^2 \left(\frac{cm^2}{s} \right) \quad (2.25)$$

If the diffusion term dominates, then the solution will be of the form:

$$V(x, t) \approx V_0 e^{-\frac{x^2}{4 * D * t}} \quad (2.26)$$

The characteristic distance that the potential diffuses “ x_D ” before it leaks across the axonal membrane is:

$$x_D = \sqrt{4 * D * \tau_m} \quad (2.27)$$

If $\frac{D}{x_D^2}$ is not of the same order of $\frac{1}{\tau_m}$, then the signal leaks across the membrane before it propagates.

$$V(x, t) \simeq V_0 e^{-\frac{t}{\tau_m}} \quad (2.28)$$

The characteristic distance for leakage of this is:

$$x_d = \left(\frac{D \tau_m}{2} \right)^{\frac{1}{2}} = \left(\frac{r R_m}{4 R_l} \right)^{\frac{1}{2}} \quad (2.29)$$

For the squid giant axon, x_D and x_d are of the same order ($x_D = \sqrt{4 * D * \tau_m} = 3.35 \text{ cm}$ and $x_d \approx 1 \text{ cm}$). Thus, “naively”, for a passive axon, a signal would only propagate over a distance $< 4 \text{ cm}$.

2.3.4 The role of active channel dynamics:

Introducing active channel changes the dynamics of the process completely. Consider a stretch of the axon. The leading edge of an action potential arrives at one end, raising the local potential. This causes sodium channels to open, which amplifies the rise in potential. Subsequently, two processes take place which counter this upswing in potential. The sodium channels themselves close (at the characteristic potential of the “h” subunit), and the potassium channels open, allowing potassium into the axon, and returning that stretch of axon to return to the resting potential. The action potential propagates in only one direction, because the membrane in it’s wake is still recovering (this is known as the refractory period).

The ionic channels also affect the passive “leakage” properties of the axon. We can define

an effective resistance:

$$R_{eff} \approx \left(\frac{1}{R_L} + \frac{1}{R_K} + \frac{1}{R_{Na}} \right)^{-1} \quad (2.30)$$

Note that this R_{eff} is potential-dependent. At the resting potential:

$$R_{eff}(0) \approx \left(\frac{1}{R_L} + G_K n^4(0) + G_{Na} m^3(0) h(0) \right)^{-1} = 1476 \Omega \cdot cm^2 \quad (2.31)$$

This corresponds to a timescale of $\tau_0 = R_{eff}(0)C_m = 1.476$ ms with associated modified characteristic distance $x_d = 0.70$ cm, somewhat smaller than the original value 2.14.

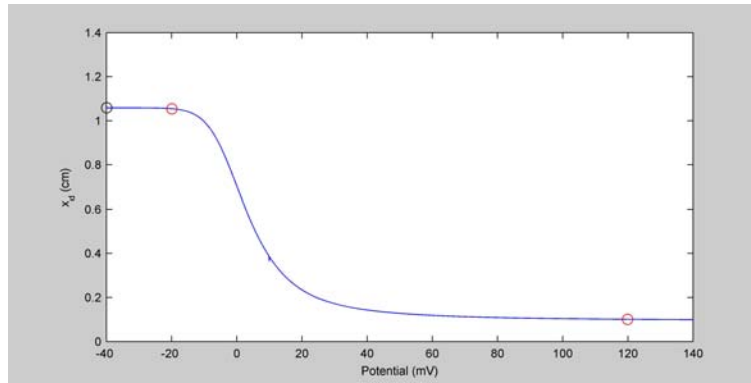


Figure 2.14: **Diffusion distance with potential sensitive channels:** At the bottom of our range, it is essentially the same as it would be without any active channels. At higher potentials, it drops to an asymptote at about twice the radius. That is, as the potential increases, the effects take place and can cascade to cause spiking behavior, and all of the associated biology we enjoy.

The timescale of the voltage upswing due to sodium channels (the “m” subunit timescale (τ_m)), is much too short to allow current influx to diffuse away in the process of channel opening (τ_m max is .5ms).

2.4 Synaptic dipole generation

The synaptic interface between two neurons, where an axon of one neurons meets the dendrite of another, mediates communication between the two neurons, and produces a transient current dipole in the downstream (“post-synaptic”) neuron. Beneath each one

of our electrodes, there are of order $\sim 5 \times 10^5$ neurons, and each of these has $\sim 10^4$ such synapses. With our arrays, we measure the aggregate potentials of these $\sim 5 \times 10^9$ induced dipole moments at each electrode.

2.4.1 *Synaptic transmission*

At the synapse, an arriving action potential on the pre-synaptic (axonal) side causes a chemical messenger (neurotransmitter) to be released at the junction. This neurotransmitter binds to a specific site (receptor) on the post-synaptic (dendritic) side. The receptor causes an ion specific channel to open, so that charged ions can enter into the dendrite and produce a characteristic dipole current. The superposition and interaction of all of the synaptic input to one neuron from all of the neurons that connect to it will produce a net change in the potential at the cell body, and if this potential change is large enough, it will initiate an action potential (as described above). The interaction of these inputs within single neurons, as well as the overall network interaction of the 2×10^{10} neurons in the human cortex [113] form the basis for the computational power of thought.

2.4.2 *The post-synaptic current*

Following input at the synapse, and subsequent opening of ion-specific channels in the dendrite, the current influx has a particular strength at the synapse, I_0 . The strength of this current source decreases exponentially with distance from the synapse, $I(x) = I_0 e^{-x/\lambda}$ (following the leaky cable equation of the previous section), with length constant $\lambda = \left(\frac{r_m}{r_s}\right)^{1/2}$ (r_m is the membrane resistance times unit longitudinal length, and r_s is the longitudinal resistance of the intracellular fluid per unit longitudinal length). λ is typically of order 0.1-0.2mm [56].

The dipole moment generated by a single synaptic event is then approximately equal to $\vec{q} = I_{psc} \lambda \hat{d}$. The post-synaptic current, $I_{psc}(t)$, has explicit time dependence. Therefore, each current dipole also varies in time. The unit vector, \hat{d} , denotes the orientation of the dendritic branch associated with the synapse. Cortical pyramidal neurons, the largest con-

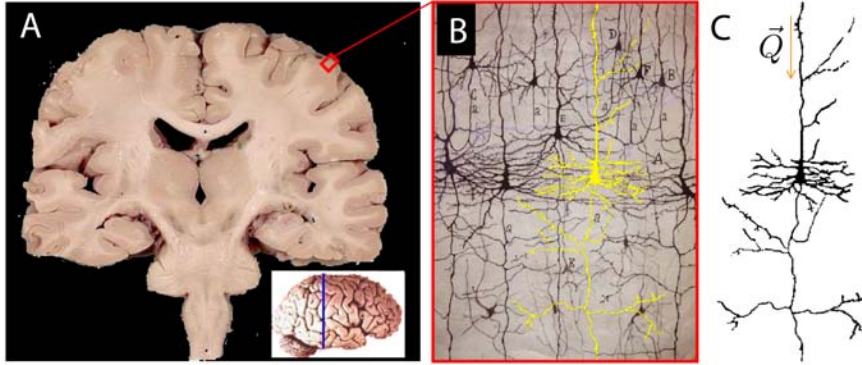


Figure 2.15: The cross section of gray matter of the cortex (A) reveals that the cortical pyramidal neurons have net directionality orthogonal to the brain surface (B). The dendritic dipole moment, \vec{Q} , runs parallel to the principal (apical) dendrite (C).

tributor to electric potential, have a primary dendrite that lies roughly normal to the cortical surface, so that the ensemble of synaptic current dipoles contributing to each electrode have a common directionality (Figure 2.15). Hamalainen, et. al. [56], estimated the individual transient dipole moments from each synapse to be of order $|\vec{q}| \approx 20 \text{ fA} \cdot \text{m}$. Murakami and Okada found that the net dipole moment produced by an entire cell, in response to various kinds of more global input is of order $|\vec{Q}_{global}| \approx 1 \text{ pA} \cdot \text{m}$, which is of the correct order to be in agreement with the Hamalainen estimate, since only a subset of synapses are activated during a more global input ([99], Figure 2.16).

2.5 Field properties of the superimposed dendritic dipoles

We briefly review here how the many superimposed dendritic dipoles create macroscopic potentials, following the rationale outlined by Nunez [105] and Hamalainen [56]. Beginning with Maxwell's Equations:

$$\vec{\nabla} \cdot \vec{E} = \frac{\rho}{\epsilon_0} \quad (2.32)$$

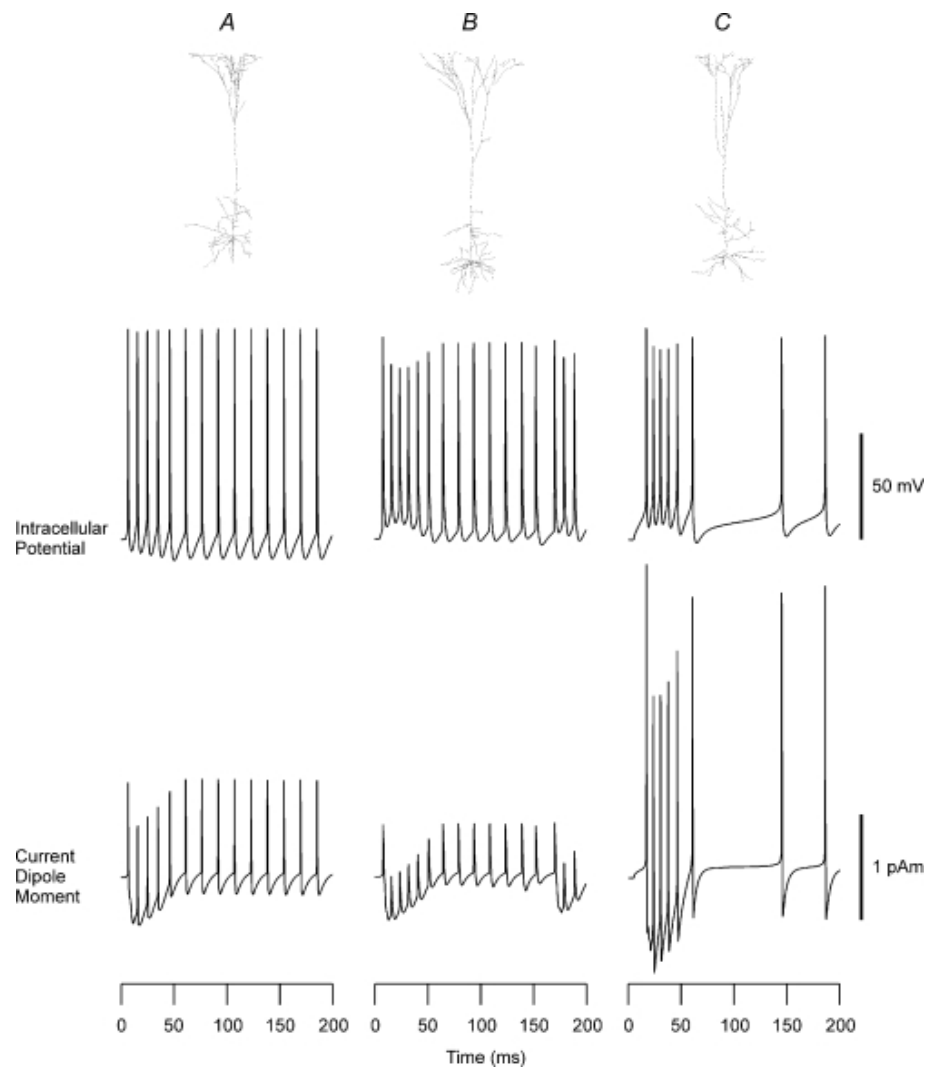


Figure 2.16: *Figure and caption from from Murakami and Okada, 2006: [99]* Reconstructed shapes, firing patterns and intracellular current dipole moments of layer V neocortical pyramidal cells Row 1: cellular geometry of the three layer V pyramidal cells taken from Stuart & Spruston (1998). Row 2: intracellular potentials produced by current injection (200 pA) into the soma. Row 3: current dipole moment Q for the layer V pyramidal cells. Passive and active properties were taken from the 1996 Mainen model. Positive polarity indicates currents directed from a deep layer to the surface.

$$\vec{\nabla} \times \vec{E} = -\frac{\partial \vec{B}}{\partial t} \quad (2.33)$$

$$\vec{\nabla} \cdot \vec{B} = 0 \quad (2.34)$$

$$\vec{\nabla} \times \vec{B} = \mu_0 \epsilon_0 \frac{\partial \vec{E}}{\partial t} + \mu_0 \vec{J} \quad (2.35)$$

with $\mu_0 \epsilon_0 = \frac{1}{c^2}$. Recall that the total current density, \vec{J}_0 is composed of the ohmic current $\sigma \vec{E}$, and polarization (“primary”) current ($\vec{J}^p = (\epsilon - \epsilon_0) \frac{\partial \vec{E}}{\partial t}$), and also the active current sources (which we will leave out for the moment):

$$\vec{J} = \sigma \vec{E} + (\epsilon - \epsilon_0) \frac{\partial \vec{E}}{\partial t} \quad (2.36)$$

Combining 2.35 and 2.36, we have:

$$\vec{\nabla} \times \vec{B} = \mu_0 \left(\sigma \vec{E} + \epsilon \frac{\partial \vec{E}}{\partial t} \right) \quad (2.37)$$

Inductive effects will not play a role if $\left| \epsilon \frac{\partial \vec{E}}{\partial t} \right| \ll \left| \sigma \vec{E} \right|$. Represent $\vec{E}(\vec{r}, t)$ as superimposed, decoupled, modes:

$$\vec{E}(\vec{r}, t) = \vec{E}_0(\vec{r}) e^{i\omega t} \quad (2.38)$$

Then this condition takes the form $\omega \ll \frac{\sigma}{\epsilon}$, imposing a characteristic frequency $\omega_c = \frac{1}{\tau} = \frac{\sigma}{\epsilon} \sim 3 \times 10^5 \text{ Hz}$ near and above which dielectric polarization would act as a low pass filter. This is well above any relevant frequency range in our recording.

In order to examine whether electric fields are induced by changing magnetic fields, $\frac{\partial \vec{B}}{\partial t}$, we determine:

$$\vec{\nabla} \times \vec{\nabla} \times \vec{E} = \vec{\nabla} (\vec{\nabla} \cdot \vec{E}) - \nabla^2 \vec{E} \quad (2.39)$$

but, we also have

$$\vec{\nabla} \times \vec{\nabla} \times \vec{E} = -\frac{\partial}{\partial t} (\vec{\nabla} \times \vec{B}) = -\mu_0 \frac{\partial}{\partial t} \left(\sigma \vec{E} + \epsilon \frac{\partial \vec{E}}{\partial t} \right) = \mu_0 (-i\omega\sigma + \omega^2\epsilon) \vec{E} \quad (2.40)$$

noting that the surface term ($\vec{\nabla}(\vec{\nabla} \cdot \vec{E})$) vanishes, we have:

$$\nabla^2 \vec{E} = -\mu_0 (-i\omega\sigma + \omega^2\epsilon) \vec{E} \quad (2.41)$$

Then a $\frac{\partial \vec{B}}{\partial t}$ induced \vec{E} would have wavelength of scale $\lambda_c \geq |\mu_0 (-i\omega\sigma + \omega^2\epsilon)|^{-\frac{1}{2}}$, so λ_c is much larger than the size of the head for $f < 500$, and inductive effects of $\frac{\partial \vec{B}}{\partial t}$ don't create changes on a scale relevant for our recordings. We can therefore make the quasi-static approximation that $\vec{E} = -\vec{\nabla}\Phi$.

2.5.1 From the current dipoles to macroscopic potential

Recall that the total current is both the primary and ohmic current

$$\vec{J} = \sigma \vec{E} + \vec{J}^s \quad (2.42)$$

We also have the continuity equation:

$$\vec{\nabla} \cdot \vec{J} + \frac{\partial \rho}{\partial t} = 0 \quad (2.43)$$

$$\vec{\nabla} \cdot \vec{E} = \rho/\epsilon \quad (2.44)$$

Combining 2.43 with 2.42 and 2.32, we have

$$\vec{\nabla} \cdot (\sigma \vec{E} + \vec{J}^s) + \frac{\partial}{\partial t} (\epsilon \vec{\nabla} \cdot \vec{E}) = 0 \quad (2.45)$$

$$\vec{\nabla} \cdot \left(\sigma \vec{E} + \vec{J}^s + \epsilon \frac{\partial \vec{E}}{\partial t} \right) = 0 \quad (2.46)$$

Using $\vec{E} = -\vec{\nabla}\Phi$, Eq. 2.46 becomes

$$\nabla^2 \left(\sigma + \epsilon \frac{\partial}{\partial t} \right) \Phi = \vec{\nabla} \cdot \vec{J}^s \quad (2.47)$$

Examining the decoupled representation, (Eq. 2.38), $\epsilon\omega \ll \sigma$, the $\epsilon \nabla^2 \frac{\partial \Phi}{\partial t}$ term is negligible for the frequencies that are relevant ($\omega \ll \omega_c$, see above), and the relation reduces to a Poisson equation.

$$\nabla^2 \Phi = \frac{1}{\sigma} \vec{\nabla} \cdot \vec{J}^s \quad (2.48)$$

defining the scalar field $P(\vec{r}) = \vec{\nabla} \cdot \vec{J}^s$, then the electric potential $\Phi(\vec{r})$ as a function of \vec{r} is equal to

$$\Phi(\vec{r}, t) = \int d\vec{r}_0 \left(\frac{1}{4\pi\sigma} \frac{P(\vec{r}_0)}{|\vec{r}_0 - \vec{r}|} \right) \quad (2.49)$$

where integration is over the location of the entire current distribution, $\vec{J}(\vec{r}_0)$.

The synaptic current sources are all localized in space, local when compared with to distance between the source and the electrode ($r \gg \lambda$). Such “charges” in $P(\vec{r})$ can be grouped into dipoles (only the post-synaptic currents count), and the field as observed at the electrode, $\Phi(\vec{r}, t)$, can be viewed as a superposition of specific electric current dipoles. Beneath each one of our electrodes, there are of order $\sim 5 * 10^5$ neurons, and each of these has $\sim 10^4$ such synapses. With our arrays, we measure, at each electrode, the superimposed potentials of these $N \sim 5 * 10^9$ electric dipole sources beneath each electrode. Therefore, the measured ECoG potential reflects the underlying correlation in these synaptic currents, in both space, and time.

At each interface, the voltage $\Phi^0(\vec{r}, t)$ changes according to the continuity conditions:

$$\Phi_{\parallel}^{(1)} = \Phi_{\parallel}^{(2)} \quad (2.50)$$

$$\frac{\Phi_{\perp}^{(1)}}{\sigma^{(1)}} = \frac{\Phi_{\perp}^{(2)}}{\sigma^{(2)}} \quad (2.51)$$

The cortex acts as a quenched random medium for these postsynaptic dipole fields, with many point “defects” (glia, etc) , line defects (axons), and planar membranes (the most dangerous ones, because field lines can not wrap around them). For example, in EEG, the skull resistivity puts the electrode effectively $\simeq 20cm$ further away from the cortex.

2.6 Evaluation of the power spectra

The electrocorticographic electrode array measures the cortical surface electric potential, as function of time, at the 0.5-1cm spatial scale. We amplify this array of signals and choose a

suitable re-referencing scheme (pair wise or common average, as discussed above). We are now faced with the task of extracting relevant information from these somewhat noisy $V(t)$ (Fig. 2.17).

First, these data streams are cut into 1-2 second long epochs to allow for ensemble averaging. We do this because we expect no relevant information to be found at frequencies below 1 Hz. In the case of specific tasks, such as individual finger flexion, the behavior changes on a timescale less than 1-2 seconds. These epochs must be both appropriately aligned with each other or with specific behavioral parameters before ensemble averaging. A large set of cross- and auto-correlations in the ensemble of $V(t)$ can potentially be studied. In this section we introduce briefly the one that appears throughout this thesis research.

2.6.1 Estimation of average spectra using the windowed Fourier Transform

The first and most common property studied is the power spectrum $P(f)$. For the best estimate of power spectral density, we calculated the power spectra in the following manner: The data was re-referenced as neighboring differential pair channels (our 32 electrode arrays have 52 differential pair channels each). For each of these channels, we obtain the power spectral density using the following prescription:

- Begin with a single differential-pair channel timeseries $V(t)$.
- Calculate windowed epochs (labelled by m) of the potential every 0.5 seconds, $V'(\tau, m) = V(t)H(t, m)$, where $H(t, m)$ is a 1 second Hann window,

$$H(t, m) = \frac{1}{2} \cos\left(\frac{2\pi\delta(t, \tau - mT/2)}{T}\right)_{-T/2 \leq \tau \leq T/2} \quad (2.52)$$

- The power spectral density of each epoch is:

$$P_0(f, m) = \frac{1}{T} \left(\sum_{\tau=0}^T e^{i2\pi(f)(\tau)/T} V'(\tau, m) \right)^2 \quad (2.53)$$

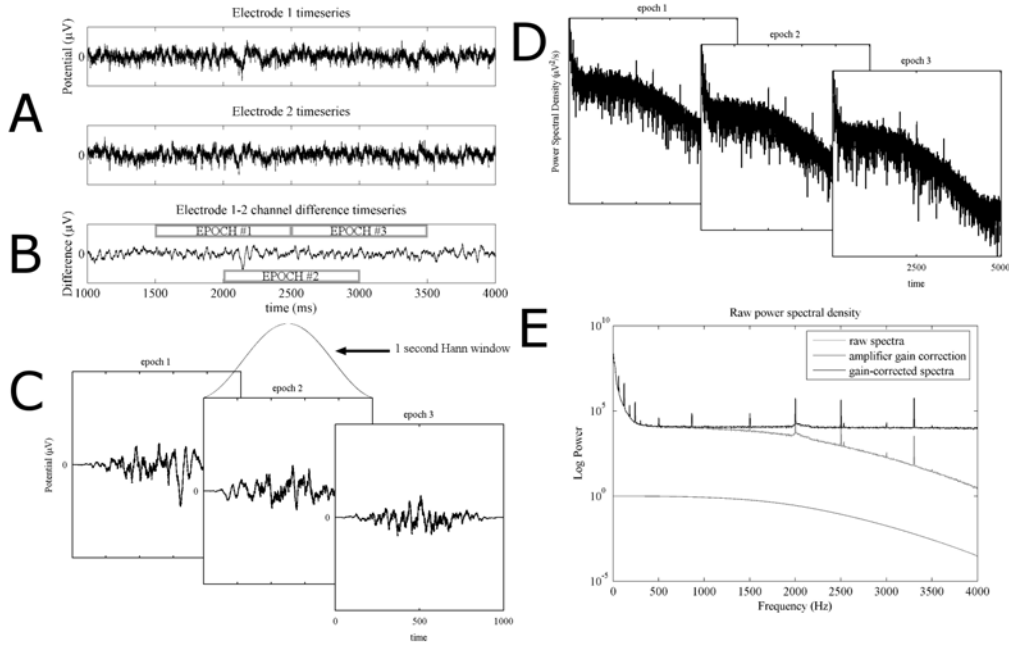


Figure 2.17: An illustration of the power spectral density calculation. The raw timeseries from two adjacent channels (shown in **(A)**) are subtracted from one another to create a pairwise difference channel (shown in **(B)**). This pairwise difference timeseries is then broken up into overlapping windows, and each of these has a Hann-window applied to it (in **(C)**). The Fast-Fourier Transform (FFT) is calculated and element-wise squared to obtain the power spectral density (PSD) for each epoch (in **(D)**). These PSD samples are then averaged to obtain a mean spectrum, which is corrected for the frequency-dependent amplifier attenuation (in **(E)**, the amplifier attenuation is shown in 4.8).

- The overall power spectral density is:

$$P(f) = \frac{1}{M \Xi^2(f)} \sum_{m=1}^M P_0(f, m) \quad (2.54)$$

where $\Xi(f)$ is the amplitude roll-off function imposed by the amplifiers (figure 4.8).

2.6.2 The relationship between the Fourier Transform and the Autocorrelation

A specific functional form in the power spectrum tells us specifically about the autocorrelational structure in the data, and is a convenient way of characterizing the data. The power

spectrum is the Fourier Transform of the autocorrelation function:

$$\begin{aligned}
F(G(t)) &= F\left(\int_{-\infty}^{\infty} d\tau (f(\tau)f^*(\tau+t))\right) = \int_{-\infty}^{\infty} dt (e^{-i\omega t}) \int_{-\infty}^{\infty} d\tau (f(\tau)f^*(\tau+t)) \\
&= \int_{-\infty}^{\infty} dt \int_{-\infty}^{\infty} d\tau (f(\tau)e^{-i\omega t}f^*(\tau+t)) \\
&= \int_{-\infty}^{\infty} d\tau (f(\tau)e^{i\omega\tau}) \int_{-\infty}^{\infty} dt (e^{-i\omega(\tau+t)}f^*(\tau+t)) \\
&= \int_{-\infty}^{\infty} d\tau (f(\tau)e^{i\omega\tau}) \int_{-\infty-\tau}^{\infty-\tau} d(\tau+t) (e^{i\omega(\tau+t)}f(\tau+t))^* \\
&= \tilde{f}(\omega)\tilde{f}^*(\omega) = P(\omega)
\end{aligned} \tag{2.55}$$

For example, purely uncorrelated data has a flat power spectrum, and a random walk has a power spectrum of the form $P(f) \sim 1/f^2$. This relationship between the autocorrelation of the timeseries and the power spectrum has important implications for our findings, as we discuss extensively in chapter 4.

Chapter 3

**SPECTRAL CHANGES IN CORTICAL SURFACE POTENTIALS
DURING MOTOR MOVEMENT**

In the first large study of its kind, we quantified changes in electrocorticographic (ECoG) signals associated with motor movement across 22 subjects with subdural electrode arrays placed for identification of seizure foci. Patients underwent a 5-7 day monitoring period with array placement, prior to seizure focus resection, and during this time they participated in the study. An interval-based motor repetition task produced consistent and quantifiable spectral shifts that were mapped on a Talairach-standardized template cortex. Maps were created independently for a high frequency band (HFB: 76-100 Hz) and a low frequency band (LFB: 8-32 Hz), for several different movement modalities in each subject. The power in relevant electrodes consistently decreased in the LFB with movement, while the power in the HFB consistently increased. In addition, the HFB changes were more focal than the LFB changes. Sites of power changes corresponded to stereotactic locations in sensorimotor cortex and to the results of individual clinical electrical cortical mapping. Sensorimotor representation was found to be somatotopic, localized in stereotactic space to Rolandic cortex, and typically followed the classic homunculus with limited extra-rolandic representation.

Keywords: Electrocorticography (ECoG), Motor, Mapping, Somatotopy, Homunculus

3.1 Introduction

Behavior-related changes in specific cortical spectral bands were described in animals as early as 1891, and similar task associated changes were demonstrated in humans brain potential measurements from the surface of the scalp (EEG) by 1929 (Brazier 1961) (Berger 1929). Most subsequent studies of human cortical electrical behavior have focused on the spectral characteristics of EEG, The EEG frequency band ranges that have classically been

associated with motor output are the 8-12 Hz (“alpha”), 18-26 Hz (“beta”), and everything greater than 30 Hz (“gamma”) (Wolpaw, McFarland et al. 1991; Kostov and Polak 2000; Pfurtscheller 2000). The lower bands have been associated with thalamocortical circuits and typically decrease in amplitude in association with actual or imagined movements (Levine, Huggins et al. 1999; Rohde, BeMent et al. 2002; Pfurtscheller, Graimann et al. 2003). Higher frequency changes, in contrast, have been found to increase in amplitude with active or imagined motor movements (Crone, Miglioretti et al. 1998; Pfurtscheller 2001; Leuthardt, Schalk et al. 2004), and may correlate with activity in local neuronal populations. The classic, though still debated (Nunez, Wingeier et al. 2001), interpretation of changes in spectral amplitude, developed by Pfurtscheller (Pfurtscheller 1981; Pfurtscheller 2000; Pfurtscheller 2001; Pfurtscheller, Graimann et al. 2003; Pfurtscheller, Brunner et al. 2006) and others, is that they reflect phase coherence of cortical circuits. With this interpretation came the suggestive labels event-related synchronization (ERS) and event-related desynchronization (ERD), and the postulate that spectral shifts in these potentials do not necessarily reflect differences in overall cortical computational activity, but rather that they reflect changes in population coherence. The present study aims to identify aspects of functional organization in the brain, using spectral shifts in the ECoG array, when the state of motor cortex is changed in a supervised, interval-based and repetitive manner. The high fidelity of ECoG signals has made them a source of interest for functional brain mapping, and this paper is not the first to use them in this capacity. Crone and colleagues (Crone, Miglioretti et al. 1998; Crone, Miglioretti et al. 1998; Crone 2000) demonstrated somatotopy in several (5) individuals using a paradigm with tonic muscle contraction. Tonic movement produced transient suppression at low frequencies, and transient potentiation at high frequencies. These studies found high frequency changes to be more spatially focal than low frequency changes, and their methods reported variable somatotopy, with much involvement outside of classically described sensorimotor cortex. Pfurtscheller and Graimann (2003), using self-paced movement, reaffirmed the finding of spatially broad mu and beta ERD in ECoG, with more focused high gamma ERS (Pfurtscheller, Graimann et al. 2003).

Loose somatotopy, unbound by rigid homuncular representation, was also reported in ECoG by Marsden (Marsden, Werhahn et al. 2000), Hoshida (Hoshida and Sakaki 2003), and Branco (Branco, Coelho et al. 2003). Consistent with previous studies, we find that in the low-frequency regime (≤ 32 Hz), distinct spectral peaks, which are present in resting intervals, decohere during movement intervals. At higher frequencies we found broad spectral increase with movement that might represent increased neuronal activity across the entire neuronal ensemble measured by a single electrode, reflecting the summation en masse of many superimposed Local Field Potentials (LFPs), each of which displays a shift in its own power law type noise spectra (Beggs and Plenz 2003; Beggs and Plenz 2004). By studying a large number of patients (twenty-two subjects) and using stereotactic normalization and averaging techniques, our results help provide a generalizable, in-depth, and comprehensive characterization of low and high frequency changes in and around sensorimotor cortex during movement.

3.2 Methods

3.2.1 Subjects

Simple motor tasks were studied in twenty-two patients (10 females, ages 18-48, Table 1) who had undergone placement of intracranial electrode arrays to localize seizure foci prior to surgical treatment of medically refractory epilepsy. The arrays were typically placed for 5-7 days with the location of the electrodes and duration of implantation determined independently by clinical criteria alone. Experiments were performed at two institutions, University of Washington (UW) and Washington University in St. Louis (WashU). Patients underwent craniotomy for electrode placement and were typically studied 4-6 days after electrode placement to allow for recovery from the surgery. Only patients with some peri-Rolandic coverage were included. Subjects gave informed consent for participation in a manner approved independently by the respective Institutional Review Boards.

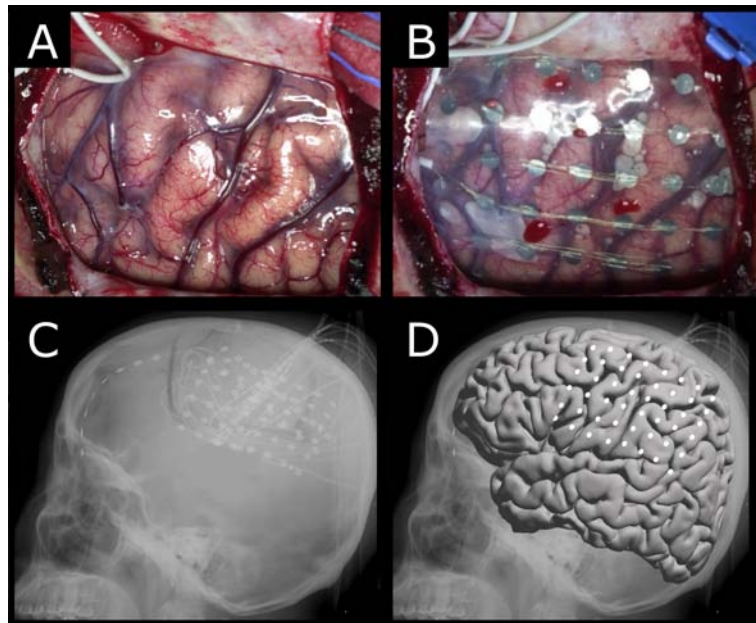


Figure 3.1: Grid placement and representation on a brain template. The brain is exposed (A) and electrodes placed in the subdural space (B) to identify seizure onset and map cortex for clinical purposes prior to resection of epileptic focus. The electrodes are localized with a lateral skull x-ray (Miller 2007) (C) and positions transformed to a standardized template (D). White dots represent the center of the electrode location in the standardized Talairach coordinate system (Talairach and Tournoux 1988).

3.2.2 Recordings

The platinum electrode arrays (Ad-Tech, Racine, WI) were typically configured as linear strips or 8x8 electrode arrays. The electrodes had 4mm diameter (2.3mm exposed), 1 cm inter-electrode distance, and were embedded in silastic. The recording system differed in technical features between the two centers. At UW, the ECoG signals were split into two identical sets. One set was fed into the clinical EEG system and the other set was recorded with Synamps2 (Neuroscan, El Paso, TX) biosignal amplifiers. At WashU, a clinical telemetry system (XLTEK, Oakville, Ontario, Canada) was used and signal acquired via the internal network. ECoG signals were then acquired from the Neuroscan or XLTEK system using the general-purpose software BCI2000 (Schalk, McFarland et al. 2004). At

UW, the sampling frequency was 1000 Hz. At WashU, the sampling rate was 300, 500, or 600 Hz. The signals were bandpass filtered from 0.15 or 0.3 Hz to 200 Hz at both institutions. In this way, the 8-100 Hz spectral regions examined in this study are outside of any filtering ranges and below any relevant Nyquist frequency.

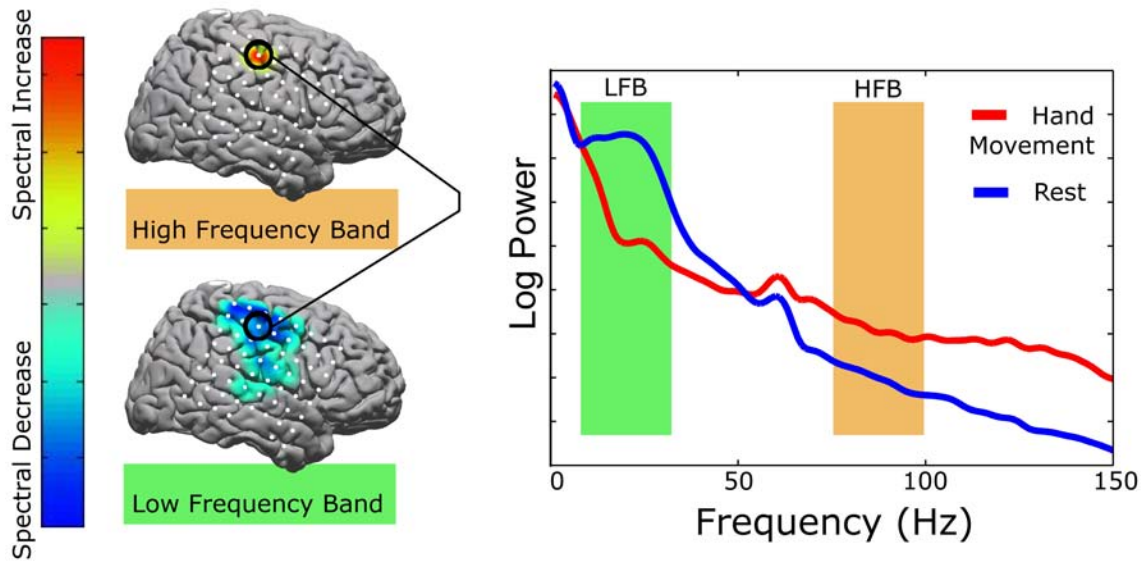


Figure 3.2: Demonstration of the analysis technique for a hand movement task in patient 5. The shaded areas in the spectral plot illustrate the bands used for analysis. The green shaded region is from 8-32 Hz (low frequency band, or LFB), and the orange shaded region is from 76-100 Hz (high frequency band, HFB). The upper cortical map shows the activation distribution for the HFB (here, reflecting an increase in spectral power with movement). The lower map, for the LFB demonstrated a decrease in spectral power with movement over a broader set of electrodes. The color bar indicates the scale used for all spectral maps: blues reflect spectral decrease, and red-yellow reflect spectral increase. Grey indicates no change. All cortical maps are scaled to the maximum increase or decrease, so there is no relevant absolute scale. Electrode locations are shown in white.

3.2.3 Tasks

Motor tasks were performed as part of a pre-screening task for closed loop brain-computer interface feedback experiments (Leuthardt, Schalk et al. 2004; Eric C. Leuthardt 2006). Pa-

tients performed simple, repetitive, motor tasks of hand (synchronous flexion and extension of all fingers, i.e. clenching and releasing a fist at a self-paced rate of approximately 1 Hz) or tongue (opening of mouth with protrusion and retraction of the tongue, i.e. sticking the tongue in and out, also at 1 Hz). These movements were performed in an interval-based fashion, alternating between movement and rest, and the side of movement was always contralateral to the side of cortical grid placement. Additional movement types were flexion and extension of a given finger, audible repetition of the word “move,” pursing and unpursing of the lips, and adduction and abduction at the hip, shoulder, and ankle. There were between 30 and 75 cue presentations for each movement modality. Cues for motor movement were delivered visually in a 10 cm by 10cm presentation window at a distance of 75 -100 cm from patient. Visual cues were presented using the BCI 2000 program(Schalk, McFarland et al. 2004) in one of three ways - a colored box, a fixation point (‘x’) cuing a specific motor movement, or a written word indicating the specific body part to be moved (typically, multiple movement types were interleaved in each experimental run). Stimuli were presented for 2 seconds (patients 1, 2, 3, 5, 8, 17) or 3 seconds (all other patients), followed by rest intervals (indicated by a blank screen) of the same length. The patients were instructed to perform repetitive, self-paced motor movement, alternating with rest intervals of the same length (indicated by the absence of the cuing target). Repetitive motion, rather than tonic contraction, was intended to accentuate the spectral shift during each interval, as attenuation of alpha (6-12 Hz) and beta (18-26 Hz) decrease (Crone, Miglioretti et al. 1998) and gamma (\geq 30 Hz) increase (Crone, Miglioretti et al. 1998) has been reported during tonic contraction. Multiple movement types were interleaved in each experimental run.

3.2.4 Signal Analysis

All ECoG data sets were re-referenced with respect to the common average. The 0.5 to 2.0 second epoch was used for analysis within each interval of activity or rest, regardless of sampling frequency or cue duration. The power spectral density of each epoch was calculated

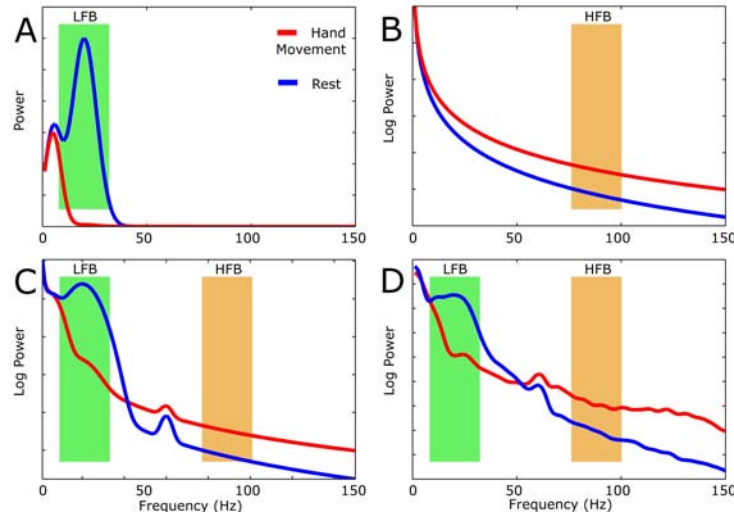


Figure 3.3: The power spectra for the motor task (red) and rest intervals (blue) illustrate the rationale, and tentative hypothesis behind the choice of spectral bands (HFB and LFB) for analysis. The first three plots (A-C) are elements of artificial schema and the 4th (D) is actual data (the same as in Figure B.2) (A) *Modeling the ERD*: In the rest condition, it is proposed that native timescales of 200 ms and 50 ms, generating spectral peaks based at 5 Hz and 20 Hz, arise from cortical regulation by thalamus and/ or other structures. With motor activation, one or more of these timescales decohere (“desynchronize”). Note that the rest period here does not necessarily reflect a baseline state, but the rest interval between actions, and may therefore be more coherent (“synchronized”) than a true baseline state. The schematic assumes 99% decoherence of the 20 Hz spectral peak with respect to the resting state. The green band reflects the analysis band (LFB) used to capture this effect. (B) *Modeling the broad spectral increase*: In this model, a power law spectral shift, from, for example, $1/f^{2.3}$ in the rest state to $1/f^2$ in the motor state, is diagrammed. This broad increase could also be a result of white noise addition to the data (a uniform shift upwards). The orange band (HFB) is chosen to capture this shift since it is away from masking by discrete, native, timescales at lower frequencies (as in (A)), and noise contamination at 60 Hz. (C) Superposition of the spectra in (A) and (B), with the addition of 60Hz noise (the same amount to each state). The orange and green bands are as before. (D) Actual shift seen. This spectrum is the same as in Figure B.2. Note the similarity to the modeled spectrum (C).

every 1 Hz from 1 to 150 Hz using a Fast Fourier Transform (FFT) using 0.25 second windows with an overlap of 0.1 second, and was averaged throughout each epoch. A Hann window (Nuttall 1981) was imposed on each data window to attenuate edge effects. The

number of rest epochs was randomly downsampled so that the number of rest epochs and the number of active epochs of each type were the same, for balanced statistical comparisons. The power at each frequency (in 1 Hz intervals) for each epoch was normalized with respect to the mean power at that frequency across all epochs in the run from which it came. We then calculated the sum of all normalized power values in two 25 Hz bands. Normalization was deemed necessary since the “typical” ECoG spectrum resembles a power law (Figure B.2), and so the changes at the lower end of either band would dominate the analysis procedure without it. The approach of taking wide frequency ranges avoided chauvinism toward any specific frequency, and accentuated the effect of broad spectral changes. (see Figures B.2 and B.3):

8-32 Hz (Low Frequency Band, LFB): This band spans is the classic “mu-beta” region of the spectra that typically exhibits amplitude decrease with motor movement. The fact that a peak in this region dissolves has led to the term “event related desynchronization” (ERD). Since it is a peak which disappears, it suggests dissolution of native timescale(s). These timescales may correspond to native thalamocortical timescales (Lopes da Silva 1991; Neidermeyer 1999), or perhaps some other inhibitory circuit which is activated when the brain region of interest is functionally engaged. This band is also picked to flank the classic range which EEG studies have focused on.

76-100 Hz (High Frequency Band, HFB): This range is chosen to be representative of the spectrally broad power increase that accompanies movement in relevant, focal, brain areas. This particular interval was chosen because it lies within this broad increase, avoids 60 Hz contamination, and matches the 25 Hz width of the LFB. Although this interval was chosen arbitrarily, and does not capture the entire broad-spectral change, supplemental figures ?? and ?? demonstrate how our results would be very much the same if we had picked a different frequency band within this broad spectral increase for our HFB analysis.

For every electrode and movement type, we calculated a high and a low activation weight by comparing the distributions of HFB and LFB values for each movement type with the corresponding rest distributions. Each such weight (A) was a signed squared cross-correlation

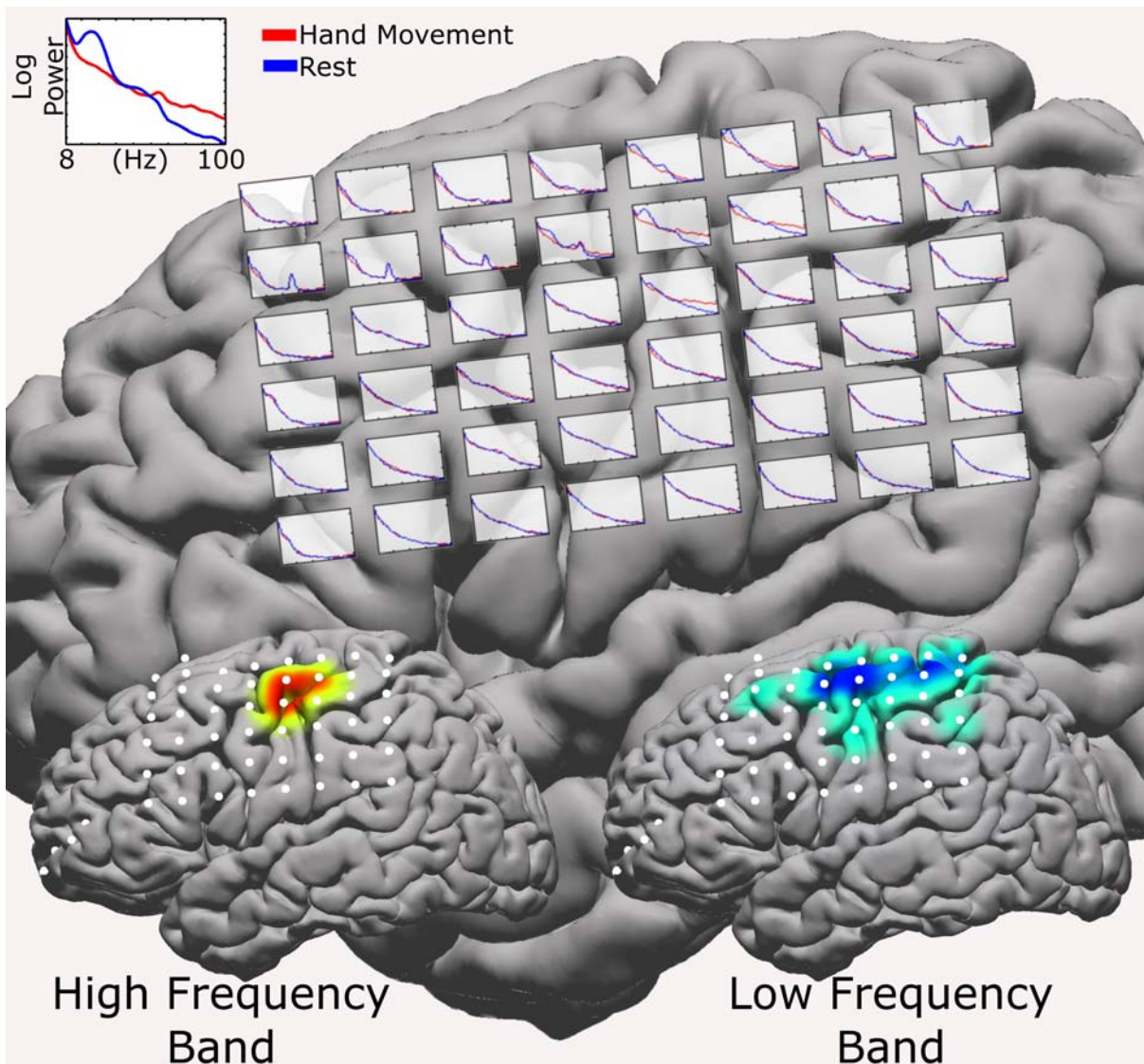


Figure 3.4: Spectra superimposed on the brain over each electrode for patient 5 during a hand movement task (red curves) and resting interval (blue curves). The frequency range (see upper left inset) is 8-100 Hz. Note that 60 Hz noise varies across electrodes (the two chosen frequency bands are away from this artifact). The lower cortical insets reflect the generated cortical activation maps, with the HFB map on the left cortex and the LFB map on the right. Note that, as expected by the lower insets, the most dramatic effects in the individual spectra are seen in the upper, middle portions of the grid.

value, a measure of how much of the variance in power across both movement and rest epochs was accounted for by the difference in the mean power between movement and rest epochs, as detailed in equation 1. We calculated the p-values associated with power in these normalized bands using a balanced, unpaired t-test with the normalized HFB and LFB power for a given movement type compared with rest. For each subject, the calculated p-value was Bonferroni corrected (Bonferroni 1936) for the number of channels.

3.2.5 *Electrode Localization*

As in other studies (Zacks, Gilliam et al. 2003; Zacks, Michelon et al. 2004), the electrode placement were documented clinically by their relation to skull table and landmarks from the saggital (lateral) and coronal (anterior-posterior) skull x-rays. We used these x-rays to derive normalized Talairach coordinates for the each of the electrode arrays using the LOC localization package (Miller submitted fall 2006), which is itself based in part on the manual procedure described in (Fox, Perlmutter et al. 1985) (see Figure B.1). Skull landmarks were used to determine brain dimension for standardization, and the position of the radio-opaque electrodes with respect to these skull landmarks allowed for calculation of each electrode's position in standardized (Talairach (Talairach and Tournoux 1988)) coordinates. In areas of low convexity with respect to the lateral x-ray (such as rolandic cortex) only an anterior-posterior ordinate and a superior-inferior ordinate were needed because the third ordinate could be uniquely determined by the convex surface of a template brain. Electrodes in areas of high convexity with respect to the lateral x-ray required the use of the AP x-ray to determine the third ordinate. Localizing electrodes based upon their relation to venous or gyral anatomy (Modayur, Prothero et al. 1997) would be subject specific and not generalizable, but interpretation of activations with respect to cortical gyri would be straightforward. The method we used of plotting these standardized locations to the AFNI - Montreal Neurological Institute (MNI) template brain (Collins 1995), in contrast, had the advantage of straightforward generalizability across subjects. It did suffer from the drawback that activation locations were calculated in this standardized space, without respect to gyri

or other known cortical structures, and any relation of activations to cortical structures in the template cortex must be interpreted with this in mind.

3.2.6 *Template Brain Mapping*

For template brain mapping, we included only electrodes with changes in power significant at the 0.05 Bonferroni-corrected level. We created activation maps independently for the HFB and LFB in each patient, for each movement type. We created these maps by linear superposition of spherical Gaussian kernels (standard deviation of 5mm) centered at the location of each electrode. The kernels were scaled by the activation weight (equation 3.1) associated with the given electrode and modality (Figure B.4), and interpolated at each point in a template brain. Maps for tongue and hand movement were averaged using linear summation of activation brain maps across all subjects for each task. While this simple linear superposition may cause areas with denser electrode coverage to artificially appear to have increased activation compared with areas which have similar activation but less coverage across which to summate, our present method did not suffer from the types of spurious artifact that can accompany other methods. (For example, scaling of individual maps prior to superposition will skew towards peripheral activation of subjects with poor coverage but some significant activation, and point-by-point interpolation must account for single patients with anomalous activation weights). For complete visualization of the analysis technique, please see the supplementary figure 7.5.

$$A_{mr} = \frac{(\bar{m} - \bar{r})^3}{|\bar{m} - \bar{r}| \sigma_{m \cap r}^2} \frac{N_m N_r}{N_{m \cap r}^2} \quad (3.1)$$

3.2.7 *Cortical stimulation mapping*

In seven patients, cortical stimulation mapping (Figure B.4) of motor cortex was performed for clinical purposes. Each such stimulation patient underwent stimulation mapping to identify motor and speech cortices as part of his/her clinical care. In this mapping, 5-10 mA square wave current pulses (.1ms in length) were passed through paired electrodes for

up to 3s (less if a response is evoked) to induce sensation and/or evoke motor responses (figure 3.8).

3.3 Results

Activation maps for hand and tongue movement are shown in figures A.5 and A.6 for all individuals and for the group average from each hemisphere. Supplementary material characterizes this for other movement types (Figures 7.6 and 7.7). A highly generalized response was found for motor tasks across individual subjects. Somatotopically defined decreases in low frequency band (LFB) and increases in high frequency band (HFB) were a consistent, significant feature in most subjects. These changes typically extended across sensorimotor cortex for the LFB and were somewhat more spatially specific for the HFB. Consistent with prior literature, spectral decreases were narrowly focused in the traditional mu/beta bands, but increases were distributed over the entire range of higher frequencies. Over sensorimotor cortex, a typical 'mu' peak was seen around 20-30 Hz that reliably decohered with activity. Along with this 'lower' frequency change, a broad, very high frequency increase in power is seen and, in our data, seems localized to sensorimotor cortex (Figure B.4 and supplementary Figure 7.8). Typically, the rest and active spectra intersected between 40Hz-50Hz in relevant electrodes (Figures B.4 and 7.8). These findings were highly consistent across subjects. For example, we found statistically significant LFB decreases in 17 of 18 subjects with hand tasks and 14 of 16 with tongue tasks, and HFB increases in 15 of the 18 subjects with hand tasks and 14 of 16 with tongue tasks (Figures A.5 and A.6), and most of those where significant changes were not found had less extensive rolandic coverage.

Taken both individually and on average (in collated, normalized, subject data), electrocorticographic signal changes were consistent with known localization of sensorimotor cortex. Figures A.5, A.6, and 3.7 demonstrate the individual and average activation maps for both HFB and LFB. The average activation locations for the HFB and the LFB (hand: high (+/-47,-15,50), low (+/-50,-15,50); tongue: high (+/-60,-6,31), low (+/-58,-6,39); in Talairach-normalized coordinates) fall within stereotactically defined Brodmann area 4 for hand and

tongue. The somatotopy of these two motor areas matched the established homuncular distribution, and the distributions of spectral changes were anatomically distinct for hand and tongue movement, as shown in Figure 3.7 (spatial separability was significant, with an associated p-value of less than 0.001 for both HFB and LFB, using a Bonferroni corrected, unpaired, t-test of all electrodes which showed a significant change for the movement of concern, with locations from all individuals concatenated).

Analysis of many movement modalities in several of the individuals (Figure 3.9) showed both loose somatotopy and peri-central localization. Supplementary motor activation was seen in a single subject with medial coverage (figure 3.9 C). Areas of activation for different modalities overlapped, and the overlap was more extensive in the LFB than the HFB.

In addition to the general changes across subjects, the localization of HFB and LFB changes corresponded with cortical stimulation mappings of motor cortex in individual patients (figure 3.8). Of the 20 electrode pairs that displayed responses to stimulation, at least one of the electrodes in the stimulated pair had a significant change in either the LFB (19 of 20 pairs) or the HFB (17 of 20 pairs), and thus 16 of the 20 pairs had significant changes in both the HFB and the LFB.

Finally, the spatial distribution for hand and tongue activations (Table 2) was broader for the LFB than for the HFB ($p < 0.01$ for both hand and tongue, using a paired t-test across patients). In other words, significantly larger areas of cortex exhibited changes in the LFB than in the HFB.

3.4 Discussion

Picoampere currents through individual membranous channels generate small changes in the local potential each time these channels open and close. Each neuron in cortex has millions of these channels. The potential changes that we measure at each electrode of an electrocorticographic (ECoG) array on the brain surface reflect innumerable numbers

of these currents. Distinct spectral shifts that are measurable, at specific frequencies, on this scale must correspond to large scale coherence at a specific timescale (Cassidy, Mazzone et al. 2002; Paradiso, Cunic et al. 2004), and disorganized (non-synchronous) but global increases in electrical activity across local neuronal populations will be reflected by broad spectral increases (C. Surya 1999). This study captured both of these types of changes in order to functionally map the cortex during a repetitive movement task.

To date, ECoG data has been analyzed on an individual subject by subject basis, partially due to a lack of methods for standardizing and comparing data across subjects, and partially due to small study sizes. The method described in this study facilitates collation of results across subjects according to stereotactically defined anatomy. Using the present method and data collected from 20 patients, this study provides an in-depth characterization of the spectral changes in the ECoG that accompany movement of the hand or the tongue. We find, across numerous subjects, that the high frequency band power changes are spatially focal with a broad frequency power increase with motor activation, while the low frequency band is spatially broad with more narrow bands of frequency power decrement. Like Crone et al. (Crone, Miglioretti et al. 1998; Crone, Miglioretti et al. 1998; Crone 2000), our study demonstrates variable somatotopy across individuals. Event related desynchronization (ERD), or spectral power reduction, was found ubiquitously at low frequency in specific peaks within the LFB, as described by Pfurtscheller, et al (Pfurtscheller 1999). As both Crone and Pfurtscheller have described, the high frequency change with movement was more focal than low frequency change, and characteristically fewer significant electrodes were detected for HFB (Table 2). We found high frequency spectral increase to be a much more focal phenomenon than low frequency ERD, and we found this high frequency change to be particularly specific to Rolandic cortex, across a large number of individuals. Additionally, the spectral power increase was much broader than that found in the lower frequency bands (supplementary figure 7.8), and the results would have been very much the same had we picked a higher 25Hz band within this broad spectral increase (supplementary figure 7.11).

While there was spatial variability in the distribution of spectral changes across individuals and specific homuncular organization (more in the LFB than the HFB), there was not as much variability as found by smaller studies. In particular, we did not find significant temporal lobe involvement, in contrast with other studies (Crone, Miglioretti et al. 1998; Crone, Miglioretti et al. 1998). Our findings do reaffirm that a rigid segmenting of motor strip somatotopy is not reflected in all aspects of the somatotopy of the electrocorticographic signal. As a particularly striking example, we found, as have Crone’s studies, that lateral cortical change during a foot movement task (Figures 3.9 and supplementary figure 7.6), well outside the inter-hemispheric somatotopic location of stimulation and lesion effects for distal lower extremity motor cortex. Though sensorimotor activation was a consistent feature of the study across the entire cohort, the occasional single subject outlier (as in fig A.5, subjects 8 and 10, and figure A.6, subject 6) might reflect task-related regional activation/deactivation patterns (Neuper, Wortz et al. 2006) or higher order cognitive processes.

Our method of accumulating results for different subjects does have some limitations that are worth noting. Variable electrode placement across individuals can confound interpretation when activations are considered when comparing subjects with non-overlapping or peripheral electrode array coverage. Conversely, since the activation on the template is the average of activation (“A”)-weighted Gaussian kernels, the peaks of activation will be somewhat blunted by similar sites with increased noise or reduced signal. Since the singular electrode activations are smeared to a template this also could lead to the possibility that two independent sites of activation are grouped together. This is especially worth considering when electrode spacing is 1cm apart. Despite these limitations, our present method still allows for the development of normalized and summated electrocorticographic data from which consistent, significant, and generalized statements of motor cortex activation have been made similar to that of fMRI. Thus far, this has been elusive in ECoG related literature.

The topographical activations for hand and tongue displayed significant concurrence to known topography of hand and tongue motor cortices. Figures A.5 and A.6 illustrate the

activations resulting from hand and tongue movement across 17 and 13 patients, respectively. The locations, when averaged, line up with the expected peri-Rolandic sensorimotor cortical sites. It is not surprising that the activations span the central sulcus, since the task involves both motor movement and sensory feedback. Taken individually, the cortical activations approximate the homunculus, with some extra-rolandic involvement. It is important to note that some of the activation maps in Figures A.5 and A.6 are limited by electrode coverage, and that this limitation must be considered when scrutinizing the activation maps. The most dramatic example of this is subject 17, in figures A.5 and A.6, where a single strip passes through classic hand motor cortex. In figure A.5, hand activation appropriately spans two electrodes in hand area; in figure A.6, however, tongue activation is present in the HFB in one electrode, and without any other rolandic coverage it is not clear whether a very small HFB increase is forced to the maximum or not. This forcing of small but significant changes in peripheral areas where there is no coverage of the primary area might help explain some of the strange findings with leg, foot, and shoulder movements (row A in figure 3.9 and several findings in supplementary figure 7.6). Electrical stimulation of the cortex to create transient lesions or to induce overt movements, extra or intra-operatively, is the established gold-standard method to functionally localize motor cortex in the human brain (Ojemann, Ojemann et al. 1989; Chitoku, Otsubo et al. 2001; Branco, Coelho et al. 2003). The present method contrasts with the classical stimulation method for functional localization because the method detailed here measures natural cortical change in response to functional behavioral change. Stimulation mapping, on the other hand, perturbs the natural state of the brain to non-selectively elicit functional behavioral change. Nevertheless, after pooling the HFB and LFB, electrocorticographic changes were universally seen at sites responsive to stimulation (Leuthardt 2006).

Our results support the notion that high and low frequency band changes arise from different physiological phenomena. Low frequency changes are postulated to arise in broad cortical areas, which are collectively regulated by central structures (e.g., the thalamus and basal ganglia). In this view, this regulation is reflected by specific, phase coherent (“syn-

chronized”), native timescales ranging from 30 to 120 ms, and seen as corresponding peaks in the power spectrum at 8-32 Hz. In some subjects, this spectral ”peak” was found to be exaggerated as a dynamic component associated with the task (see supplemental Figure 7.9), even though it is a feature localized to non-movement epochs of the task, supporting the hypothesis that it is reflecting a regulatory process. That we found this is not surprising, since a rebound in power in EEG beta following movement, beyond resting power, has been well documented by Pfurtscheller and Neuper. Electrical stimulation of the cortex to create transient lesions or to induce overt movements, extra or intra-operatively, is the established gold-standard method to functionally localize motor cortex in the human brain (Ojemann, Ojemann et al. 1989; Chitoku, Otsubo et al. 2001; Branco, Coelho et al. 2003). The present method contrasts with the classical stimulation method for functional localization because the method detailed here measures natural cortical change in response to functional behavioral change. Stimulation mapping, on the other hand, perturbs the natural state of the brain to non-selectively elicit functional behavioral change. Nevertheless, after pooling the HFB and LFB, electrocorticographic changes were universally seen at sites responsive to stimulation (Neuper and Pfurtscheller 1996; Pfurtscheller, Zalaudek et al. 1998). Also, monkey LFP experiments have shown load-based increases in this peak during rest periods a gripping task with variable resistance, suggesting that it is dynamically related to movement task properties (Jackson, Spinks et al. 2002). Recent studies comparing this movement-associated beta rebound in subjects with and without ventrolateral thalamotomy have demonstrated a role for the intact thalamus in the dynamic nature of the beta rhythm (Van Der Werf, Sadikot et al. 2006). Other studies involving both modeling (Destexhe, Contreras et al. 1998) and experiment indicated the importance of both the thalamus (Paradiso, Cunic et al. 2004) and basal ganglial structures (Cassidy, Mazzone et al. 2002; Foffani, Bianchi et al. 2005) in beta modulation in humans. Beginning at 40-50 Hz, a broad task-dependent increase in spectral power is measured reliably across patients and movement modalities (as in Figures B.2, B.3, B.4, and supplementary figure 7.8). It has been suggested that this spectral power increase at these higher frequencies

is correlated with increased BOLD signal in fMRI studies(Mukamel, Gelbard et al. 2005), that (as we demonstrate here) high frequency changes are a specific correlate of local behavior(Hoogenboom, Schoffelen et al. 2006; Womelsdorf, Fries et al. 2006), and we postulate that they may directly reflect an increase in local cortical computation. Thus, it is possible that the observed high-frequency effect is caused by the integrated activity of firing rates of cells immediately underneath the electrodes. That is, a global shift in the power law noise spectra(C. Surya 1999), accompanying an increase in local, cortico-cortical activity (as observed in LFPs(Beggs and Plenz 2003)), would be also present at low frequencies. However, observation of this shift at low frequencies could be masked by the influence of thalamocortical and basal ganglia-cortical interactions reflected at discrete timescales in the low frequency spectral region. This implies that the notions of synchronization and desynchronization might not be applicable to these changes and that the effect of increase in band power might actually extend across all frequencies including those in the mu/beta range.

3.5 Conclusion

Electrocorticography can provide the basis for functional maps that reveal motor cortical organization in an efficient and reproducible fashion. Using simple localization methods and spectral analyses, we derived robust motor activations, consistent across individuals and concurrent with parallel cortical stimulation maps. High frequency spectral power increased with activity, was spectrally broad, and may reflect activity of local neuronal populations. The increases in activity seem to conform to exponential or power law noise behavior with shifts in the critical exponent that correlate with behavior, rather than demonstrating increases at a specific frequencies. Low frequency spectral power decreased with activity, was spectrally focused narrowly over traditional mu/beta frequency ranges, and thus may reflect the dissolution of spectral peaks which may themselves reflect the regulatory timescales involved with the interaction between central brain structures and the cortical surface (i.e., thalamocortical and basal ganglia-cortical). We quantified and mapped these effects across

a large number of patients, showing the spatial distribution of the low frequency (regulatory) band to be spatially broader than the high frequency (activity-based) band. The results of the topographical mapping reveal somatotopic representation of these signals which typically follow the traditional homunculus model. In summary, our results provide, for the first time, an in-depth characterization of spectral changes in ECoG signals during movement across a reasonably large number of subjects; the techniques presented in this paper provide a basis for electrocorticography-based, quantitative mapping of motor modalities in the human brain.

3.6 Supplemental Figures

Figures with descriptions that should help to understand the main content of the text.

This figure details the analysis procedure for a hand and tongue interleaved movement epoch task. (A) Raw data, recorded during the cued interval based task, is segmented. The raw data from a single channel is shown the trace, and durations with the cue for hand movement are shown in blue; those for tongue movement are shown in red; and those for rest are shown in black. The .5 to 2 second duration of each 3 second change is isolated, and these durations are designated by solid bars beneath the trace. (B) Spectra are calculated every 100ms for 250 ms windows throughout each duration indicated in A, and these spectra are averaged for each movement or rest epoch are shown in the traces in B. These traces reflect this averaged power from 0 to 100ms. (C) Each spectra shown in B is divided by the mean spectra across the entire task run, and these are shown directly below their appropriate traces from B. The green (8-32 Hz) and orange (76-100 Hz) bands are used to characterize high and low frequency aspects of the signal. The total power in each of these bands is calculated for each task-related interval. (D) The power of the high frequency band for each hand movement and a matched number of rest epochs across an entire task run are shown, with 30 individual hand movement epoch band-power samples shown in blue, and 30 rest epoch band-power samples shown in black. (E) A activation weight associated with the difference in the hand movement is calculated. m denotes the distribution of hand movement interval band-power samples, r denotes the distribution of rest interval weights, with $m \cup r$ denoting the union of the two distributions. N is the number of elements in each distribution, (σ) is the standard deviation, and $\bar{}$ denotes distribution mean. (F) Activation weights from each electrode are plotted to a template brain. Spherical Gaussian kernels of standard deviation 5mm are centered at the location of each electrode, scaled by the activation calculated in E, and linearly superimposed to obtain a cortical map. If the distributions shown in D are not separable with an associated p-value of less than .5, after Bonferroni correction for the total number of channels, then the activation for that electrode is scaled to zero, and doesn't contribute to the cortical map.

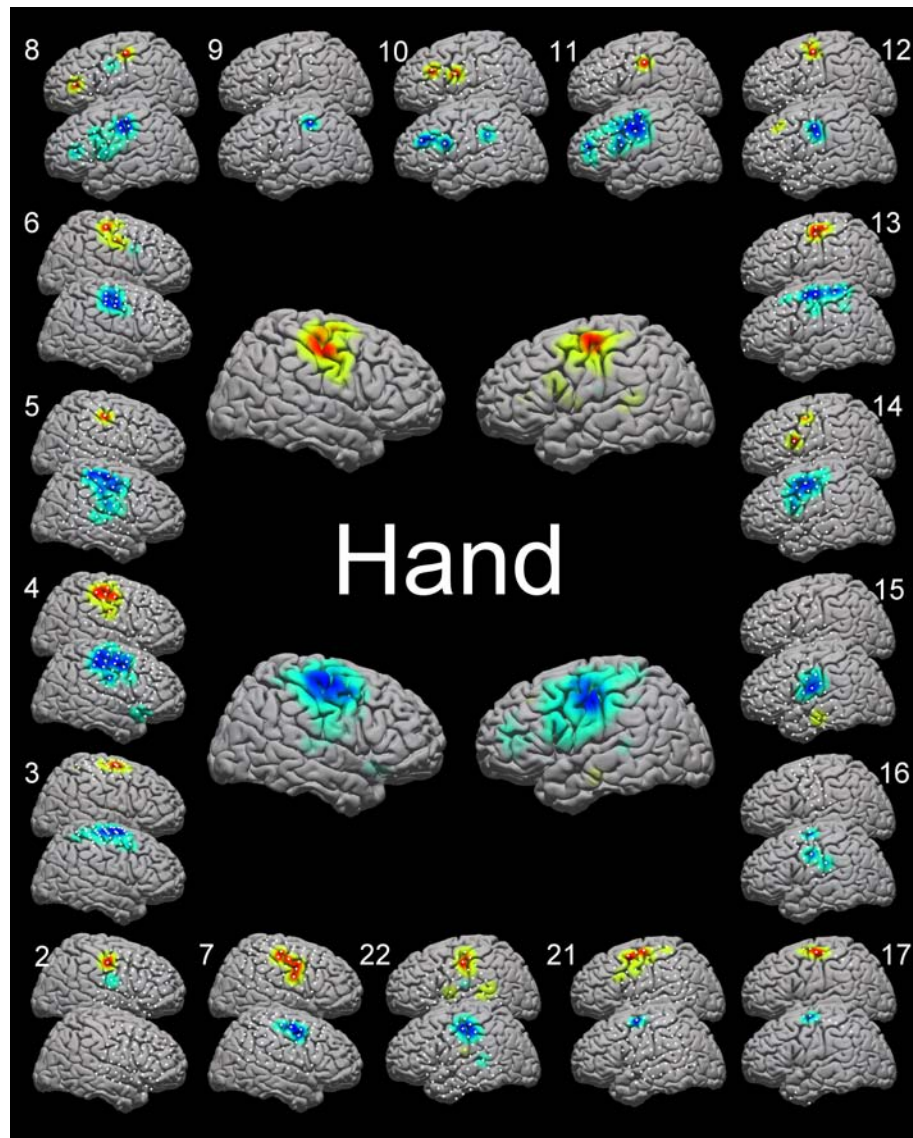


Figure 3.5: Cortical activation maps for hand and tongue movements. Electrode locations are shown in white. The upper cortex of each pair is the HFB activation, and the lower is the LFB activation. *Outer brains:* Individual patients are reflected by brain pairs around the outside of the figure, with the number next to the brain indicating the patient number, as detailed in Table 1. *Central brains:* The average activations for hand and tongue movement for left and right cortices (right and left hand movement, depending on the patient's electrode locations).

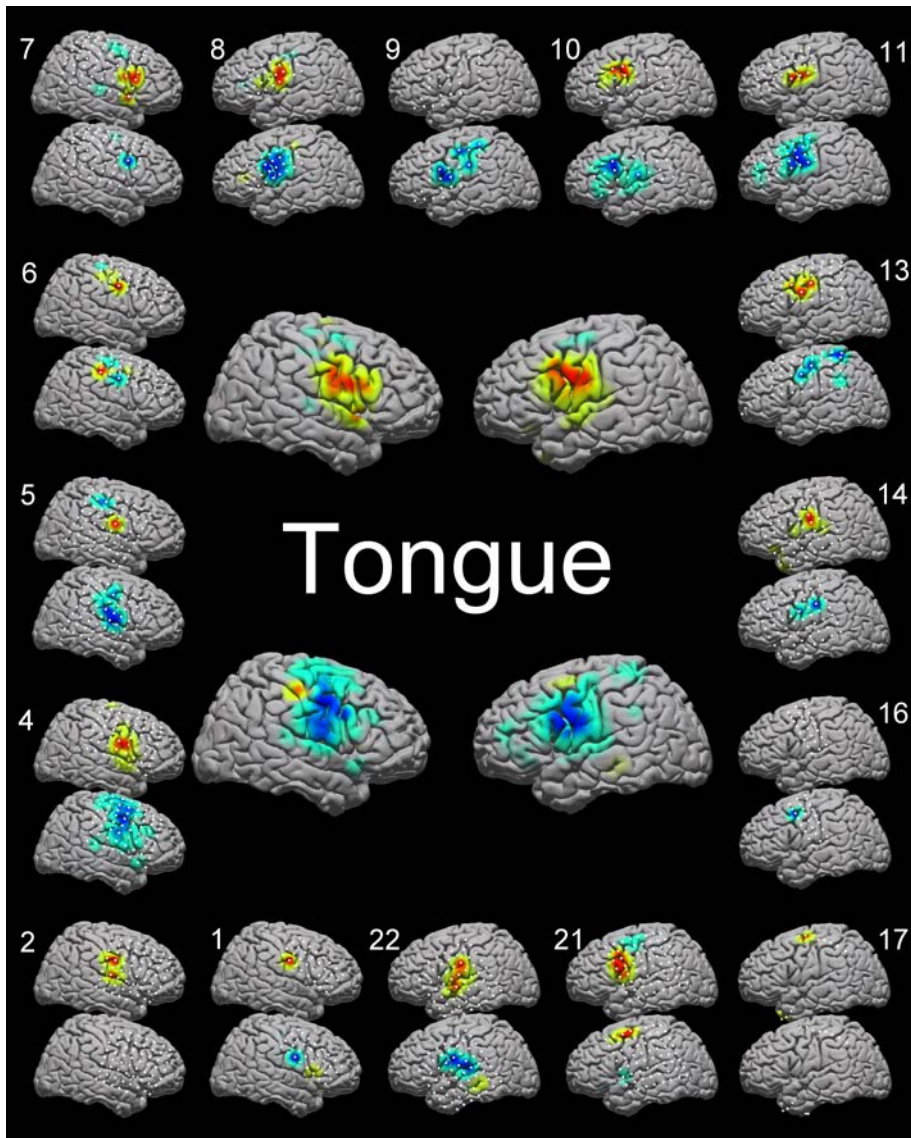


Figure 3.6: See caption for figure 5.

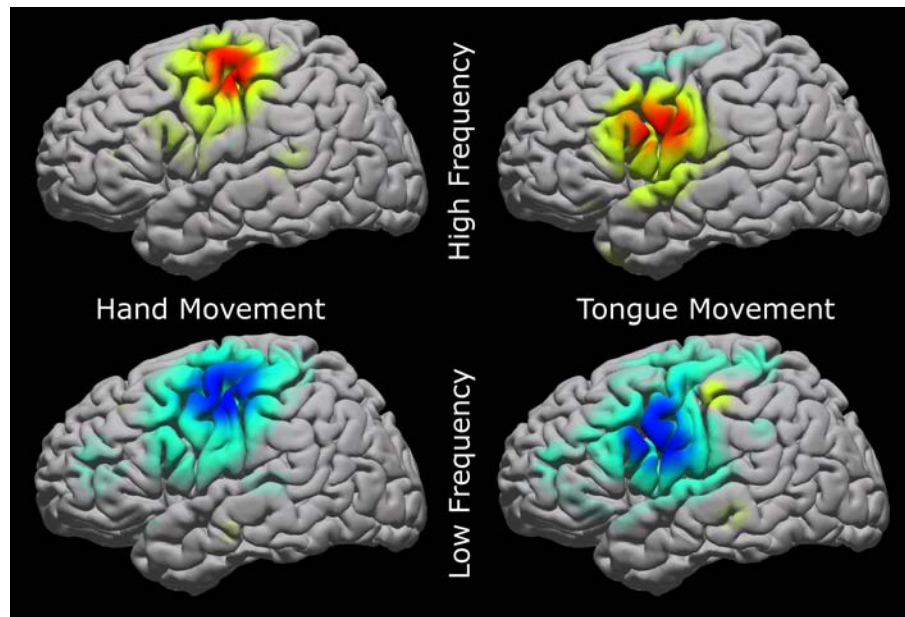


Figure 3.7: Average representation with contralateral electrode locations mirrored to one side (left brain). Each is scaled for the maximum increase or decrease. The somatotopic distribution of the activations is evident comparing the hand (left panels) and tongue (right panels). Additionally, there is qualitatively less spatial overlap between the HFB representations (upper panels) than the LFB (lower panels). The qualitative properties of each type of activation are detailed in Table 2. Please see the supplemental discussion for more depth about types of interpolation across individuals and why this particular technique was chosen.

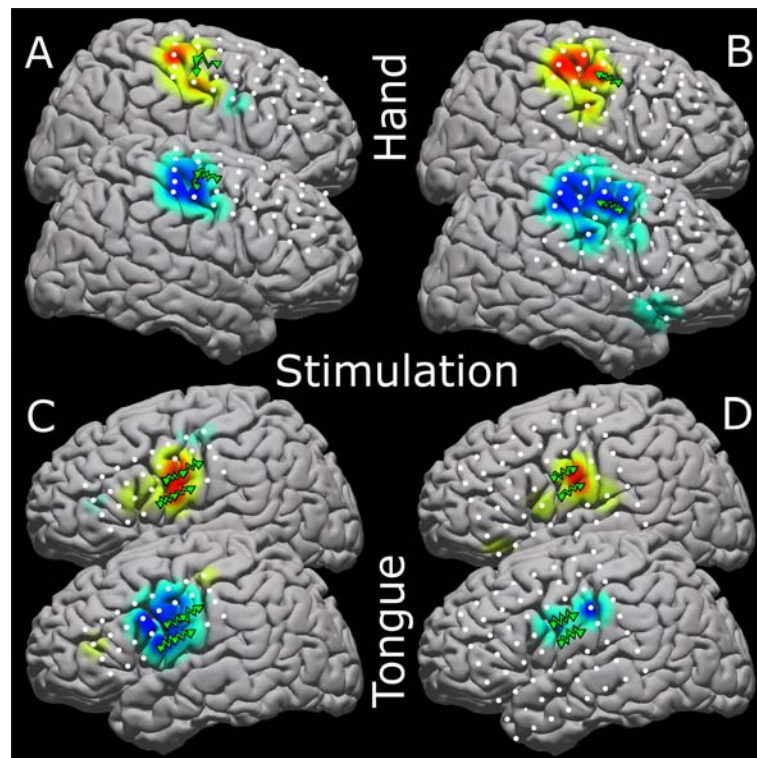


Figure 3.8: Four magnified brain maps to show stimulation resulting in motor movement along with the activation for the same modality. Stimulation is done pair-wise, so elicited motor movement may be due to cortex beneath only one of the electrode pair. Positive electrode stimulation locations are shown with green triangles connected by jagged green lines. The upper cortex of each pair is the high frequency representation, and the lower is the low frequency representation. Hand movements with stimulation are shown for patients 16 (A) and 6 (B). Tongue movements are shown for patients 1 (C) and 3 (D). Please see the supplemental discussion regarding the stimulation process.

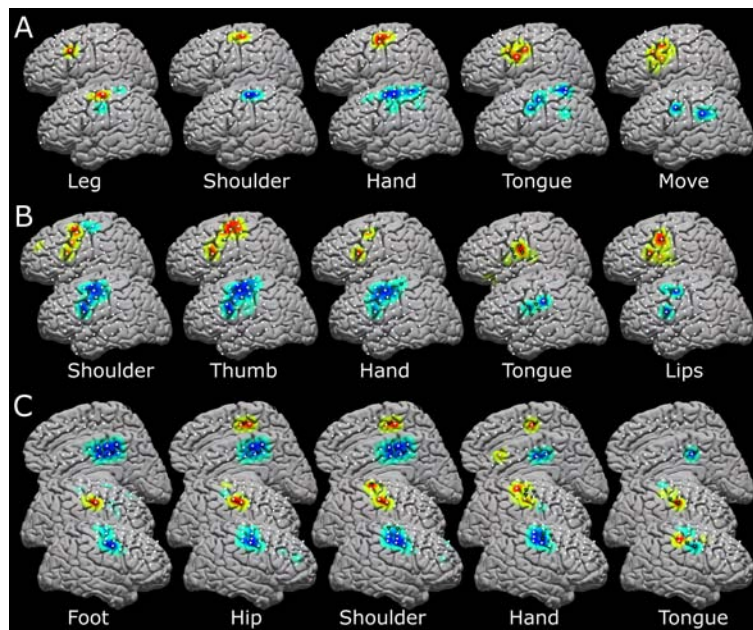


Figure 3.9: Five different movement modalities within the same patient for three different patients, with each relevant modality labeled. The upper brains are high frequency band representation, and the lower are low frequency representation. White dots indicate electrode positions, and the green triangles reflect the pairwise stimulation sites which elicited movement of the concerned modality. Data for subjects 9 (A), 3 (B), and 16 (C) are shown. The medial representations in (C) reflect activation as reflected by a 2x8 interhemispheric strip, and the activations seen are likely supplementary motor areas rather than sensorimotor cortex.

Table 2. Parameters associated with all hand and tongue movement findings

Motor modality	Hand	Tongue
Total electrodes	892	764
Number of high band electrodes	75	85
Mean high band y position	-15 ± 11	-6 ± 13
Mean high band z position	50 ± 11	31 ± 19
Number of low band electrodes	172	129
Mean low band y position	-15 ± 14	-6 ± 14
Mean low band z position	50 ± 14	39 ± 18

The position values refer to Talairach standardized coordinates (Talairach and Tournoux, 1988) (in mm), and the x coordinates are omitted because data from the lateral surface of both hemispheres has been combined. The \pm symbol denotes SD in position (square-root of the variance).

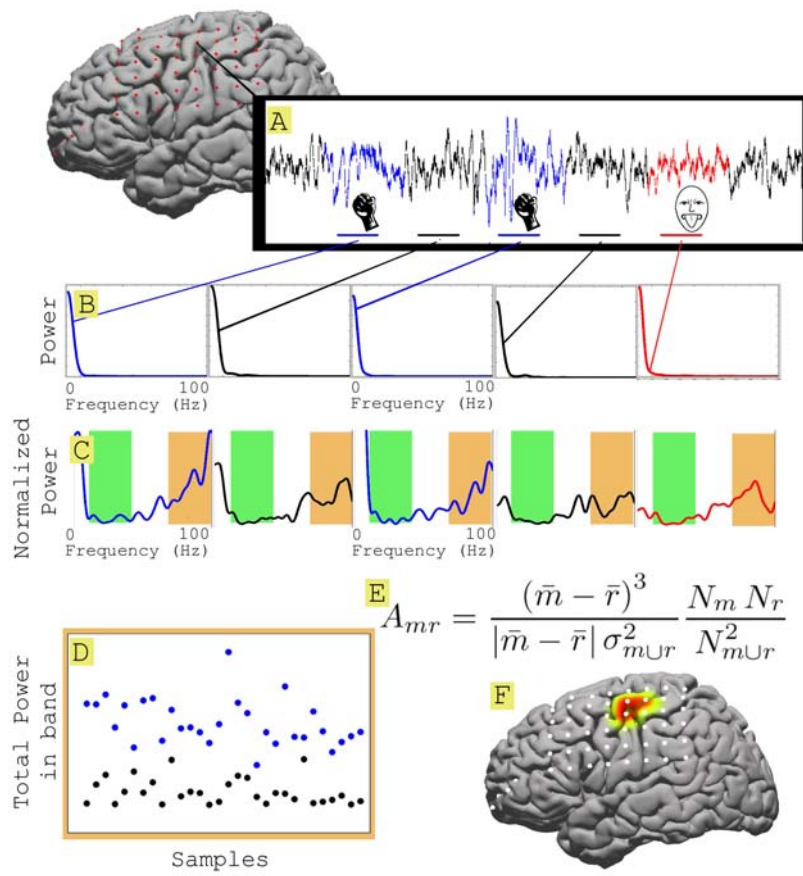


Figure 3.10:

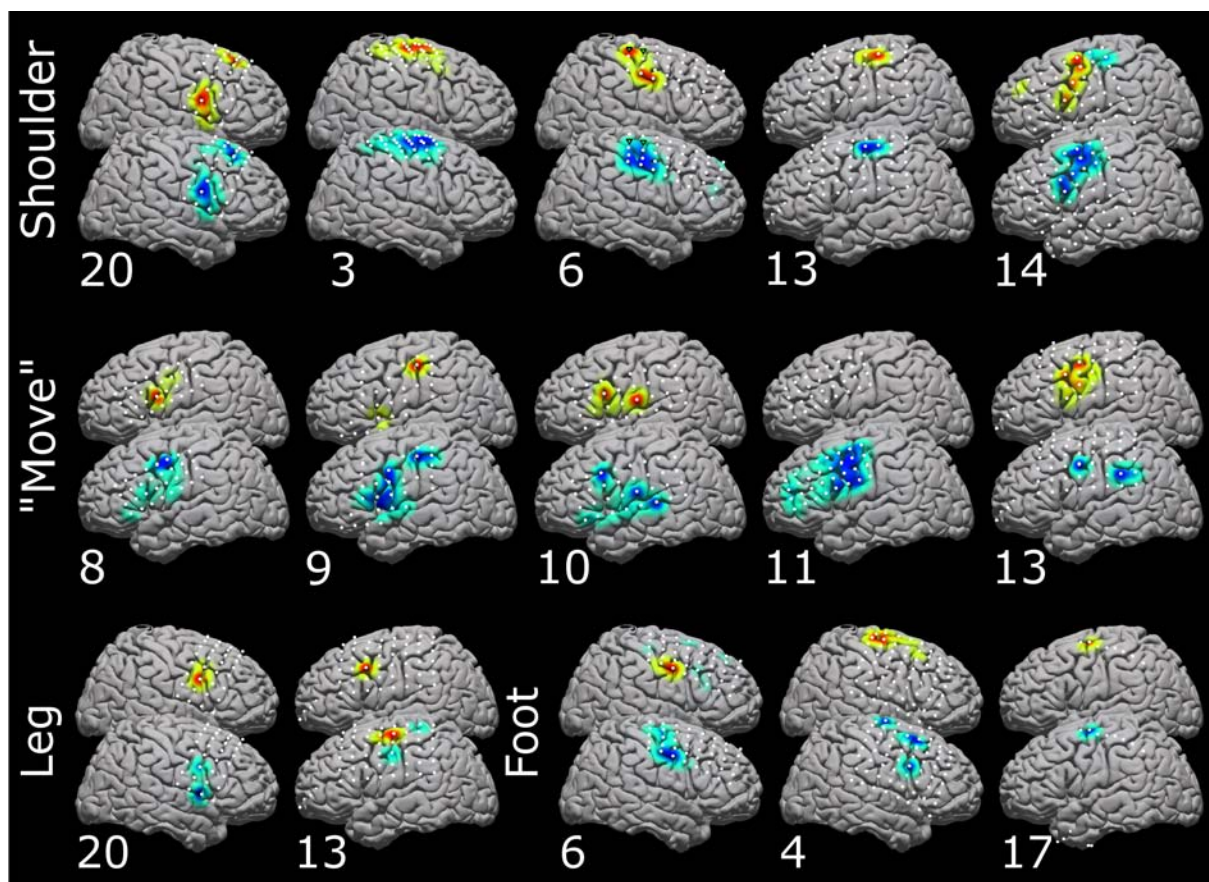


Figure 3.11: These figures illustrate activation for repetition of the word "move," and adduction and abduction at the hip ("Leg"), shoulder, or ankle ("Foot") across several individuals. The shoulder action was a 'chicken-wing' motion. The number next to each brain pair indicates the subject number, as detailed in Table 1. Electrode locations are shown in white. The upper cortex of each pair is the HFB activation, and the lower is the LFB activation. Note that the lateral representations of leg and foot diverge from the classic description of the homunculus, but agree with Crone's findings (Crone, Miglioretti et al. 1998; Crone, Miglioretti et al. 1998).

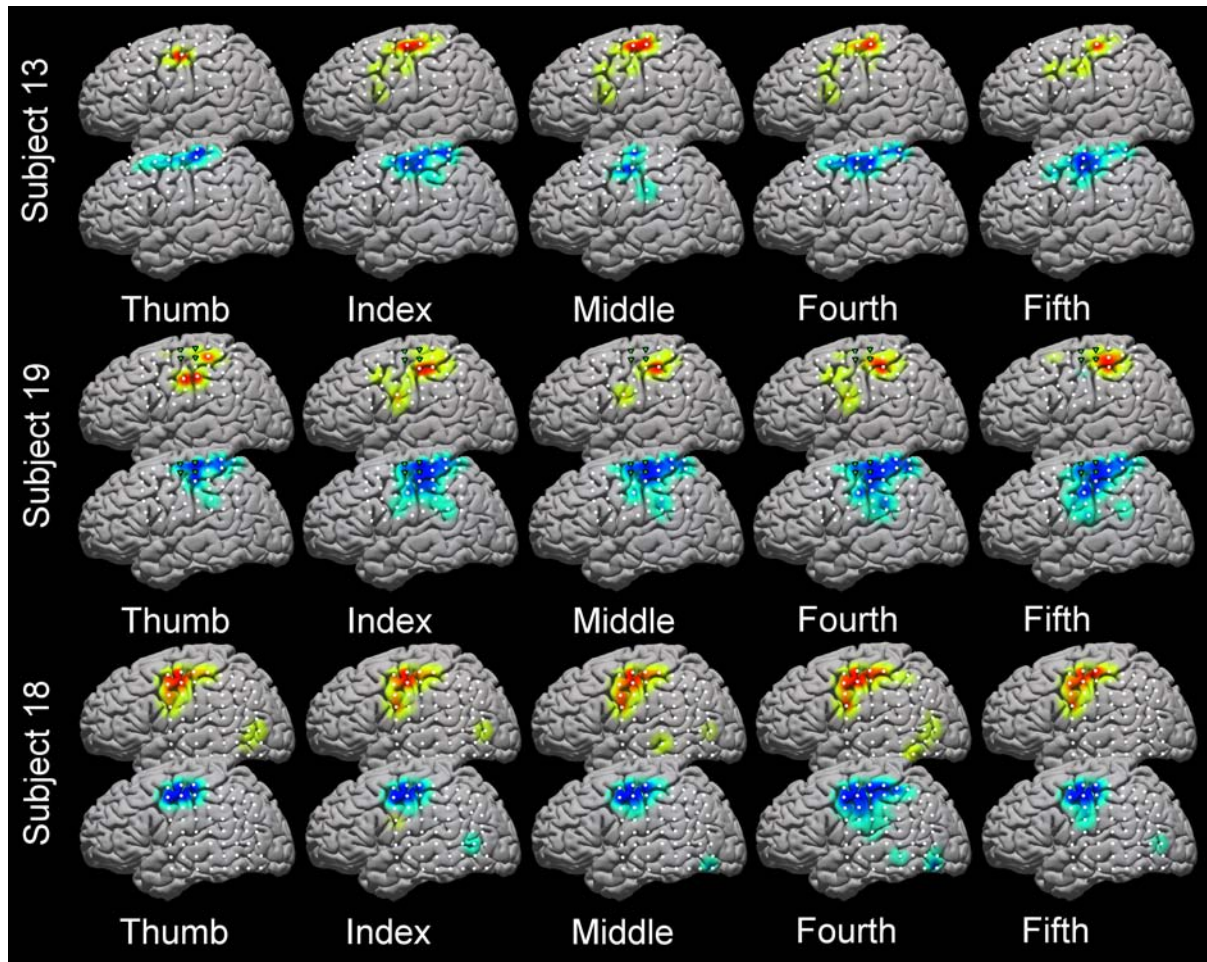


Figure 3.12: These are the cortical activation maps for individual finger movement in subjects 13 (top row) and 19 (middle row), and 18 (bottom row) respectively. Pinkie movement is on the far left, with thumb movement on the far right. Electrode locations are shown in white. The upper cortex of each pair is the high frequency representation, and the lower is the low frequency representation. The green triangles reflect the pairwise stimulation sites which elicited non-specific hand movement. Note that, while there is overlap, each digit is visually distinct from the others. The 2nd and 3rd digits appear to be closely correlated with each other, as do the 4th and 5th.

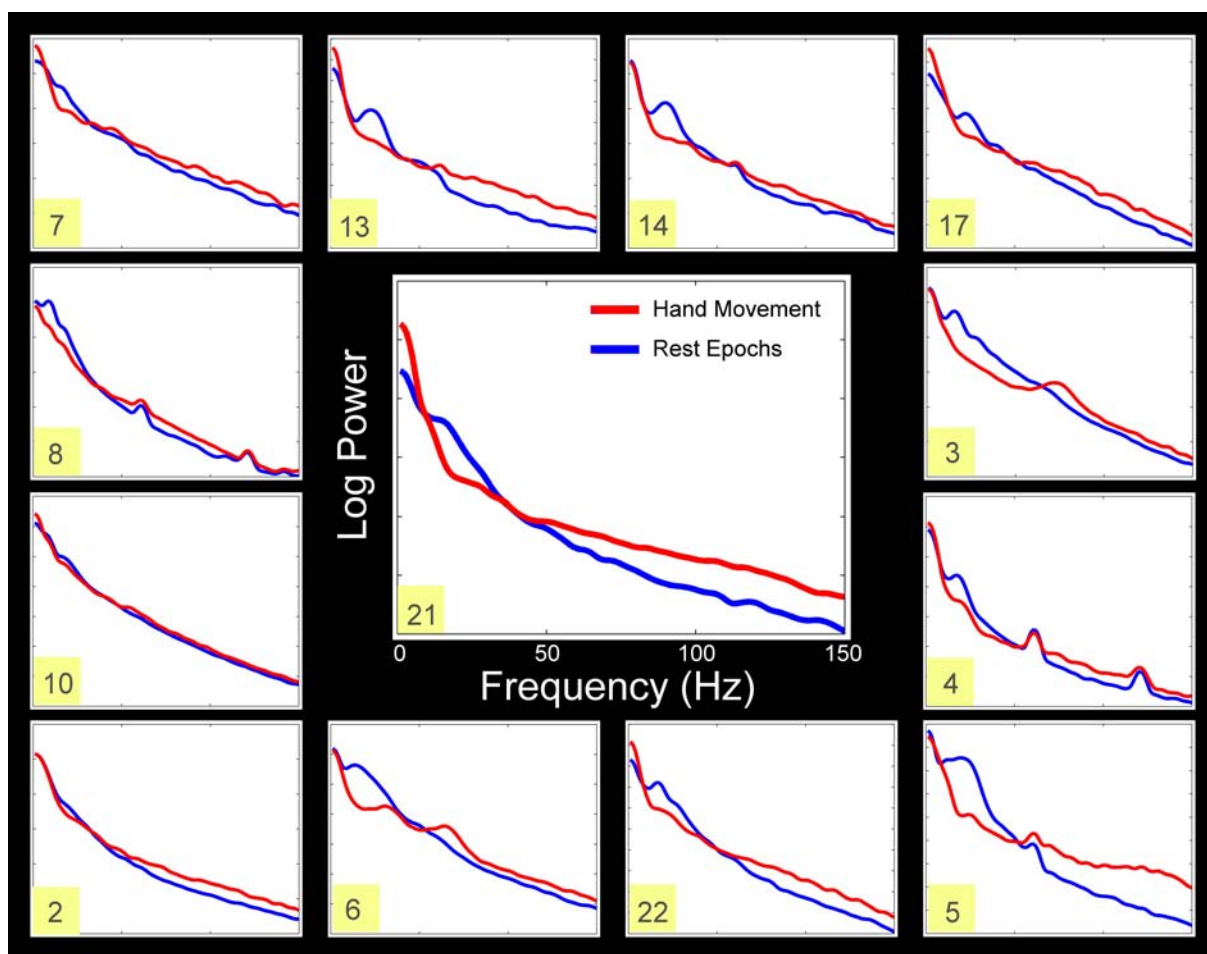


Figure 3.13: This figure shows the spectral shift with hand movement in the most significant electrode (determined by the product of the activation weight of the HFB times the activation weight of the LFB) across several subjects. The number in each inset is the subject number from Table 1. The axes labels and scales in the center (expanded) inset applies to all of the insets.

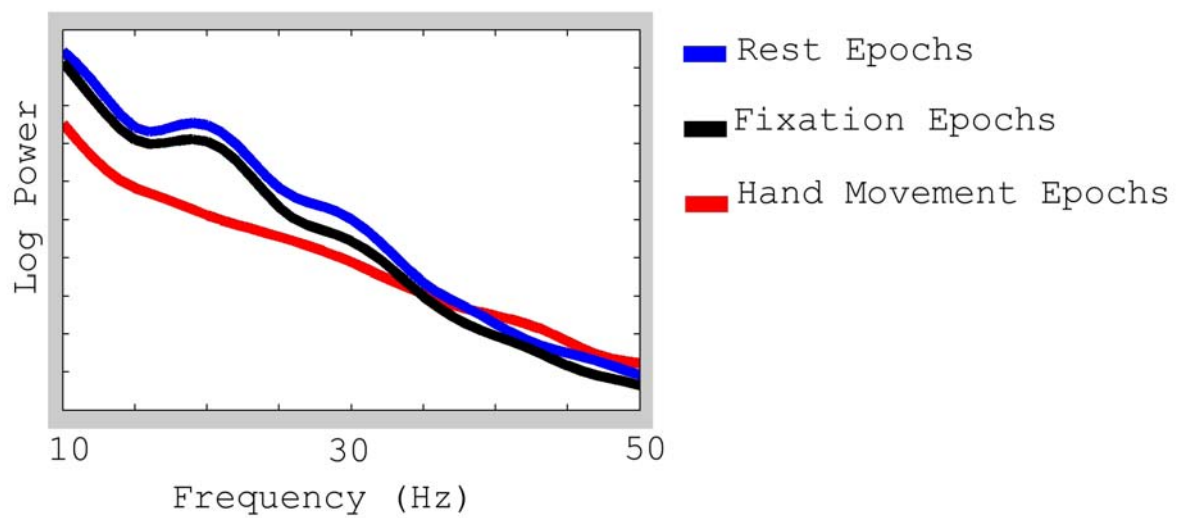


Figure 3.14: This figure demonstrates task-related change in the “resting-spectra.” That is, it shows that the spectra during resting durations of the movement task are not the same as the spectra during a simple fixation task in the low frequency regime. Epochs taken from a fixation task and analyzed in the same way as task related epochs reveal this, and spectral power during the fixation task in the LFB (8-32 Hz) for the subject shown here (subject 13) is significantly different from movement epochs and rest epochs during the movement task ($p < .01$ for both fixation vs. hand movement epochs, and fixation vs. rest epochs).

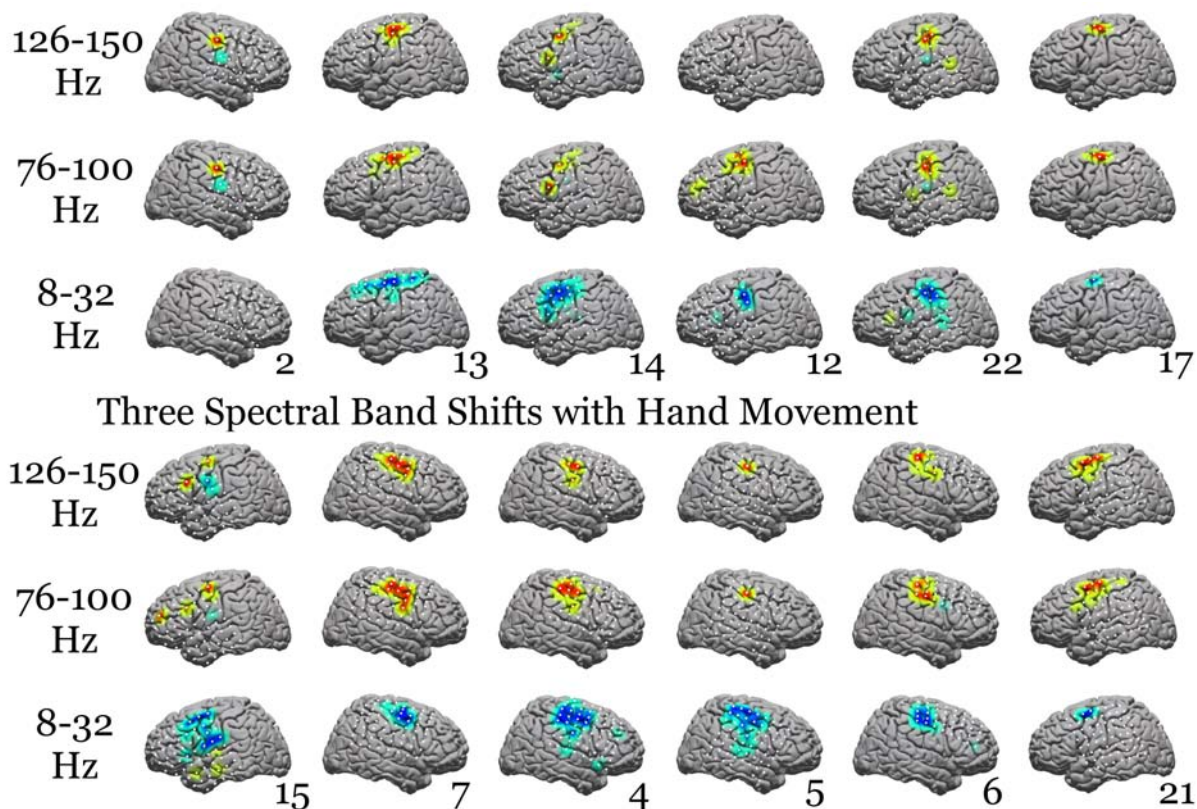


Figure 3.15: Cortical activation maps during hand movement for twelve individuals (those sampled at 1000 Hz.) Each column is a subject, and the rows within each column denote activations for three different frequency bands, 8-32 Hz (LFB - bottom row), 76-100 Hz (HFB - middle row), and 126-150 Hz (top row). The subjects are designated by a number at the bottom of each column, corresponding to subject numbers from table 3. The choice of a higher frequency band had little effect on the homuncular map. The average activation locations during hand movement for each of the three bands was calculated: for 126-150 Hz $y = -15.6 \pm 8.7$ and $z = 46.4 \pm 9.4$; for 76-100 Hz, $y = -14.6 \pm 10.7$ and $z = 46.7 \pm 9.6$; and for 8-32 Hz, $y = -13.3 \pm 16.0$, $z = 45.4 \pm 15.0$. As we could expect from the broad nature of the high frequency increase in the spectral curves figures B.2 and 7.8, and as we show here, if a higher frequency band had been chosen for our arbitrary HFB, the cortical activation maps would be very much the same. Motor maps of more select motor behaviors may prove to be sensitive to the specific choice of bandwidth.

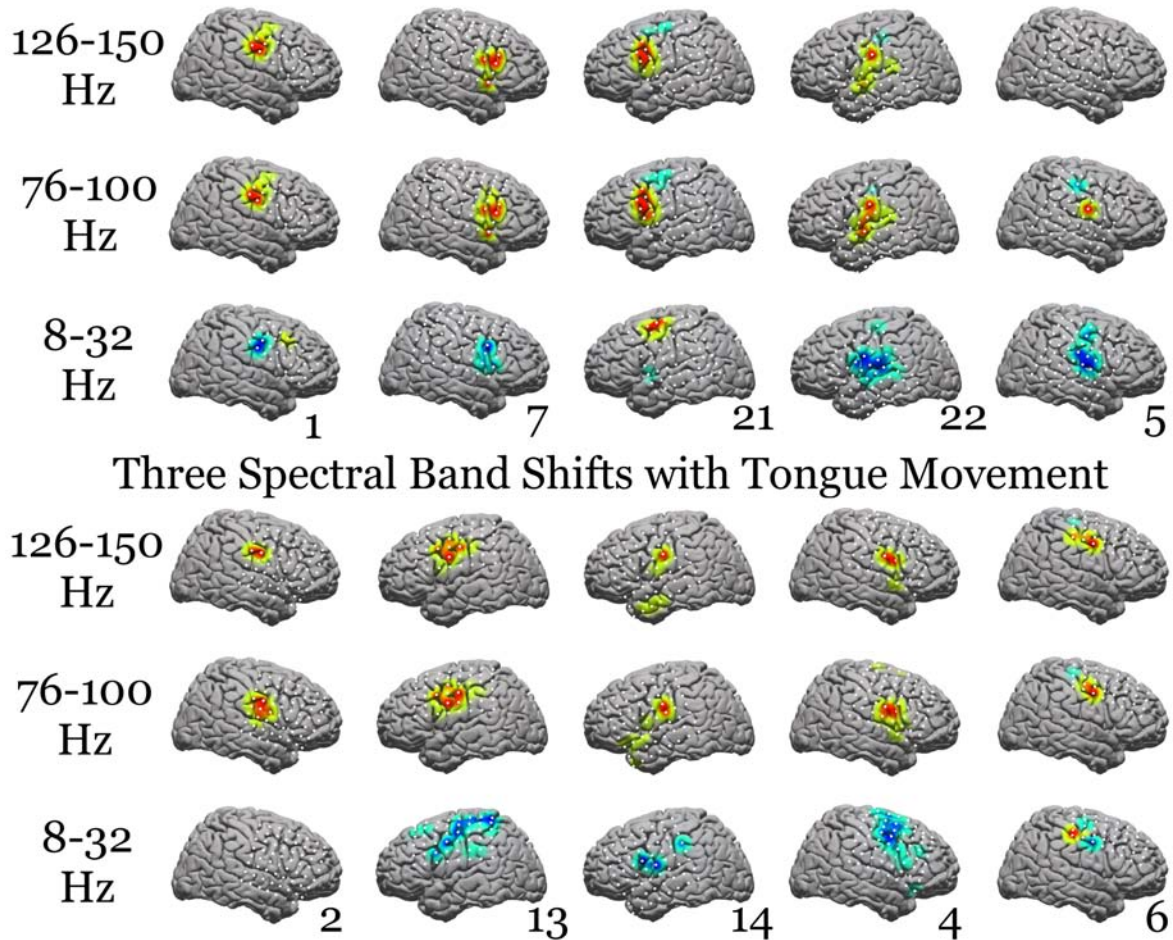


Figure 3.16: Cortical activation maps during tongue movement for ten individuals (those sampled at 1000 Hz.) Each organized as in Figure 7.11. The average activation locations during tongue movement was similarly invariant to the specific high frequency band selected: for 126-150 Hz , $y=-6.5\pm 12.8$ and $z=34.6\pm 15.7$; for 76-100 Hz, $y=-5.7\pm 11.5$ and $z=31.7\pm 16.8$; and for 8-32 Hz, $y=-3.4\pm 12.2$ and $z=37.9\pm 16.1$.

Chapter 4

ECOG OBSERVATIONS OF POWER-LAW SCALING IN THE HUMAN CORTEX

We report the results of our search for power-law electrical signals in the human brain, using subdural electrocorticographic recordings from the surface of the cortex. The power spectral density (PSD) of these signals has the power-law form $P(f) \sim f^{-\chi}$ from 80 to 500 Hz. This scaling index $\chi = 4.0 \pm 0.1$ is universal, across subjects, area in the cortex, and local neural activity levels. The shape of the PSD does not change with local cortex activity, only its amplitude increases. We observe a knee in the spectra at $f_0 \simeq 70$ Hz, implying the existence of a characteristic time scale $\tau = (2\pi f_0)^{-1} \simeq 2 - 4$ msec. For $f < f_0$ we find evidence for a power-law with $\chi_L \simeq 2.0 \pm 0.4$.

The human brain is arguably the most complex structure known to mankind and on the verge of starting to grasp its own inner workings. How do our brains compute? How fast do they compute? How do they store information? How universal is all of the above? Ever since the first electroencephalography (EEG) recordings in 1924, the study of the electrical activity of the human brain has focused on its prominent low-frequency features, in particular the excitatory and inhibitory rhythms at specific frequencies, like the α (10 Hz) and β (20 Hz) rhythms [101]. Traditional EEG studies are limited to $f < 100$ Hz. The fundamental processes at the individual neuron scale suggest a role of higher frequencies: the time of flight of a spike along an axon, the synaptic neuro-transmitter diffusion time, the integration time of the dendritic arbor. They are all near or sub 10 ms [145]. Synchronization and correlations associated with them are expected to exist at least up to 1 kHz.

Electrocorticographic (ECoG) recordings from the subdural surface of the cortex have recently made it possible to examine the electrical activity of the human neocortex with finer spatial and temporal fidelity than EEG. An array of electrodes is placed directly on

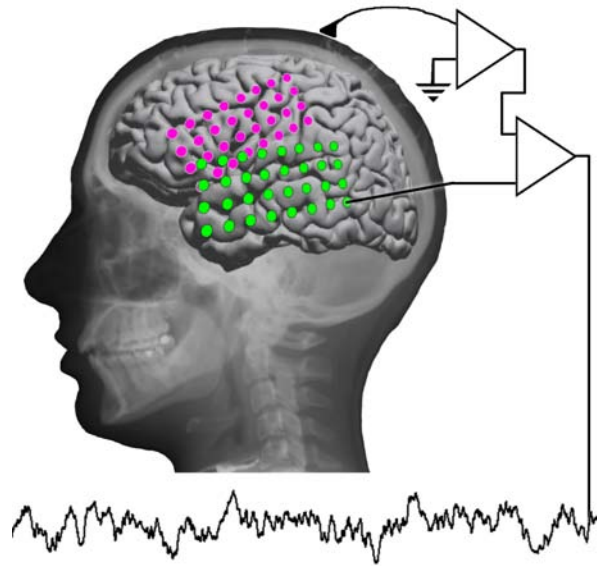


Figure 4.1: The electrode array locations are shown on a template brain for subject 1 (S1 - purple, temporal) and subject 2 (S2 - green, fronto-parietal). Potentials of all 32 channels are measured simultaneously with respect to a scalp reference and ground before pairwise re-referencing.

the surface of the cortex, see Fig. 5.5. The absence of the skull and surrounding tissue increases the electrode voltage while the close proximity to the cortex means that ECoG records very local phenomena. For example, changes in the classical α & β rhythms appear spatially uniform for a given set of tasks in EEG, but vary strongly spatially within the ECoG array for the same tasks [28].

The cortical surface potentials from sub-dural arrays reported in this study were obtained from 20 participants receiving clinical monitoring for the localization of seizure foci prior to resection. Each was informed about, and consented to participate in, the University of Washington internal-review-board-approved experimental protocol. The voltage was sampled at 10 kHz (2 subjects) or 1 kHz (18 subjects) using Synamps2 amplifiers (Compumedics-Neuroscan, San Antonio, TX) in parallel with long term monitoring (Xltek, Oakville, ON) from 32 platinum electrodes, encased in silastic, in an 8x4 configuration

(4 mm in diameter, with 2.3 mm exposed, separated by 1 cm, center-to-center, Ad-Tech, Racine, WI).

Our earlier studies [92] revealed the absence of distinct peaks in the power spectrum beyond $f \simeq 60$ Hz. We hypothesized the existence of a power-law of the form $P(f) \simeq Af^{-\chi}$ at these higher frequencies, and named it the χ -band/index, but the 1 kHz sampling rate truncated the signal at these high frequencies. The purpose of the study reported here was to determine, as accurately as possible, whether there is indeed such a power-law in the human cortical power spectrum, and how it might change with cortical activity (universality), by using a higher, 10 kHz sampling rate.

Power-laws represent scale free behavior, the finding of which immediately evokes scale free networks, complexity, avalanches, and self-organized criticality (SOC). Unfortunately, many such networks and processes are not large enough or can not be monitored precisely long enough to establish the scale invariance convincingly [23, 35]. The human brain is arguably the most complex and largest network available and may provide the best opportunity to observe scale free behavior in a natural setting. Each ECoG electrode measures the voltage power spectral density from a specific cortical surface area associated with a specific set of functions. An electrode pair probes about 10^6 neurons, and each neuron has up to 10^4 synapses [145]. This has not gone unnoticed, and the neuroscience literature is awash with attempts to interpret experimental low-frequency data with scale free concepts and models; with only limited success and leaving many questions [7]. In this paper we firmly establish the existence of the power-law in the χ -band and the actual value of the scaling index, χ . We obtain remarkable accuracy, particularly compared to many recent studies of power-law phenomena in nature [23]. Our accuracy approaches that of what was required and customary in equilibrium critical phenomena [35].

We characterized the power-law in the cortical spectrum during a simple fixation task. The subjects fixated on an “×” on the hospital room wall 3 m away from the bed for 130 s (subject S1) or 190 s (subject S2), with their eyes open. The time-dependent voltage between each electrode and the reference electrode was measured at 10 *kHz*, digitized, and stored

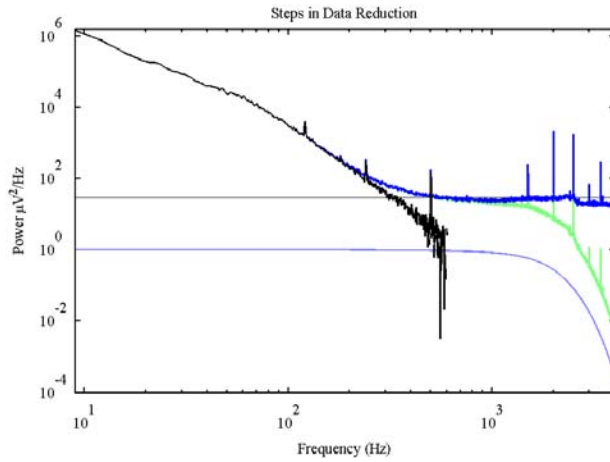


Figure 4.2: Illustration of the steps taken to remove the amplifier roll-off and noise floors from the raw power spectra (green to dark blue to black). The amplifier built-in amplitude attenuation was determined by scanning through 15-4000 Hz sine waves and fitting a smooth function to the attenuation at each frequency (light blue). A characteristic distribution of amplifier noise floors (current and potential noise) was generated by measuring the potential across an equivalent conformation of resistors (grey). The sharp line noise spikes at 60 Hz and its harmonics were excluded in our analysis.

for spectral analysis. To further reduce the common mode noise from the environment, the digitized electrode voltages were converted digitally into a set of voltage differences between each near-neighbor pair of electrodes. This significantly removed the high-frequency common mode noise and made it possible to measure well above 100 Hz. For our 4 by 8 array, the 32 individual electrode voltages produce 52 near-neighbor voltages (Fig. 5.5). All of the measurements reported in this Letter are for near-neighbor voltages.

We carefully characterized the amplifiers, their low pass filtering and their noise floor. These external factors affect the power spectrum measurement dramatically. They mask and obscure the underlying power-law from the brain signal. Demonstration of the power-law would not have been feasible without these corrections. Fig. 4.2 shows these corrective steps in the data reduction. First, the power spectral density is calculated from the Fourier transform of the time-varying near-neighbor voltages in 1 s Hann-windowed epochs, over-

lapping by 0.5 s. These are averaged into uncalibrated spectra (marked green in Fig. 4.2). They suggest a power-law shape, but the roll-off, apparent above 1 kHz, masks it. This roll-off does not represent a characteristic high-frequency in the brain. It originates in the amplifiers. We measured the gain versus frequency of the amplifiers independently. Their spectral bandwidth shape follows a classic low-pass filter (shown as blue in Fig. 4.2). Removing the amplifier response from each uncalibrated spectrum leads to spectra (dark blue) that level-off at high frequencies, indicating that we hit a noise floor. This noise floor does not reside in the cortex either. We measured the amplifier input noise for our amplifier-digitizer system independently. It is of order $\simeq 4 \mu\text{V}$ per root Hz for every amplifier. Subtracting this from the spectrum leads to a power spectrum that remarkably tightly fits a straight line in the log-log plot (the black line see Fig. 4.2) until at 500 Hz the signal disappears into the fluctuations of the amplifier noise floor. Future experiments with lower noise floor amplifiers will tell how high in frequency the power-law actually continues.

Small variations and uncertainties in the amplifier noise floor C significantly affect the quantitative analysis of the power-law. For that reason we perform 3 parameter fits, $P(f) = Af^{-\chi} + C$. All such estimates for C are within the uncertainty of our independent amplifier noise floor measurements.

Fig. 4.3 shows the combined spectrum, averaged over electrode pairs, for each subject. We exclude electrode pairs where one of the electrodes sits primarily on top of a vasculature, resulting in a much lower power in the signal and increased sensitivity to noise (4 channels for S1, 5 channels for S2). The inserts illustrate the quality of the power-law, the jitter around the average curve is more than one decade down from the signal, for all $f < 200$ Hz, beyond which the amplifier noise floor fluctuations start to kick-in. The exponent χ and the parameters A and C are estimated via a set of log-log type least-squares linear fits of the power spectral density between 80 and 400 Hz, excluding harmonics of 60 Hz. This leads to $\chi = 4.03 \pm 0.1$ for S1 and $\chi = 3.96 \pm 0.1$ for S2. The error bars are based on robustness against range shrinking as well as the deviations of the best fit with respect to the actual data across the entire frequency range $80 < f < 400$ Hz.

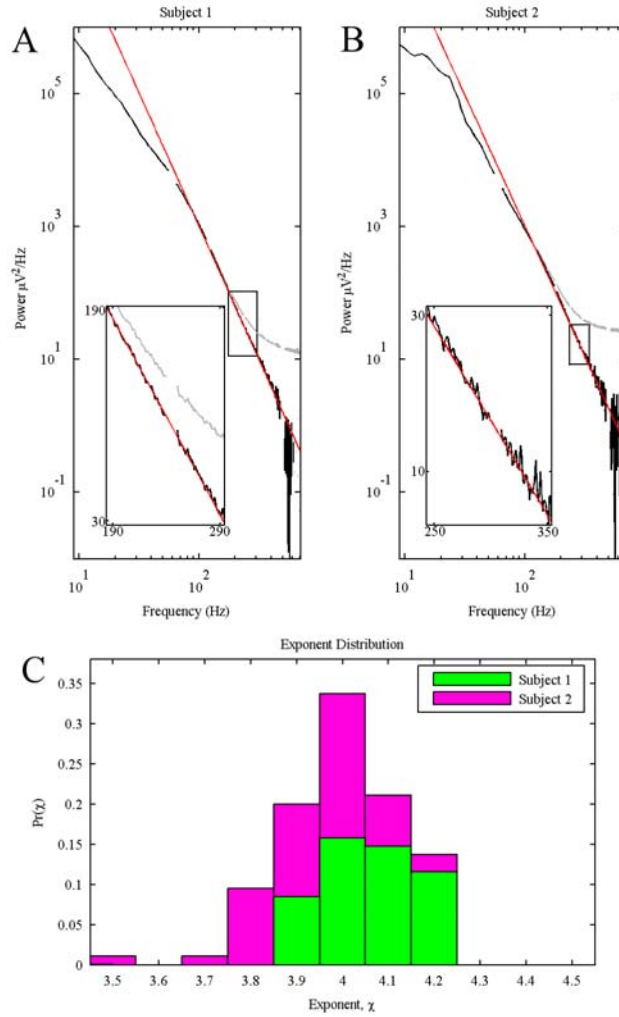


Figure 4.3: (A)-(B): Averaged electrode-pair power spectra (black) for subjects S1 and S2. The red lines, the best power-law fits (see text) with $\chi = 4.03$ (S1) and $\chi = 3.96$ (S2), fit the data very well from 80-500 Hz. The spectrum before noise floor subtraction is shown in gray. The S1 spectrum has a knee at $f_0 = 70$ Hz and appears linear below f_0 . (C): histogram of power-law fits from individual electrode-pair spectra, with mean values $\chi = 4.06$ (S1; green) and $\chi = 3.94$ (S2 purple).

To test for universality, we also performed the exact same type of fits to each individual electrode pair spectrum. The histograms for S1 and S2 in Fig. 4.3 overlap well and the

variations within each can easily be attributed to stochastic external issues, such as variations in electrode-cortex distance and vasculature. As such, we reached the accuracy limit imposed by the experimental set-up. Within this accuracy, χ is universal; it does not vary with subject nor specific brain areas. The mean value of the histogram exponents for S1 is $\chi = 4.06$ (STD=0.10, N=48), and for S2 $\chi = 3.94$ (STD=0.13, N=47), consistent with the above fitting analysis on the two averaged spectra. We conclude that $\chi = 4.0 \pm 0.1$ throughout the frequency range $80 < f < 400$ Hz.

Previous estimates of a power-law in the cortical spectrum [5] focused on low frequencies. The averaged power spectrum of S1, in Fig. 4.3 shows a knee at $f_0 \simeq 70$ Hz, and suggests a different power-law below f_0 . Both seem absent in S2. The α & β rhythms are strongly pronounced in every channel pair of S2 (and are clearly visible in Fig. 4.3). They obscure whatever power-law might be present underneath. Eight electrode pairs from S1 lack α & β rhythms. They may be absent in these local cortical areas, or so tightly synchronized that they cancel out in the electrode pair voltage difference. A simple minded $P(f) \simeq Af^{-\chi_L}$ fit through their average from 15-80 Hz, yields $\chi_L = 2.57 \pm 0.15$ (N=8). However, such local fits are inherently dangerous. They are blind to the global properties of the spectrum. Our high frequency analysis of χ is already a clear illustration of this. The amplifier roll-off and noise floors truncate our data only beyond $f \simeq 400$ Hz, but they affect the spectrum already at much lower frequencies (Fig. 4.2). Similarly, the high frequency $\chi = 4.0$ power-law is already in-play below f_0 . Indeed, the global two-powerlaws form

$$P(f) \sim A \frac{1}{1 + \left(\frac{f}{f_L}\right)^{\chi_L}} \frac{1}{1 + \left(\frac{f}{f_0}\right)^{\chi_H}}$$

with constraint $\chi_L + \chi_H = \chi = 4$, shifts χ_L down to $\chi_L = 1.99$ (STD=0.21, N=8), with cutoff $f_L \ll 15$ Hz.

The 8 S1 channels form a dangerously small ensemble. We performed the same analysis on 1 kHz data for the exact same 2 minute fixation task from 16 subjects, with electrode arrays in the lateral frontal/temporal/parietal cortex. The spectra were determined and corrected for amplifier-digitizer frequency dependent attenuation in the same way as the

10 kHz data. We selected again only those channel pairs (N=116) that lacked the α & β rhythms. Naive fits from 15-80 Hz (excluding 57-63 Hz line noise) of these corrected spectra yield again $\chi_L = 2.5$ (STD=0.4, N=116); while the same global two power-law form, shifts this down again to $\chi_L = 2.0$ (STD=0.4, N=116) when setting $f_L = 1$ and $f_0 = 70$.

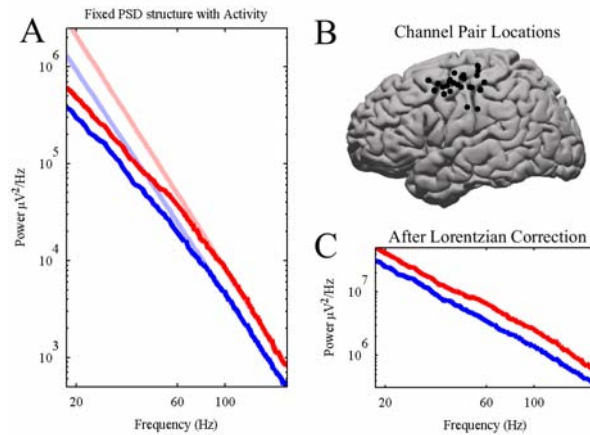


Figure 4.4: The average shift in power spectral density in electrodes after the PCA decomposition in the hand cortical area during finger movement, for subjects 3-8; 5 electrode-pair channels each (30 total). (A) demonstrates that movement (red) increases the overall power by a factor 1.8 while preserving the shape of the rest (blue) spectrum. $f > f_0$ power-law fits (grey) are consistent with $\chi = 4$. (B) Electrode pair channel locations (interpolated) across all subjects, projected to the left-hand side. (C) Remaining spectra after dividing out a Lorentzian, $1/(1 + (f/70)^2)$ to illustrate consistency with the two-powerlaws form with $\chi_L \simeq 2$.

The uncertainty in the value of x_L remains quite large. Even the existence of this low frequency power-law remains in question, until we collect more 10 kHz data. The analysis also requires a reliable decomposition of the low frequency α & β rhythms from the background. We demonstrated that principle component analysis (CPA) techniques can achieve this [?, 92]. Fig. 4.4 illustrates this for 1 kHz data. Five subjects performed a finger movement task. A visual cue indicated when to move a given finger (repeatedly flex/extend one finger at a time; opposite side of body from grid placement), and the position of each finger was recorded using a dataglove (5dt; Irvine, CA). Samples of movement spectra of

each type were calculated from the FFT of 1 s Hann-windowed epochs centered at the maximum displacement of the finger during each flexion. Rest spectra were calculated from epochs in which there was no hand movement. The spectra were corrected for amplifier-digitizer frequency dependent attenuation. Differences between variations in $\alpha&\beta$ versus high frequency allows a PCA removal of the $\alpha&\beta$ peaks from all the power spectra. We were able to identify electrode pair channels which demonstrated significant shifts in power during specific activity (single finger movement type) versus rest. A subset of five such channels was chosen naively (based upon significance rather than being hand picked) from each subject, and the average spectrum for the specific movement type causing change (the “active” state) was compared to the average rest spectrum (the “inactive” state), after the $\alpha&\beta$ peaks had been decoupled and largely removed.

Fig. 4.4 addresses several issues: Earlier [92, 28], we observed changes in the χ -band during behavior tasks and hypothesized how those can be used directly to quantify activity in the brain in a variety of practical settings; e.g., the total power in the χ - band increases with activity versus rest. Fig. 4.4 demonstrates that this increase in spectral power with activity extends over all frequencies. Moreover it strongly suggests that the shape of the spectrum is preserved (universality). The above $\chi_L - \chi_H$ two-powerlaws form fits the shape well; with $f_0 \simeq 70$ Hz, $\chi \simeq 4$, and $\chi_L \simeq 2$, within 10%; a level of accuracy to be expected within the limitations of the 1 kHz nature of this data. The active/inactive power ratio R (between the amplitudes A) is unlikely a universal number. In this data set its geometric mean is equal to $R = 1.81$ with a variation of order 0.34 (N=25).

What does all of this teach us about computations and correlations in the brain? EEG and ECoG voltages represent the superposition of the electric current dipole fields generated by the very large collective of nearby neurons and their associated ionic channel currents, propagated through the complex mass of ionic extracellular liquid and neuronal and glial membranes. This is a quite complex phenomenon and not yet well understood quantitatively. Moreover, the underling neuron computational issues remain in flux, e.g, understanding the relative roles of computations at the level of dendritic trees versus those

at larger length and time scales associated with the connectivity the network of neuron.

If the value of the high-frequency exponent $\chi = 4.0 \pm 0.1$ were distinct from an integer, we could have reported safely to have observed SOC type complex scale free behavior in the cortex. The uncertainty in $\chi_L = 2.0 \pm 0.4$ still leaves room for this. Perhaps SOC behavior (if it exists) is only expressed in more subtle ways in ECoG. In the case $\chi_L = 2$, the spectrum is well described as a product of two $1/(1 + (f/f_c)^2)$ Lorentzian shapes. These can originate without any SOC complexity: such as white noise with two filters; as the product of an exponential decaying correlation function and a temporal form factor; as two processes with definite correlation times; etc.

Our results place definite constraints on future brain modeling. ECoG spectra definitely scale as $P \sim f^{-\chi}$ across all $70 < f < 400$ Hz. The value $\chi = 4.0 \pm 0.1$ is universal, across subjects, areas in the cortex, and local neural activity levels. The knee in the spectra at $f_0 \simeq 70$ Hz, implies the existence of a characteristic time scale $\tau = (2\pi f_0)^{-1} \simeq 2 - 4$ msec, probably originating at the neuron length scale and surviving the coarse graining to the 2 mm electrode size length scale.

4.1 Supplement

In this supplement we present details of the experimental set up, in particular the characterization of the amplifier roll-off and noise floor; and we discuss details of the data handling and power law analysis steps.

Eighteen human subjects (ages 18-45, 8 females), see table in Fig.4.1, were implanted with subdural electrode arrays for the localization of seizure foci prior to surgical treatment of medically refractory epilepsy. The arrays were typically placed for 5-7 days with the location of the electrodes and duration of implantation determined independently by clinical criteria alone. Experiments were performed at Harborview hospital at the University of Washington (UW). Subjects were typically studied 4-6 days after craniotomy and electrode placement to allow for recovery from the surgery. Subjects gave informed consent for participation in a manner approved by the Institutional Review Board of the University of Washington.

Subject	Age	Sex	Hand	Sampling Rate	Cognitive Capacity	Grid Location	Seizure Focus
hh				10 kHz			
hi01				10 kHz			
AL	1	31	F	R	1 kHz	Normal**	R Frontotemporal R Insula
ca				1 kHz			
CC	9	21	M	R	1 kHz		R Frontotemporal R Frontal
de				1 kHz			
FP	12	23	M	R	1 kHz	Normal*	L Frontotemporal L Temporal
gc				1 kHz			
GF	2	24	F	R	1 kHz	Normal	R Frontotemporal R Orbitofrontal and Temporal
JM	15	41	M	L	1 kHz	Normal	L Frontotemporal L Temporal
MVB	18	45	F	R	1 kHz	Normal*	L Frontotemporal L Frontal
RH	4	38	M	R	1 kHz	Borderline (IQ -70)	R Frontal R Frontal
UG	6	39	F	R	1 kHz	Normal	R Frontal R Frontal
WM	5	19	F	R	1 kHz		R Fronto-parietal R Parietal
JC	13	18	F	R	1 kHz	Normal	L Frontal L Frontal
JP	3	35	F	R	1 kHz		L Fronto-Temporal L Fronto-temporal-parietal L Temporal
WC	6	32	M	R	1 kHz		B Fronto-temporal-parietal L Temporal
ZT	7	27	F	R	1 kHz	Normal	L Frontal L Parietal - Temporal - Occipital
HT	8	26	M	R	1 kHz		L Frontal/Temporal/Occipital

All data were recorded at the bedside with Neuroscan Synamps² amplifiers (Compumedics-Neuroscan, San Antonio, TX), in parallel with a clinical recording system (xltek, city, state or bmsi city, state), as shown schematically in Fig. 4.5. The signal was split outside of the head, prior to amplification. The two amplifiers used common ground and reference

(both from the scalp). The platinum electrodes (Ad-Tech, Racine, WI) were configured as

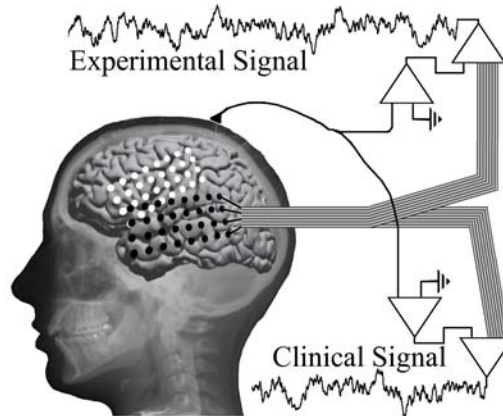


Figure 4.5: Recording Setup with amplifiers

$8 \times \{4,5,6,8\}$ rectangular arrays. The electrodes were 4mm in diameter (2.3mm exposed), at 1 cm inter-electrode distance, and embedded in silastic. The arrays were placed on the lateral frontal, temporal, and parietal cortex - shown for subjects 1 (S1 - black) and 2 (S2 - white) on a template brain in Fig. 4.5 and on the actual brains in fig.4.6

All experiments were performed at the bedside. In this fixation task, the subjects fixated on a 10cm "x", on the wall 3m away, for 2 or 3 minutes (120/180s) at a time. They were instructed to remain motionless and keep their eyes open, blinking if they needed to.

Fig.4.7 illustrates the steps taken to transform the raw voltage time series from each electrode into power spectra. The data was re-referenced in terms of neighboring differential pair channels, $V(t) = V_i(t) - V_j(t)$ (our 32 electrode arrays have 52 differential pair channels each). This significantly reduced the overall noise in the signal. This reduction is to be expected, since it removes various non-local contributions to the signal, while the signal of interest originates from the neurons (about 5×10^5 of them) immediately underneath each electrode. Next, the time series were broken-up into 1 second long intervals, overlapping by 0.5 second (we have no interest in phenomena with frequencies below 1Hz). Each of

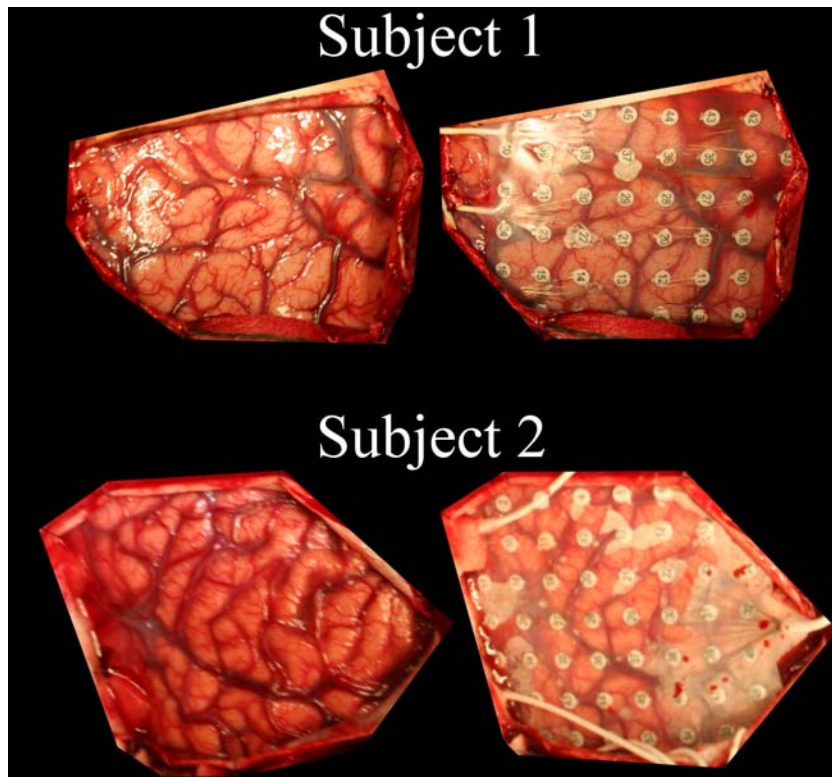


Figure 4.6: Electrode array placement on cortex for subjects S1 and S2.

these epochs was windowed

$$V'(\tau, m) = V(\tau + \frac{1}{2}mT)H(\tau) \quad (4.1)$$

with a Hann-window $H(\tau)$ of the form

$$H(\tau) = \frac{1}{2} \left[1 + \cos \left(\frac{2\pi}{T} \tau \right) \right] \quad (4.2)$$

inside time interval $-T/2 \leq \tau \leq T/2$ with $T = 1$ sec, and $H(\tau) = 0$ at all other times. The power spectral density (PSD) for each epoch follows from the Fourier transform

$$P(f, m) = \frac{1}{T} \left(\sum_{\tau=1}^T V'(\tau, m) e^{i2\pi f\tau} \right)^2 \quad (4.3)$$

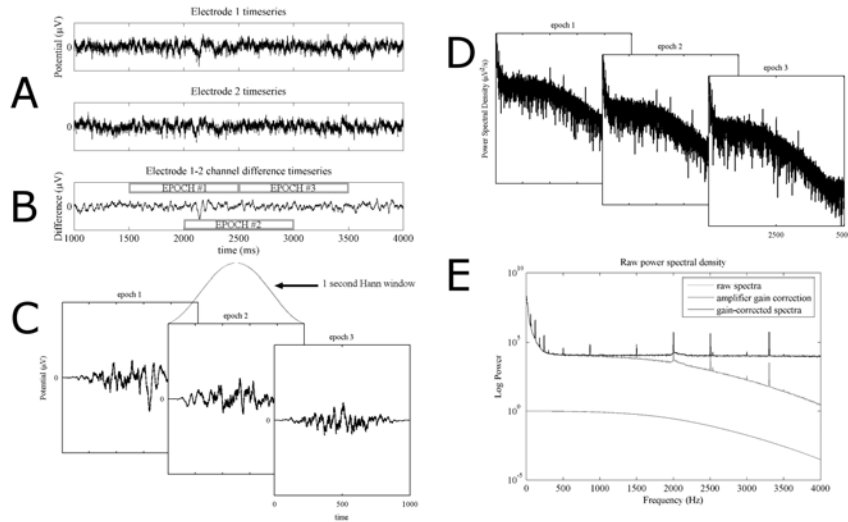


Figure 4.7: Power Spectral Density Calculation: (A) and (B) show voltage time series of 2 nearby electrodes during rest. Their difference, shown in (C) (local pair electrode referencing) is broken-up into 1 second long segments, and each is Hann windowed and Fourier transformed to generate the power spectra, shown in (D). Each is very noisy, but their average, shown as the green line in (D) is smooth.

Each of these individual spectra is quite noisy; examples of this are shown in Fig.4.7.D. Taking the average PSD over all epochs

$$P_R(f) = \frac{1}{M} \sum_{m=1}^M P(f, m) \quad (4.4)$$

quiets this down into a smooth PSD for each channel pair, as illustrated by the green line in Fig.2 of the main text and again in Fig.4.7.E. (The same curve but shown with a linear frequency scale instead of a logarithmic one.) Each PSD represents the Fourier transform of the voltage auto-correlation function

$$G(\tau) = \int dt V(t + \tau)V(t) \quad (4.5)$$

averaged over the entire time interval of the experiment.

The properties of the amplifiers proved a major issue in the data analysis: their (surprisingly high) noise floors and low pass filtering (roll-off). The Green curve in Fig.4.7.E

follows a characteristic low pass filter type shape. Its onset changes with the sampling rate setting of the amplifier (10kHz versus 1kHz). This strongly suggests that this low pass filter resides within the amplifiers (FDA approved Neuroscan Synamps2 amplifiers; Compumedics-Neuroscan, San Antonio, TX), and not inside the brain.

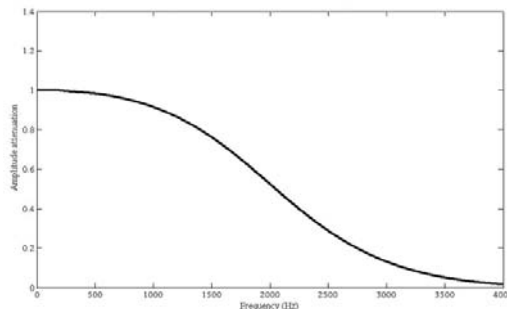


Figure 4.8: Frequency-dependent amplifier amplitude attenuation at 10KHz sampling rate

We determined the amplitude attenuation function $R(f)$ (roll-off factor) independently by means of an external function generator by repeatedly sweeping (at a rate of 10 seconds) at fixed amplitude through all frequencies between 15Hz and 4000Hz at the 10KHz sampling rate setting, and between 10 Hz and 300 Hz at the 1KHz sampling rate setting. This $R(f)$ followed a Lorentzian type shape as expected, see Fig.4.8. We divided our PSD's by this filter, $P(f) = P_R(f)/R(f)$. It completely removed the roll-off from the PSD's, as illustrated in Fig.2 of the main text and also in Fig.4.7.E. The green line was corrected to produce the red line. A definite noise floor came into focus.

The magnitude of this noise floor is atypically large for experimental amplifiers; but we established that they are the source. This type of noise may be standard in FDA-approved clinical amplifiers. This noise does not reside inside the brain. The amplifier noise floor was determined experimentally by measuring the potential across an equivalent conformation of resistors electrode pairs, see Fig.4.9. This was done in situ in the sense that the parallel clinical amplifiers remained attached. Following on-line measured impedance, $R2$ was set to $10\text{k}\Omega$ and $R1$ to 0.5Ω (although noise values were robust against increasing $R1$ to $1\text{k}\Omega$).

The result is shown as the grey line in Fig.2 of the main text.

We do not present further details of our independent amplifier noise floor experiments, because the cortex data suggests that the floors vary slightly between subjects and might thus drift in time. Therefore we treat the noise floor as a free (to be fitted) parameter in the data analysis, as discussed below. However, these independent noise floor experiments demonstrated that the noise floor in the cortex data originates from the amplifiers, not inside the cortex, and that this amplifier noise is almost white (near constant in frequency) over all experimentally relevant frequencies. The blue line in Fig.2 of the main text transforms into a remarkable straight (black) line after subtraction of the noise floor (grey line) in this log-log plot, strongly suggesting a power law form $P \simeq Af^{-\chi}$ at frequencies $f > f_0 \simeq 70$ Hz.

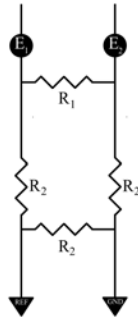


Figure 4.9: Equivalent resistor network during amplifier noise floor estimation

We need to perform fits of the form $P \simeq Af^{-\chi} + C$. It is logical to try to separate out the noise floor C by fitting it directly to the data at high frequencies, near say 1000 Hz, where C totally overpowers the cortical signal. From Fig. 4.10 for subject S1 we can conclude that the noise floor has a value in the range $C = 12500 - 15500$. Such a range is consistent with the spread between individual channel pair data. These floors are slightly higher than in the independent noise floor measurements discussed above. Those correlate better with the ones in the S2 data. Indeed the independent noise floor measurements were taken immediately after the S2 data sets.

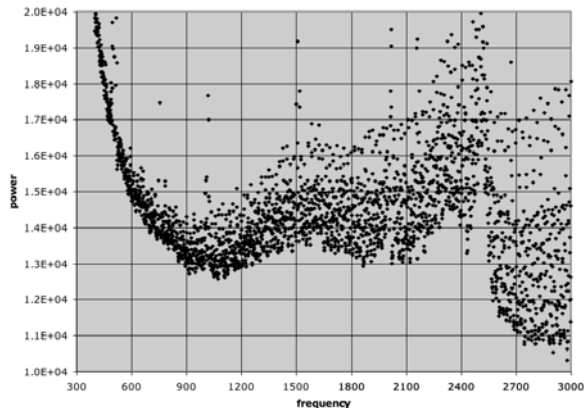


Figure 4.10: Pairwise referenced and averaged power spectrum of S1 at very high frequencies after roll-off removal.

The very high frequency $f > 1000\text{Hz}$ data is certainly not quiet and does not behave like simple white noise floor. The origins of this remain unresolved. It might reflect sensitivity to details of the amplifier roll-off function $R(f)$ (amplified by the division). It might originate from the internal electronics of the amplifiers. It could reflect an external high frequency source that is not fully removed by the nearest neighbor pair referencing. In light of these uncertainties, we felt that the only proper approach is a self-consistent fitting procedure limited to the frequency range $80\text{ Hz} < f < 500\text{ Hz}$.

Figs.4.11 demonstrates that the power law with exponent $\chi \simeq 4$ is stable and insensitive to the exact value of the noise floor in the frequency range $80 < f < 200\text{ Hz}$. Note that the noise floor choice $C = 15500$ extends the power law fit all the way to 500 Hz. Before we continue, we like to stress how well the PSD data follow that power law. Fig. 3 of the main text and also Fig.4.12.A illustrate this. The curves follow straight lines exceptionally well. Power law scaling extends over four decades in power and (because $\chi \simeq 4$ is large) over one decade in frequency. We encounter a quantitative level of power law scaling rarely seen in experimental data, and obtain unusually high accuracy in the value of the exponent χ .

We fitted the PSD to the form $P(f) \simeq Af^{-\chi} + C$ in the frequency interval 80 Hz

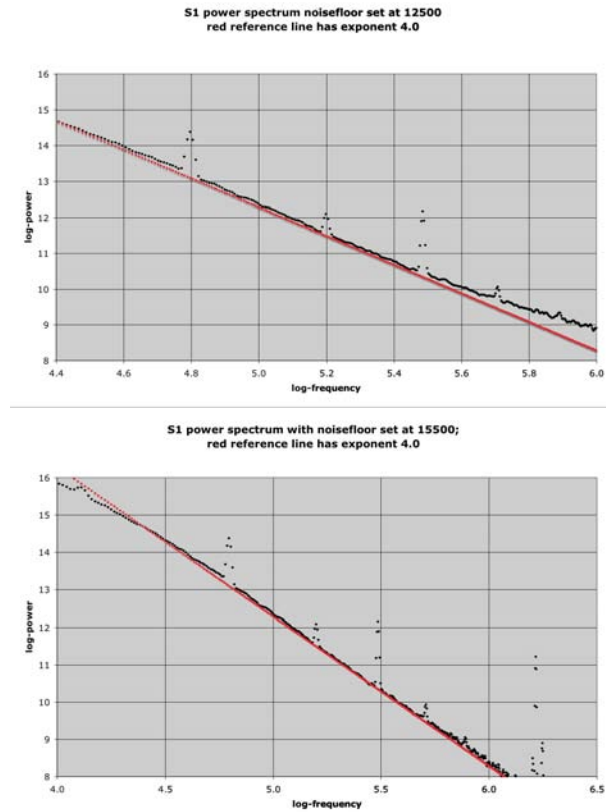


Figure 4.11: Power law fit of S1 in frequency range $80 < f < 200$ for (top) noise floor $C = 15500$ and (bottom) $C = 12500$, demonstrating that the exponent $\chi = 4$ is insensitive to the noise floor value at these frequencies and that (A) provides a better global fit.

$< f < 500$ Hz. The simplest approach would be to plot $\log(P(f) - C)$ versus $\log(f)$ for a range of guesses of the noise floor C , and choose the value of C for which the curve straightens out best into a straight line; like in Figs.4.11. The slope of that line being the value of the exponent χ .

An infamous mistake in this procedure is to apply global least square fits. Most weight must be given to the middle frequencies $80 < f < 200$ Hz. The PSD crosses over to a different form at the low end, near $f_0 \simeq 70$ Hz (as discussed below). The noise floor becomes the important factor at the high end, $f > 400$ Hz. The conventional approach to

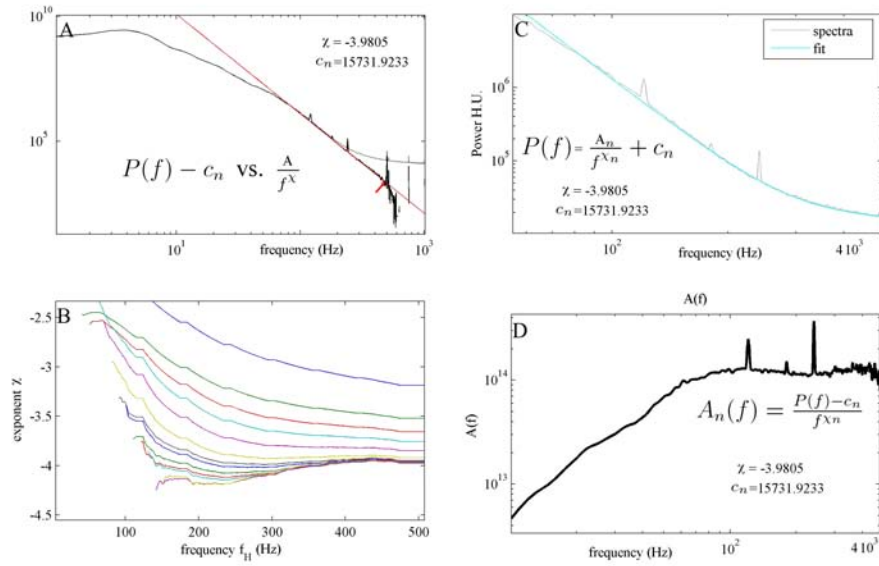


Figure 4.12: Illustrations of the recursive range shrinking fitting protocol of the PSD to the form $P(f) \simeq Af^{-\chi} + C$ over frequency range $80 \text{ Hz} < f < 500 \text{ Hz}$ discussed in the text.

this is to determine local slopes $\chi(f)$ by performing least square fits to the curve over only narrow frequency intervals $f_L < f < f_H$ along the curve, and plot these $\chi(f)$ estimates for a range of choices of the noise floor C . The best fit for C is the $\chi(f)$ curve with the widest flat plateau. The best value for χ is that plateau value. A potential problem in this is that such local slopes become increasingly noisy for narrow fitting intervals $f_L < f < f_H$, and the plateaus can then drown in the noise. In light of this, and because of the need to automatize the fitting procedure due to the large amount of data, we use the following recursive protocol.

It starts with an initial guess for value of the exponent, χ . That value is used for an initial estimate for the noise floor C by means of a straight line fit of the form $P(f) = Ay + C$ as function of $y = f^{-\chi}$, using the high end of our frequency range, $250 \text{ Hz} \leq f \leq 490 \text{ Hz}$. Next, we use this estimate of C to improve on the estimate of χ by performing least square fits to $\log(P(f) - C)$ versus $\log(f)$ between $f_L < f < f_H$ with the $f_L < f_H$ interval covering

(expanding and shrinking over) the entire frequency range $80 \text{ Hz} < f < 500 \text{ Hz}$. We plotted these estimates $\chi(f_L, f_H)$, as illustrated in Fig.4.12.B, with f_H along the horizontal axis and different lines representing different values of f_L . (The onset of the lines mark the values of f_L , because f_L is always smaller than f_H .) The quality of each fit is reflected by the presence of horizontal segments in the curves, by the width of those segments with f_H , and by collapse of those segments with the curves at nearby f_L . For example, from Fig.4.12.B we would conclude that $\chi = 3.95 \pm 0.1$; and then use this estimate to start the next iteration cycle by setting $\chi = 3.95$ in $y = f^{-\chi}$ for the next $P(f) = Ay + C$ estimate of the noise floor C ; and so on. This iteration scheme always converged for our data. The quality of the fit can be further judged by plotting $A(f) = (P(f) - C)f^\chi$, to check how well the final amplitude A is frequency independent, see Fig.4.12.D.

The curves $\chi(f_L, f_H)$ in Fig.4.12.B have distinct minima for intermediate values of f_L and f_H . This shows how easily the exponent χ can be underestimated. Choosing f_L too close to $f_0 \simeq 70 \text{ Hz}$, where the PSD crosses over to a less steep curve, systematically underestimates the exponent. Under estimating the noise floor C has the same effect at the high frequency side; and results in an up-swing in the $\chi(f_L, f_H)$ curves at high frequencies. Overestimating the noise floor leads to negative values of $P(f) - C$ at high frequencies and a collapse to erratic behavior in the $\chi(f_L, f_H)$ curves at high frequencies. It is significant therefore that the curves deepen during the iteration process in the interval where f_L and f_H both take intermediate frequency values.

We performed this fitting protocol on the electrode pair averaged PSD of subjects S1 and S2, with as result $\chi = 4.0 \pm 0.1$. Note that the electrode arrays in those two subjects are located at different parts of the motor cortex. We applied the same fits also to the more noisy individual electrode pair PSD's from both subjects, leading to a narrow distribution of exponents χ centered at the same value $\chi = 4.0$ and with a width consistent with the above error estimate. This is shown in Fig.3 of the main text and addressed there.

A logical follow-up issue is to check for possible systematic effects in the individual electrode pair signals. The total power in each electrode varies greatly, by about 10 percent,

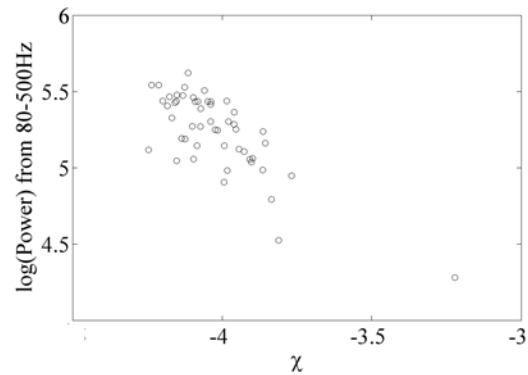


Figure 4.13: Correlations between the fitted values of the exponent χ and the total power in the signal between $80 \text{ Hz} \leq f \leq 500 \text{ Hz}$ in the individual electrode pairs of subjects S1 and S2. Red dots indicate channel pairs rejected because of vasculature as discussed in the text.

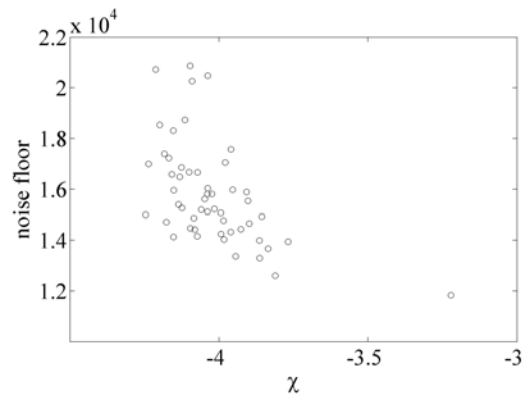


Figure 4.14: Correlations between the fitted values of the exponent χ and the fitted noise floor C in individual electrode pairs of subjects S1 and S2.

as seen in Fig.4.13. This has various reasons. The most important one is probably the proximity of blood vessels and/or variations in quality of electrode-pia-cortex contact. The most anomalous (weakest) signals are cleanly correlated visually, in Fig.4.6, with electrodes sitting on vasculature; we removed them therefore from our analysis: For subject 1, this corresponded to channels: 38 (between electrodes 17 & 25), 39 (18 & 26), 46 (25 & 26), 47

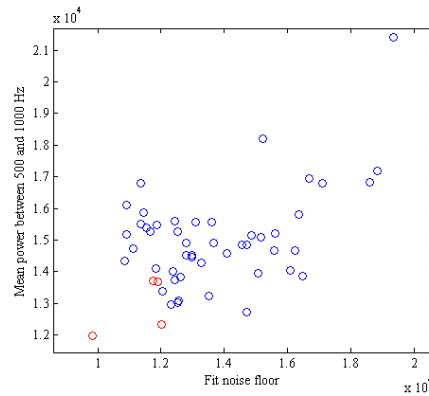


Figure 4.15: Correlations between the fitted noise floor C and the average power in the high frequency range $500 \text{ Hz} \leq f \leq 1000 \text{ Hz}$, for individual electrode pairs of subjects S1 and S2.

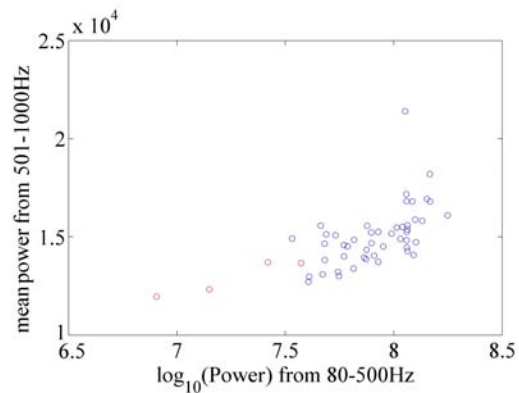


Figure 4.16: Correlations between the average power in the high frequency range $500 \text{ Hz} \leq f \leq 1000 \text{ Hz}$ and the total power between $80 \text{ Hz} \leq f \leq 500 \text{ Hz}$, for the individual electrode pairs of subjects S1 and S2.

(26 & 27). For subject 2, this corresponded to channels: 46 (25 & 26), 47 (26 & 27), 39 (18 & 26), 38 (17 & 25), 31 (17 & 18).

Fig.4.13 tests for correlations between the value of the fitted exponent χ and the total power in each channel pair. A weaker signal makes that the PSD drowns into the noise floor at a lower frequency. That is likely to result in a poorer fit and to a systematically smaller

value of χ . Fig.4.13 shows that this effect is weak.

Fig.4.14 tests for possible systematic correlations between the fitted values of χ and C . It appears that such correlations are weak compared to the channel pair statistical noise. The fitted values of the amplifier noise floors C in specific electrode pairs vary widely, by roughly 20 %. This is not due to the fitting protocol, because in Fig.4.15 the fitted noise floors correlate well to the average high frequency power (at $500 \text{ Hz} \leq f \leq 1000 \text{ Hz}$).

Finally, Fig.4.16 shows that this average $500 \text{ Hz} \leq f \leq 1000 \text{ Hz}$ high freq power is slightly correlated to the total power between $80 \text{ Hz} \leq f \leq 500 \text{ Hz}$. Possibly suggesting that the amplifier noise floors vary with input power.

In conclusion, Figs.4.13-4.16 suggest some systematic effects, but they are rather weak compared to statistical variations between the electrode pairs. It does not seem proper to pursue them further at this point.

The PSD changes its slope below $f_0 \simeq 70 \text{ Hz}$. This knee at f_0 is more pronounced in S1 than in S2, which correlates with the near absence of the low frequency, narrow-band (classic EEG) rhythms, the $\alpha - \beta$ type peaks, in S1. Those rhythms obscure the underlying broad band features. There are two possible approaches to this:

(1) We can try to decouple/remove the rhythms from the broad band features. We achieved this already qualitatively using a principle component type analysis (reference decoupling paper); and we obtained qualitative consistency with the results discussed below. Qualitatively the exponents do not seem to vary with the types of tasks, like finger movement versus rest. A quantitatively reliable and consistent improvement on this needs to be developed.

(2) ECoG, being a more local probe than classic EEG has the advantage of being able to observe spatial variations in the strengths of the EEG rhythms. In certain local regions of the cortex, the EEG rhythms are invisible in electrode pair PSD's. 8 channel pairs of S1 data qualify for this (at 10 kHz sampling rate). Moreover, we selected (in an unbiased manner) 116 electrode pair data involving the same fixation task from 25 subjects sampled at 1KHz rate. The latter data have as disadvantage that the high frequency power $\chi \simeq 4$

can not be verified independently (not to the same level of accuracy presented above). For these reasons, the following results for the low frequency broad band features are not as accurate as for χ above.

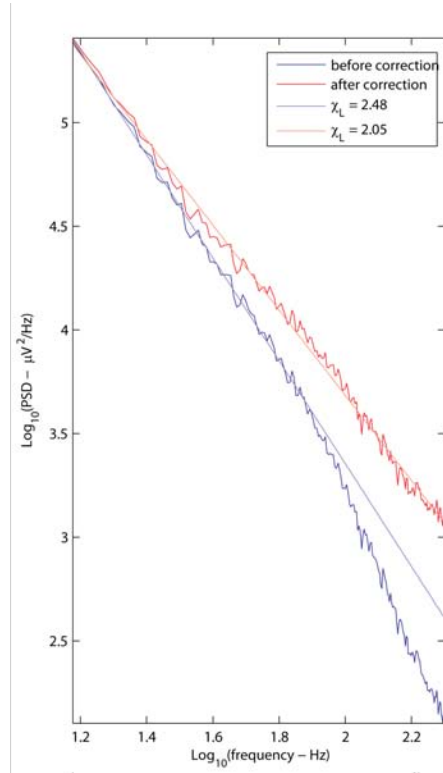


Figure 4.17: Power law fits for the averaged 8 channel pair PSD's from subject S1 lacking the low frequency EEG rhythms, sampled at 10 kHz . The naive fit to the sub knee $f_0 \simeq 70$ Hz curve yields the (erroneous) exponent $\chi_L = 2.5 \pm 0.4$ (shown in blue). The PSD straightens out to a single power law form after multiplying with the factor $1 + \left(\frac{1}{70}\right)^{\chi_H}$, with $\chi_L = 4 - \chi_H = 2.0 \pm 0.4$ (shown in red).

We propose the following phenomenological global fitting form

$$P(f) \simeq \frac{A f^{-\chi_L}}{1 + \left(\frac{f}{f_0}\right)^{\chi_H}} \quad (4.6)$$

applied over the frequency range $10 \text{ Hz} \leq f \leq 500 \text{ Hz}$ for the 10KHz sampling rate data,

and over $10 \text{ Hz} \leq f \leq 200 \text{ Hz}$ for the 1KHz sampling data. We impose the condition that the two exponents add-up to the value $\chi = \chi_L + \chi_H = 4.0 \pm 0.1$ as established above.

We average the PSD's from the 8 channel pairs of S1 that lack EEG rhythms. This average follows a seemingly nice looking straight line in the log-log plot shown in Fig.4.17; but a somewhat noisy one because it only involves 8 channel pairs. A naive fit to its slope, over $10 \text{ Hz} \leq f \leq 70 \text{ Hz}$, yields an (effective but erroneous) exponent $\chi_L = 2.5 \pm 0.4$. Next, we multiply the PSD with the factor $1 + \left(\frac{1}{70}\right)^{\chi_H}$ and find that the knee at $f_0 \simeq 70 \text{ Hz}$ vanishes and the PSD follows a straight line globally. This leads to $\chi_L = 4 - \chi_H = 2.0 \pm 0.4$, see Fig.4.17.

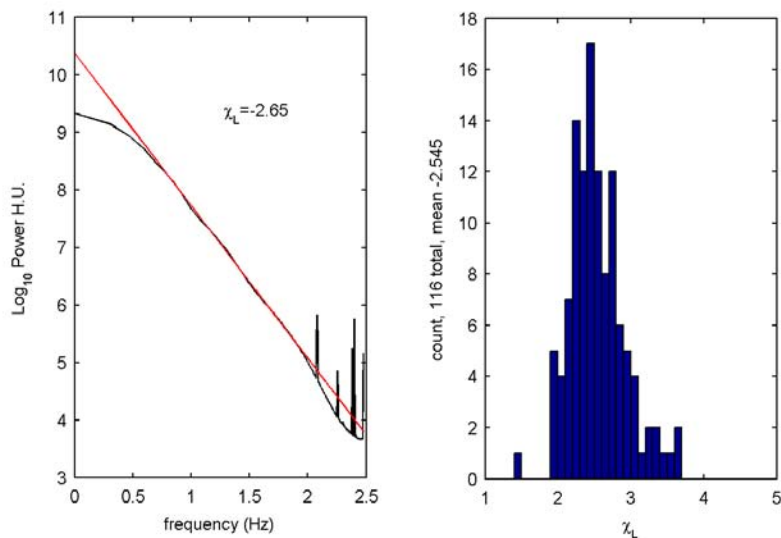


Figure 4.18: Naive low frequency power law fits to the 116 channel pair PSD's from 25 subjects sampled at 1 kHz, over frequency range $10 \text{ Hz} \leq f \leq 80 \text{ Hz}$, leading to the erroneous value $\chi_L = 2.5 \pm 0.4$

We selected channel pairs from 16 subjects all sampled at 1KHz, and only kept all 116 of them that lacked the low frequency EEG rhythms. Note that these data corresponded to a wide variety of (motor) cortex areas. This yielded a much less noisy averaged PSD than the 8 channels of S1, see Fig.4.18. The naive power law fit to this averaged PSD over 15

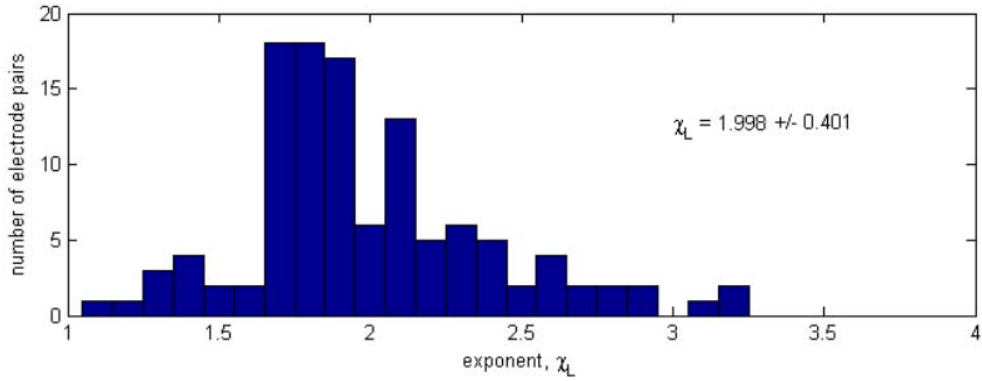


Figure 4.19: Low frequency fits to the 112 channel pair PSD's from 25 subjects, sampled at 1 kHz over frequency range $10 \text{ Hz} \leq f \leq 120 \text{ Hz}$, after multiplying the PSD's with $1 + \left(\frac{1}{70}\right)^2$, as suggested by the fitting form Eq.4.6

$\text{Hz} \leq f \leq 80 \text{ Hz}$ yielded the same (effective but erroneous) value $\chi_L = 2.5 \pm 0.4$; and the histogram of individual power law fits to all 116 channel pairs in Fig.4.18 is quite narrow.

This 1kHz data did not extend in frequency far enough to obtain a reliable estimate of the high frequency power law with $\chi \simeq 4$ in clear view, but the 70 Hz knee was clearly visible. It was therefore not possible to perform a reliable test of the global fitting form Eq.(4.6). However, multiplying the PSD's with the factor $1 + \left(\frac{1}{70}\right)^2$, yielded consistency with the 10KHz data from S1, i.e., the exponent shifts again to $\chi_L = 2.0 \pm 0.4$.

Chapter 5

**DECOUPLING THE CORTICAL POWER SPECTRUM REVEALS
INDIVIDUAL FINGER REPRESENTATION IN HUMANS**

High fidelity spatiotemporal resolution in neural recordings from the brain is important for investigating brain mechanisms and controlling brain-machine interfaces. The highest spatiotemporal resolution is obtained by recording activity of individual or multiple neurons through microelectrodes implanted inside the brain. A clinically more accessible measure is electrocorticography (ECoG), recorded from the surface of the brain, which reflects the summed activity of neural populations. We here report a new method of extracting and removing the low frequency α and β rhythms to reveal a behaviorally modulated broadband signal in the ECoG power spectrum that provides significantly improved spatial resolution of localized cortical populations, with high (≈ 20 ms) temporal resolution. This technique has provided the first resolution of real-time signals correlated with individual finger movements in adjacent sites of human motor cortex.

5.1 Introduction

How can we measure population-scale neural dynamics in the brain, at timescales relevant to behavior? A common approach focuses on one or a few neurons at a time, but does not provide an aggregate measurement. A measurement that samples the activity of entire populations of neurons at once is the field potential. Field potential recordings from the brain surface (electrocorticography, ECoG) have been used to study the relationship between functional cognitive change and the power spectral density of these cortical electric potentials in specific frequency ranges. ECoG changes with voluntary movement were reported as early as 1949 (Jasper and Penfield 1949; Gastaut 1952). Early studies of the ECoG power spectrum found a decrease in power in the α (8-12Hz) and β (18-25Hz) rhythms over large

areas of sensorimotor cortex with movement (Arroyo, Lesser et al. 1993; Crone, Miglioretti et al. 1998; Aoki, Fetz et al. 1999). These classic band rhythms (α , β , θ , δ) are in the low frequency range ($<50\text{Hz}$), and have not produced a measurement technique that can reliably resolve local ($<1\text{cm}$) cortical activity on the timescale of behavior ($>200\text{ms}$). However, later studies that examined the higher frequencies in the spectrum ($>75\text{Hz}$) showed task-related increases in power with more focal cortical distribution (Crone, Miglioretti et al. 1998; Aoki, Fetz et al. 1999; Miller, Leuthardt et al. 2007), with a spatial extent in closer agreement with stimulation mapping (Miller, denNijs et al. 2007) and functional magnetic imaging studies (Logothetis, Pauls et al. 2001; Mukamel, Gelbard et al. 2005).

We previously demonstrated that cortical regions showing high-frequency increase were spatially more focused than the areas of low-frequency decrease with motor tasks (Miller, Leuthardt et al. 2007). The high-frequency increase is broad-band and appears to reflect an activity-dependent shift in amplitude with a power law relating power spectral density and frequency (viz., Power of PSD $\sim Af^{-\chi}$). This relationship is obscured by narrow-band oscillations (α , β , θ , δ) at lower frequencies. We hypothesized (Miller, Leuthardt et al. 2007), and later demonstrated (Miller, Sorensen et al. 2008), that the high-frequency phenomenon was, in fact, a frequency-independent power law increase, revealed at frequencies above the classic rhythms. In order to maximize the spatiotemporal fidelity of spectral changes with ECoG, the modulation of a power law in the frequency spectrum of these potentials must be isolated from the modulated alpha and beta rhythms that peak at specific frequencies in the spectrum. To decouple these two types of phenomena, we investigated a set of tasks that would engage cortical areas that were sufficiently close enough for the low-frequency phenomena to overlap between the different tasks, yet spatially distant enough to avoid overlap of any unique high-frequency phenomenon between tasks. The separate covariance in the spectral density across tasks of these two processes would allow decomposition by principal-component analysis. If individual fingers are represented distinctly on the cortex, then a simple isolated finger movement task would meet these criteria. If, on the other hand, finger representation is primarily overlapping (as has been suggested (Schieber and

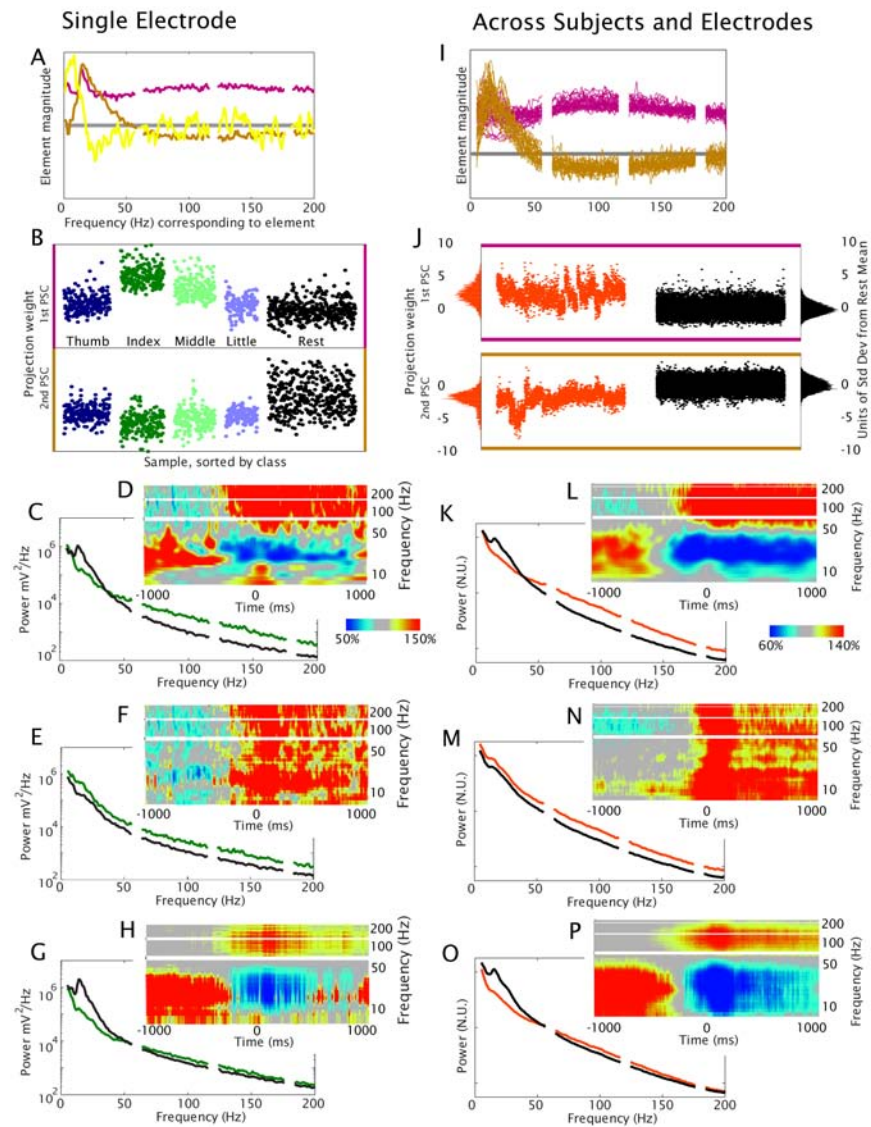


Figure 5.1: **Representative spectral changes** See text for complete explanation

Hibbard 1993; Schieber 2001)), a specific measure of local activity might not accurately discriminate between digits on the 1cm scale of clinical ECoG.

Here, we isolate a band-independent, power-law, change from α and β rhythms, and demonstrate individual finger somatotopy at the 0.5-1 cm scale. The amplitude of this

measure as a function of time, “ χ ”, reflects the cortical activity associated with movement of different fingers on different electrodes, resolved to a timescale of 10-15ms.

5.2 Method Summary

Subdural, 1-cm spaced, platinum electrode ECoG rectangular grid arrays were chronically implanted in 10 individuals with intractable epilepsy to determine seizure onset. Subjects gave informed consent for participation in a 10-minute task, in which each finger, contralateral to the hemisphere of the ECoG array, was flexed repetitively in response to 2s visual cues (100-150 total flexions per finger), with 2s of rest between each cue. There were 30 cues per finger, randomly interleaved. Analysis of the ECoG potential recordings during the task reveal that just prior to the initiation of finger movement, there is the characteristic decrease in power at lower frequencies (α/β range), and a spectrally broad, but spatially focal, increase in power at higher frequencies (above 40Hz) (figures B.1E and B.2D). This is not due to an event-related potential (figure 7.9) and is a phenomenon well established for coarser movements (Crone, Miglioretti et al. 1998; Aoki, Fetz et al. 1999; Miller, denNijs et al. 2007; Miller, Leuthardt et al. 2007).

We then sought to decouple the spatially focal, broad spectral increase in power and the spatially wider, low frequency decrease in power. Power spectral density (PSD) samples were computed from 1s windows flanking the time of maximum flexion for each finger movement, and from random times during rest. Principal component analysis on these PSD samples separated these two phenomena based on the differing effect of tasks on the covariance in the power across frequency bands. The extracted principal spectral components (PSCs) represent the power spectral change between task and resting states. These PSC components capture archetypes, or motifs, for the spectral change with activity and reveal how the power at different frequencies contributes to each motif. The original PSD curves may be reconstituted without one or more of these motifs (see lower panels of figure B.1).

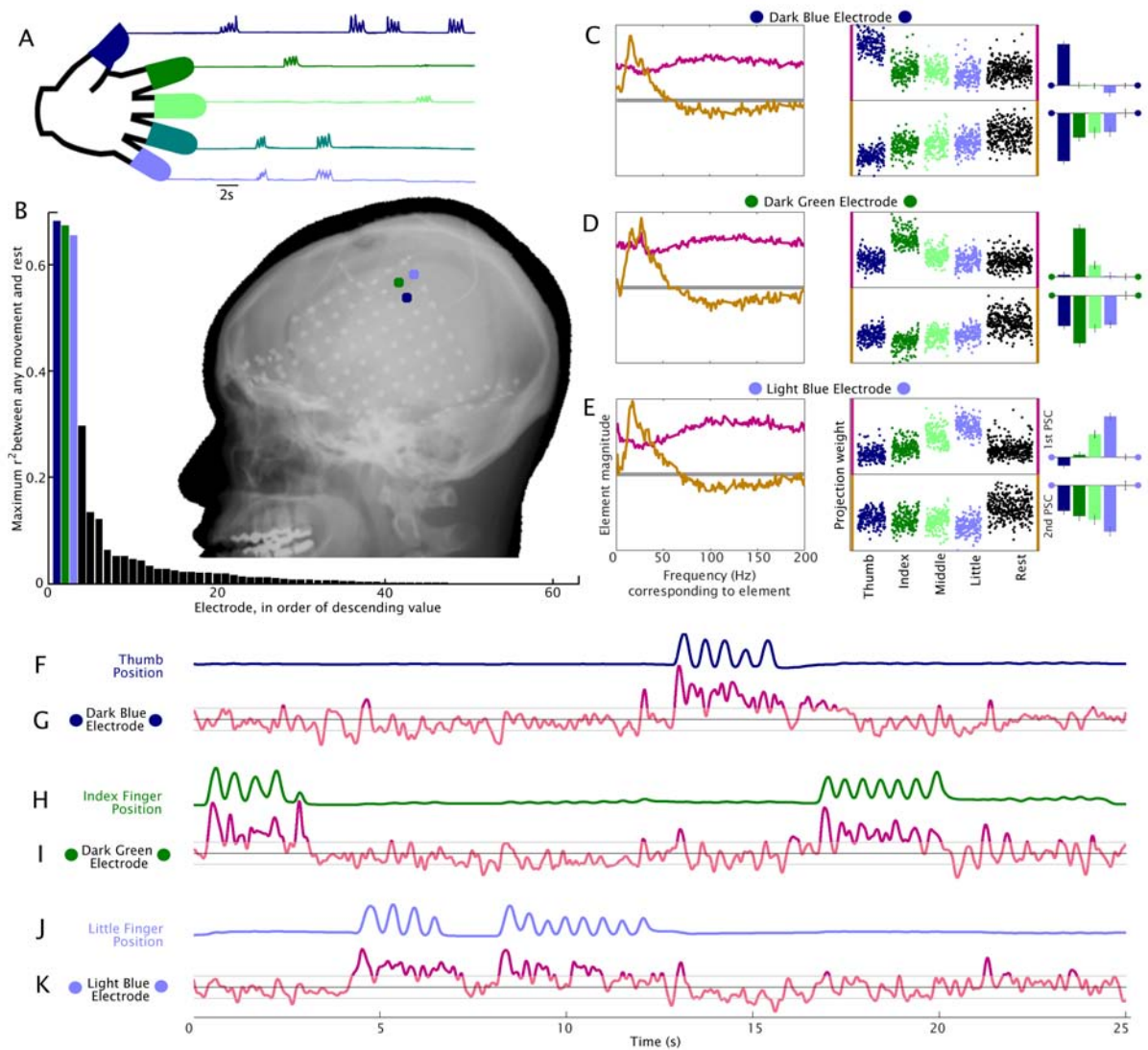


Figure 5.2: Capturing local cortical activity - Individual digit representation in adjacent electrodes in subject 1
See text for complete explanation

5.3 Results and Discussion

We found that the first, most significant (largest eigenvalue), PSC consistently shows the same pattern of non-zero, roughly equal, after normalization, contribution across all fre-

quencies (figures B.1A&I, Figure B.2C-E). This suggests that the reported "high γ " changes (Brovelli, Lachaux et al. 2005; Canolty, Edwards et al. 2006) may, in fact, be a reflection of this broad spectral phenomenon. The location of the increase in this projection weight reveal separable individual finger somatotopy in all subjects (figures B.2,B.3, 7.8). The most common organization showed thumb, index, middle, and little fingers located in ventral to dorsal sites, in agreement with Penfield's (Penfield and Boldrey 1937), and later Woolsey's (Woolsey, Settlage et al. 1952), stimulation findings. We found mostly distinct representation of different fingers, and, furthermore, much of the apparent overlap in cortical representation in digits coexisted with the well-known correlation in the movement of the fingers (figure ??, (Schieber 1995)). Finger movements evoked by electrocortical stimulation universally agreed with the identified motor somatotopy of the first PSC (figure 7.15).

We have previously found empirically that the integrated signal is described by a power law, $P \sim Af^{-\chi}$, which shifts amplitude, but not form, with activity (Miller, Sorensen et al. 2008), as captured by the 1st PSC. Such a power law distribution is consistent with, but not limited to, a coarse-grained measurement of local, Poisson-distributed, synaptic inputs to the $\sim 5 \times 10^5$ neurons in the grey matter beneath each electrode, without evidence for a favored timescale, and specifically without an activity-induced 'peak' in the "high- γ " range (Brovelli, Lachaux et al. 2005; Canolty, Edwards et al. 2006).

The second PSC is peaked in the α/β range, reflecting a process in a narrow range of frequencies, beginning near zero and rising to a central frequency of peak importance (figures B.1A&I). For projection to the 2nd PSC, all finger movement types were different from rest, and corresponded to decreases in power in the α/β range. This finding is consistent with the phenomenon of "event-related desynchronization" (ERD, (Pfurtscheller 1999)), and likely reflects distant synchronous input to large cortical populations that suppresses function, and broadly decreases when a subset of that population is activated.

Finger position and the χ measurement from individual electrodes were highly correlated in individual digits, with average correlation $r=0.37$, and as high as $r=0.62$, over 10 minutes of continuous recording (Figures B.2 and B.4). The mean latency of approximately 100 ms

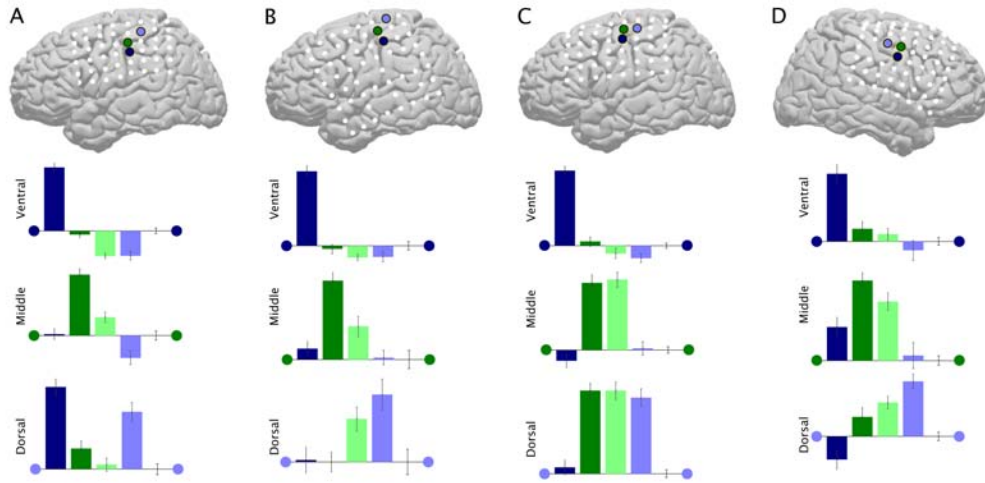


Figure 5.3: **Projection magnitudes, sorted by class**

(A) Mean of projection magnitudes in three electrodes of samples for each finger movement class, after subtraction of the mean of the rest time samples, for subject 2 (as in the right hand column of insets C-E in Figure B.2). The color of the dots flanking axes indicate corresponding electrode on the cortical schematic. Redundancy in color between electrode color and movement type is meant to provide intuition, but also indicates electrode-movement type pairings used for averaging in figure B.1. (B-D) Same as (A), but for subjects 3-5 (B-subject 3; C-subject 4; D-subject 5).

(Figure B.4) is consistent with the delay between cortical signals in movement initiation (Evarts 1973; Cheney and Fetz 1984). This high correlation, specific for movement of a single finger, demonstrates that activation of local neural populations can be measured at the 10-15 ms timescale, at a spatial resolution of at least the 0.5-1cm spacing of the clinical ECoG array.

Extended Explanation of Figure 1

Figure 1 illustrates the Principal component decomposition of the cortical spectrum during single finger movements.

Panels (A-H) are for an electrode in Subject 6, in Talairach location -41, 4, 51, Motor Cor-

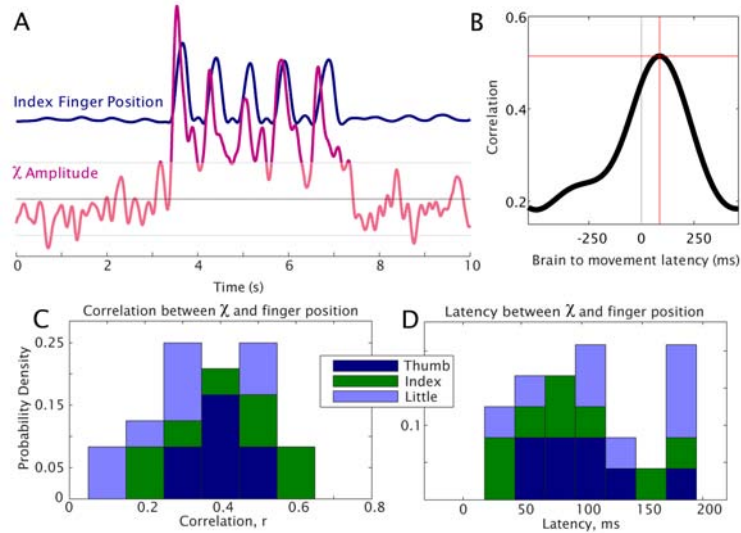


Figure 5.4: **Correlation between 1st PSC (χ) and finger position.**

(A) A single trial showing χ in an associated electrode and thumb movement, demonstrating delay from the cortex to movement onset, from subject 10. (B) Correlation in the electrode-movement pair from (A) as a function of latency between the two, over the full 10 minute period. (C) The correlation between χ and paired finger movement was 0.37 (SD=0.1430, N=24) across 8 of the subjects, 3 electrodes each (subjects 2 and 8 excluded, because their cortices were not “tuned,” as shown in the supplement). (D) The mean latency between χ and finger movement was 98 ms (SD=53 ms, N=24).

tex. The subject repeatedly flexed and extended different fingers of his contralateral hand . Samples of the normalized power spectral density (PSD) of the potential timeseries were calculated from 1s windows centered at times of maximum flexion and also during rest. (A) Normalized PSD samples were decomposed using principal components to identify covariation in power at different frequencies. The elements of the first principal spectral component (1st PSC, pink) are non-zero across all frequencies, consistent with change in a power-law in the cortical power spectral density. The 2nd PSC (gold) is peaked between 15-25Hz (β rhythm range). The 3rd PSC (yellow) is a 0-10 Hz (θ , α) peak. (The 4th - 179th PSCs are not shown). (B) The projection magnitudes of each spectral sample to the first (top) and second (bottom) PSCs, sorted by movement type (color coded as in (R)), Black indicates

rest. Note that the 1st PSC has specific increase from rest for index finger movements, and, to a lesser degree, for middle finger. The second PSC shows decrease from rest for all finger types. This generalizes across subjects and electrodes (J). (C) Mean PSD of index finger movement samples (dark green) and rest samples (black). (D) Average time-varying PSD (scaled as percentage of mean power at each frequency) with respect to first index finger movement from each movement cue (N=30). (E) Mean of reconstructed PSD samples, and (F) average reconstructed time-varying PSD, with 2nd and 3rd PSC omitted. This is consistent with the increase in the amplitude of a power law with local cortical activity. (G) Mean of reconstructed PSD samples, and (H) average reconstructed time-varying PSD, using only 2nd and 3rd PSCs. This is consistent with a change in the α and β rhythms. Note that $C=E+G$ and $D=F+H$.

Panels (I-P) are from 30 electrodes, (10 subjects, 3 electrodes each), where one movement type (thumb, index, little) was paired with each electrode (indicated by color code in figures B.2, B.3 and 7.8-7.15). (I) All 1st (pink) and 2nd (gold) PSCs, normalized by area, demonstrating same structure for all subjects and electrodes. Note the expected residual variance between the two phenomena reflected by the small negative residual weight in the 2nd PSC above 50Hz. (J) All projection magnitudes of the PSCs from (A) for the paired-movement type (orange, indicating thumb, index, or little finger movement samples, corresponding to the specificity of each electrode) and rest (black), flanked by the appropriate probability density functions. The plots are in units of standard deviation from the mean of the projection weight of rest samples. (K) Normalized mean PSD, averaged across subjects and electrodes (Power in normalized units (by mean power above 55Hz): "N.U."), of paired-movement samples (orange) and rest samples (black). (L) Averaged time-varying PSD (geometric mean, scaled as % of mean power at each frequency) with respect to first paired-movement from the associated cue (N=29-33, per electrode). (M) Mean of reconstructed PSD samples, omitting the 2nd and 3rd PSCs. Power goes up with movement at all frequencies, consistent with the increase of the pre-factor, A, in a power law $P \sim Af^{-\lambda}$.

(N) Average reconstructed time-varying PSD, with 2nd and 3rd PSCs omitted. (O) Mean of reconstructed PSD samples, using only 2nd and 3rd PSCs. The decrease in power with movement is confined to peaks in the classic α/β rhythm range. (P) Average reconstructed time-varying PSD, from only 2nd and 3rd PSCs.

Extended Explanation of Figure 2

(A) The position of each finger was measured using a transducing glove during cued flexion-extension. The color coding of each digit is same for all figures. (B) The histogram plots, for each grid electrode, the maximum squared cross-correlation (r^2) between sample projection weights to the 1st PSC, between any single movement type and rest, illustrating that cortical representation is sparse (also see figures 7.8-7.11). The corresponding locations of the top three electrodes are shown in the inset x-ray and (C-E). Each of these shows specificity for a different type of finger movement, and the color code redundancy between the electrodes in (B-K) and digit movement type in (A) reflects this. (C) Left: 1st (pink) and 2nd (gold) PSCs generated from finger movements and rest, for the electrode shown in dark blue in the x-ray inset in (B). Middle: projection weights of the PSD samples to the 1st (top) and 2nd (bottom) PSCs, sorted by movement type and colored as in (A) (black: rest period samples). Projections to the 1st PSC specifically increase during thumb movement, but not during any other finger movement or rest, but projections to the 2nd PSC non-specifically decrease for every movement type with respect to rest. Right: mean projection magnitudes for each finger type, with mean of projected rest samples subtracted. Error bars indicate +/- 3 times the standard error (3σ) of the mean (The right most, rest, "bar" is always zero, since its mean is subtracted, although the error bar is shown). The upper bars represent the first PSC, and the lower are for the second. (D&E) As in (C), but for the dark green (D - specific for index finger) and light blue (E - specific for little finger) electrodes. (F, H, J) Traces of thumb, index, and little finger position for a 25s period. (G, I, K) Projections of the time-frequency representation to the 1st PSC, " χ ", for each of the three electrodes for same 25s. The darker pink indicates that the projection is greater than 1 standard deviation

(light grey line) from the mean (dark grey line) of rest periods. Each electrode is specifically and strongly correlated with one movement type ($r=0.49$ χ from dark blue electrode-thumb movement; $r=0.60$ green electrode-index finger movement; $r=0.31$ light blue electrode-little finger movement; cross-combinations had a mean correlation of 0.07, indicating a tendency of this subject to lightly hyperextend the other fingers while flexing the appropriate finger), over 10 minutes of continuous data (3.6×10^6 samples). Note: digit 4 is not shown because its movements were highly correlated with movements of the middle or little finger in every subject.

5.4 Discussion

Single unit recordings have found that M1 finger representation at that level is distributed, and perhaps overlaps extensively (Schieber and Hibbard 1993; Schieber 2001). Axon tracing studies have found both widespread projections of single descending M1 axons to multiple motor neuronal pools across different joints (Shinoda, Zarzecki et al. 1979). Physiological studies show convergence of axons from widespread territories in M1 onto a single hand muscle motor neuron pools (Phillips and Porter 1977) and divergence of effects from single M1 cells to multiple muscles (Cheney and Fetz 1984). In the context of our findings, this suggests that an overlapping representation can be overwhelmed by integrating across the neuronal population. This finding of a separable, continuous, measure for different finger movements in adjacent cortical areas supports further use of digit-based paradigms to study human motor cortex, and for use in applications such as clinical mapping and brain-machine interface.

The isolation of this broad-band, power-law phenomenon in the cortical spectrum promises to be applicable to assessing local cortical function in a wide variety of contexts. This approach represents a powerful new method of accessing activity of neural populations resolved at behavioral timescales.

5.5 *Supplemental Methods*

There is a methods section, followed by supplemental figures which reinforce the primary text, and provide a deeper illustration for the more involved reader.

5.5.1 *Experimental Protocol*

All 10 subjects in the study were epileptic patients at Harborview Hospital in Seattle, WA (18-45 years old, 6 female). Sub-dural grids were placed for extended clinical monitoring and localization of seizure foci. Each subject gave informed consent to participate in an internal-review-board (IRB) approved experimental protocol. All patient data was anonymized according to IRB protocol, in accordance with HIPAA mandate. Stimulation mapping was performed clinically, and anonymized findings reported to researchers.

Recordings

Experiments were performed at the bedside, using Synamps2 amplifiers (Neuroscan, El Paso, TX) in parallel with clinical recording (BMSI amplifiers for subjects 2, 4, 7, and xltek for all others). Stimuli were presented with a monitor at the bedside using the general purpose BCI2000 stimulus and acquisition program (interacting with the proprietary Neuroscan software), which also recorded and recorded the behavioral parameters and cortical data.

Sub-dural platinum electrode arrays (Ad-Tech, Racine, WI), 32-64 in number, and were arranged in 8x[4-8] arrays. The electrodes had 4mm diameter (2.3mm exposed), 1 cm inter-electrode distance, and were embedded in silastic. The potentials were sampled at 1000 Hz, with respect to a scalp reference and ground (Fig. 5.5). These signals had a software-imposed filter from 0.15 to 200 Hz, but the higher frequency roll-off from this was corrected for attenuation after the power spectral density was calculated (see below).

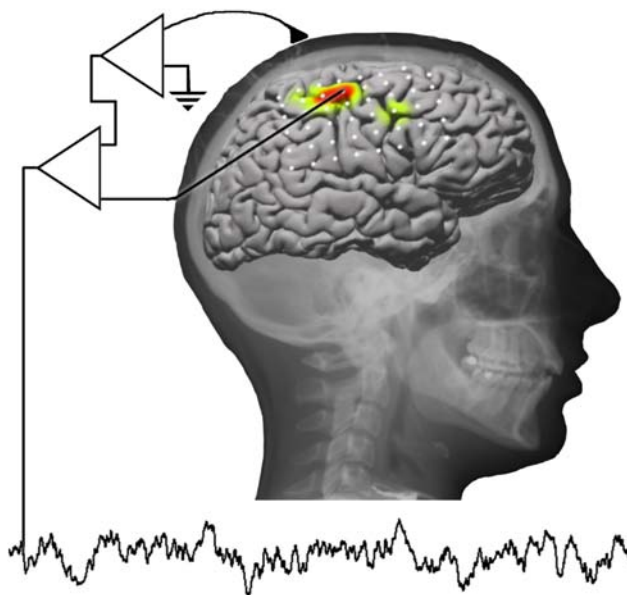


Figure 5.5: Potentials $V_n^0(t)$ were measured with respect to a scalp reference and ground before re-referencing with respect to the common average.

Cortical stimulation mapping

In five of the patients, cortical stimulation mapping¹ of motor cortex was performed for clinical purposes. Each such stimulation patient underwent stimulation mapping to identify motor and speech cortices to obtain a surgical margin as part of his/her clinical care. In this mapping, 510 mA square wave current pulses (1 ms in length) were passed through paired electrodes for up to 3 s (less if positive finding) to induce sensation and/or evoke motor responses (see supplemental figure 5.14).

Finger Movement task

The subjects were cued visually with a word on a monitor at the bedside to move individual fingers during 2-second stimulus trials, as shown in Figure 5.6. They typically moved each

¹Ojemann, 1982; Ojemann et al., 1989; Chitoku et al., 2001

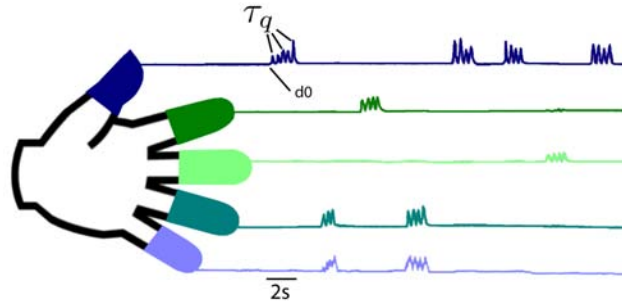


Figure 5.6: Capturing Individual finger movement times: Individual fingers were moved several times in response to each visual cue, and position was recorded using a dataglove. The peak displacement of each finger movement was marked with an event marker, τ_q (e.g. black arrow). The beginning and end times of each movement were also marked. Event markers, to characterize non-movement spectra for the “rest state” were chosen at random times at least one-half second from any movement event, and one-quarter second from each other. The onset of first movement of type in response to the visual cue d_0 . The ring (4^{th}) finger was not assessed after the PCA process because it’s movements were always correlated with middle (3^{rd} or little (5^{th} finger movement).

finger 3-5 times during each trial, but some subjects and trials had many more movements (as in Figure 1 J and K of the main text). A 2-second rest trial (blank screen) followed each stimulus trial. There were 30 movement stimulus cues for each finger (except subjects 4 and 7, whose trials were aborted at roughly 20 and movement cues per digit each), and trials were interleaved randomly. Finger position was recorded using a 5 degree-of-freedom dataglove (Racine, WI). Event markers were calculated marking initiation, peak (denoted τ_q), and termination of each movement. There were typically 100-150 movement events for each finger type. Random “rest” events (included in τ_q) were defined during periods at least 500 ms from any movement initiation or termination, and each rest event was at least 250 ms from any other rest event. There were typically 150-250 rest events for each subject. The lag between the dataglove position measurement recording and the amplifier measurement is 37ms (± 3 ms, SEM), this was accounted for when calculating the latency between brain activity and finger movement.

5.5.2 Spectral Decoupling

Calculation of samples of power spectral density

Electrocorticographic (ECoG) sub-dural potentials, $V_n^0(t)$, were measured with respect to a reference and ground from the scalp, as in Fig.5.5. These potentials were then re-referenced with respect to the common average reference across all N electrodes:

$$V_n(t) = V_n^0(t) - \frac{1}{N} \sum_{m=1}^N V_m^0(t) \quad (5.1)$$

A set of epochs surrounding events of maximum finger flexion, τ_q , were extracted from each timeseries $V_n(t)$, each epoch was of duration T , $\tau_q - \frac{1}{2}T < t < \tau_q + \frac{1}{2}T$ (see Fig. 5.7 A).

The epochs were sorted according to movement type q , and labeled by their event markers τ_q . The power spectral density (PSD) of each epoch was calculated as

$$P_n(f, q) = \left| \frac{1}{\sqrt{T}} \sum_{t=-\frac{1}{2}T}^{+\frac{1}{2}T} S(f, t) V_n(\tau_q + t) H(t) \right|^2 \quad (5.2)$$

with Hann window ² $H(t) = \frac{1}{2} \left(1 + \cos \left(\frac{2\pi t}{T} \right) \right)$, and sinusoid $S(f, t) = \exp \left(i \frac{2\pi}{T} (f - 1) t \right)$ as illustrated in Fig.5.7 B-C.

Principal Component Decoupling of Power Spectral Density Samples

The samples of the PSD, $P_n(f, \tau_q)$, were normalized in two steps prior to decomposition. First, each sample was normalized with respect to the average spectrum. This was necessary because the power law form of the PSD means that most of the variance, before normalization, is accounted for by the lower frequencies. Second, the log was taken. This places the ratios between 0 and 1 (-infinity to 0 after log) on equal footing with ratios between 1 and infinity (0 to infinity after log), see Fig. 5.7 D.

$$\tilde{P}(f, \tau_q) = \ln \left(P(f, \tau_q) \right) - \ln \left(\frac{1}{N_q} \sum_{p=1}^{N_q} P(f, \tau_p) \right) \quad (5.3)$$

²in "Particular Pairs of Windows." published in "The Measurement of Power Spectra, From the Point of View of Communications Engineering", New York: Dover, 1959, pp. 98-99.

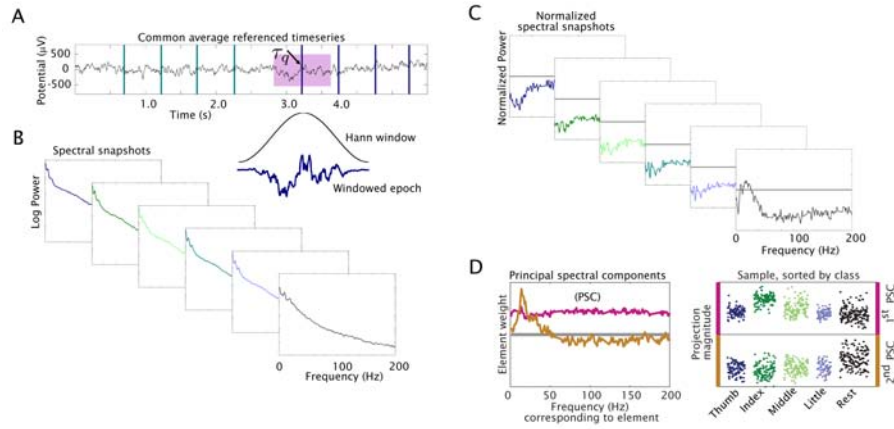


Figure 5.7: Signal Processing Steps: **(A)** The common averaged referenced signal, $V_n(t)$, is shown with event markers. The colors of the event markers distinguish between fingers, as in Fig. 5.6. A 1 sec Hann window $H(t)$ centered at each event marker, is imposed on the data to select the epoch corresponding to that specific event marker. **(B)** Samples of the power spectral density (PSD, $P_n(f, \tau_q)$) associated with each event marker are obtained for each epoch by Fourier transformation. **(C)** Each individual epoch power spectrum is normalized as described in the text, and the Principal Component method is applied to the logarithm of these normalized spectra. **(D)** Principal Spectral Components (PSCs, \vec{e}_k) are calculated across these across these sets of epoch power spectra $\log(\tilde{P}_n(f, \tau_q))$ (Left panel). The first is primarily flat across all frequencies (pink, \vec{e}_1), and the second is peaked in the classic α/β range (brown, \vec{e}_2). This structure is highly conserved, as shown in figure 2A of the main text. The panel on the left shows back projections of the first PSC (upper - pink, $W(1, \tau_q)$) and second PSC (lower - brown, $W(2, \tau_q)$) to the power spectral density samples, sorted by class. Note that the first PSC is specific for forefinger, and the second shows significant decrease for all movement classes with respect to rest (consistent with ERD).

(We drop the channel label, n , for brevity.)

The time ordering of the N_q epochs is explicitly ignored. In that case, the epochs represent an ensemble of N_q independent measurements of the underlying power spectrum $\tilde{P}(f)$ during the different types of finger movement. That power spectrum might include several distinct features that fluctuate with different movement phenomena; in our case, the α & β rhythms versus the underlying broad band power law shape. The PCA method³ attempts to identify the robust common features in such ensembles and decompose them by diagonalizing the second moment tensor of the corresponding distribution function, i.e.,

³Principal Component Analysis, IT Jolliffe - 1986 - Springer-Verlag

it determines the eigenvalues λ_k and eigenvectors \vec{e}_k of the matrix

$$C(f, \tilde{f}) = \sum_{\tau_q, \tilde{\tau}_q} \tilde{P}(f, \tau_q) \tilde{P}(\tilde{f}, \tilde{\tau}_q) \quad (5.4)$$

We intentionally center the covariance measure with respect to the log of the mean spectrum, rather than to the mean of log spectra. These eigenvectors, $\hat{C} \vec{e}_k = \lambda_k \vec{e}_k$, the ‘‘Principal Spectral Components’’ (PSCs), reveal which frequencies vary together. They are orthogonal vectors, because \hat{C} is a symmetric, $N_f \times N_f$ dimensional matrix. We normalize them, and order them according to the eigenvalues as $\lambda_1 > \lambda_2 > \dots > \lambda_{N_f}$. The PSC’s with largest λ ’s are the most significant ones. (Note that the variances are not normalized; a large λ reflects a large contribution to the total signal, and less likely to be a weak component with large within-movement-type fluctuations).

The PSCs represent a new orthogonal basis in frequency space. If we define the rotation matrix $A(f, k) = (\vec{e}_1, \vec{e}_2, \dots, \vec{e}_{N_f})$, then the projection, $W(k, \tau_q)$, of each individual original spectrum in the ensemble onto the new basis vector k is

$$W(k, \tau_q) = \sum_f A(k, f) \tilde{P}(f, \tau_q) \quad (5.5)$$

as illustrated in Fig.5.7D. The inverse rotation matrix \hat{A}^{-1} , $\hat{A}^{-1} * \hat{A} = \hat{I}$, allows us to compare and visualize specific PSC components with the original full spectrum in frequency space (for each member of the ensemble),

$$\tilde{P}_k(f, \tau_q) = \sum_f A^{-1}(f, k) W(k, \tau_q) \quad (5.6)$$

It turns out that the classic peaked rhythms are typically accounted for by the 2nd and 3rd PSCs. Therefore we define the ‘‘ μ -rhythm’’ back-projection as

$$\tilde{P}_\mu(f, \tau_q) = \sum_{k=2,3} \sum_f A^{-1}(f, k) W(k, \tau_q) \quad (5.7)$$

and we associate the complement with the power-law like broad band

$$\tilde{P}_{pl}(f, \tau_q) = \sum_{k \neq 2,3} \sum_f A^{-1}(f, k) W(k, \tau_q) \quad (5.8)$$

The 1st PSC on its own, $\tilde{P}_1(f, \tau_q)$, typically reconstructs most of the power law shape.

5.5.3 Time-Frequency approximation (Dynamic Spectrum)

Time-Frequency approximations (dynamic spectra) were made using a wavelet approach. In this way, a time-varying Fourier component $\tilde{V}(t, f)$ (channel label dropped) is obtained at each Hz, with fixed uncertainty between the estimate of the instantaneous amplitude and phase vs. the temporal resolution. The projection of each principal spectrum can then be estimated at each point in time.

Wavelet

A wavelet ⁴ of the form: $\psi(t, \tau) = \exp \frac{i2\pi t}{\tau} \exp \frac{-t^2}{2\tau^2}$ is convolved with the timeseries to get a time-frequency estimate for every $f = 1/\tau$:

$$\tilde{V}\left(t, 1/\tau\right) = \sum_{t'=-5\tau/2}^{5\tau/2} V(t+t')\psi(t', \tau) \quad (5.9)$$

A total of 5 cycles is used to estimate the amplitude and phase of the signal at each frequency for every point in time.

Movement-triggered average of time-frequency power estimate

This time-frequency approximation can be used to calculate mean power in relation to the onset of each type of digit movement:

$$\bar{P}^d(f, t) = \frac{1}{N_{d0}} \sum_{\tau_{d0}} \left(\frac{|\tilde{V}(t + \tau_{d0}, f)|^2}{\frac{1}{T} \sum_{t'=1}^T |\tilde{V}(t', f)|^2} \right) \quad (5.10)$$

Where $d0$ is the first movement of type d in response to the visual cue (5.6). These normalized maps of power as a function of time and frequency provide important information about characteristic spectral changes with local cortical function, as shown in figure 1 of the main text and figures 5.11, 5.15, and 5.17 of this supplement.

⁴P. Goupillaud, A. Grossman, and J. Morlet. Cycle-Octave and Related Transforms in Seismic Signal Analysis. *Geoexploration*, 23:85–102, 1984

Wavelet projection to the 1st PSC

the time evolution of each PSC, $W^c(k, t)$ can be estimated from the wavelet type time varying estimate of the power spectral density (using the same normalization as in equation 5.3),

$$P^{(n)}(f, t) = \ln \left(\frac{|\tilde{V}(t, f)|^2}{\frac{1}{T} \sum_{t=1}^T |\tilde{V}(t, f)|^2} \right) \quad (5.11)$$

by projecting

$$W^c(k, t) = \sum_f A(k, f) P^{(n)}(f, t) \quad (5.12)$$

We apply this to the first PSC. Recall that the 1st PSC captures a broad change across the entire frequency range. Our previous attempts to capture this phenomenon dubbed it the so-called χ -band or χ -index feature, so here we will call attempts to capture it in real-time, χ , which, as before, is connected to the exponent in changes of a power law process in the cortical spectrum, $P \sim Af^\chi$. The $\alpha - \beta$ -rhythms are projected into lower-ranked PSC's; into the 2nd and 3rd in particular. The wavelet dynamics of the 1st PSC, smoothed with a gaussian (SD=15ms), χ , with finger movement is shown, and discussed, in the main text (see Figs. 2 and 4). Because of the high correlation between behavioral parameters and χ in specific electrodes (Fig. 2), we propose that χ can be used generically as a correlate of local cortical function.

Back-projection from PSC to time-frequency power

The constrained back-projection matrices, \hat{A}_{pl}^{-1} and \hat{A}_μ^{-1} (defined in equations 5.8 and 5.7), were applied to $W^c(k, t)$ to obtain time-frequency estimates, $P_{pl}(f, t)$ and $P_\mu(f, t)$ of the power change:

$$\hat{P}_{pl} = \exp \left(\hat{A}_{pl}^{-1} * W^c \right) \quad (5.13)$$

$$\hat{P}_\mu = \exp\left(\hat{A}_\mu^{-1} * W^c\right) \quad (5.14)$$

Event-averaged (in the same way as equation 5.10), constrained, back-projections are demonstrated in figure 1 of the main text and figures 5.12 and 5.15 of this supplement.

Movement-onset to phase relationship

Figure 5.17 shows the relations between the phase $\theta(t, f)$ and magnitude of the complex signal, $\tilde{V}(f, t) = |\tilde{V}(f, t)|e^{i\theta(f, t)}$ in terms of polar plots, i.e., by plotting the real and imaginary parts of $\tilde{V}(f, t)$ along the x respectively y-axis.

The relationship of the phase of the complex signal $\tilde{V}(t, f)$ to the onset of finger movement can be examined by examining the average phase vector at each frequency, with respect to the first movement of each cue of each type, for each point in time, with respect to each cue.

If the complex form of $\tilde{V}(t, f)$ is expressed as $\tilde{V}(t, f) = x(f, t) + i y(f, t)$, then the unit magnitude phase vector at a given time and frequency is:

$$\vec{\phi}(f, t) = \frac{x(f, t) \hat{x} + y(f, t) \hat{y}}{\sqrt{(x(f, t))^2 + (y(f, t))^2}} \quad (5.15)$$

The average phase vector, with respect to the first movement of type d , denoted $d0$ from each cue.

$$\vec{\phi}^d(f, t) = \frac{1}{N_{d0}} \sum_{\tau_{d0}} \vec{\phi}(f, t + \tau_{d0}) \quad (5.16)$$

Supplemental Figures

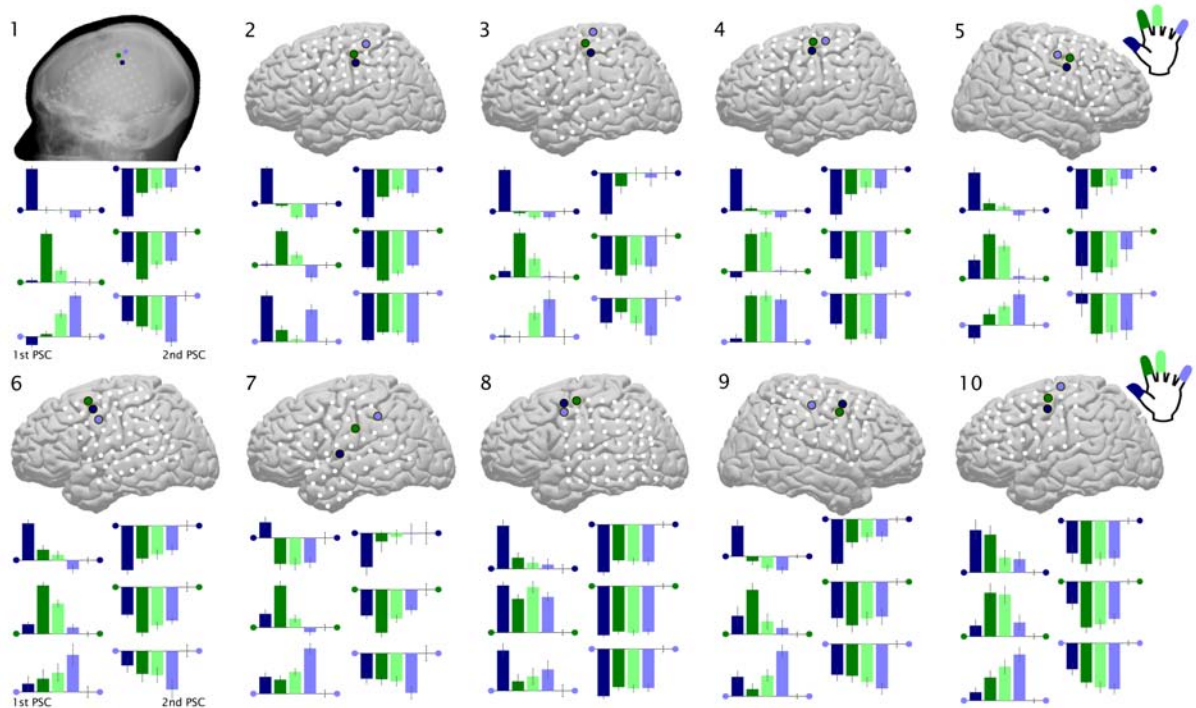


Figure 5.8:

Supplemental figure S1

Somatotopy for all individuals: The mean projection magnitudes to samples of different finger movements for the first (left) and second (right) PSCs in subjects 1-10, with respect to the mean of rest samples. The colored dots flanking each axis correspond to the electrode that they reflect the activity of. The axis indicates the mean of rest period samples. The colors on the bars indicate the appropriate finger (from left to right: thumb, index, middle, little), and the 3σ error bars indicate ± 3 times the standard error of the mean. The 3σ error bars on the right most portion of the axis are ± 3 times the standard error of the mean of the rest period samples. The element weights of the first PSC are non-zero and roughly equal across all frequencies consistent with a power-law like change,

where power at all frequencies fluctuates together, and this structure is highly conserved, as shown in figure 1A of the main text. The elements of the second PSC (gold) are peaked in the $\alpha / \beta / \mu$ range, reflecting a process where just these frequencies vary together around a central frequency of peak importance (conserved as also shown in figure 1A). *The difference in the distribution in the two components is evident:* **(1)** The first PSC is specific for a single movement type, and the projection magnitude increases with respect to rest (therefore the power in the original power spectral samples). **(2)** The second PSC is non-specific, there is a decrease in projection magnitude for samples of each movement type with respect to rest samples. These two observations illustrate how it was possible to pull these apart because the classic, low-frequency, peaked phenomena decrease in power with local activity, and do so over a large spatial area. Since the representations of different fingers are close to each other, but distinct, the peaked phenomena and the power law phenomena vary in a separable way, and can therefore be decoupled using the principal component analysis method.

Observations about individual subjects: **(Subject 2)** The lower set of bars for the first PSC (light blue electrode) shows significant change vs. rest for both thumb and little finger samples. **(Subject 3)** 1st PSC - Note partial representation of middle finger along with both little and index fingers. 2nd PSC - In the dark blue electrode, only thumb samples are different from rest. **(Subject 4)** 1st PSC - Index and middle fingers are strongly represented in the dark green and light blue electrodes, but the little finger is only represented in the light blue electrodes. The correlation in the representation of the index and middle fingers may be due in part to the fact that the movements themselves were correlated, as shown in figure 5.16. **(Subject 5)** 2nd PSC - Conjugate observation: Little finger is not represented in the dark blue electrode, and thumb electrode is not represented in the light blue electrode. The correlation between index and middle finger may be due in part to movement correlation (figure 5.16). **(Subject 7)** The dark blue electrode was selected based upon statistics, but it is clearly not in motor area, and clearly different from any other in the study. It is likely in a pre-motor or supplementary area. In the 1st PSC,

index, middle, and little finger movements samples are all decreased from rest samples, while thumb is increased. In the 2nd PSC, there is no significant change from rest, except for thumb movement. **(Subject 8)** The grid lies inferior to most of hand area, and the significant electrodes were all significant for thumb movement. The green electrode was significant for all types of finger movement samples.

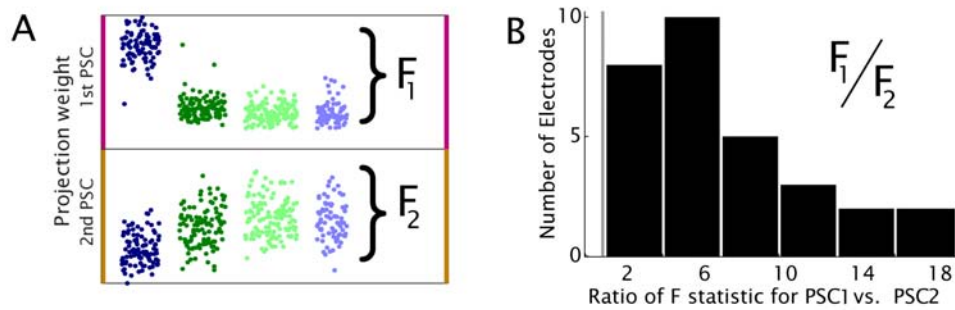


Figure 5.9:

Supplemental figure

Quantifying difference in sparse distribution of finger representation for the 1st and 2nd PSCs. In order to demonstrate that the 2nd PSC is less sparse than the 1st, overall, an ANOVA was calculate for the distribution of different finger movements, for spectral sample projections to the 1st PSC, and the 2nd PSC, independently, as shown in (A). Every electrode was significant at $p < .05$ for one or more finger movement types being different from the others. However, the more different one class is from the rest in an ANOVA, the larger the associated Fano will be, so the relative magnitudes of the Fano factors for the 1st PSC and the 2nd PSC in a single electrode will tell us about their relative sparsity . As shown in the histogram of ratios F_1/F_2 in (B), every such ratio F_1/F_2 was greater than 1, demonstrating that the representation of the 1st PSC is more sparse than the 2nd PSC in every single case (N=30, 3 electrodes in 10 subjects).

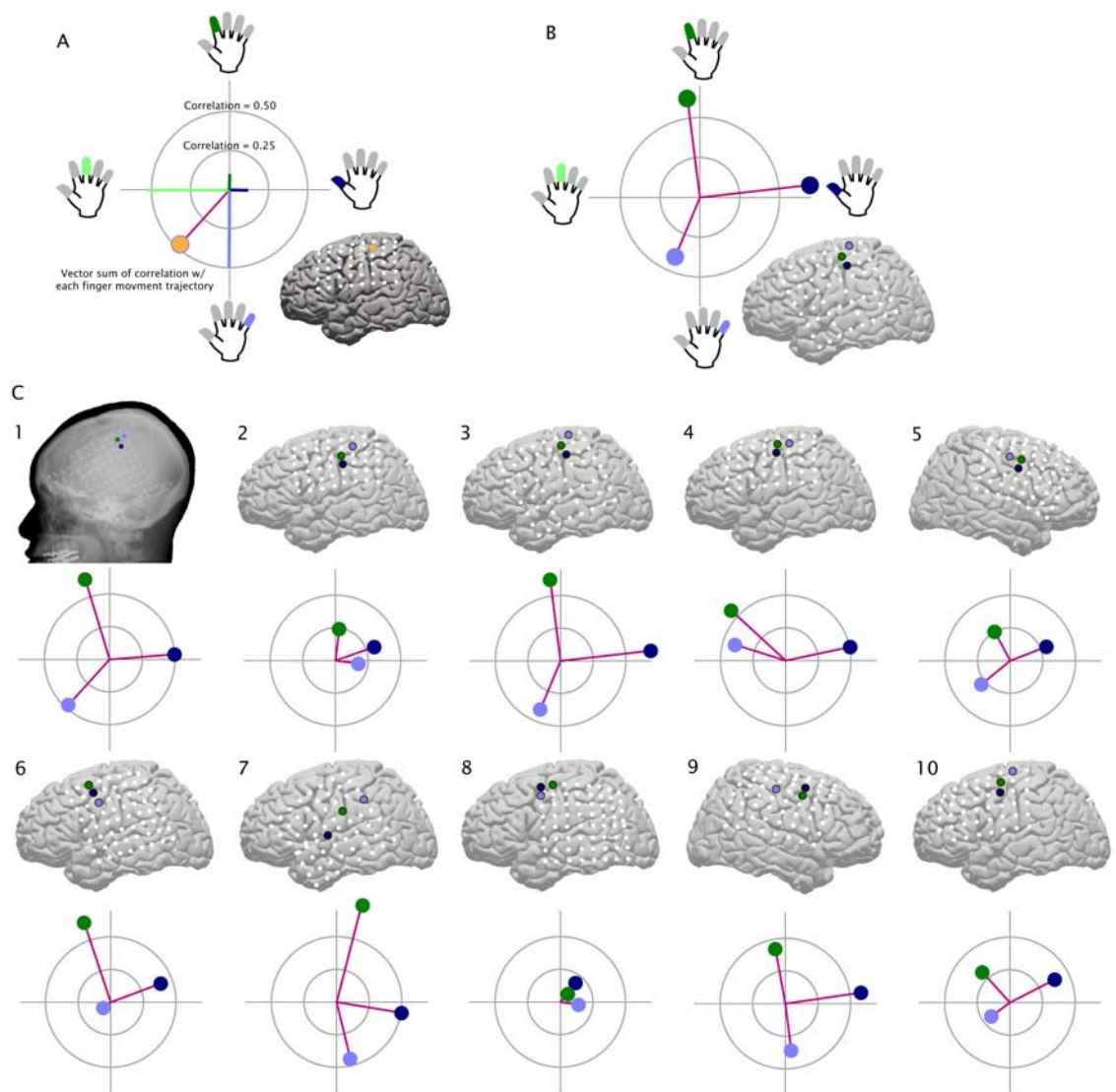


Figure 5.10:

Supplemental figure

Somatotopic cortical tuning for different fingers. (A) *Cortical tuning plot schematic:* The correlation, r of χ (projection of 1st PSC to the dynamic spectrum) with the finger

position is projected on polar axes. The correlation with thumb position is shown at 0 deg, index finger at 90 deg, middle finger at 180 deg, and little finger at 270 deg. The vector sum of these is shown as a pink line with a color-coded dot at the end, denoting the appropriate electrode on the inset brain. The inner circle denotes a correlation of $r=0.25$, and the outer circle denotes a correlation of $r=0.50$. **(B)** Each of the three paired electrodes is shown on the same polar plot, for each subject. **(C)** For each subject (numbered 1-10), the appropriate cortical tuning plot is shown. All subjects except 2 and 8 were strongly tuned (for this reason, subjects 2 and 8 were excluded from the grand average shown in figure 4 of the main text).

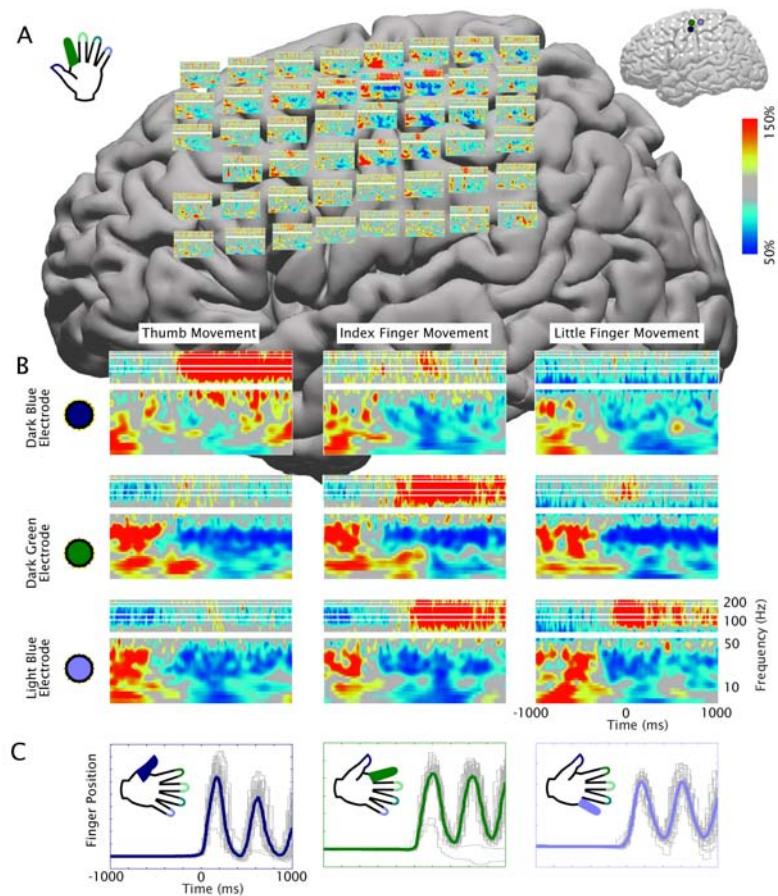


Figure 5.11:

Supplemental figure

Time Frequency Plots for 3 adjacent electrodes and 3 different finger movements in subject 4. (A) Average time-varying PSD (scaled as % of mean power at each frequency) with respect to first index finger movement from each index finger movement cue ($N=27$), for each electrode, shown in the approximate position of the electrode that it corresponds to. The axes are scaled as detailed in the lower right of (B). Note that the decrease in lower frequencies prior to movement onset is predominant over a large area, but pronounced increase in power at high frequencies is limited to 2 electrodes. (B) The temporal development

of the PSD is shown averaged over each of the three for each the three movement types most "relevant" for each of three electrodes (position shown in right of (A)). Note that all electrodes have characteristic decrease in power with movement onset in the low frequency range, and increase in power at higher frequencies is specific. These are fully decoupled with the principal component method, as shown in supplemental figure 5.12.

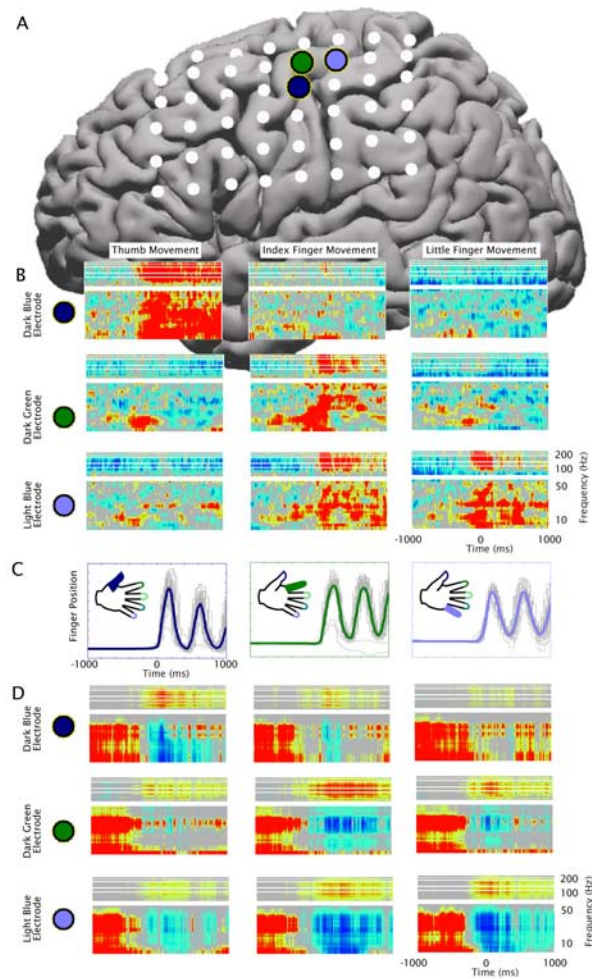


Figure 5.12:

Supplemental figure

Several movements and several electrodes, decoupled: Decoupled time frequency plots from supplemental figure 5.11 . The lower set clearly shows the event-related desynchronization at lower frequencies. The upper set shows the more specific power law.

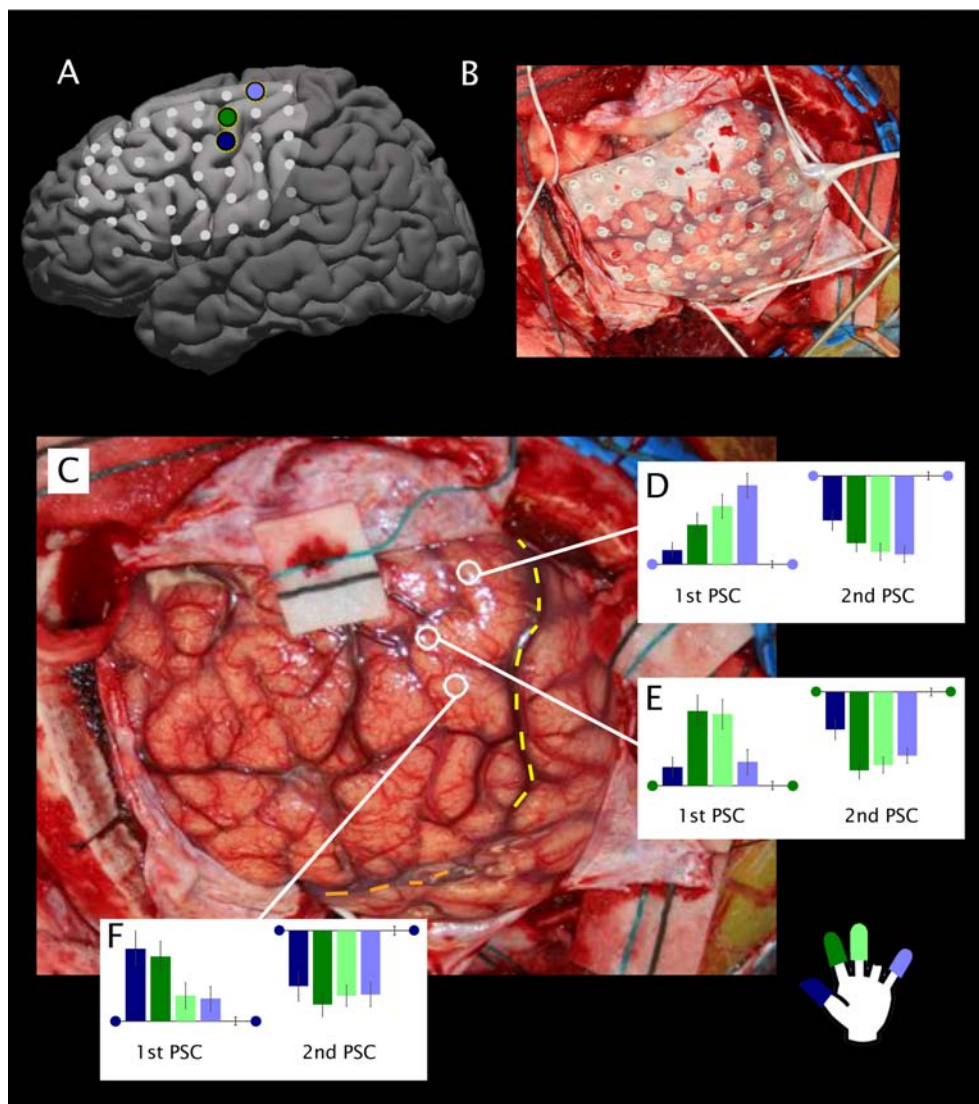


Figure 5.13:

Supplemental figure

Locations of electrodes on intra-operative surgical photograph. (A) The interpolated locations of the three paired electrodes for subject 10. **B & C** In subject 10, a surgical photograph was taken, pre- and post- grid implantation. The sites of the 3 paired electrodes

(**D-F**, as in supplemental figure 5.8.10) could be identified on the cortical surface. They all lie in the classic pre-central hand area. *Yellow line denotes the central (Rolandic) sulcus, and the orange dotted line denotes the transverse (Sylvian) sulcus, left is rostral, right is caudal, up is dorsal, and down is ventral.*

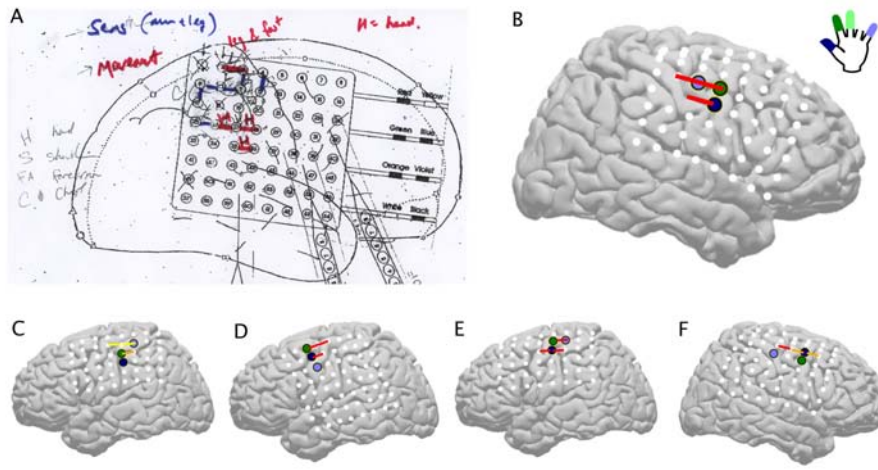


Figure 5.14:

Supplemental figure

Relation to clinical stimulation findings: Clinical stimulation mapping was performed on a subset of the subjects. In each of the subjects, the clinical goal was to obtain an acceptable surgical margin, so not all of the electrodes were surveyed. Stimulation was performed pairwise. In two of the cases (subject 2 in (C) and subject 9 in (F)), the clinicians reported specific digit movement. In both of these cases, the specific movements reported were the same as the specific digit identified by the 1st PSC. (A) Clinical schematic showing hand area in subject 5, note that there were both motor and sensory findings, and both hand and foot motor areas were identified. In all cases, electrodes connected by a red bar indicate a report of non-specific hand/finger movement. Because stimulation was pairwise, the assumption is that the area of cortex which produced the given motor phenomena was under one or both of the electrodes, or the cortex bridged by the pair, or a combination of all 3. (B) Subject 5: Yellow bars indicate ring and little finger movement with stimulation; orange bar indicates little and middle finger movement with stimulation. Stimulation was not performed inferior (ventral) to these sites. (C) Subject 2. (D) Subject 6. (E) Subject 4. (F) Subject 9: Orange bar indicates thumb movement with stimulation.

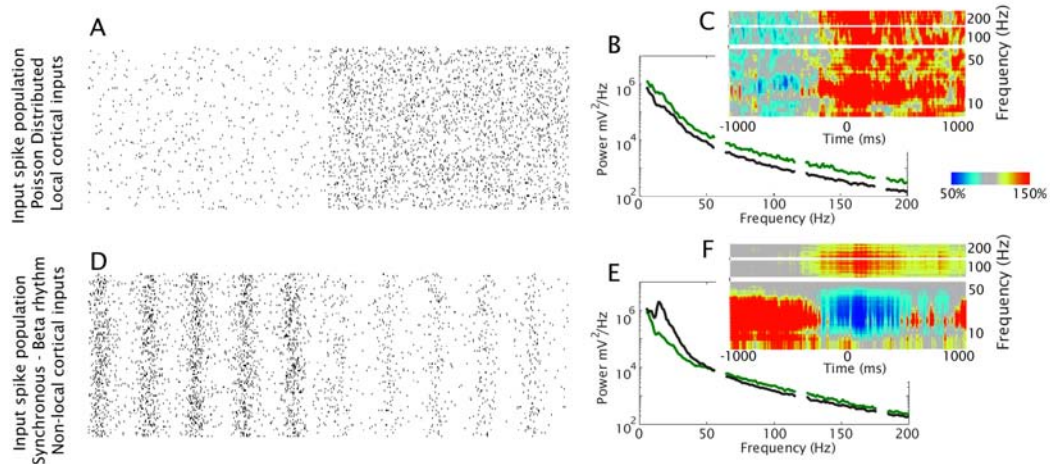


Figure 5.15:

Supplemental figure

Hypothetical input - spectral change relation: (A) The power law changes we found, with exponent 2 (after correction, see Power Law manuscript), are consistent with many superimposed Poisson distributed input spikes, filtered by the shape of the post-synaptic potential. With an increase in local activity, the rates of these processes increase, and the corresponding power spectral changes, shown in (B & C) correspond to an increase in the coefficient, A , of a power law of form $P \sim Af^{-\chi}$. (D) The peaked changes we found are consistent with a set of synchronized input spikes with synchronous frequency in the β range. With activity, the synchronous activity dissipates, or perhaps remains constant but loses synchronous timing, which would be in contrast to the schematic here. The corresponding spectral changes for this type of process were found in our 2nd and 3rd Principal Spectral components, projected in (E & F). Panels B, C, E, and F were taken from the single-electrode example in figure 1 of the main text.

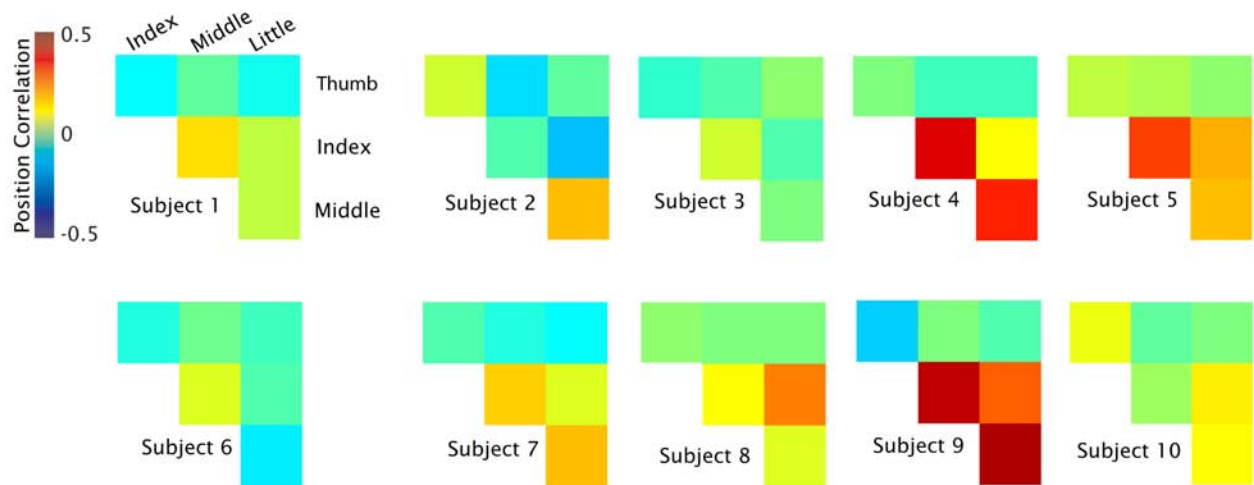


Figure 5.16:

Supplemental figure

Correlation between different digit movements: Finger movement traces were correlated to varying degree on a subject by subject status. This meant that individual spectral samples labeled as one type of finger movement may actually have had movement for more than one type, and brain activity during these samples is really for both fingers together. Index often correlated with middle, and little often correlated with middle. The movement of the ring finger was highly correlated in every case with either little or middle fingers (depending on subject) - it was excluded from examination altogether after the PCA step was performed.

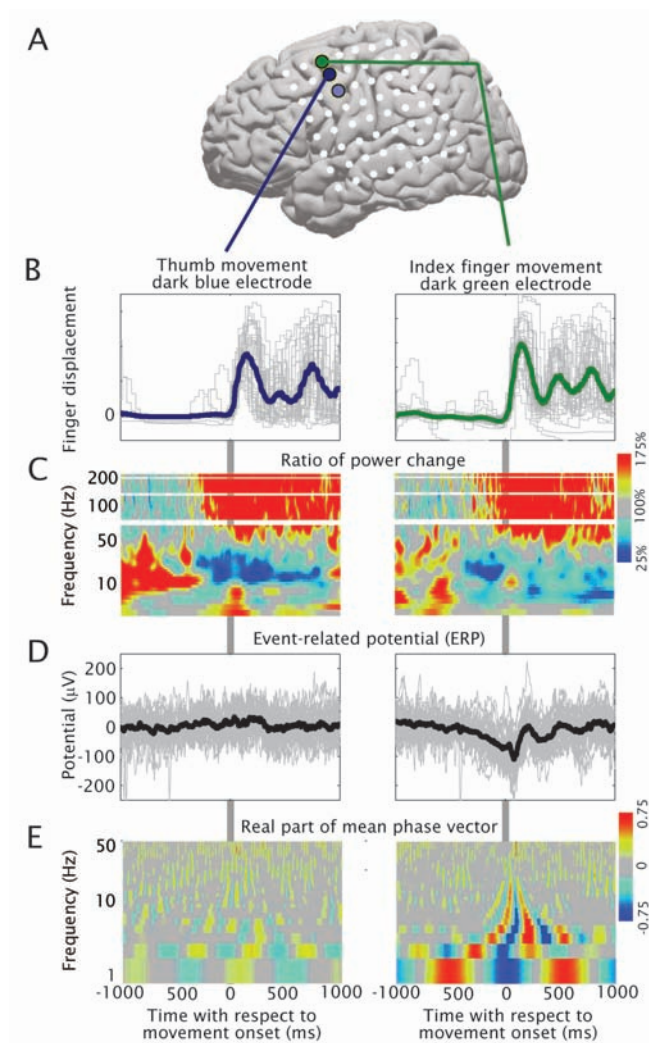


Figure 5.17:

Supplemental figure

Event-Related Potential: Illustration that the characteristic changes in the power spectral density changes with activity are not due to an reproducible event related potential shift (ERP). Two adjacent electrodes in subject 6. One has an ERP, and one does not, but both have the characteristic peri-movement spectral changes. (A) Individual (grey)

and averaged thumb movement (dark blue), locked to the first movement from each thumb movement cue. **(B)** The normalized power spectral density ("PSD") as a function of time. It demonstrates the classic spectral changes just prior to movement onset. **(C)** Individual and averaged traces around each of the first movements from appropriate thumb movement epochs. There is no significant stimulus event-related potential (ERP) effect. Note that the decrease in power at lower frequencies ($\alpha / \beta / \mu$ range), and the increase in power at higher frequencies (above 40Hz) both begin before movement onset. **(D)** Real part of mean phase vector at each point in time/frequency, locked to movement onset. The envelope of this is what would classically be called the "inter-trial coherence". It is not significant for this task/electrode. **(E)** Same as (A), but for averaged index finger movement (dark green). **(F)** Same as (B), demonstrating the standard spectral changes. **(G)** Individual and averaged traces around each of the first movements from appropriate index finger movement epochs, as in (C). Here there is an significant stimulus event-related potential (ERP) effect. **(H)** Real part of mean phase vector at each point in time/frequency, locked to movement onset. This demonstrates evidence of "phase locking to stimulus" classically associated with the ERP.

Chapter 6

**REAL-TIME FUNCTIONAL BRAIN MAPPING USING
ELECTROCORTICOGRAPHY**

We demonstrate the feasibility of real-time cortical mapping from arrays of subdural electrodes using the electrocorticographic signal power in the higher spectral frequencies (76-200Hz, or “ χ -index”). Hand area was mapped offline in eight individuals using brief baseline and hand-movement measurements. In one patient, hand sensorimotor cortex was identified online during a handshake. We propose that this high frequency component of the electrocorticogram provides a generic, reliable, clinically useful correlate of local cortical function.

6.1 Introduction

The gold-standard method of determining cortical functional organization in the context of neurosurgical intervention is electro-cortical stimulation (ECS) which acts by disruption of normal cortical function to evoke movement or create transient functional disruption (Haglund, 1994; Keles, 2004). In contrast, methods that read endogenous signals, such as somatosensory evoked potentials or fMRI, reflect normal cortical function. Electro-corticography (ECoG) has been suggested as another such method of mapping endogenous cortical function (Crone, 1998; Leuthardt, 2007; Miller, 2007; Pfurtscheller, 2003; Crone, 2006). Previous reports (Miller, 2007) suggested that broad spectral increases of the ECoG signal provide a correlate of local cortical activity, but that they are masked by changes in band-specific peaks at low frequencies (classically named event-related desynchronization, or ERD; Pfurtscheller, 1999). In motor tasks, these conjugate processes cause behavioral splits at 48 ± 9 Hz (\pm -SD, hand) and 40 ± 8 Hz (tongue) (Miller, 2007). We aim to isolate this broad spectral increase, which we denote the “ χ -index,” by focusing well above

these behavioral splits and well above 60 Hz line noise, choosing specifically from 76-200Hz (our amplifiers have a built in low-pass at 200 Hz), to assess local cortical function (Figure B.1). We illustrate that changes in power in the “ χ -index” during repeated hand movement rapidly localize cortical hand area. These changes are characterized with only several seconds of data collection, giving a rapid, specific, and straightforward method for locating functional areas in cortex with the ECoG signal.

6.2 Methods

Electrocorticographic recordings in eight patients (mean age 35yo (18-48yo), 3 Female) with peri-Rolandic (4 left sided) subdural platinum electrodes (4mm diameter, 1cm inter-electrode spacing, Ad-Tech, Racine, WI) were recorded using SynAmps2 (Neuroscan, El Paso, TX) amplifiers, set to sample at 1kHz and band-pass filter from .15 to 200 Hz. Data was collected and processed online at the bedside using the BCI2000 (Schalk, 2004) software on a laptop computer. Patients gave informed consent through a protocol approved by the University of Washington Institutional Review Board. Each patient performed repeated opening and closing of the contralateral hand for 3s blocks, alternating with equal periods of rest. Each block was visually cued, for both movement and rest periods. The hand movement was repeated 30 times, but only the first 5 blocks (15 sec) of movement were used for this analysis. Ten seconds of baseline data was collected prior to movement blocks. All data was band-passed for the χ -index with a notch filter at 120Hz to remove ambient noise. Log power in 80ms windows of data (overlapping by 40ms) was calculated throughout the task. The mean and standard deviation of the log power was determined for the baseline period, and, for the activity period, the baseline mean was subtracted from each windowed measurement, and scaled by the baseline standard deviation. A running sum of all data above 2 (in units of baseline standard deviation) was calculated for each channel. These sums are shown in bar plots, and interpolated on a standardized brain (Figures B.1 and B.2). Weights were calculated for each channel by subtracting the mean across channels from each channel, thresholding at zero, and dividing by the maximum. Gaussian kernels centered at

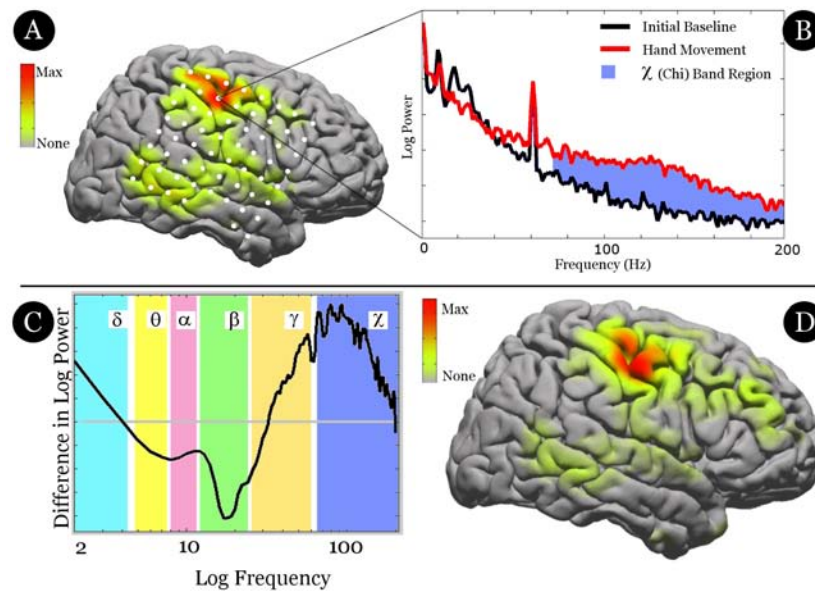


Figure 6.1: **Electrocorticographic motor mapping**

A. Map of hand movement compared to rest (patient G). Fifteen seconds of movement compared to a 10s baseline (see methods) contributed to the interpolated map, scaled to the maximum response. Electrode locations are shown in white.

B. The spectrogram (mean log power vs. frequency) from a single, peri-central electrode, for hand movement (15s) and resting baseline (10s). An increase in power occurs over a broad spectral range. This difference (shaded blue) is evident in even brief epochs of activity.

C. The difference in log power between movement and baseline, averaged across the most responsive electrode in each of 8 subjects, is shown along with spectral bands. The increase with movement is seen midway through the gamma band and extends to 200Hz. The ‘ χ -index’ is designed to capture the broad spectral power increase where separation between task and rest is most clearly observed. Note the classic decrease in α and β , and the broad increase in the χ -index (76-200Hz).

D. Mean, superimposed, activation across all 8 patients, re-scaled to the maximum. A highly focal response is seen indicating the consistency of the change across subjects.

each electrode location were scaled by this amount and linearly superimposed to generate an interpolated cortical activation map, on the Talairach-standardized AFNI template cortex, for each patient. Electrode locations, in standardized Talairach coordinates, were calculated

from post-implantation skull x-rays, using the LOC package (Miller, 2007). As significant changes were demonstrated within 2-3s, we applied this prescription online for real-time brain mapping (a handshake - Figure B.3) in one patient (patient C from figure B.2).

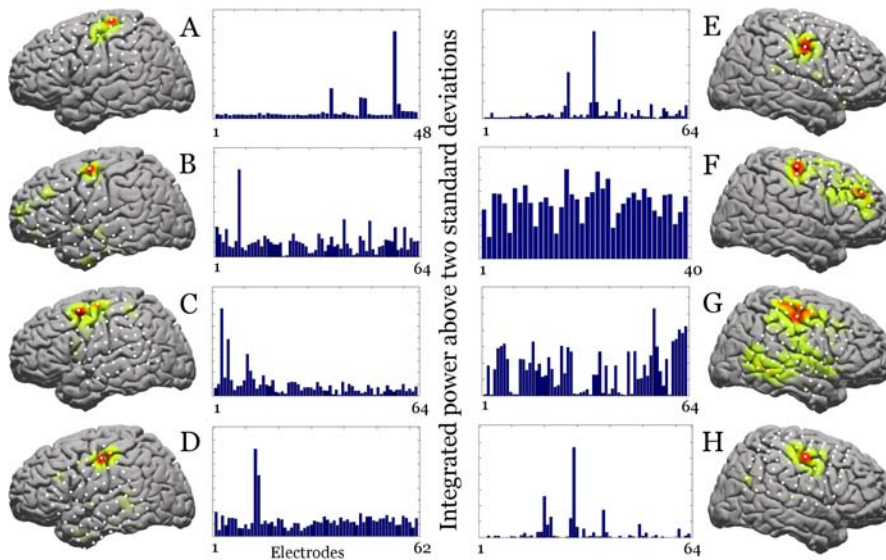


Figure 6.2: **Offline hand motor area mapping**

Activation during hand movement as detailed in method section. The bar plots indicate the sum of suprathreshold activity for each electrode with corresponding interpolated brain plots for each patient. Electrode locations are in white. Note that the activation localizes to hand area in each individual, and that this activation in subjects A-E and H is very sparse. The first 15s of motor activity was used except for pt F whose data is from 30-45s into the task (see text).

6.3 Results

In each patient, localized activity was demonstrated for the first 15s of movement (Figure B.2). In patient F, the initial activity map demonstrated weak motor but strong pre-motor activity. As she may have been developing familiarity with the task, a later 15s block of movement was analyzed (beginning 30s into the task) demonstrating stronger primary motor activation, with some remaining frontal activity. Based upon electrode locations

in Talairach coordinates (Miller, 2007), the strongest activation in each cortical map was consistently stereotactically localized to Brodmann Area 4, demonstrating efficacy in hand motor cortex identification (Figure B.2). In three patients, clinical stimulation mapping was performed and identified the same electrodes as this procedure (see supplement). Real-time mapping (Figure B.3) demonstrated supra-threshold activity immediately upon initiation of the handshake, and showed clear delineation of hand sensorimotor cortex throughout the handshake.

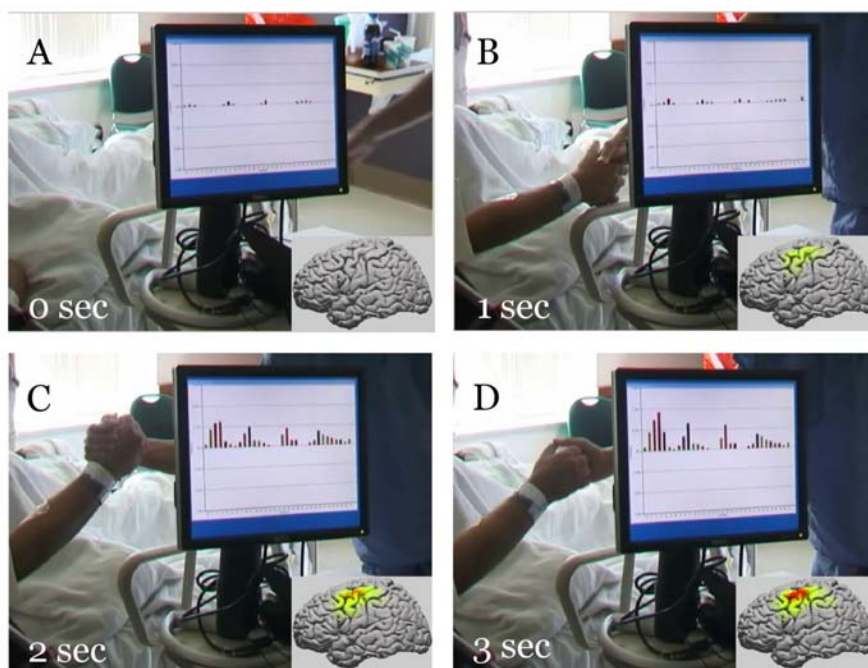


Figure 6.3: Real-time identification of sensorimotor cortex

Four frames from a real-time video (with times at lower left) demonstrate evolution of the mapping during a three-stage handshake (in patient C from figure B.2), following a 10s baseline period. The inset brains demonstrate the cortical map throughout the, scaled to the final weight. The three stages of are shown in insets B, C, and D. The full video is contained in the supplementary material of the manuscript, online.

6.4 Discussion

Change with activity in the electrocorticographic power in the χ -index (chosen here to be 76-200Hz) was found consistently, for all 8 subjects, in a focal portion of cortex in classic hand areas. Unlike the power at lower frequencies, which, due to rhythms at specific frequency bands, may show little change or spatially broad decrease with motor function (eg., mu rhythm) a reliable increase with function was found over the entire 76-200Hz interval (Figure B.1). Previous studies looking up to 100Hz have shown higher frequency power (named “high gamma” by some) increases with motor function that are more focal (Crone, 1998; Leuthardt, 2007; Miller, 2007; Pfurtscheller, 2003) than the power decreases at lower frequencies. High frequency changes correlate with changes in the BOLD signal (Mukamel, 2005), and localized cortical dynamics have been specifically attributed to the 80-200Hz band (Grenier, 2001). This real-time mapping technique should be robust across paradigms and brain areas, as focal high frequency changes have been demonstrated in motor (Crone, 1998; Leuthardt, 2007; Miller, 2007; Ohara, 2000), somatosensory (Bauer, 2006; Szurhaj, 2005), vision (Hoogenboom, 2006; Lachaux, 2005), auditory (Crone, 2001; Edwards, 2005; Kaiser, 2005), memory (Sederberg, 2003), and language (Crone, 2001; Sinai, 2005) paradigms. Previous reports of motor related ECoG changes (Crone, 1998; Leuthardt, 2007; Miller, 2007; Pfurtscheller, 2003; Crone, 2006) have required more elaborate post-acquisition analyses and long acquisition times (at least several minutes) to characterize cortical motor changes, and none have yet been implemented in real-time. Using only the power in the “ χ -index”, rapid and reliable maps of cortical function can be obtained which agree with stimulation result. The results can be assessed immediately, in real time, and repeated if ambiguous. As the “ χ -index” power appears to be a reliable marker of local cortical function, we propose that this method can be applied generically to clinical and research mapping of human cortex.

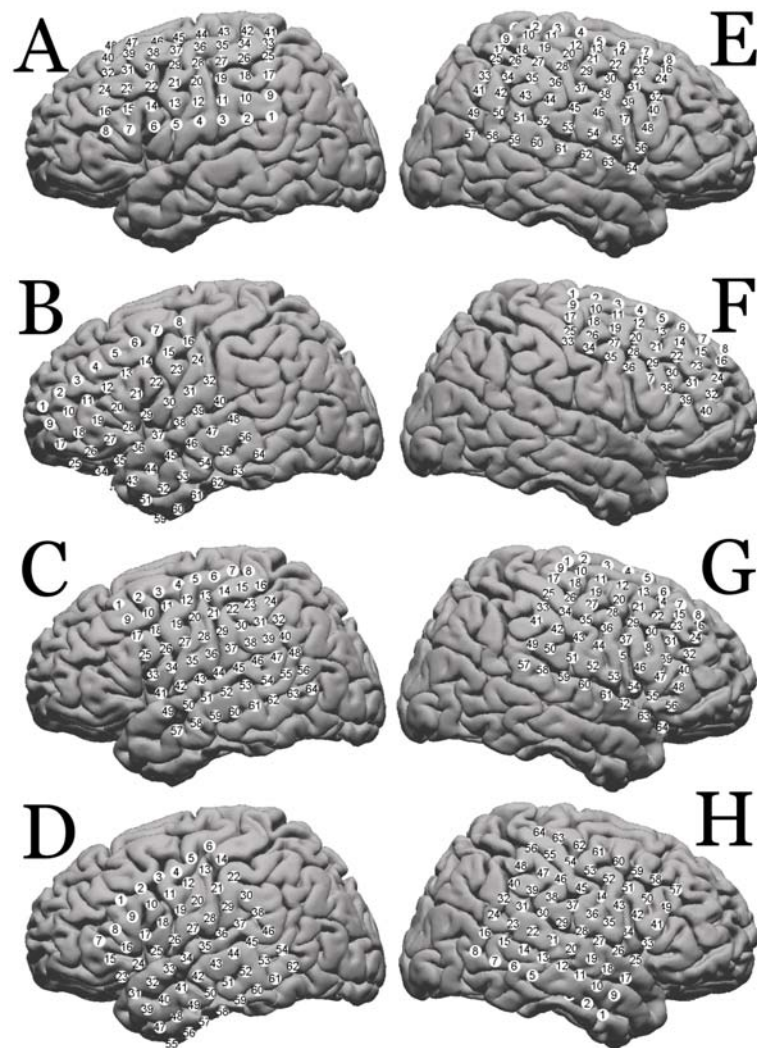


Figure 6.4: **Electrode positions for study subjects**
 Electrode positions, labeled for subjects A-H.

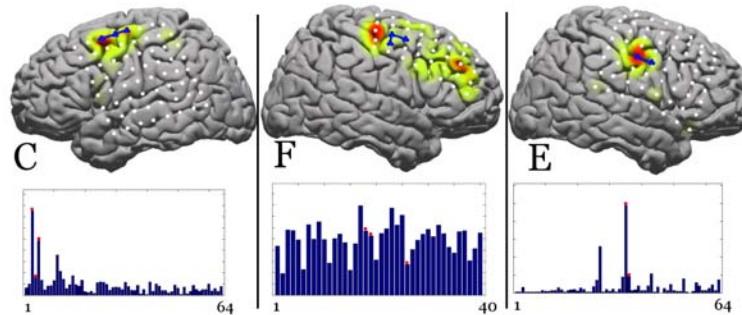


Figure 6.5: **Supplemental Figure 2**

Stimulation results, for subjects C, F, and E from figure 2. Electrodes pairs where clinical stimulation produced motor movement in the hand are shown in blue on the brain schematics. The bar plots are the integrated power, and the red dots indicate electrodes in each positive stimulation pair. Electrical stimulation of the cortex to create transient lesions or induce overt movements, extra or intra-operatively, is the established method to clinically localize function in the brain (Ojemann, Ojemann et al. 1989; Chitoku, Otsubo et al. 2001; Branco, Coelho et al. 2003). This process of stimulation is critical to minimize risk in neurological surgeries which involve resection of seizure focus, tumor, or vascular malformation (Berger, Kincaid et al. 1989; Burchiel, Clarke et al. 1989; Haglund, Berger et al. 1994), and predicts functional outcome (Haglund, Berger et al. 1994; Keles, Lundin et al. 2004). The pair-wise stimulation mapping process in the context of subdural electrode arrays is often incomplete either because it is prematurely aborted by an induced seizure, or stopped once an acceptable surgical margin is obtained, so the only meaningful question in the context of the mapping method described here is whether the method captures one electrode site from each positive pair. Five of the activation maps in this study are devoid of stimulation locations and the remaining three (shown here) contain incomplete stimulation information. In this sense, there are only positive stimulation results, without negative control. For example, the middle patient (subject F) had two pair-wise stimulation positive results, but the cortex near only 1 electrode (at the vertex in the figure) was the only meaningful one of the three, and the procedure stopped, with an adequate margin, before reaching the posterior portion of the grid, where the center of cortical hand representation was. Stimulation which induces sensation is not shown, which, in contrast to the mapping technique, which almost certainly will reflect some sensory feedback component. For a more in depth study of the relation between high frequency ECoG changes and cortical stimulation, please see (Leuthardt, E.C., Miller, K.J., Anderson, N., Schalk, G., Dowling, J., Moran, D., Ojemann, J.G., 2007 Electrocorticographic Frequency Alteration Mapping (EFAM), A Novel Clinical Technique for Mapping Motor Cortex. *Neurosurgery*, in press, 2007).

Chapter 7

**AUGMENTATION OF CORTICAL ACTIVITY BY MOTOR
IMAGERY-BASED LEARNING**

Motor imagery plays an important role in learning complex new motor skills, from learning to serve in tennis to perfecting a pirouette in ballet. What are the neural substrates that underlie motor imagery-based learning? We measured cortical potentials from the surface of the human brain in eight human subjects during both overt motor movement and imagery of the same movement. We found that the spatial distribution of cortical spectral changes during motor imagery mimicked that of actual motor movement, including activation of primary motor cortex, though imagery typically elicited smaller magnitude changes than actual movement. However, as subjects learned to use motor imagery to control a cursor using visual feedback, significant augmentation of cortical spectral activity occurred. In some cases, imagery-related activity after learning exceeded that observed during overt movement. Our findings suggest that the motor cortex adapts not only to sensory feedback from overt movements but also to feedback resulting from motor imagery.

7.1 Introduction

Motor imagery has been shown to be crucial for motor skill learning in a variety of situations, ranging from learning new skills in sports (Murphy 1994) to overcoming the effects of neurological conditions (Dijkerman, Ietswaart et al. 2004; Page, Levine et al. 2007). Many recent efforts to build "brain-computer interfaces" for paralyzed patients have also relied on motor imagery (Hochberg, Serruya et al. 2006; Schalk, Miller et al. 2008). Demonstration of cortical activity during imagery in motor areas in paraplegic individuals (Alkadhi, Brugger et al. 2005) and stroke victims (Sharma, Pomeroy et al. 2006) implies that motor imagery has a significant role to play in rehabilitation and prosthesis, rather than just a

convenient control signal in intact individuals. Human brain imaging studies have shown that motor imagery activates many of the same neocortical areas as those involved in planning and execution of motor movements (e.g., medial supplemental motor area, premotor cortex, dorso-lateral prefrontal cortex, and posterior parietal cortex) (Jeannerod and Frak 1999), but whether primary motor cortex is also activated in motor imagery has remained unclear due to conflicting evidence (Porro, Francescato et al. 1996; Roth, Decety et al. 1996; Schnitzler, Salenius et al. 1997). It is also unclear how these imagery-related responses in the motor system change during imagery-based learning. To address these questions, we recorded, in eight human subjects, electrical signals from the surface of the cerebral cortex using electrocorticography (ECoG). Subjects had undergone placement of intracranial ECoG electrode arrays to localize seizure foci prior to surgical treatment of epilepsy [Supp. Methods and Table S1].

7.2 Brief Methods

In an initial set of experiments, the subjects performed an interval-based task in which they alternated between several seconds of movement and several seconds of rest. The subjects then repeated the task, except that rather than actually moving, they were instructed to imagine the cued movement during a fixed period (overt movement excluded by movement sensors or EMG, Fig. 7.11). We examined changes in the power spectrum of the ECoG signal from all electrodes before and during the cue period. As in previous reports (Miller, Leuthardt et al. 2007), we found a decrease in power in a low frequency band (8-32 Hz) and a spatially more focal increase in power in a broad high frequency band (76-100 Hz) during movement compared to rest in motor-related areas (Figs. B.1, B.2, 7.5). A similar phenomenon was observed when actual movement was replaced by motor imagery, but the spectral changes were of smaller magnitude. We found that the magnitude of the active-rest shift in the high-frequency band during imagery was 25% of the change seen during actual movement, while for the low frequency range, this shift was 50% (figs B.1B, 7.5, 7.9, and table S2).

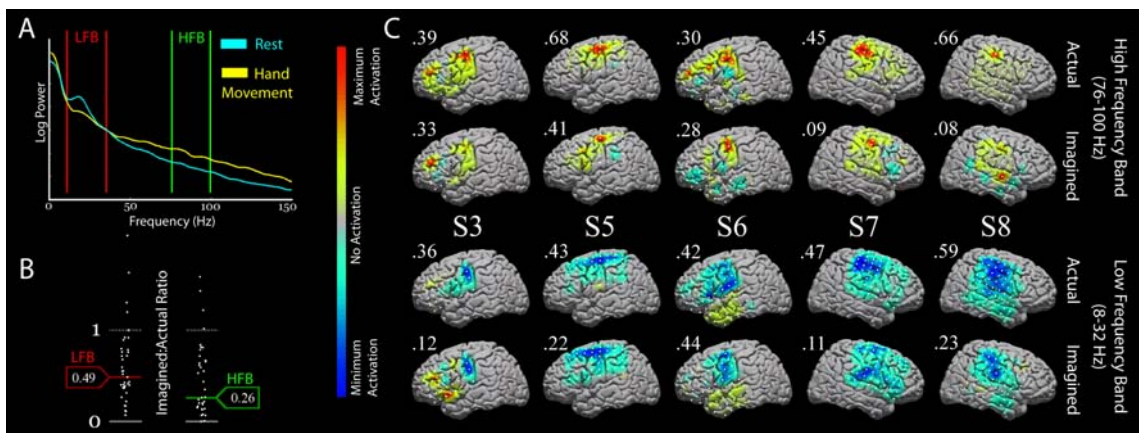


Figure 7.1: Spectral Changes in Cortical Surface Potentials during Actual and Imagined Hand Movements.

(A) Characteristic shift in the cortical power spectrum between movement and rest (Sub 5, electrode in Brodmann area 4). In accordance with previous findings ((Crone, Miglioretti et al. 1998; Crone, Miglioretti et al. 1998; Aoki, Fetz et al. 1999; Miller, Leuthardt et al. 2007)), there is a characteristic decrease in power at low frequencies ("LFB" = 8-32 Hz), and a characteristic increase in power at high frequencies ("HFB" = 76-100 Hz). (B) Comparison of ECoG activation between motor imagery and motor movement. The plot shows the ratio of mean shift in active-rest power between imagery and actual movement (Fig. 7.9, Table S2) for electrodes in which the action vs. rest significance was $p < .05$ (t-test, Bonferroni corrected for the number of electrodes in that subject) for both the LFB and HFB. Each white dot indicates the ratio at an individual electrode. In this paired comparison (38 total electrodes, 21 for tongue, 17 for hand), the geometric mean of the ratio for the LFB, 0.49, was significantly larger ($p = .005$ by resampling bootstrap, 105 iterations) than the geometric mean ratio of the HFB change, 0.26. (C) ECoG-based brain activation maps for actual and imagined hand movement for 5 subjects (denoted by S#). ECoG activation was computed between movement and rest (NOTE 1; Fig 7.6). The activation (HFB: top two rows, LFB: bottom two rows) is scaled to the maximum absolute activation (number indicated in the upper left corner of the map), and plotted to a template cortex, for each subject independently, with the colorscale indicated by the colorbar. Note that all subjects show the characteristic focal high frequency increase and broad low frequency decrease.

We computed ECoG activation between movement/imagery and rest in each electrode

¹. As seen in Figure B.1C for hand movement and Figure B.2 for tongue movement, the

¹The "activation" is the signed cross-correlation $A_{mr} = \frac{(\bar{m} - \bar{r})^3}{|\bar{m} - \bar{r}| \sigma_{m \cup r}^2} \frac{N_m N_r}{N_{m \cup r}}$, comparing distribution of the normalized power in the HFB or LFB for the movement/imagery cues or active targets (m denotes

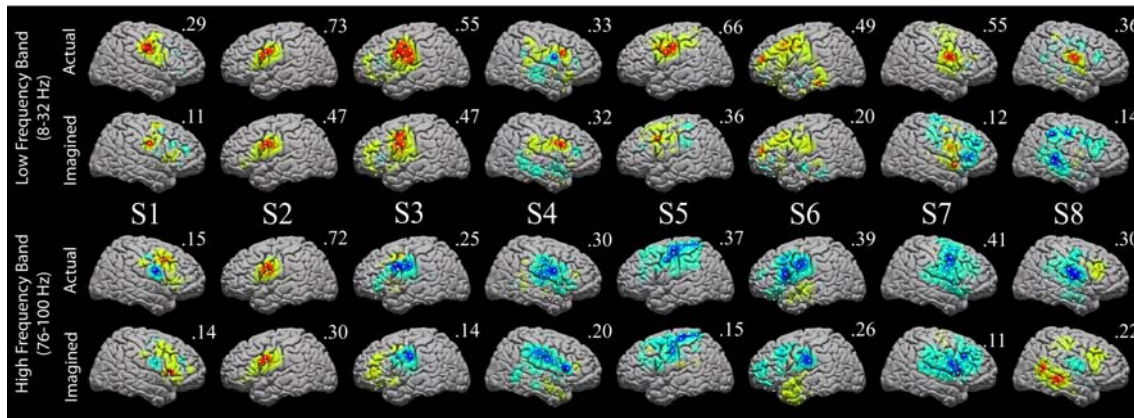


Figure 7.2: **Actual and imagined tongue movement activations for 8 subjects, as in fig B.1C**

Note that subject 2 had an increase with activity in the LFB for both imagined and actual tongue movement. The reason for this is compelling - there was no prominent α/β rhythm to desynchronize with activity, and the underlying shift in the power-law like activity is revealed at low frequencies (Fig. 7.7). Subject 4 showed a robust decrease in HFB actual that was not present in HFB imagined. Interestingly, this is not because of a decrease in activity during tongue movement periods, but a selective increase in activity during rest epochs following tongue movement epochs (figure 7.12).

ECoG activation for motor imagery had a spatial distribution similar to that elicited by actual movement, although the magnitude of activation was consistently less. These brain activation maps show that primary motor cortex (identified by both ECoG spectral changes and Electrocortical Stimulation mapping (Miller, denNijs et al. 2007)) is indeed involved in motor imagery, complementing other evidence from non-invasive techniques such as fMRI (Porro, Francescato et al. 1996) and EEG (Cochin, Barthelemy et al. 1999).

In a second set of experiments, we examined how imagery-based learning affects the cortical representation of motor imagery. Four of the subjects participated in a motor imagery-based cursor control task. Based on the cortical changes seen in the simple imagery, electrode-and-frequency band power combinations were chosen as "features" for controlling

distribution, with mean \bar{m}) and for rest/idling cues or passive targets (r). The joint distribution is denoted $m \cup r$, and N_x denotes the number of samples in distribution x . See Fig. 7.8 for a detailed illustration.

a cursor on a computer screen (Figure B.3A). The subject was instructed to imagine (via kinesthetic and not visual imagery (Neuper, Scherer et al. 2005)) the movement corresponding to the selected feature in order to move a visually-displayed cursor toward one target ("active" direction) and to rest (or "idle") in order to move the cursor to the other target ("passive" direction) , as in Fig. B.3A.

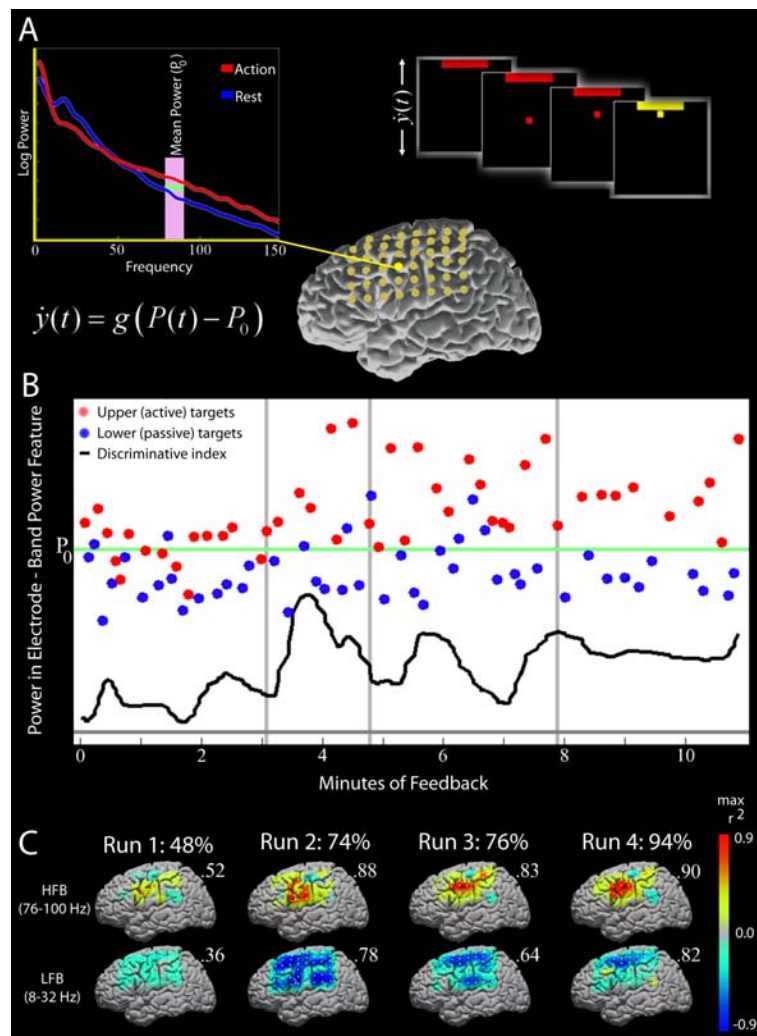


Figure 7.3: Changes in cortical activity during imagery-based learning (shown here for subject 5).

See text for complete explanation

7.3 Results

Subjects rapidly (in 5-7 minutes) learned to control the power in the associated electrode-frequency band using motor imagery (Table S3). While the spatial distribution of high-frequency ECoG activity was conserved, the strength of the imagery-associated change was significantly augmented by learning (Figs B.3, B.4, 7.14, and 7.15). In 4 of the 5 cases, the imagery-associated spectral change exceeded that seen during actual movement (in the fifth case, the change was almost equal to that during movement). After several runs, subjects reported abstraction away from linked imagery to just thinking about cursor moving up or down (fig B.3).

Extended Explanation of Figure 3

A: Specific channel-frequency combination features were identified from the initial motor imagery task and the power in each of these features was coupled to the velocity of a cursor. The instantaneous power $P(t)$ in a selected electrode-frequency band combination was calculated every 40ms based upon the previous 280ms and mapped to the cursor trajectory using a simple linear relation as shown. The instantaneous power was compared with a "reference" power P_0 between movement and rest, and scaled by a gain g to determine the cursor trajectory (Schalk, McFarland et al. 2004). The subject was instructed to imagine (via kinesthetic imagery) the particular movement associated with the selected feature in order to move the cursor toward one target (the "active" direction) and to rest (or "idle") to move the cursor to the other target (the "passive" direction). The order of active and passive targets was random, and the number of each was approximately equal. Individual target trials were terminated when the cursor hit any target or at a designated timeout duration (7200ms). A 1s reward duration (yellowed target for correct hit) was given at trial termination, and there was a 1s rest between the reward duration and beginning of the next target trial. B: The power in the electrode-frequency band features is shown during the 4 experimental runs of the cursor task based upon word repetition imagery (imagining saying

the word "move"). Red dots indicate the mean power during active (upper) target trials, and blue dots indicate mean power during passive (lower) target trials. The black line indicates a "discriminative index" between the targets (the smoothed difference between the mean power during the past 3 active target trials and the past 3 passive target trials). It demonstrates that optimal target accuracy is obtained when the subject finds a middle dynamic range, not the maximum amplitude changes in power (which were obtained in the 2nd run, with mediocre success). C: Distribution of HFB and LFB activations during each experimental run. The maps here are scaled to the same global maximum. Note that the final activations are accentuated in precisely the electrode-frequency band features which were being used for cursor control (table S3).

7.4 Discussion

Our results are consistent with the emerging view of motor imagery as subliminal activation of the motor system (Jeannerod and Frak 1999). The fact that primary motor cortex was activated in our subjects during motor imagery provides independent support for earlier results obtained using fMRI implicating this area in motor imagery (Porro, Francescato et al. 1996; Roth, Decety et al. 1996). Feedback paradigms engage attentional mechanisms in a way that simple imagery does not, and this could explain why spectral change during feedback imagery exceeds simple imagery. But by what mechanism is spectral change during imagery-based feedback able to exceed that of overt motor movement? Augmentation in our imagery-based learning finding may share mechanistic similarity with recent results in the primate motor system (Tkach, Reimer et al. 2007) where "mirror-neuron" like activation was seen in primary motor cortex during visual observation of cursor movement after the monkey had learned to control the cursor with a manipulandum. In fMRI studies, primary motor cortex activation during imagery was reported to be ~30% of the level observed during execution, a result consistent with our HFB findings of reduced (~30%) ECoG spectral change during imagery. However, our results additionally demonstrate that this activation can be significantly augmented over a surprisingly short period of time as the subject learns

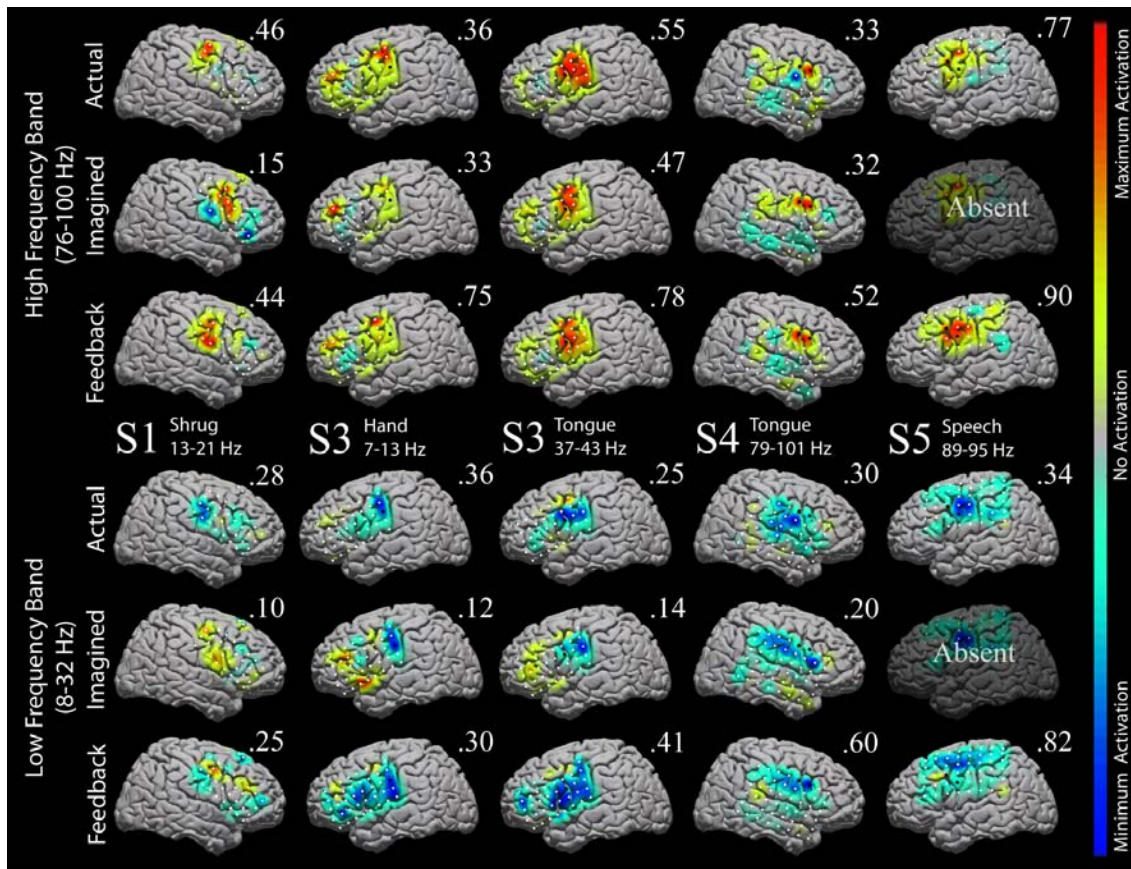


Figure 7.4: **Augmentation of cortical activity after learning in HFB and LFB.**

Feedback sites are shown with black dots. Subject numbers, movement/imagery modality, and frequency range are shown across the center of the figure. Brain activation maps are individually scaled, as in figs B.1 and B.2. The specific electrodes, frequency ranges, and target accuracy during the cursor control task are shown in supplemental table S3. The activation (NOTE 1) during the cursor task is calculated by comparing active and passive targets, rather than action and rest epochs (the entire data stream during target presentation is used, rather than a sub interval).

to control a cursor through motor imagery and visual feedback. It has long been known that neurons in the motor system can adapt to correct errors in body movement (e.g., hand movement) based on visual feedback (Fetz 1969; Georgopoulos, Kalaska et al. 1983). Our findings reveal that motor cortical neurons can additionally significantly alter their firing

patterns, on the population level, to optimize movements linked to motor imagery.

7.5 Supplemental Methods

7.5.1 Subjects

Simple motor tasks were studied in 8 patients (2 Females, ages 12-48, Table S1) who had undergone placement of intracranial electrode arrays to localize seizure foci prior to surgical treatment of medically refractory epilepsy. The arrays were typically placed for 5-7 days with the location of the electrodes and duration of implantation determined independently by clinical criteria alone. Experiments were performed at Children's Hospital (subject 2) and Harborview Hospital (all others) at the University of Washington (UW), Seattle, USA. Patients underwent craniotomy for electrode placement and were typically studied 3-5 days after electrode placement, to allow for recovery from the surgery. Only patients with some peri-Rolandic coverage were included. Subjects gave informed consent for participation, in a manner approved by the University of Washington Institutional Review Board.

7.5.2 Recordings

The platinum electrode arrays (Ad-Tech, Racine, WI) were typically configured as linear strips, and 8 x 4-8 electrode grids. The electrodes had 4mm diameter (2.3mm exposed), 1 cm inter-electrode distance, and were embedded in silastic. ECoG signals were split into two identical sets. One set was fed into the clinical EEG system (XLTEK, Oakville, Ontario, Canada) and the other set was recorded with Synamps2 (Neuroscan, El Paso, TX) biosignal amplifiers (Harborview) or Guger (Gugertech, Graz, Austria) amplifiers (Children's). ECoG signals were then acquired from the Neuroscan or Gugertech system using the general-purpose software BCI2000 (Schalk, McFarland et al. 2004). At Harborview (Children's), the sampling frequency was 1000 Hz (1200 Hz). The signals were bandpass filtered from 0.3 Hz to 200 Hz at Harborview. In this way, the 8-100 Hz spectral regions examined in this study are well outside of any filtering ranges and below any relevant Nyquist frequency. Surface EMG were placed for clinical purposes only and thus were available only in a subset

of patients. Finger position was recorded using a sensor dataglove (5dt, Irvine, CA) to verify that subjects were not moving their hands (see fig 7.11).

7.5.3 Tasks

A series of three experiments were performed: interval-based active motor movement, interval-based motor imagery, and a cursor-to-target task to provide feedback to motor imagery. First, subjects performed simple, repetitive, motor movement (Miller, Leuthardt et al. 2007) of the hand (synchronous flexion and extension of all fingers, i.e., clenching and releasing a fist at a self-paced rate of approximately 1 Hz), tongue (opening of mouth with protrusion and retraction of the tongue, i.e. sticking the tongue in and out, also at 1 Hz), shrug (shoulder raise at 1Hz), or simple word vocalization (saying the word "move"). These movements were performed in an interval-based fashion, alternating between 3 second movement blocks and rest. The side of actual or imagined movement was always contralateral to the side of cortical grid placement. There were 30 text cues ("Hand", "Tongue", "Shrug", "Move") for each movement modality, delivered visually as 2.5 cm high text at a distance of 75 -100 cm from the subject, using the BCI2000 program (Schalk, McFarland et al. 2004). Cues of different type were interleaved randomly so no particular movement type could be anticipated.

Following the overt movement experiment, each subject performed an identical task, but with movement imagery rather than actual movement. The imagery was kinesthetic (Neuper, Scherer et al. 2005) ("Imagine yourself performing the actions like you just did", i.e., don't imagine what it looked like, but imagine making the motions).

Half of the subjects (1, 3, 4, 5) went on to participate in an imagery-based feedback learning task. In this task, a specific electrode-and-frequency range combination feature was chosen from the simple imagery task (features shown in table 1), and the power in this feature was coupled to the trajectory of a cursor. Targets were presented in random order, on one of two sides of the presentation screen. The subject was instructed to imagine (again, via kinesthetic imagery) a particular movement in order to move a cursor toward

one target (the "active" direction), and to rest (or "idle") to move the cursor to the other target (the "passive" direction). Targets were presented continuously for 2 minute runs, and there were typically 3-5 such runs in the experiment (If the target was present for more than 7 seconds, or the target was hit, a new target was presented.)

7.5.4 Signal Analysis

A high frequency band (HFB) and a low frequency band (LFB) were chosen for analysis, as in previous papers (Miller, Leuthardt et al. 2007), to capture the event-related desynchronization in the LFB, and the power law change in the HFB. For the cursor-to-target task, the offline analysis was the same as for movement and imagery, except rather than a sub-window from each offline movement cue period, normalized mean-spectra were calculated throughout the entire time of cursor presentation for each target presentation. The online analysis is articulated in further detail by Leuthardt et al (Leuthardt, Miller et al. 2006) and Schalk et al (Schalk, Miller et al. 2008).

7.5.5 Electrode Localization and Template Brain Mapping

Electrode locations were estimated based upon their relation to skull table and landmarks from the sagittal (lateral) and coronal (anterior-posterior) skull x-rays using the LOC package (Miller, Makeig et al. 2007). We also used this package to plot electrode locations with respect to the AFNI - Montreal Neurological Institute (MNI) template brain. Activation maps were created for the HFB and LFB independently in each patient, for each movement type. We created these maps by linear superposition of activation (Equation 1) weighted by spherical Gaussian kernels (standard deviation of 5mm) centered at the location of each electrode, and interpolated the superposition at each point in a template brain.

$$A_{mr} = \frac{(\bar{m} - \bar{r})^3}{|\bar{m} - \bar{r}| \sigma_{m \cup r}^2} \frac{N_m N_r}{N_{m \cup r}}$$

Equation 1: Activation, quantified using the square of the cross-correlation (r^2), signed to reflect whether the significance represents an increase or a decrease in the band-limited

PSD for movement with respect to rest (or, in the case of a target task, whether one target represents an increase or decrease in power with respect to the other target). What this metric tells us is how much of the variation in the joint data set $\sigma_{m \cup r}^2$ can be accounted for by the fact sub-distributions m and r might have different means, \bar{m} and \bar{r} (N_m , N_r , and are the number of samples of type m , r , respectively, and $N_{m \cup r} = N_m + N_r$) see fig 7.6 for illustration.

7.6 *Supplemental Figures and Tables*

Patient	Age	Sex	Hand	Grid Location	Seizure Focus
1	31	F	R	R Frontotemporal	R Insula
2	12	M	R	L Frontotemporal	R Temporal
3	23	M	R	L Frontotemporal	L Temporal
4		M		R Frontotemporal	
5	18	F	R	L Frontal	L Frontal
6	41	M	L	L Frontotemporal	L Temporal
7	38	M	R	R Frontal	R Frontal
8	48	M	R	R Temporal-parietal-occipital	R Temporal-occipital

*Prior L ATL

**Congenital absence of left arm

Table S1: Patient descriptions and characteristics

Table S1

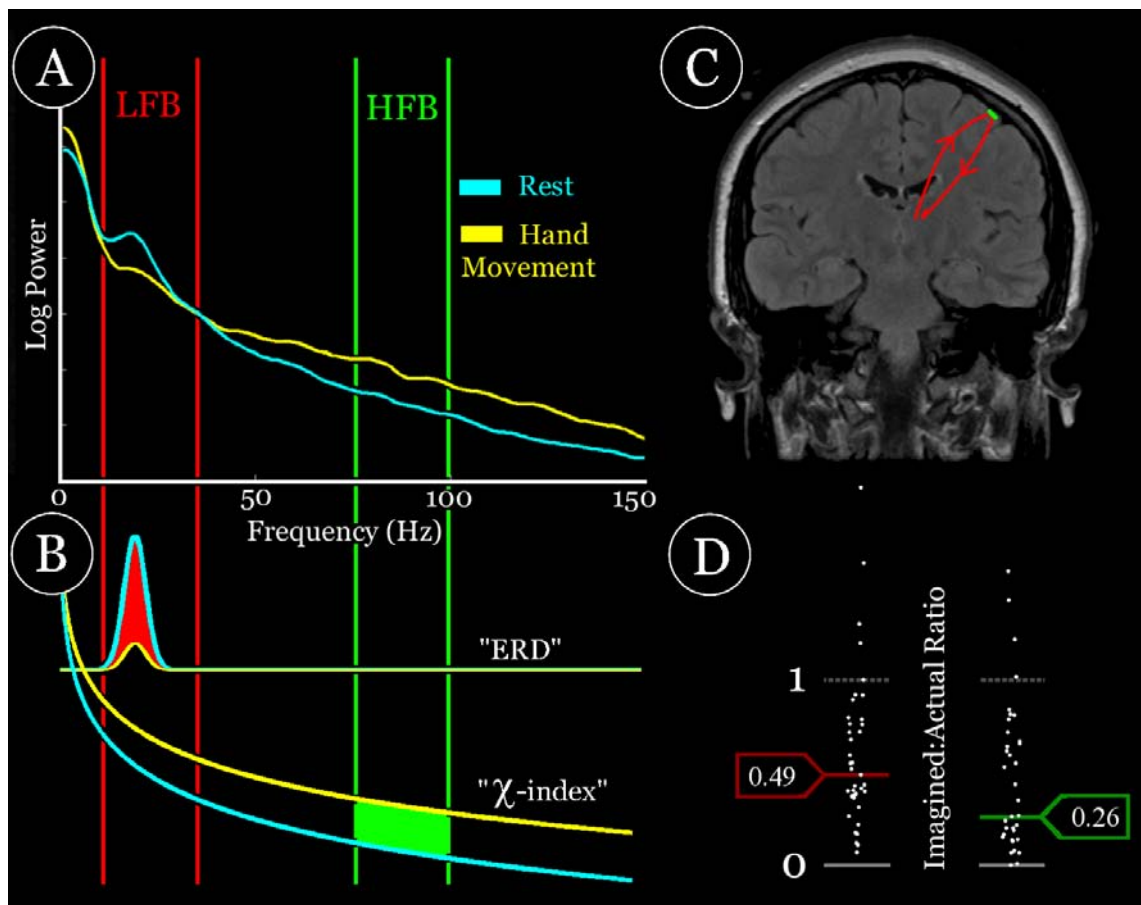


Figure 7.5:

Supplemental figure 1

Changes in the cortical spectrum: A: Characteristic shift in the cortical power spectrum between movement and rest (Subject 5, electrode in Brodmann area 4). In accordance with previous findings (Crone, Miglioretti et al. 1998; Crone, Miglioretti et al. 1998; Aoki, Fetz et al. 1999; Miller, Leuthardt et al. 2007), there is a consistent decrease in power at low frequencies, and a characteristic increase in power at high frequencies. B: The changes in the cortical spectrum may be decoupled into distinct phenomena (Miller, Zanos et al.

2008). At low frequencies, there is a band limited spectral peak which decreases with activity, consistent with event-related desynchronization (ERD). At high frequencies, a broad, power-law like increase in power (which happens across the entire spectrum), may be observed. This functional change has been denoted the “ χ -band” or “ χ -index” when explicitly targeting this broad spectral feature (Miller, denNijs et al. 2007; Miller, Zanos et al. 2008), and “high- ” when seen as a band-specific increase in power at high frequencies (Crone, Miglioretti et al. 1998; Brovelli, Lachaux et al. 2005; Canolty, Edwards et al. 2006). As in previous papers (Miller, Leuthardt et al. 2007), a low frequency band (LFB, 8-32 Hz, red) is chosen to capture ERD changes (α/β) in the classic EEG range, and a high frequency band (HFB, 76-100 Hz, green) is chosen to capture the power-law like broad spectral changes most easily seen at high frequencies. C: We propose that the feature captured by the HFB corresponds to local cortical activity (green). The LFB changes, which represent peaked features in the power spectrum (and thus have special timescales) have been proposed to be due to feedback between cortical and sub-cortical structures, such as a thalamocortical feedback loop (Feige, Scheffler et al. 2005). D: The ratios of the action-rest shift between motor imagery tasks and motor movement tasks. This ratio ($\bar{m} - \bar{r}$ for imagery vs. $\bar{m} - \bar{r}$ for movement, figure B.4D), is for electrodes in which the action vs. rest significance was $p < .05$ (t-test, Bonferroni corrected for the number of electrodes in that subject), for both the HFB and LFB. The values for ratios at individual electrodes are shown with white dots. In this paired comparison (38 total electrodes, 21 for tongue, 17 for hand), the geometric mean of the ratio for the LFB, 0.49, was significantly larger ($p = .005$ by resampling bootstrap, 10^5 iterations) than the geometric mean ratio of the HFB change, 0.26. The geometric standard deviation of the HFB was significantly larger than the LFB ($p = .016$ by resampling bootstrap, 10^5 iterations). Similar comparisons for unpaired distributions are found in figure 7.9 and table S2.

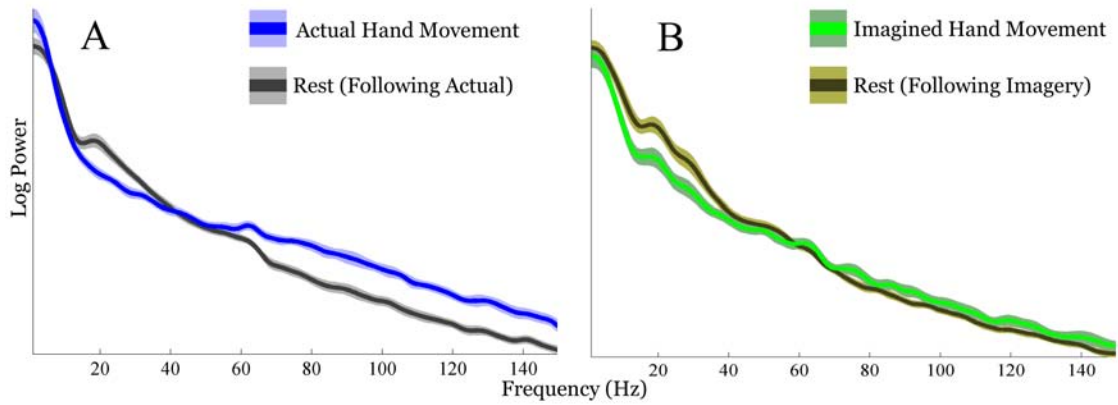


Figure 7.6:

Supplemental figure 2

Paired comparison of active and rest epochs from an electrode (#35, cortical plot - table S2, row 5, column 2) in subject 5 during a hand movement (A) task and a hand movement imagery (B) task. The central line indicates the mean log power across all epochs of each type, and the shaded outer region is the 95

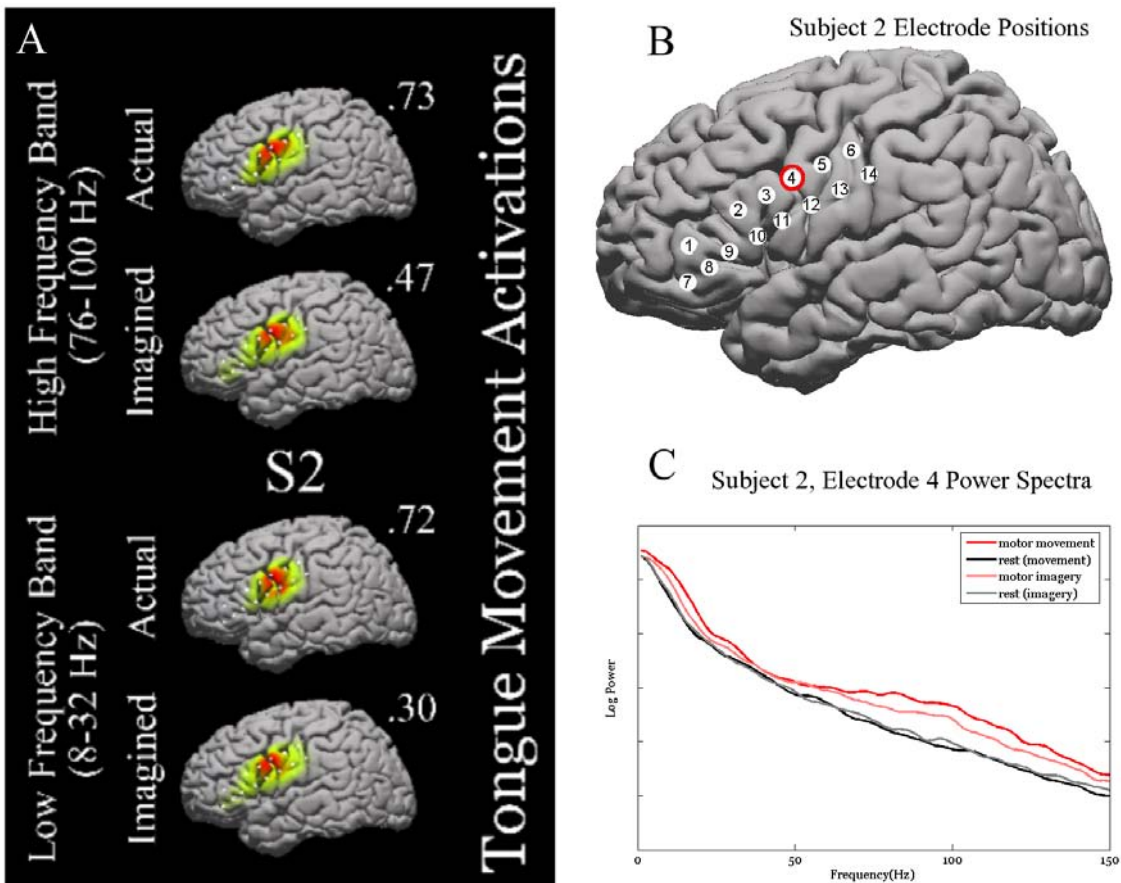


Figure 7.7:

Supplemental figure 3

As shown in (A), subject 2 did not have the characteristic decrease in power in the LFB with tongue motor movement or imagery. Further inspection, illustrated here for the electrode shown with a red circle in (B), revealed that subject 2 lacked the classic low frequency (α/β) rhythm. This can be seen in (C). Accordingly, the underlying broad spectral increase with movement or imagery normally evident only in the HFB is now unmasked in the maps of the LFB in (A) and the spectra in (C).

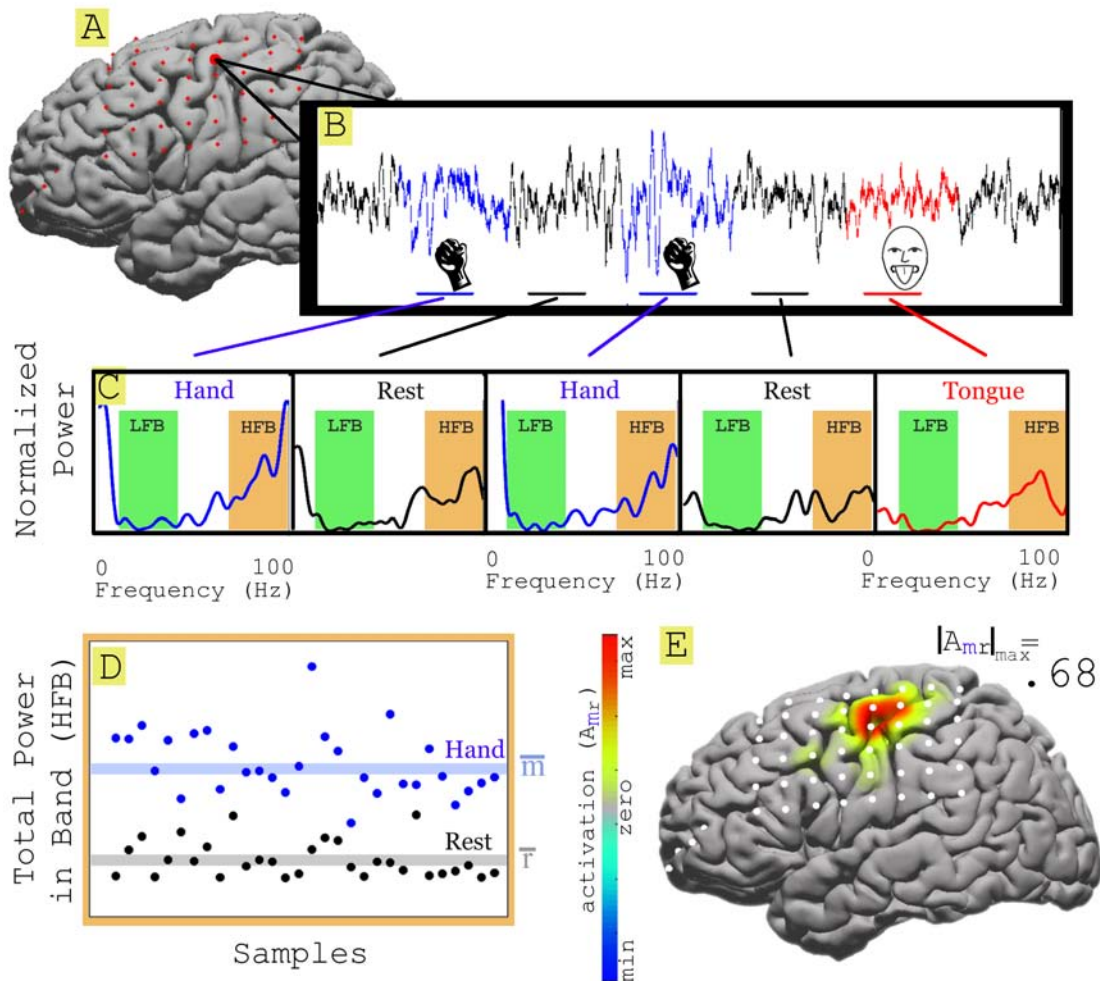


Figure 7.8:

Supplemental figure 4

Method for calculating and displaying “activation” (A_{mr} -equation 1) between action and imagery. A-B: A subject performed an interval-based motor movement or kinesthetic imagery (Neuper, Scherer et al. 2005) task. The raw signal (re-referenced with respect to the common average) from each electrode is broken up into 3 second epochs based upon the stimulus to move (or imagine moving) the hand or tongue, and resting. A subset of

each epoch, the time corresponding to .5-2 seconds into that epoch (shown in the horizontal lines below the raw data), is selected for analysis. This is done because of behavioral lag with respect to the changing stimulus. C: The power spectral density of each epoch was calculated every 1 Hz from 1 to 150 Hz using a Fast Fourier Transform (FFT) using 0.25 second Hann windowed segments, stepping with an overlap of 0.1 second (Welch's averaged periodogram method). Each power spectrum is then normalized by dividing the power at each frequency bin by the average power at that frequency bin, taken across all epochs. D: The total power in a low frequency band (LFB, 8-32 Hz) and a high frequency band (HFB, 76-100 Hz) is calculated for each epoch of each type. E: The activation, A_{mr} (equation 1), is calculated for each movement or imagery modality. In the case of a mixed modality experimental run, the distribution of samples of power for each modality are only compared with the samples of power for rest epochs that followed epochs of that kind (i.e. hand movement epochs are compared with rest epochs which followed hand movement, and not those which followed tongue movement). The activation obtained for each electrode is used to scale a spherical gaussian kernel ($\sigma = 5\text{mm}$) centered at the Talairach location obtained for that electrode using the LOC package (Miller, Makeig et al. 2007), and all kernels are linearly superimposed to obtain a cortical map. The activation is scaled to the maximum absolute activation (indicated to the upper left of the map), with the colorscale shown (dark red \sim maximum increase in activation, dark blue \sim maximum decrease in activation, grey \sim no activation). These maps are generated for each subject, each band (HFB or LFB), and each movement or imagery modality.

Significance constraints (HFB and LFB)	N (LFB)	N (HFB)	GeoMean (LFB)	GeoMean (HFB)	P(GeoMean) (HFB vs. LFB)	GeoSTD (LFB)	GeoSTD (HFB)	P(GeoSTD) (HFB vs. LFB)
Both Bands	38	38	0.49	0.26	p=0.005	2.1	3.6	p=0.016
Independent	141	104	0.41	0.28	p=0.003	2.9	3.4	p=0.226
Top 5 Only	57	54	0.53	0.24	p=0.0002	3.1	3.4	p=0.390
Independent (Hand Only)	90	33	0.38	0.31	p=0.156	2.4	4.0	p=0.011
Independent (Tongue Only)	51	71	0.49	0.26	p=0.003	3.9	3.1	p=0.772

Table S2

For Both Bands, 21 were hand-task specific, and 17 were tongue-task specific. Imagined to real ratios for the shift in the low frequency band (LFB, 8-32Hz) and the high frequency band (HFB, 76-100Hz). p-values were calculated using a resampling bootstrap, 105 iterations.

The geometric mean, $\overline{s_{geo}}$ (GeoMean), of sample distribution s_i is: $\overline{s_{geo}} = \left(\prod_i s_i \right)^{\frac{1}{i}}$

The geometric standard deviation, $\sigma_{geo}(s)$, of sample distribution is: $\sigma_{geo}(s) = \exp \left(\sqrt{\frac{\sum_i (\ln(s_i) - \ln(\overline{s_{geo}}))^2}{N-1}} \right)$,

Where N is the number of samples in sample distribution s_i . See the caption of fig 7.11 for further explanation of Significance Constraint.

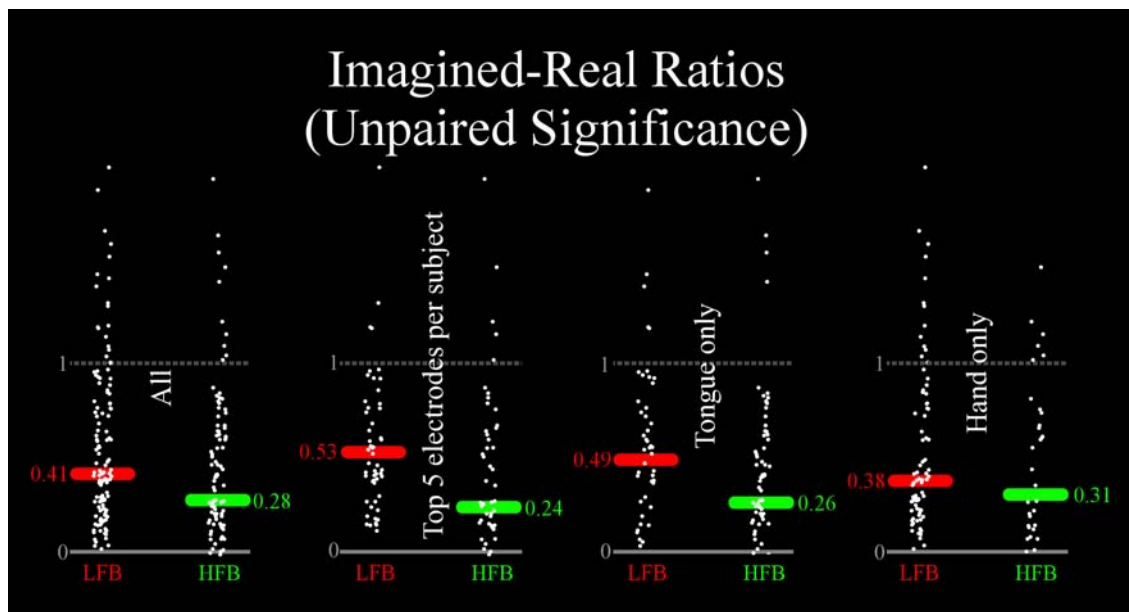


Figure 7.9:

Supplemental figure 5

Imagined to Real ratios for the shift in the low frequency band (LFB, 8-32Hz) and the high frequency band (HFB, 76-100Hz), as in figure B.1B. The average ratios flanking the individual electrode ratios (shown with white dots) are geometric means. Imagery to Movement ratios were considered for electrodes which had an associated action to rest p-value of $p < .05$ after Bonferroni correction (Bonferroni 1936) for the number of electrodes in that subject's array. HFB and LFB were considered independently.

“All” ~ Significant changes for hand or tongue were lumped together.

“Top 5” ~ For a given subject, modality (hand or tongue), and band (HFB or LFB), only the top 5 most significant electrodes are considered (so that the average isn't dominated by one or a few subjects); tongue and hand are lumped together.

“Tongue only” and “Hand only” ~ the ratios from “All”, but with tongue and hand modalities separated.


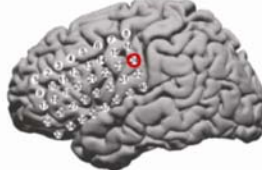
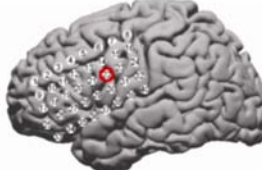
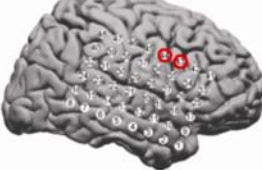

Subject (Feedback Modality)	Electrode Positions	Electrode Position (Feedback Frequency)	Feedback Target Accuracy
Subject 1 (Shoulder Shrug)		2, 7, 55 (13-21Hz)	85%
Subject 3 (Hand)		-61, -15, 33 (7-13 Hz)	74%
Subject 3 (Tongue)		-60, 4, 25 (37-43Hz)	90%
Subject 4 (Tongue)		58, 14, 28 (79-101Hz) 59, 4, 32 (79-101Hz)	100%
Subject 5 (Speech)		-53, 8, 38 (89-95Hz) -60, -3, 30 (79-85Hz)	94%

Figure 7.10:

Table S3

Electrode - frequency band combinations for feedback, and associated target task performance. The electrode locations are in Talairach coordinates. Spatial activations associated

with this feedback are shown in figure B.4.

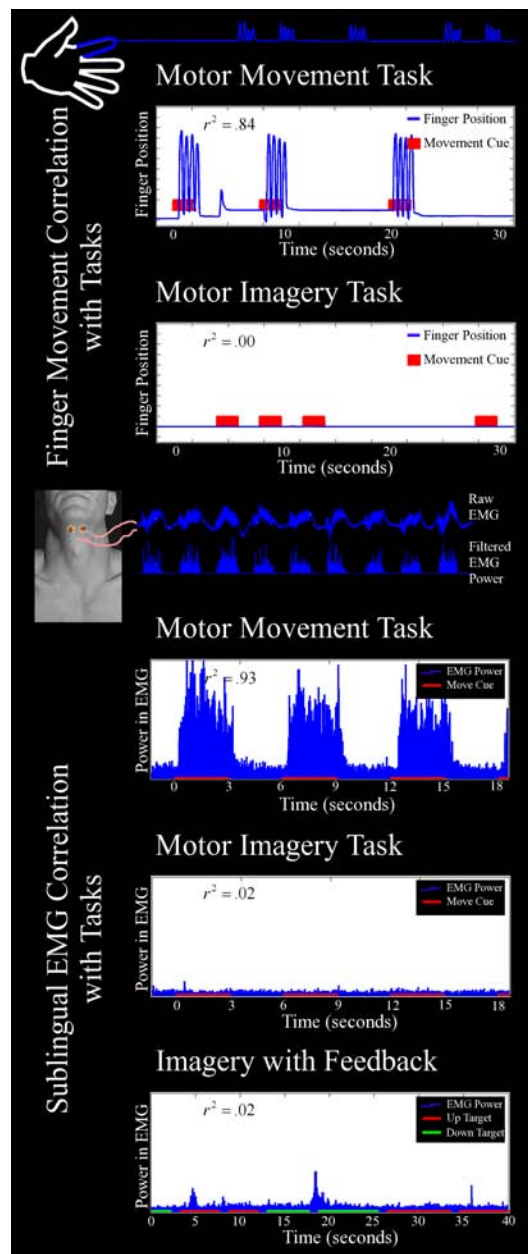


Figure 7.11:

Supplemental figure 6

Validation of imagery.

Upper 2 panels: Subject 5 wore a dataglove (5dt, city, state) which recorded index finger position during the interval-based finger movement task. During the motor movement task, the squared correlation of index finger position with the cue (movement vs. rest) was significant ($r^2=.84$, $p<.001$). There was no significant correlation of finger position with cue during the hand motor imagery task.

Lower 3 panels: Subject 4 had a sublingual differential EMG pair in place during a tongue motor task, a tongue motor imagery task, and an imagery based feedback task. The EMG signal was band-stop filtered from 57-63Hz, 117-123Hz, and 177-183Hz to reject line noise (3rd order Butterworth digital filter, forward and backward to eliminate phase distortion). It was then high-pass filtered at 20Hz noise (3rd order Butterworth digital filter, forward and backward), and squared to obtain the "filtered EMG power". The power in the EMG was significantly correlated with the tongue motor movement task (cross correlation $r^2=.93$, $p<.001$), but was not correlated with either the tongue imagery or imagery-based feedback task.

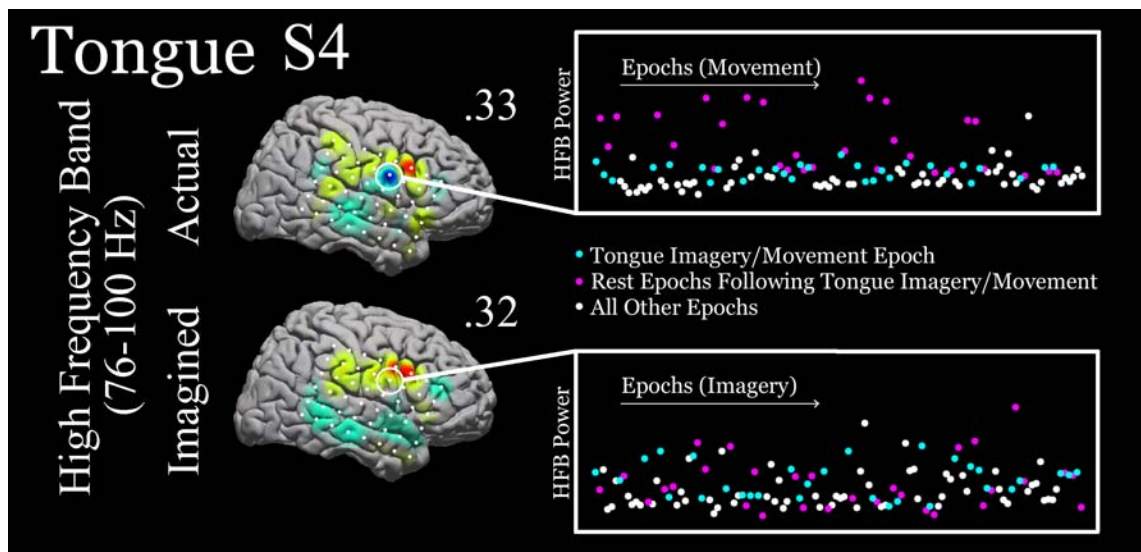


Figure 7.12:

Supplemental figure 7

This illustrates that the robust “decrease” in the HFB for movement w.r.t rest epochs (absent in imagery w.r.t. rest epochs) is in fact due to amplification of HFB power in the rest epochs (purple) following tongue movement, and is not seen in tongue movement epochs (light blue) or hand movement/rest epochs (white). The anatomical location of the electrode in question is shown below (figure 7.13).

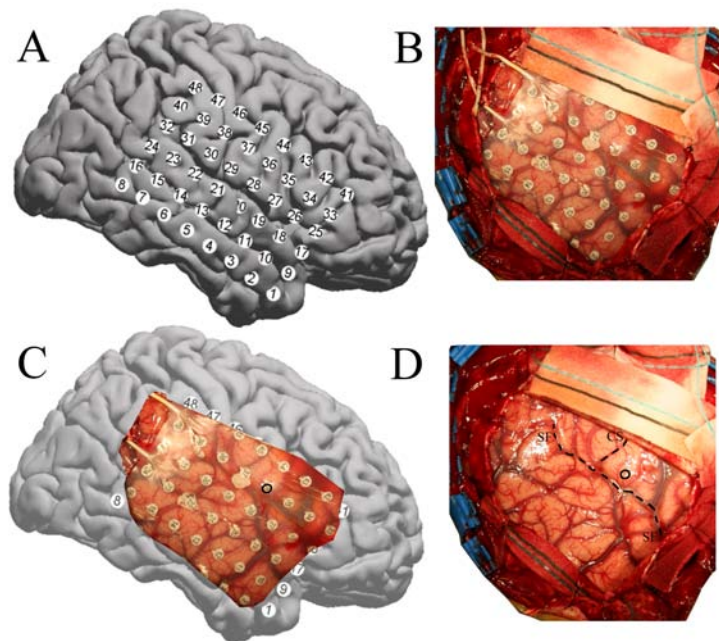


Figure 7.13:

Supplemental figure 8

The anatomical location of the HFB amplification for rest following tongue movement (Figure 7.12), shown as a black circle in insets C and D.

A: Electrode positions interpolated from x-ray (on the AFNI template) estimated with the LOC package.

B: Electrode positions shown from an intra-operative picture.

C: The aperture in (B) projected onto (C), with the relevant electrode from figure 7.9 shown with a black circle.

D: The location of the electrode on the exposed brain (intraoperative picture). "SF" denotes the Sylvian Fissure, and "CS" denotes the Central Sulcus.

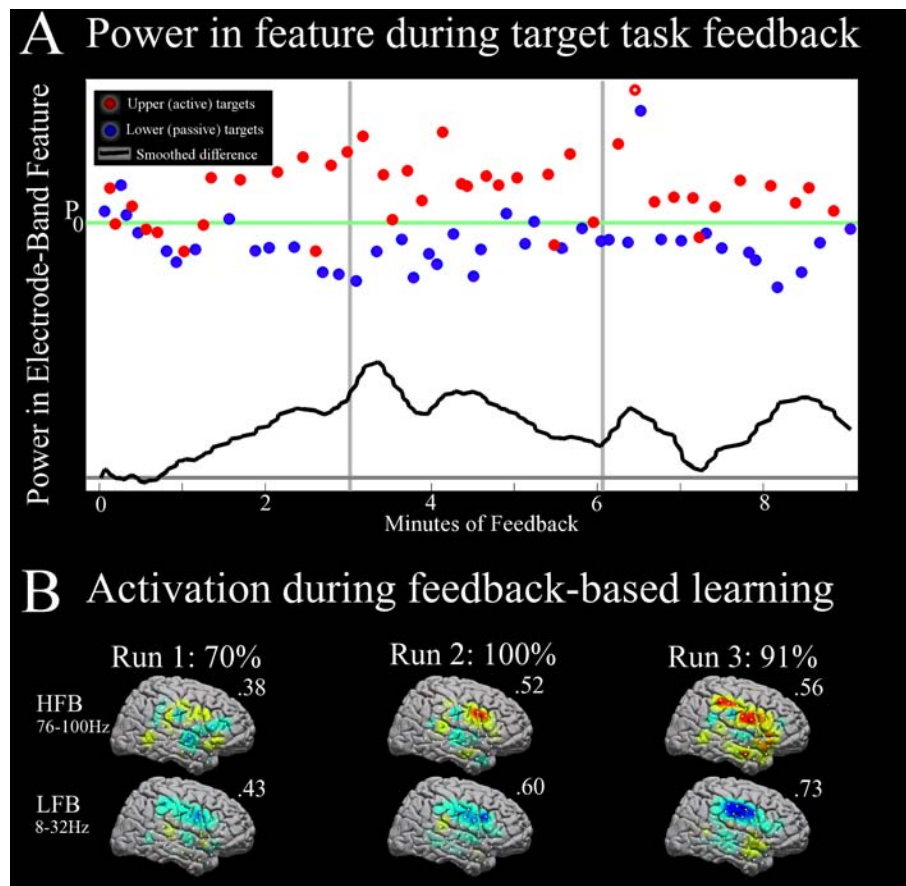


Figure 7.14:

Supplemental figure 9

Figure S9: As in Figure B.3, but for subject 4 and tongue movement. Three consecutive runs with feedback are shown. The subject reported being disinterested in the last run.

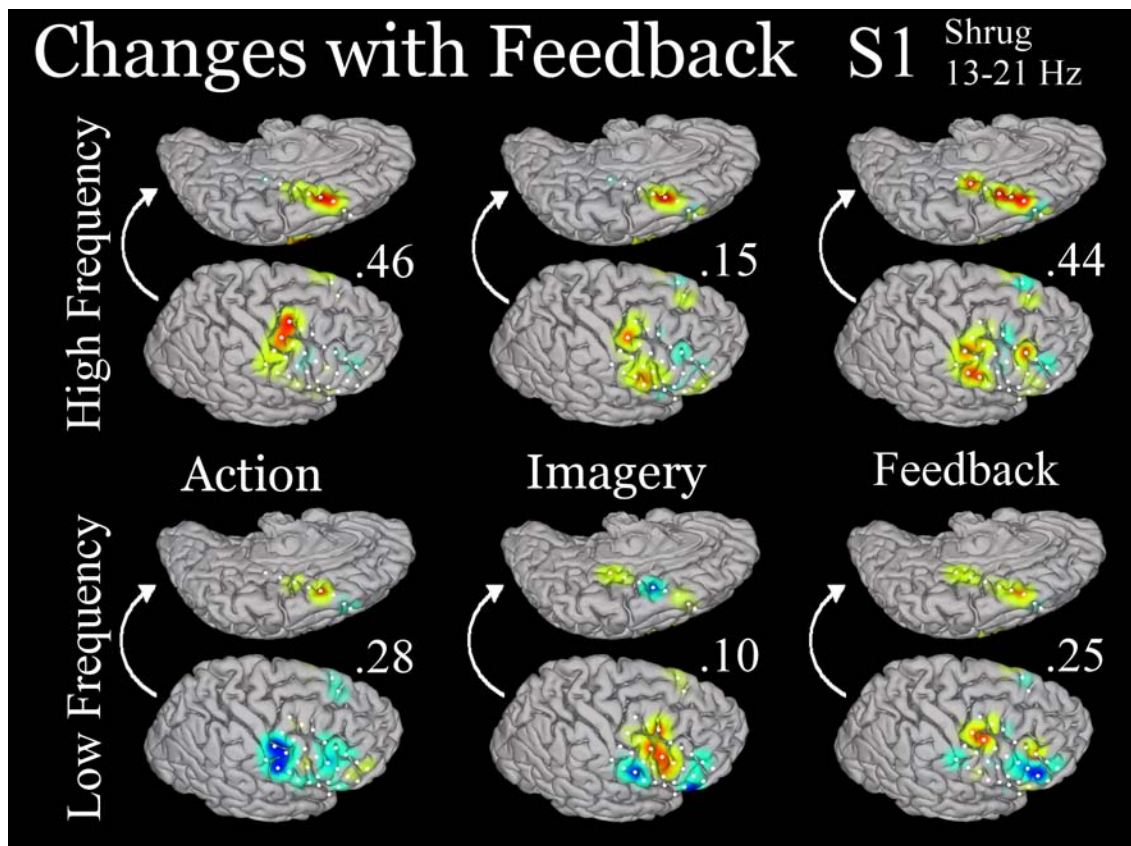


Figure 7.15:

Supplemental figure 10

Spectral changes in ECoG with feedback for subject S1, shrug modality (feedback from 13-21Hz) on a medial electrode (see table S3).

BIBLIOGRAPHY

- [1] H. Alkadhi, P. Brugger, S. H. Boendermaker, G. Crelier, A. Curt, M. C. Hepp-Reymond, and S. S. Kollias. What disconnection tells about motor imagery: evidence from paraplegic patients. *Cereb Cortex*, 15(2):131–40, 2005.
- [2] F. Aoki, E. E. Fetz, L. Shupe, E. Lettich, and G. A. Ojemann. Increased gamma-range activity in human sensorimotor cortex during performance of visuomotor tasks. *Clin Neurophysiol*, 110(3):524–37, 1999.
- [3] S. Arroyo, R. P. Lesser, B. Gordon, S. Uematsu, D. Jackson, and R. Webber. Functional significance of the mu rhythm of human cortex: an electrophysiologic study with subdural electrodes. *Electroencephalogr Clin Neurophysiol*, 87(3):76–87, 1993.
- [4] M. Bauer, R. Oostenveld, M. Peeters, and P. Fries. Tactile spatial attention enhances gamma-band activity in somatosensory cortex and reduces low-frequency activity in parieto-occipital areas. *J. Neurosci.*, 26:490–501.
- [5] C. Bedard and A. Destexhe. *PRL*, 9:118102.
- [6] J. M. Beggs and D. Plenz. Neuronal avalanches in neocortical circuits. *J Neurosci*, 23(35):11167–77, 2003.
- [7] J. M. Beggs and D. Plenz. Neuronal avalanches are diverse and precise activity patterns that are stable for many hours in cortical slice cultures. *J Neurosci*, 24(22):5216–29, 2004.
- [8] H. Berger. ber das elektroenkephalogramm des menschen. *Arch Psychiatr Nervenkr*, 1929.
- [9] T Blakeley, K. J. Miller, R. P. Rao, and J. G. Ojemann. Localization and classification of phonemes using high spatial resolution ecog grids. *IN SUBMISSION – * denotes equal contribution*, 2008.
- [10] T Blakeley, K. J. Miller, S. Zanos, R. P. Rao, and J. G. Ojemann. Robust long term control of an electrocorticographic brain computer interface with fixed parameters. 2008.

- [11] B. Blankertz, G. Dornhege, M. Krauledat, K. R. Muller, and G. Curio. The non-invasive berlin brain-computer interface: fast acquisition of effective performance in untrained subjects. *Neuroimage*, 37(2):539–50, 2007.
- [12] CE Bonferroni. Teoria statistica delle classi e calcolo delle probabilit. *Pubblicazioni del R Istituto Superiore di Scienze Economiche e Commerciali di Firenze.*, 8:3–62, 1936.
- [13] D. M. Branco, T. M. Coelho, B. M. Branco, L. Schmidt, M. E. Calcagnotto, M. Portuguez, E. P. Neto, E. Paglioli, A. Palmini, J. V. Lima, and J. C. Da Costa. Functional variability of the human cortical motor map: electrical stimulation findings in perirolandic epilepsy surgery. *J Clin Neurophysiol*, 20(1):17–25, 2003.
- [14] M. A. Brazier. Recordings from large electrodes. *Methods Med Res*, 9:405–32, 1961.
- [15] M Brett, IS Johnsrude, and AM Owen. The problem of functional localization in the human brain. *Nat.Rev.Neurosci.*, 3:243–249, 2002.
- [16] A. Brovelli, J. P. Lachaux, P. Kahane, and D. Boussaoud. High gamma frequency oscillatory activity dissociates attention from intention in the human premotor cortex. *Neuroimage*, 28(1):154–64, 2005.
- [17] Ed. C. Surya. *Proceedings of the 15th International Conference on noise in Physical Systems and 1/f Fluctuations*. IEEE Proceedings. 1999.
- [18] R. T. Canolty, E. Edwards, S. S. Dalal, M. Soltani, S. S. Nagarajan, H. E. Kirsch, M. S. Berger, N. M. Barbaro, and R. T. Knight. High gamma power is phase-locked to theta oscillations in human neocortex. *Science*, 313(5793):1626–8, 2006.
- [19] M. Cassidy, P. Mazzone, A. Oliviero, A. Insola, P. Tonali, V. Di Lazzaro, and P. Brown. Movement-related changes in synchronization in the human basal ganglia. *Brain*, 125(Pt 6):1235–46, 2002.
- [20] P. D. Cheney and E. E. Fetz. Corticomotoneuronal cells contribute to long-latency stretch reflexes in the rhesus monkey. *J Physiol*, 349:249–72, 1984.
- [21] Y. Cheng, A. N. Meltzoff, and J. Decety. Motivation modulates the activity of the human mirror-neuron system. *Cereb Cortex*, 17(8):1979–86, 2007.
- [22] S. Chitoku, H. Otsubo, Y. Harada, V. Jay, J. T. Rutka, S. K. Weiss, M. Abdoll, and 3rd Snead, O. C. Extraoperative cortical stimulation of motor function in children. *Pediatr Neurol*, 24(5):344–50, 2001.

- [23] A Clauset and et. al. Power-law distributions in empirical data. *arXiv: 0706.1062*.
- [24] S. Cochin, C. Barthelemy, S. Roux, and J. Martineau. Observation and execution of movement: similarities demonstrated by quantified electroencephalography. *Eur J Neurosci*, 11(5):1839–42, 1999.
- [25] CL; Peters TM; Evans AC Collins, DL; Holmes. Automatic 3-d model-based neuroanatomical segmentation. *Hum Brain Mapp*, 3(3):190–208, 1995.
- [26] D. L. Collins, P. Neelin, T. M. Peters, and A. C. Evans. Automatic 3d intersubject registration of mr volumetric data in standardized talairach space. *J Comput Assist Tomogr*, 18(2):192–205, 1994.
- [27] N. E. Crone. Functional mapping with ecog spectral analysis. *Adv Neurol*, 84:343–51, 2000.
- [28] N. E. Crone, D. L. Miglioretti, B. Gordon, and R. P. Lesser. Functional mapping of human sensorimotor cortex with electrocorticographic spectral analysis. ii. event-related synchronization in the gamma band. *Brain*, 121 (Pt 12):2301–15, 1998.
- [29] N. E. Crone, D. L. Miglioretti, B. Gordon, J. M. Sieracki, M. T. Wilson, S. Uematsu, and R. P. Lesser. Functional mapping of human sensorimotor cortex with electrocorticographic spectral analysis. i. alpha and beta event-related desynchronization. *Brain*, 121 (Pt 12):2271–99, 1998.
- [30] N.E. et al. Crone. Electrocorticographic gamma activity during word production in spoken and sign language. *Neurology*, 57:2045–2053.
- [31] N.E. et al. Crone. High-frequency gamma oscillations and human brain mapping with electrocorticography. *Prog Brain Res*, 159:275–295.
- [32] AM Dale, B Fischl, and MI Sereno. Cortical surface-based analysis. i. segmentation and surface reconstruction. *Neuroimage*, 9:179–194, 1999.
- [33] P Dayan and LF Abbot. *Theoretical Neuroscience*. MIT Press, 2001.
- [34] M. P. Deiber, V. Ibanez, M. Honda, N. Sadato, R. Raman, and M. Hallett. Cerebral processes related to visuomotor imagery and generation of simple finger movements studied with positron emission tomography. *Neuroimage*, 7(2):73–85, 1998.
- [35] Marcel den Nijs. Growth in scale invariance. *APCTP Bulletin*, 3:18–23.

- [36] A. Destexhe, D. Contreras, and M. Steriade. Mechanisms underlying the synchronizing action of corticothalamic feedback through inhibition of thalamic relay cells. *J Neurophysiol*, 79(2):999–1016, 1998.
- [37] H. C. Dijkerman, M. Ietswaart, M. Johnston, and R. S. MacWalter. Does motor imagery training improve hand function in chronic stroke patients? a pilot study. *Clin Rehabil*, 18(5):538–49, 2004.
- [38] E. Edwards, M. Soltani, L.Y. Deouell, and R.T. Berger, M.S. and Knight. High gamma activity in response to deviant auditory stimuli recorded directly from human cortex. *J Neurophysiol*, 94:4269–4280.
- [39] Gerwin Schalk Rajesh P.N. Rao Eric C. Leuthardt, K. J. Miller and Jeffrey G. Ojemann. "electrocorticography-based brain computer interface - the seattle experience.". *IEEE Trans Neural Syst Rehabil Eng*, 2006.
- [40] E. V. Evarts. Motor cortex reflexes associated with learned movement. *Science*, 179(72):501–3, 1973.
- [41] B. Feige, K. Scheffler, F. Esposito, F. Di Salle, J. Hennig, and E. Seifritz. Cortical and subcortical correlates of electroencephalographic alpha rhythm modulation. *J Neurophysiol*, 93(5):2864–72, 2005.
- [42] E. A. Felton, J. A. Wilson, J. C. Williams, and P. C. Garell. Electrocorticographically controlled brain-computer interfaces using motor and sensory imagery in patients with temporary subdural electrode implants. report of four cases. *J Neurosurg*, 106(3):495–500, 2007.
- [43] E. E. Fetz. Operant conditioning of cortical unit activity. *Science*, 163(870):955–8, 1969.
- [44] G. Foffani, A. M. Bianchi, G. Baselli, and A. Priori. Movement-related frequency modulation of beta oscillatory activity in the human subthalamic nucleus. *J Physiol*, 568(Pt 2):699–711, 2005.
- [45] LR Fortney. *Principles of electronics: analog and digital*. Oxford University Press, New York, 1987.
- [46] Mick Fox and Angela Uecker. Talairach daemon client. <http://ric.uthscsa.edu/projects/talairachdaemon.html>. *Neuroimage*, 2005.

- [47] P. T. Fox, J. S. Perlmutter, and M. E. Raichle. A stereotactic method of anatomical localization for positron emission tomography. *J Comput Assist Tomogr*, 9(1):141–53, 1985.
- [48] KJ Friston, RE Passingham, JG Nutt, JD Heather, GV Sawle, and RS Frackowiak. Localisation in pet images: direct fitting of the intercommissural (ac-pc) line. *J.Cereb.Blood Flow Metab*, 9:690–695, 1989.
- [49] H. Gastaut. [electrocorticographic study of the reactivity of rolandic rhythm.]. *Rev Neurol (Paris)*, 87(2):176–82, 1952.
- [50] A. P. Georgopoulos, J. F. Kalaska, R. Caminiti, and J. T. Massey. Interruption of motor cortical discharge subserving aimed arm movements. *Exp Brain Res*, 49(3):327–40, 1983.
- [51] B. Graimann, J. E. Huggins, S. P. Levine, and G. Pfurtscheller. Visualization of significant erd/ers patterns in multichannel eeg and ecog data. *Clin Neurophysiol*, 113(1):43–7, 2002.
- [52] F. Grenier, I. Timofeev, and M. Steriade. Focal synchronization of ripples (80-200 hz) in neocortex and their neuronal correlates. *J Neurophysiol*, 86:1884–98.
- [53] C. Guger, H. Ramoser, and G. Pfurtscheller. Real-time eeg analysis with subject-specific spatial patterns for abrain-computer interface (bci). *IEEE, TNSRE*, 8(4):447–456.
- [54] M.M. Haglund, M.S. Berger, M. Shamseldin, E. Lettich, and G.A. Ojemann. Cortical localization of temporal lobe language sites in patients with gliomas. *Neurosurgery*, 34:567–576.
- [55] U. Halsband and R. K. Lange. Motor learning in man: a review of functional and clinical studies. *J Physiol Paris*, 99(4-6):414–24, 2006.
- [56] M Hamalainen, R Hari, Risto J. Ilmoniemi, Jukka Knuutila, and Olli V. Lounasmaa. Magnetoencephalographytheory, instrumentation, and applications to noninvasive studies of the working human brain. *Rev. Mod. Phys.*, 65:413–497.
- [57] Hann. *In: The Measurement of Power Spectra, From the Point of View of Communications Engineering*. Dover, New York, 1959.
- [58] L. R. Hochberg, M. D. Serruya, G. M. Friehs, J. A. Mukand, M. Saleh, A. H. Caplan, A. Branner, D. Chen, R. D. Penn, and J. P. Donoghue. Neuronal ensemble control of prosthetic devices by a human with tetraplegia. *Nature*, 442(7099):164–71, 2006.

- [59] C.J. Holmes, R. Hoge, L. Collins, R. Woods, A.W. Toga, and A.C. Evans. Enhancement of magnetic resonance images using registration for signal averaging. *J. Comp. Asst. Tomograph.*, 22(2):324–333, 1998.
- [60] N. Hoogenboom, J. M. Schoffelen, R. Oostenveld, L. M. Parkes, and P. Fries. Localizing human visual gamma-band activity in frequency, time and space. *Neuroimage*, 29(3):764–73, 2006.
- [61] T. Hoshida and T. Sakaki. [functional brain mapping detected by cortical stimulation using chronically implanted subdural electrodes: basic knowledge of clinical nerve physiology for neurosurgeons]. *No Shinkei Geka*, 31(7):811–8; discussion 818–9, 2003.
- [62] S. Hotz-Boendermaker, M. Funk, P. Summers, P. Brugger, M. C. Hepp-Reymond, A. Curt, and S. S. Kollias. Preservation of motor programs in paraplegics as demonstrated by attempted and imagined foot movements. *Neuroimage*, 39(1):383–94, 2008.
- [63] A Hyvrinen and E Oja. Independent component analysis: algorithms and applications. *Neural Netw.*, 13(4-5):411–430.
- [64] A Jackson, R. L. Spinks, T. C. B. Freeman, D. M. Wolpert, and R. N. Lemon. Rhythm generation in monkey motor cortex explored using pyramidal tract stimulation. *J. Physiology*, 541(3):685–699, 2002.
- [65] J. Jarvelainen, M. Schurmann, and R. Hari. Activation of the human primary motor cortex during observation of tool use. *Neuroimage*, 23(1):187–92, 2004.
- [66] Herbert Jasper and Wilder Penfield. Electrocorticograms in man: Effect of voluntary movement upon the electrical activity of the precentral gyrus. *European Archives of Psychiatry and Clinical Neuroscience*, 183(1-2):163–174, 1949.
- [67] M. Jeannerod and V. Frak. Mental imaging of motor activity in humans. *Curr Opin Neurobiol*, 9(6):735–9, 1999.
- [68] J. Kaiser and W. Lutzenberger. Human gamma-band activity: a window to cognitive processing. *Neuroreport*, 16:207–211.
- [69] ER Kandel, JH Schwartz, and TM Jessell. *Principles of Neural Science*. McGraw-Hill, Norwalk, CT, 2000.
- [70] N Kanwisher, J McDermott, and MM. Chun. The fusiform face area: a module in human extrastriate cortex specialized for face perception. *J. Neurosci.*, 17:4302–4311, 1997.

- [71] G.E. Keles and et. al. Intraoperative subcortical stimulation mapping for hemispherical peritumoral gliomas located within or adjacent to the descending motor pathways: evaluation of morbidity and assessment of functional outcome in 294 patients. *J Neurosurg*, 100:369–375.
- [72] P. R. Kennedy and R. A. Bakay. Restoration of neural output from a paralyzed patient by a direct brain connection. *Neuroreport*, 9(8):1707–11, 1998.
- [73] C Koch. *Biophysics of Computation: Information Processing in Single Neurons*. Oxford University Press, 1999.
- [74] A. Kostov and M. Polak. Parallel man-machine training in development of eeg-based cursor control. *IEEE Trans Rehabil Eng*, 8(2):203–5, 2000.
- [75] D Kovalev, J Spreer, J Honegger, J Zentner, A Schulze-Bonhage, and HJ. Huppertz. Rapid and fully automated visualization of subdural electrodes in the presurgical evaluation of epilepsy patients. *Am.J.Neuroradiol.*, 26:1078–1083,.
- [76] P Kwan and MJ. Brodie. Early identification of refractory epilepsy. *N.Engl.J.Med.*, 342:314–319.
- [77] J. P. Lachaux, N. George, C. Tallon-Baudry, J. Martinerie, L. Hugueville, L. Minotti, P. Kahane, and B. Renault. The many faces of the gamma band response to complex visual stimuli. *Neuroimage*, 25(2):491–501, 2005.
- [78] JL Lancaster, PT Fox, H Downs, DS Nickerson, TA Hander, M El Mallah, PV Kochunov, and F. Zamarripa. Global spatial normalization of human brain using convex hulls. *J.Nucl.Med.*, 40:942–955.
- [79] S. Lemm, B. Blankertz, G. Curio, and K. R. Muller. Spatio-spectral filters for improving the classification of single trial eeg. *IEEE Trans Biomed Eng*, 52(9):1541–8, 2005.
- [80] R Lesser, B Gordon, R Fisher, J Hart, and S. Uematsu. Subdural grid electrodes in surgery of epilepsy. in Luders H, editor. *Epilepsy Surgery*. Raven Press: New York, 40:399–408.
- [81] Anderson Schalk Dowling Moran Ojemann Leuthardt, Miller. Electrographic frequency alteration mapping (efam), a novel clinical technique for mapping motor cortex. *Neurosurgery*, in print, 2006.

- [82] E. C. Leuthardt, K. J. Miller, G. Schalk, R. P. Rao, and J. G. Ojemann. Electro-corticography-based brain computer interface—the seattle experience. *IEEE Trans Neural Syst Rehabil Eng*, 14(2):194–8, 2006.
- [83] E. C. Leuthardt, G. Schalk, J. R. Wolpaw, J. G. Ojemann, and D. W. Moran. A brain-computer interface using electrocorticographic signals in humans. *J Neural Eng*, 1(2):63–71, 2004.
- [84] S. P. Levine, J. E. Huggins, S. L. BeMent, R. K. Kushwaha, L. A. Schuh, E. A. Passaro, M. M. Rohde, and D. A. Ross. Identification of electrocorticogram patterns as the basis for a direct brain interface. *J Clin Neurophysiol*, 16(5):439–47, 1999.
- [85] N. K. Logothetis, J. Pauls, M. Augath, T. Trinath, and A. Oeltermann. Neurophysiological investigation of the basis of the fmri signal. *Nature*, 412(6843):150–7, 2001.
- [86] F. H. Lopes da Silva. Neural mechanisms underlying brain waves: from neural membranes to networks. *Electroenceph clin Neurophysiol*, 79:81–93, 1991.
- [87] J. F. Marsden, K. J. Werhahn, P. Ashby, J. Rothwell, S. Noachtar, and P. Brown. Organization of cortical activities related to movement in humans. *J Neurosci*, 20(6):2307–14, 2000.
- [88] D. J. McFarland, L. A. Miner, T. M. Vaughan, and J. R. Wolpaw. Mu and beta rhythm topographies during motor imagery and actual movements. *Brain Topogr*, 12(3):177–86, 2000.
- [89] K. J. Miller, T. Blakeley, G. Schalk, R. P. Rao, and J. G. Ojemann. Three cases of feature correlation in an electrocorticographic bci. *IN SUBMISSION*, 2008.
- [90] K. J. Miller, M. denNijs, P. Shenoy, J. W. Miller, R. P. Rao, and J. G. Ojemann. Real-time functional brain mapping using electrocorticography. *Neuroimage*, 37(2):504–7, 2007.
- [91] K J Miller and et. al. Cortical surface localization from x-ray and simple mapping for electrocorticographic research: The location on cortex (loc) package for matlab. *Journal of Neuroscience Methods*, submitted fall 2006.
- [92] K. J. Miller, E. C. Leuthardt, G. Schalk, R. P. Rao, N. R. Anderson, D. W. Moran, J. W. Miller, and J. G. Ojemann. Spectral changes in cortical surface potentials during motor movement. *J Neurosci*, 27(9):2424–32, 2007.

- [93] K. J. Miller, S. Makeig, A. O. Hebb, R. P. Rao, M. denNijs, and J. G. Ojemann. Cortical electrode localization from x-rays and simple mapping for electrocorticographic research: The "location on cortex" (loc) package for matlab. *J Neurosci Methods*, 162(1-2):303–8, 2007.
- [94] K. J. Miller, P. Shenoy, M. den Nijs, L. B. Sorensen, R. N. Rao, and J. G. Ojemann. Beyond the gamma band: the role of high-frequency features in movement classification. *IEEE Trans Biomed Eng*, 55(5):1634–7, 2008.
- [95] K. J. Miller, L. B. Sorensen, J. G. Ojemann, and M. den Nijs. Ecog observations of power-law scaling in the human cortex. *In Review (pre-print available at arxiv.org)*, 2008.
- [96] K. J. Miller, S. Zanos, E. E. Fetz, M. den Nijs, and J. G. Ojemann. Decoupling the cortical power spectrum reveals individual finger representation in humans. *In Submission*, 2008.
- [97] K.J. Miller. Hodgkin-huxley model in appendix. *SfN meeting*.
- [98] B. Modayur, J. Prothero, G. Ojemann, K. Maravilla, and J. Brinkley. Visualization-based mapping of language function in the brain. *Neuroimage*, 6(4):245–58, 1997.
- [99] S Murakami and Y Okada. Contributions of principal neocortical neurons to magnetoencephalography and electroencephalography signals. *J. Physiol.*, 575(3):925–936.
- [100] S. M. Murphy. Imagery interventions in sport. *Med Sci Sports Exerc*, 26(4):486–94, 1994.
- [101] E. Neidermeyer. Electroencephalography: basic principles, clinical applications and related fields. page 149173. Williams and Wilkins, Baltimore, 4th edition, 1999.
- [102] C. Neuper and G. Pfurtscheller. Post-movement synchronization of beta rhythms in the eeg over the cortical foot area in man. *Neurosci Lett*, 216(1):17–20, 1996.
- [103] C. Neuper, R. Scherer, M. Reiner, and G. Pfurtscheller. Imagery of motor actions: differential effects of kinesthetic and visual-motor mode of imagery in single-trial eeg. *Brain Res Cogn Brain Res*, 25(3):668–77, 2005.
- [104] C. Neuper, M. Wortz, and G. Pfurtscheller. Chapter 14 erd/ers patterns reflecting sensorimotor activation and deactivation. *Prog Brain Res*, 159:211–22, 2006.

- [105] P. L. Nunez, B. M. Wingeier, and R. B. Silberstein. Spatial-temporal structures of human alpha rhythms: theory, microcurrent sources, multiscale measurements, and global binding of local networks. *Hum Brain Mapp*, 13(3):125–64, 2001.
- [106] Paul L. Nunez and Brian A. Cutillo. *Neocortical dynamics and human EEG rhythms*. Oxford University Press, New York, 1995.
- [107] AH Nuttall. Some windows with very good sidelobe behavior,. *IEEE Transactions on Acoustics, Speech, and Signal Processing*, 29(1):84–91, 1981.
- [108] S. Ohara, A. Ikeda, T. Kunieda, S. Yazawa, K. Baba, T. Nagamine, W. Taki, N. Hashimoto, T. Mihara, and H. Shibasaki. Movement-related change of electrocorticographic activity in human supplementary motor area proper. *Brain*, 123 (Pt 6):1203–15, 2000.
- [109] G. Ojemann, J. Ojemann, E. Lettich, and M. Berger. Cortical language localization in left, dominant hemisphere. an electrical stimulation mapping investigation in 117 patients. *J Neurosurg*, 71(3):316–26, 1989.
- [110] G. A. Ojemann. Models of the brain organization for higher integrative functions derived with electrical stimulation techniques. *Hum Neurobiol*, 1(4):243–9, 1982.
- [111] J. G. Ojemann, E. C. Leuthardt, and K. J. Miller. Brain-machine interface: Restoring neurological function through bioengineering. *Clin Neurosurg*, 54(28), 2007.
- [112] S. J. Page, P. Levine, and A. Leonard. Mental practice in chronic stroke: results of a randomized, placebo-controlled trial. *Stroke*, 38(4):1293–7, 2007.
- [113] B Pakkenberg, D Pelvig, and L et al. Marner. Aging and the human neocortex. *Exp Gerontol*, 38:95–99.
- [114] G. Paradiso, D. Cunic, J. A. Saint-Cyr, T. Hoque, A. M. Lozano, A. E. Lang, and R. Chen. Involvement of human thalamus in the preparation of self-paced movement. *Brain*, 127(Pt 12):2717–31, 2004.
- [115] W. Penfield and E. Boldrey. Somatic motor and sensory representation in the cerebral cortex of man as studied by electrical stimulation. *Brain*, 37:389443, 1937.
- [116] G. Pfurtscheller. Central beta rhythm during sensorimotor activities in man. *Electroencephalogr Clin Neurophysiol*, 51(3):253–64, 1981.

- [117] G. Pfurtscheller. *Event-Related Desynchronization (ERD) and Event Related Synchronization (ERS)*. Electroencephalography: Basic Principles, Clinical Applications and Related Fields. Williams and Wilkins, Baltimore, 1999.
- [118] G. Pfurtscheller. Spatiotemporal erd/ers patterns during voluntary movement and motor imagery. *Suppl Clin Neurophysiol*, 53:196–8, 2000.
- [119] G. Pfurtscheller. Functional brain imaging based on erd/ers. *Vision Res*, 41(10-11):1257–60, 2001.
- [120] G. Pfurtscheller, C. Brunner, A. Schlogl, and F. H. Lopes da Silva. Mu rhythm (de)synchronization and eeg single-trial classification of different motor imagery tasks. *Neuroimage*, 2006.
- [121] G. Pfurtscheller, B. Graimann, J. E. Huggins, S. P. Levine, and L. A. Schuh. Spatiotemporal patterns of beta desynchronization and gamma synchronization in corticographic data during self-paced movement. *Clin Neurophysiol*, 114(7):1226–36, 2003.
- [122] G. Pfurtscheller and F. H. Lopes da Silva. Event-related eeg/meg synchronization and desynchronization: basic principles. *Clin Neurophysiol*, 110(11):1842–57, 1999.
- [123] G. Pfurtscheller, K. Zalaudek, and C. Neuper. Event-related beta synchronization after wrist, finger and thumb movement. *Electroencephalogr Clin Neurophysiol*, 109(2):154–60, 1998.
- [124] C. G. Phillips and R. Porter. The pyramidal projection to motoneurons of some muscle groups of the baboon's forelimb. *Prog Brain Res*, 12:222–45, 1964.
- [125] C. G. Phillips and R. Porter. Corticospinal neurones. their role in movement. *Monogr Physiol Soc*, (34):v–xii, 1–450, 1977.
- [126] C. A. Porro, M. P. Francescato, V. Cettolo, M. E. Diamond, P. Baraldi, C. Zuiani, M. Bazzocchi, and P. E. di Prampero. Primary motor and sensory cortex activation during motor performance and motor imagery: a functional magnetic resonance imaging study. *J Neurosci*, 16(23):7688–98, 1996.
- [127] G Rajkowska and PS. Goldman-Rakic. Cytoarchitectonic definition of prefrontal areas in the normal human cortex: Ii. variability in locations of areas 9 and 46 and relationship to the talairach coordinate system. *Cereb.Cortex*, 5:323–337.

- [128] B Razavi. *Design of Analog CMOS Integrated Circuits (Chapter 7: Noise)*. New York, 2000.
- [129] G. Rizzolatti and L. Craighero. The mirror-neuron system. *Annu Rev Neurosci*, 27:169–92, 2004.
- [130] M. M. Rohde, S. L. BeMent, J. E. Huggins, S. P. Levine, R. K. Kushwaha, and L. A. Schuh. Quality estimation of subdurally recorded, event-related potentials based on signal-to-noise ratio. *IEEE Trans Biomed Eng*, 49(1):31–40, 2002.
- [131] M. Roth, J. Decety, M. Raybaudi, R. Massarelli, C. Delon-Martin, C. Segebarth, S. Morand, A. Gemignani, M. Decorps, and M. Jeannerod. Possible involvement of primary motor cortex in mentally simulated movement: a functional magnetic resonance imaging study. *Neuroreport*, 7(7):1280–4, 1996.
- [132] G. Schalk, J. Kubanek, K. J. Miller, N. R. Anderson, E. C. Leuthardt, J. G. Ojemann, D. Limbrick, D. Moran, L. A. Gerhardt, and J. R. Wolpaw. Decoding two-dimensional movement trajectories using electrocorticographic signals in humans. *J Neural Eng*, 4(3):264–75, 2007.
- [133] G. Schalk, D. J. McFarland, T. Hinterberger, N. Birbaumer, and J. R. Wolpaw. Bci2000: a general-purpose brain-computer interface (bci) system. *IEEE Trans Biomed Eng*, 51(6):1034–43, 2004.
- [134] G. Schalk, K. J. Miller, N. R. Anderson, J. A. Wilson, M. D. Smyth, J. G. Ojemann, D. W. Moran, J. R. Wolpaw, and E. C. Leuthardt. Two-dimensional movement control using electrocorticographic signals in humans. *J Neural Eng*, 5(1):75–84, 2008.
- [135] et. al. Scherer, R. Frequency component selection for an ecog-based brain-computer interface. *Biomed Tech (Berl)*, 48(1-2):31–36.
- [136] R. Scherer, B. Graimann, J. E. Huggins, S. P. Levine, and G. Pfurtscheller. Frequency component selection for an ecog-based brain-computer interface. *Biomed Tech (Berl)*, 48(1-2):31–6, 2003.
- [137] M. H. Schieber. Muscular production of individuated finger movements: the roles of extrinsic finger muscles. *J Neurosci*, 15(1 Pt 1):284–97, 1995.
- [138] M. H. Schieber. Constraints on somatotopic organization in the primary motor cortex. *J Neurophysiol*, 86(5):2125–43, 2001.

- [139] M. H. Schieber and L. S. Hibbard. How somatotopic is the motor cortex hand area? *Science*, 261(5120):489–92, 1993.
- [140] A. Schnitzler, S. Salenius, R. Salmelin, V. Jousmaki, and R. Hari. Involvement of primary motor cortex in motor imagery: a neuromagnetic study. *Neuroimage*, 6(3):201–8, 1997.
- [141] P. B. Sederberg, M. J. Kahana, M. W. Howard, E. J. Donner, and J. R. Madsen. Theta and gamma oscillations during encoding predict subsequent recall. *J Neurosci*, 23(34):10809–14, 2003.
- [142] N. Sharma, V. M. Pomeroy, and J. C. Baron. Motor imagery: a backdoor to the motor system after stroke? *Stroke*, 37(7):1941–52, 2006.
- [143] P. Shenoy, K. J. Miller, J. G. Ojemann, and R. P. Rao. Generalized features for electrocorticographic bcis. *IEEE Trans Biomed Eng*, 55(1):273–80, 2008.
- [144] Shepherd. *The Synaptic Organization of the Brain*. Oxford University Press, 1998.
- [145] Shepherd. *The Synaptic Organization of the Brain*. Oxford University Press, 1998.
- [146] Y. Shinoda, P. Zarzecki, and H. Asanuma. Spinal branching of pyramidal tract neurons in the monkey. *Exp Brain Res*, 34(1):59–72, 1979.
- [147] A. Sinai, C. W. Bowers, C. M. Crainiceanu, D. Boatman, B. Gordon, R. P. Lesser, F. A. Lenz, and N. E. Crone. Electrocorticographic high gamma activity versus electrical cortical stimulation mapping of naming. *Brain*, 128(Pt 7):1556–70, 2005.
- [148] J Talairach and P Tournoux. *Talairach: Co-planar stereotaxic atlas of the human brain*. Stuttgart: Thieme, 1988.
- [149] D. Tkach, J. Reimer, and N. G. Hatsopoulos. Congruent activity during action and action observation in motor cortex. *J Neurosci*, 27(48):13241–50, 2007.
- [150] M. A. Umiltà, E. Kohler, V. Gallese, L. Fogassi, L. Fadiga, C. Keysers, and G. Rizzolatti. I know what you are doing. a neurophysiological study. *Neuron*, 31(1):155–65, 2001.
- [151] Y. D. Van Der Werf, A. F. Sadikot, A. P. Strafella, and T. Paus. The neural response to transcranial magnetic stimulation of the human motor cortex. ii. thalamocortical contributions. *Exp Brain Res*, 175(2):246–55, 2006.

- [152] J Wellmer, J von Oertzen, C Schaller, H Urbach, R Konig, G Widman, D Van Roost, and CE Elger. Digital photography and 3d mri-based multimodal imaging for individualized planning of resective neocortical epilepsy surgery. *Epilepsia*, 43:1543–1550.
- [153] J. A. Wilson, E. A. Felton, P. C. Garell, G. Schalk, and J. C. Williams. Ecog factors underlying multimodal control of a brain-computer interface. *IEEE Trans Neural Syst Rehabil Eng*, 14(2):246–50, 2006.
- [154] J. R. Wolpaw, N. Birbaumer, D. J. McFarland, G. Pfurtscheller, and T. M. Vaughan. Brain-computer interfaces for communication and control. *Clin Neurophysiol*, 113(6):767–91, 2002.
- [155] J. R. Wolpaw and D. J. McFarland. Control of a two-dimensional movement signal by a noninvasive brain-computer interface in humans. *Proc Natl Acad Sci U S A*, 101(51):17849–54, 2004.
- [156] J. R. Wolpaw, D. J. McFarland, G. W. Neat, and C. A. Forneris. An eeg-based brain-computer interface for cursor control. *Electroencephalogr Clin Neurophysiol*, 78(3):252–9, 1991.
- [157] T. Womelsdorf, P. Fries, P. P. Mitra, and R. Desimone. Gamma-band synchronization in visual cortex predicts speed of change detection. *Nature*, 439(7077):733–6, 2006.
- [158] C. N. Woolsey, P. H. Settlage, D. R. Meyer, W. Sencer, T. Pinto Hamuy, and A. M. Travis. Patterns of localization in precentral and "supplementary" motor areas and their relation to the concept of a premotor area. *Res Publ Assoc Res Nerv Ment Dis*, 30:238–64, 1952.
- [159] J. M. Zacks, F. Gilliam, and J. G. Ojemann. Selective disturbance of mental rotation by cortical stimulation. *Neuropsychologia*, 41(12):1659–67, 2003.
- [160] J. M. Zacks, P. Michelon, J. M. Vettel, and J. G. Ojemann. Functional reorganization of spatial transformations after a parietal lesion. *Neurology*, 63(2):287–92, 2004.

Appendix A

**A SIMPLE, SPECTRAL-CHANGE BASED,
ELECTROCORTICOGRAPHIC BRAIN-COMPUTER INTERFACE**

Brain-computer interface (BCI) requires a strong, reliable signal for effective implementation. A wide range of real-time electrical signals have been used for BCI, ranging from scalp recorded electroencephalography (EEG) (see, for example, (Wolpaw, Birbaumer et al. 2002; Wolpaw and McFarland 2004)) to single neuron recordings (see, for example, (Kennedy and Bakay 1998; Hochberg, Serruya et al. 2006)). Electrocorticography (ECoG) is an intermediate measure, and refers to the recordings obtained directly from the surface of the brain(Ojemann, Leuthardt et al. 2007). Like EEG, ECoG represents a population measure, the electrical potential that results from the sum of the local field potentials resulting from 100,000s of neurons under a given electrode. However, ECoG is a stronger signal and is not susceptible to the artifacts from skin and muscle activity that can plague EEG recordings. ECoG and EEG also differ in that the phenomena they measure encompass fundamentally different scales. Because ECoG electrodes lie on the cortical surface, and because the dipole fields(Nunez and Cutillo 1995) which produce the cortical potentials fall off rapidly , the ECoG fundamentally reflects more local processes.

Currently, ECoG takes place in the context of clinical recording for the treatment of epilepsy. After implantation, patients recover in the hospital while they wait to have a seizure. Often, that requires a week or longer of observation, during which time patients may chose to participate in experiments relevant to using ECoG to drive BCI. Recently, researchers have used the spectral changes on the cortical surface of these patients to provide feedback, creating robust brain-computer interfaces, allowing individuals to control a cursor on a computer screen in a matter of minutes (Leuthardt, Schalk et al. 2004; Leuthardt, Miller et al. 2006; Wilson, Felton et al. 2006; Felton, Wilson et al. 2007; Schalk, Miller et

al. 2008). This chapter discusses the important elements in the construction of these ECoG based BCIs: signal acquisition, feature selection, feedback, and learning.

A.1 Signal acquisition

ECoG is available from frequently performed procedures in patients suffering from medically intractable epilepsy (Figure 1). Such patients undergo elective placement of electrodes on the surface of the brain when the seizure localization is not evident from non-invasive studies. These electrodes are also placed, in some situations, to localize function such as movement or language prior to a neurosurgical resection. The same electrodes can record ECoG and stimulate to evoke disruption in the function of the underlying cortex. The implanted electrode arrays are typically only those which would be placed for diagnostic clinical purposes. Most often, these are 2.5mm in diameter have a spacing of 1-cm from center-to-center (Figure 2). While this is somewhat coarse, it is fine enough to resolve individual finger representation and may be sufficient to extract many independent control signals simultaneously (Miller, Zanos et al. 2008). At some institutions, preliminary results are coming out using smaller electrodes and higher resolution arrays (Blakeley, Miller et al. 2008), and it may become apparent that finer resolution grids produce resolve independent function and intention better than the current clinical standard. Intra-operative photographs, showing the arrays in-situ can be useful for identifying which electrodes are on gyri, sulci, and vasculature, and also which are near known cortical landmarks. . The ECoG recording is, by necessity, in the context of clinical amplification and recording, so the experimental recording must take place in the context of clinical amplification with commercially available amplifiers (eg, XLTEK, Synamps, GugerTech, Grass). Most clinically relevant EEG findings are detected visually and classically the information explored is between 3-40Hz, so the settings on the clinical amplifiers may be adequate to obtain clinical information, but not for research purposes. Recent advances have suggested that faster frequencies may be clinically relevant so many newer systems include higher sampling rate (at least 1kHz) as an option to allow for measurement of signals of 200Hz or higher, but this varies by institution,

and the clinical recording settings will vary even within institutions, depending upon the clinical and technical staff managing the patient. Experimentalists must obtain either the clinically amplified signal, or split the signal and amplify it separately. Using the clinical signal has the advantage that less hardware is involved, and that there are no potential complications because of the dual-amplification process. Such complications include artifact/noise introduction from one system to the other, currents between separate grounds if the two do not share a common ground. Splitting the signal has the advantage that the experimentalist can use higher fidelity amplifiers and set the amplification parameters at will, rather than having to use the clinical parameters, which typically sample at a lower frequency than one would like, and often have built in filtering properties which limit the usable frequency range. The ground chosen, which must be the same as the clinical ground to avoid complication, will typically be from the surface of the scalp. Most amplifiers will have a built in choice of reference, which each electrode in the array will be measured with respect to. These may also be from the scalp, as they often are clinically, or they may be from an intra-cranial electrode.

The experimenter will often find it useful to re-reference the electrode array in one of several ways. Each electrode may be re-referenced with respect to a single electrode from within the array, chosen because it is relatively “dormant,” each may be re-referenced to a global linear combination of electrodes from the entire array, or each may be referenced to one or more nearest neighbors. Re-referencing with respect to a single electrode is useful when the one in the experimental/clinical montage is sub-optimal (noisy, varies with task, etc), but it means that the experimenter has introduced an assumption about which electrode is, in fact, appropriate. The simplest global referencing is a common average re-reference: the average of all electrodes is subtracted from each electrode. The advantage of this is that it is generic (unbiased, not tied to an assumption), and it will get rid of common-mode phenomena. One must be careful that there are not any electrodes that are broken, or have extremely large contamination, or every electrode will be contaminated by the re-referencing process. Local re-referencing may also be performed, such as subtracting

the average of nearest-neighbors (Laplacian), which ensures that the potential changes seen in any electrode are spatially localized. One may also re-reference in a pair-wise fashion, producing bipolar channels which are extremely local, but phenomena cannot be tied to a specific electrode from the pair.

Choosing a sampling frequency is important - there is often a trade-off between signal fidelity and the practical issues of manageable data sizes and hardware limitations. Whatever sampling rate is chosen, one should be sure to have high signal fidelity up to at least 150Hz (ie. Sampling rate should be above 300 Hz. The sampling rate may have to be higher if the amplifiers used have built in filtering properties.) The reason for this is that there is a behavioral split in the power spectrum which can be as high as 60 Hz (Miller, Shenoy et al. 2008). In order to capture the spatially focal high frequency change, one must have large bandwidth above this behavioral split.

A.2 Feature Selection

In order to implement a BCI paradigm, a specific signal feature must be chosen. This will need to be a feature that can be determined in a computationally rapid fashion. Second, the feature must be translated into a specific output. The choice of signal feature should be an empiric one. There are two complementary approaches to choosing a BCI feature. One approach is to start with a strictly defined task, such as hand movement, and look for a particular feature at the signal change associated with this task. Then, the most reliable signal is identified and used to run a BCI. Another approach is to choose a signal that is less well characterized behaviorally and then, over time, to allow the subject to learn to control the feature by exploiting feedback, and then control the BCI. In a dramatic example of the latter, it was found that the spike rate from an arbitrary neuron that grew into a glass cone could be trained to run BCI (Kennedy and Bakay 1998), with no a priori knowledge about the preferred behavioral tuning of the given neuron.

The most straightforward approach is a motor imagery-based, strictly defined, task-related change for feature control. In order to identify appropriate simple features to couple

to device control, a set of screening tasks is performed. In these screening tasks, the subject is cued to move or imagine (kinesthetically) moving a given body part for several seconds and then cued to rest for several seconds (Miller, Leuthardt et al. 2007). Repetitive movement has been found to be useful in generating robust change because cortical activity during tonic contraction is quickly attenuated (Crone, Miglioretti et al. 1998; Crone, Miglioretti et al. 1998). Different movement types should be interleaved, so that the subject does not anticipate the onset of each movement cue. Of course, there are multiple forms of motor imagery. One can imagine what the movement looks like, one can imagine what the movement feels like, and one can imagine the action of making the muscular contractions which produce the movement (kinesthetic) (Neuper, Scherer et al. 2005). It was demonstrated by Neuper, et. al. (Neuper, Scherer et al. 2005) that kinesthetic imagery produces the most robust cortical spectral change, and, accordingly, we and others have used kinesthetic motor imagery as the paired modality for device control. In order to establish that the control signal is truly imagery, experimenters should exclude, by surface EMG and other methods, subtle motor movement as the underlying source of the spectral change. In the screening task, thirty to forty such movement/imagery cues for each movement/imagery type should be recorded in order to obtain robust statistics. The power spectral density during each of these cue and rest periods can be calculated for each electrode. "Feature maps" of statistically significant changes at each frequency, in each electrode, can be calculated by comparing rest and movement cues (see Figure 3). Figure 4 demonstrates how the cortical spectral changes in motor cortex show characteristic changes during movement of the opposite (contralateral) hand when compared to rest.

As with EEG, one feature-driven approach is to look across channels and frequency bands to obtain complex features for feedback (Leuthardt, Schalk et al. 2004; Wolpaw and McFarland 2004; Leuthardt, Miller et al. 2006; Schalk, Miller et al. 2008). This can be done manually, selecting spectral features from intuitive cortical areas, such as sensorimotor cortex. It can also be done using naive, blind-source deconvolution and machine learning techniques (Grimann, Huggins et al. 2002; Pfurtscheller, Grimann et al. 2003; Scherer,

Graimann et al. 2003; Lemm, Blankertz et al. 2005; Blankertz, Dornhege et al. 2007; Muller, Tangermann et al. 2008; Shenoy, Miller et al. 2008). Sophisticated recombination techniques, optimized for an offline screening task, face the potential confound that the resulting mapping is not intuitive for subject control, particularly if the distribution of cortical spectral change is different for screening than it is for feedback studies (which it can be). Simple features, in contrast, may be employing only a fraction of the potential signal for the feedback task, and also may suffer because the simple feature chosen is not the best out of a family of potential simple features. Our approach, which we describe in detail here, has been to keep feature selection as simple and straightforward as possible, and then examine how brain dynamics change, with feedback, over time. Future strategies will have to take both approaches into account.

Adaptive feature techniques, which dynamically change the parameterization between brain signal and feedback, represent another approach, where the machine iteratively 'learns' the signals that the subject is attempting to use during the BCI task. The potential advantage of such adaptive techniques is that they might be robust against non-stationarity in the distribution of cortical spectral change and compensate for shifts in the signal. The disadvantage is that a subject may be trying to adapt the signal at least as fast as the machine algorithm, and we have at times found a negative feedback between these processes. If the brain dynamics are trying to converge on given parameterization, and the adaptive algorithm is continuously changing the parameterization, there is the potential that no stable interface can be converged upon. Recent ECoG studies, however, have demonstrated that, for a simple ECoG BCI, stable control can be maintained for many consecutive days without any change in the feedback feature parameters(Blakeley, Miller et al. 2008).

A.3 Feedback

The power in this identified feature, P , is then linked to the velocity, v , of a cursor on the computer screen, using the simple translation algorithm $P = k(v - v_0)^2$, where k is a power level somewhere between movement imagery and rest, and v_0 is a velocity parameter. This difference is then

coupled to the movement of a cursor, with speed determined by the parameter α , which can be adjusted in the beginning of the task to be comfortable to the subject.. The subject is instructed to adjust the position of the cursor so that it hits a target (figure 5). Modification of the imagery behavior is allowed, even encouraged, to maximize target accuracy.

Interestingly, even with the most robust signal features, once the behavior is linked to a different task (i.e., the subject is now aiming for a target not just performing the given movement) the electrocorticographic signal may change. We have used the concept of 're-screening' to make use of the fact that a given signal at a given electrode may be subtly or even dramatically different when the task condition is changed to include a BCI component (Figure 6).

For applications in patients with certain neurologic impairments, overt motor activity will, of course, not be accessible for a BCI device. Therefore, attempting to drive BCI with other features is of particular interest. The methods discussed here employ imagined movement and imagined speech to generate screening features. The areas of cortex engaged by, for example, imagined hand movement are remarkably similar to those involved in overt hand movement, though of much weaker strength (Figure 7A). Because of the weaker signal, initial control can be more difficult with an imagined task, however, the presence of cursor feedback reliably produces an enhancement of the ECoG signal resulting in improved performance. This remarkable ability to enhance the signal has been reported in different imagined motor tasks and silent speech (Miller, Ojemann et al. 2008).

In most circumstances, accuracy increases over time, usually within a few trials (Figure 7B, see (Leuthardt, Miller et al. 2006; Schalk, Miller et al. 2008)). BCI2000 allows for a recursive tuning of the weights of a given feature so that the program learns, based on the signal of correct and incorrect trials, what the ideal translation between feature and cursor position should be. However, subjects show a robust learning on their own - the brain is able to learn, as with any new motor task (riding a bike, etc) to subconsciously modify activity based on feedback. Taken to an extreme, this concept has allowed BCI to occur even when the behavior of the cortex underlying the chosen electrode is less well

defined(Wilson, Felton et al. 2006).

Though originally the cursor control is explicitly linked to the behavior, the subject is free to explore mental states that achieve better cursor control. Anecdotally, successful control often is associated with a wide range of experiential strategies. Some control evolves to being achieved with a throat sensation or, in the most striking example of behavioral plasticity, the subject simply imagines the cursor to move in the preferred direction, no longer using the originally prescribed behavior as an intermediate, as happened with the subject described in the case study at the end of this chapter.

A.4 Learning

In this particular paradigm, stability of signal is hard to determine given the primary purpose of the implants is clinical and the implant is removed once the seizure focus is determined. However, we have had occasion to assess the stability over multiple days in a 5 day, repeated testing region. Since the recording devices are on the brain, not fixed to it, one could imagine day-to-day variations in the signal. In fact, the use of ECoG appears to rely upon a population signal that is not overly sensitive to daily fluctuations(Blakeley, Miller et al. 2008) and the same features can be reused with minimal re-training required to achieve accurate cursor control.

In one dimensional experiment, the learning process is rapid (3-24mins, see (Leuthardt, Miller et al. 2006)). Though not always highly focal, we have observed cortical activity that increases with improved performance (Figure 7B). Anecdotally, this is associated with a psychological 'de-linking' of the screening behavior (e.g., hand movement imagery) and the cursor control, where the cursor gains some kind of abstract, tool-like, representation with the subject. Recent results (an example is illustrated in Figure 7C) have demonstrated efficacy using ECoG for two-dimensional control(Schalk, Miller et al. 2008). This requires two independent signals to drive the two degrees (typically up-down and left-right cursor position, as shown in figure 7C). The motor system allows for some intuitive, separable features, using, for example, hand and mouth, which are distinct when high-frequency

ECoG features are used (Miller, Leuthardt et al. 2007; Miller, Ojemann et al. 2008; Miller, Shenoy et al. 2008; Schalk, Miller et al. 2008). Despite success, simultaneous 2D control has been less robust than for one dimension. One reason for this is that it requires a good deal more mental coordination by the subject. For example, in this simple form of a 2D target task BCI, there is fundamental uncertainty in the null condition. When increased power in one channel drives the cursor up and a lack of power down, with increased power in another channel driving the cursor to the left, then weak power in both channels could be ambiguous when targeting a down or right sided target. It takes practice learning to coordinate the two null directions. Even if the signals are not overlapping during the screening for the two different tasks, when combined to achieve two-dimensional cursor control they may have some initial independence. Through feedback, however, these can be segregated by some individuals (Miller, Blakeley et al. 2008; Schalk, Miller et al. 2008).

A.5 Summary

ECoG provides robust signals that can be used in a BCI system. Using different kinds of motor imagery, subjects can volitionally control the cortical spectrum in multiple brain areas simultaneously. The experimenter can identify salient brain areas and spectral ranges using a cue based screening task. These different kinds of imagery can be coupled to the movement of a cursor on a screen in a feedback process. By coupling them first separately, and later in concert, the subject can learn to control multiple degrees of freedom simultaneously in a cursor based task.

Acknowledgements: Special thanks to Gerwin Schalk for his consistent availability and insight. The patients and staff at Harborview Medical Center contributed invaluable of their time and enthusiasm. Author support includes NSF 0130705 and NIH NS07144.

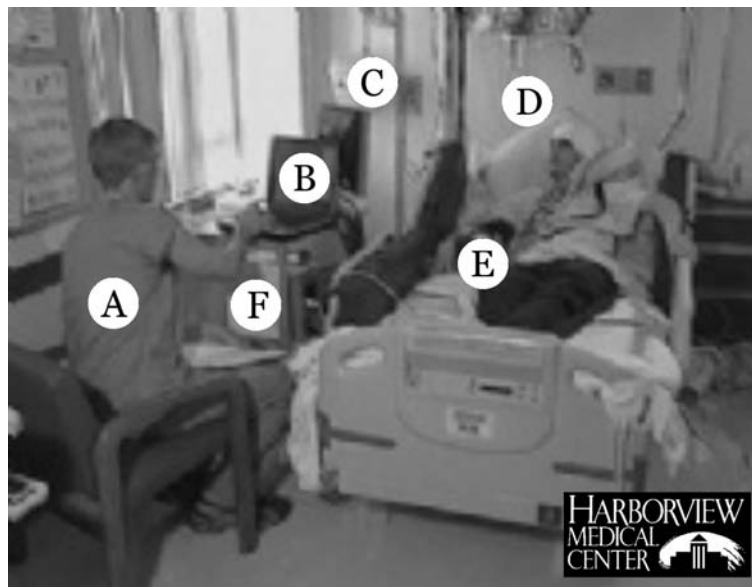


Figure A.1: *The necessary components of the electrocorticographic BCI experimental setting.*

(A) The experimenter. While this element may seem trivial or an afterthought, the individual who interacts with the subject, in the clinical setting, must have an agreeable disposition. There are several reasons for this. The first is that the subjects are patients in an extremely tenuous position, and it is important to encourage and reinforce them with genuine compassion. Not only is this a kind thing to do, but it is the difference between 10 minutes and 10 hours of experimental recording and participation. The second is that the hospital environment requires constant interaction with physicians, nurses, and technicians, and all of these individuals have responsibilities that take priority over the experimental process at any time. It is important to cultivate and maintain a sympathetic relationship with these individuals. The last reason is that the hospital room is not a controlled environment. There is non-stationary contamination, a clinical recording system to be managed in parallel, and constant interruption from a myriad of sources. The researcher must be able to maintain an even disposition and be able to constantly troubleshoot. **(B) A central computer.** This computer will be responsible for recording and processing the streaming

amplified potentials from the electrode array, translating the processed signal into a control signal, and displaying the control signal using an interface program. The computer must have a large amount of memory, to buffer the incoming data stream, a fast processor to perform signal processing in real-time and adequate hardware to present interface stimuli with precision. Therefore, it is important to have as powerful a system as possible, while remaining compact enough to be part of a portable system that can easily be brought in and out of the hospital room. An important element not shown in the picture is the software which reads the incoming datastream, computes the power spectral density changes, and uses these changes to dynamically change the visual display of an interface paradigm. We use the BCI2000 program (Schalk, McFarland et al. 2004) to do all of these things simultaneously. **(C) A second monitor.** It is a good idea to have a second monitor for stimulus presentation. It should be compact with good resolution. **(D) The subject.** It is important to make sure that the subject is in a comfortable, relaxed position. Not just because it's nice, but also because an uncomfortable subject will have extraneous sensorimotor phenomena in the cortex and also will not be able to focus on the task. **(E) Signal splitters.** If a second set of amplifiers (experimental or clinical) is being used in parallel with the clinical ones used for video monitoring, the signal will be split after leaving the scalp, and before the clinical amplifier jack-box. The ground must be split as well, and be common between both amplifiers, or else there is the potential for current to be passed between the two grounds. Several clinical systems have splitters built in to the clinical wire ribbons, and these should be used whenever possible. **(F) Amplifiers.** These will vary widely by institution, and, also depending on the institution, will have to have FDA approval (the process of obtaining FDA approval is associated with both higher cost and lower quality amplifiers). Many amplifier systems will have constrained samplerates (A/D rates), built in filtering properties, and large noise floors which obscure the signal at high frequencies. Regardless of which system is used, it is important to characterize the amplifiers independently using a function generator.



Figure A.2: *Co-registration of electrodes and plotting of data on template cortices.*

(A) Clinical schematic. A clinical schematic will typically be obtained from the surgeon. The position of each electrode may then be correlated with potential recordings from each amplifier channel. **(B) Diagnostic imaging.** Different diagnostic imaging may be obtained from the course of the clinical care, or through specially obtained high-fidelity experimental imaging. The level and quality of this may be highly variable across time and institutions, from x-ray only, to high-fidelity pre-operative magnetic resonance imaging (MRI) and post-operative fine-cut computed tomography (CT). **(C) Cortical electrode position reconstruction.** The clinical schemata and diagnostic imaging may be used in concert to estimate electrode positions, recreate cortical locations, and plot activity and analyses. The most simple method for doing this, using x-rays, is the freely-available LOC package (Miller, Makeig et al. 2007), although there is the promise of more sophisticated methodology for doing this, when higher fidelity diagnostic imaging is obtained.

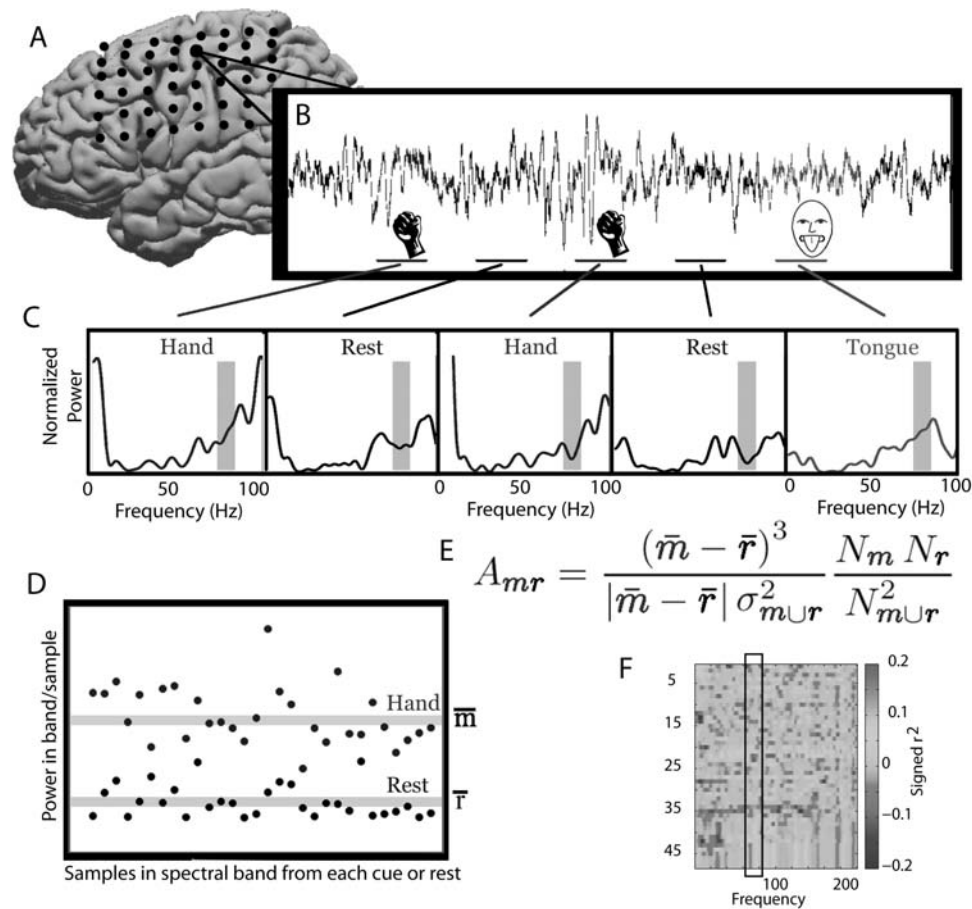


Figure A.3: Identifying areas of activity during simple tasks using cross-correlation

(A) Each electrode is treated independently, although generally it is a good idea to re-reference each electrode by subtracting the average timeseries from the time series of each electrode (common average re-referencing)(Miller, Leuthardt et al. 2007). (B) The potential is measured during a sequence of cues. Here, the cues are for hand and tongue movement in a screening task, with rest interleaved, but the process can also be used for online data, comparing periods where different targets were on the screen. (C) The normalized power spectral density (PSD) can be calculated for each cue (or target) period. This is done by calculating the raw power spectral density for each period, and

then dividing each by the average. A sample of the PSD of a specific range for each cue is used to compare cues of different types (one is shown here as the shaded bar in the back of each). **(D) Samples of band-limited PSDs** for cues of different type illustrate the difference in the distribution of hand movement samples and rest samples, in this example. **(E) Activation**, quantified using the square of the cross-correlation (r^2), signed to reflect whether the significance represents an increase or a decrease in the band-limited PSD for movement with respect to rest (or, in the case of a target task, whether one target represents an increase or decrease in power with respect to the other target). What this metric tells us is how much of the variation in the joint data set $\sigma_{m \cup r}^2$ can be accounted for by the fact sub-distributions m and r might have different means, m and r (N_m , and N_r , are the number of samples of type m , r , respectively, and $N_{m \cup r} = N_m + N_r$). **(F) "Feature maps" can tell us about which electrode-frequency combinations discriminate between cues.** We can calculate A_{mr} for each electrode, frequency band combination, to create feature maps of discriminative potential. When performed on a screening task with overt or covert movement cues, we can identify specific electrode-frequency power features as candidates for feedback.

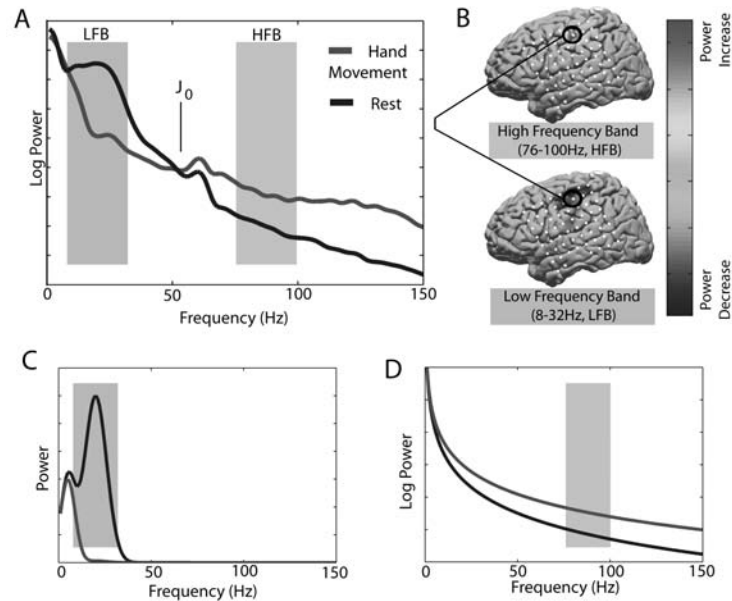


Figure A.4: Characteristic changes in the power spectrum with activity.

(A) **Example of a characteristic spectrum** that demonstrates the spectral shift between hand movement and rest for a task-specific electrode. There is a decrease in the power at lower frequencies with activity, and an increase in the power at higher frequencies (Crone, Miglioretti et al. 1998; Crone, Miglioretti et al. 1998; Aoki, Fetz et al. 1999; Miller, Leuthardt et al. 2007). The intersection in the spectrum dubbed the "primary junction" (J_0). In a recent study (Miller, Shenoy et al. 2008), involving hand and tongue movement, it was found that, for hand movement, $J_0 = 48 \pm 9$ Hz (mean \pm SD) (range 32-57Hz), and, for tongue movement, $J_0 = 40 \pm 8$ Hz (range 26-48Hz). Rather than this indicating two phenomena, a "desynchronization" at low frequencies, and a "synchronization" at high frequencies, as some have proposed (Crone, Miglioretti et al. 1998; Pfurtscheller, Graimann et al. 2003), this might instead reflect the superposition of the phenomena (Miller, Leuthardt et al. 2007), described in (C) and (D), that produce an intersection (J_0) in the power spectrum in the classic gamma range (shown shaded). Choices for feedback features should explicitly

avoid J_0 . The left shaded region is from 8 to 32Hz (LFB), and the right shaded region is from 76 to 100 Hz (HFB). **(B) Demonstration different spatial extent of changes in these high and low frequency ranges on the cortical surface.** The top cortical map shows the activation distribution for the HFB (here, reflecting an increase in spectral power with movement). The bottom map, for the LFB, shows a decrease in spectral power with movement over a broader set of electrodes. **(C) Decoherence of discrete peaks in the power spectrum with movement (ERD).** This is consistent with the classic event-related desynchronization at lower frequencies(Crone, Miglioretti et al. 1998; Pfurtscheller 1999; Miller, Leuthardt et al. 2007). **(D) Power-law like power spectrum that shifts upward with movement.** It is most easily observed at high frequencies because it is masked by peaked ERD at low frequencies. Recent findings have hypothesized and demonstrated that this power-law like process and the ERD may be decoupled from each other and that the power-law like process(Miller, Leuthardt et al. 2007; Miller, Sorensen et al. 2008; Miller, Zanos et al. 2008) may be used as an extremely good correlate of local activity, with extremely high (10-15ms) temporal precision(Miller, Zanos et al. 2008).

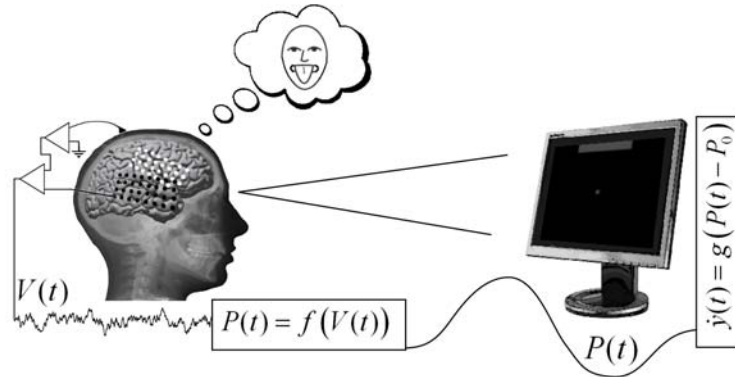


Figure A.5: Schematic representation of the closed-loop brain-computer interface that we use.

An individual performs movement imagery. The potential, $V(t)$, is measured from each electrode with respect to a ground, and amplified. The ground may come from the scalp, or from an internal ECoG electrode, but is dictated by the primary clinical system because of the necessity for a common ground between the two amplifiers. These potentials are then converted to an estimate of the power, in a specific range, at each point in time $P(t) = f(V(t))$. The function $f(t)$ will first use a window in time to calculate a power spectrum - a longer window will produce a better estimate of the spectrum, a shorter window will allow for a higher effective bitrate of the BCI, and the optimal window size will represent a tradeoff between the two (we typically use a quarter-second window). The power $P(t)$ will be chosen from a confined frequency range from the spectrum. It is important that the window length be significantly longer than the $(\text{lowest frequency used})^{-1}$, so that the lowest frequency used may be estimated with some accuracy. Papers that are submitted, and forget to do this, are rejected (really). The spectral estimation method used may be a Fourier Transform technique, or may be a parameterized estimation technique, like the autoregressive model method. Parameterized techniques have the potential advantage of better spectral estimation using shorter time windows, but the drawback that it can be hard to know how many parameters to use (model order), and that different model orders

can produce widely different results. We couple the power, $P(t)$, to the movement of a cursor in a given direction, according to the simple linear relation $\dot{y} = g(P(t) - P_0)$, where P_0 , is a power level somewhere between movement imagery and rest, determined from a screening task (as in Figure 3). This difference is then coupled to the movement of a cursor, with speed determined by the parameter g , which can be adjusted in the beginning of the task to be comfortable to the subject. The subject views changes in the cursor trajectory, and the subject then modifies the nature of the imagery to cause the cursor to move toward their target choice. After 8-10 minutes, in the 1-D task, subjects will abstract away from the imagery and are able to imagine the movement of the cursor itself and produce appropriate spectral changes.

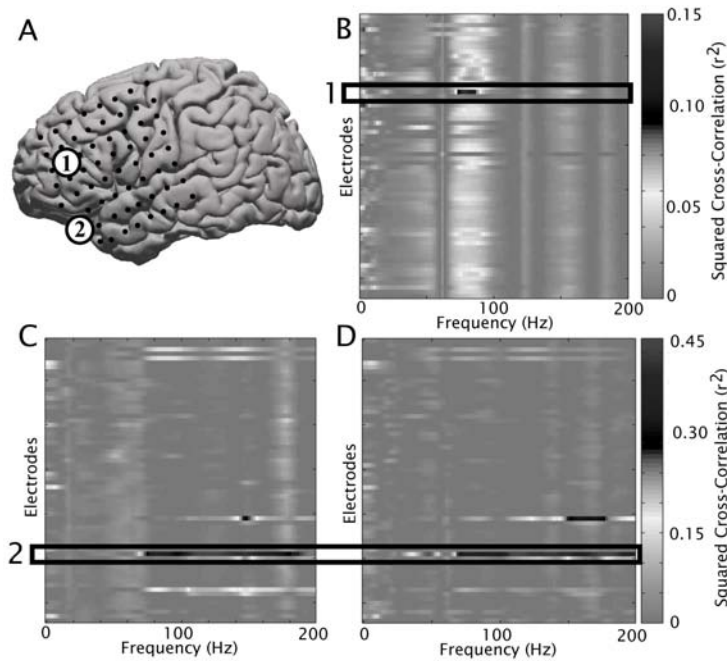


Figure A.6: Feature reassessment after feedback during a speech imagery task.

(A) **Two different feedback sites.** An initial feedback site was chosen at site "1", and, upon reassessment, a secondary feedback site was chosen at site "2". (B) **The**

feature map from a speech imagery screen identified a frontal site for control (labeled "1" in (A)), which was coupled to a cursor control task. The subject was not able to accurately control the cursor in the task, obtaining only 45%. **(C) A feature map from this unsuccessful feedback** run demonstrated that, while there was no significant difference at the feedback site, there was a different site (labeled "2" in (A)). **(D) The feature map following feature reassessment.** The subject was able to rapidly attain 100% target accuracy with the new feature, and the most significant change was in the reassessed electrode.

A.6 A step-by-step walkthrough of the BCI process

We conclude this chapter with a step-by-step example of successful implementation of electrocorticographic BCI.

A.6.1 Background:

The patient is an 18 year old right handed woman with intractable seizures related to a left frontal lesion. Electrodes were placed to map seizures and localize speech function prior to resective surgery, and the array covered speech areas and primary, peri-central, sensorimotor cortex. This excellent coverage of motor cortex made her an ideal candidate for multiple degree of freedom cursor control. Signals were split outside of the patient, with a common ground and reference to the clinical system. The experiments were conducted in three stages spanning two sessions in the same day. The subject was positioned comfortably in her hospital bed throughout the experimental process, and the experimental setting is illustrated in figure 5. The electrode localization and cortical plotting were performed using the LOC package (Miller, Makeig et al. 2007).

The three steps that the experiment was constructed upon were cue-based screening for feature identification, independent one-dimensional cursor-to-target feedback, and combined two-dimensional cursor-to-target feedback.

A.6.2 Screening for feature identification.

In response to 3 second cues, she repetitively moved either her hand or her tongue in repetition, resting for 3 seconds in between each cue. There were 30 cues each for hand and tongue, and they were interleaved in random order to reduce the influence of anticipation. Following the six minutes of overt movement, an identical task was performed, except that rather than actually move the hand and tongue, she imagined moving her hand and tongue. She was explicitly instructed to imagine the kinetics of the movement, not just the sensation (this was found to produce the most robust signal change in a study by Neuper

et. al.(Neuper, Scherer et al. 2005)). A comparison of movement and rest periods (as shown in figure 3) produced feature maps for movement and imagery, shown in the top row of (A). These reveal that changes during imagery mimic those of overt movement, but are less intense (note that the color bar scales are different for movement than imagery). Cortical projections of the imagined and real changes for both high (76-100Hz) and low (8-32Hz) frequency changes reveal that the spatial distributions are similar, but the imagery associated change is more focal(Miller, Ojemann et al. 2008). The number to the top right of each cortical projection indicates the maximum absolute value of the activation, since each brain is scaled to the maximum. Electrodes weights with statistically insignificant change were not projected. These types of projections can be a very useful sanity check to verify that the locations of features identified on a feature map make sense anatomically. A similar screening for repetition of the word "move" was performed, to select a feature for the imagery-based feedback shown in part (B).

A.6.3 One-dimensional cursor feedback

In the second stage, we provided the subject with feedback based upon movement and speech imagery. The imagery was coupled to cursor movement, as detailed in figure 5. Figure inset (B) demonstrates the feature chosen, an 80-95Hz frequency range from an electrode in primary mouth motor area. The mean power, P_0 , lied between the mean power during speech imagery and rest. If the mean power, during the task, was above this level (obtained by speech imagery) then the cursor would move up, and if it was below, the cursor would move down, according to the relation $\dot{y} = g(P(t) - P_0)$. The speed parameter, g , was determined online prior to the first experimental run, such that it was "reasonable" i.e. the cursor velocity changes on roughly the same timescale as the electrode-frequency range feature. In theory, this could be estimated offline prior to the first run by examining the variation in the power of the feature during the screening task, but in practice, the rapid adjustment parameter built into the BCI2000 program(Schalk, McFarland et al. 2004) is a much easier way to get a comfortable speed parameter. The right-most portion of (B)

demonstrates the activation during the 4 (~2 minute) trials of imagery based feedback. Each cortical projection represents the activation between upper targets (speech imagery) and lower targets (rest); because the feature chosen was at a high frequency, above the intersection in the power spectrum (shown in figure 4), the power in the feature increases with activity. She rapidly learned to control the cursor, with the signal becoming both more pronounced and more focused in the feedback area. After the third run, she reported having gone from the coupled imagery (imagined speech) to just thinking about the cursor moving up and down. Again, only significant changes were plotted to the template cortex. The activity in the most ventral posterior electrode (bottom right) hints at activity in Wernicke's area, and persists throughout (it appears to be less, but only because the primary areas are becoming more pronounced, and the overall scale (to the top right) is increasing). Similar one dimensional tasks were performed for tongue and hand. The hand movement was coupled to left-right cursor movement, in preparation for the combination of the two into a two dimensional task.

A.6.4 Two-Dimensional Cursor Feedback

In the last stage of the experiment, two one dimensional control signals are combined into a single cursor to target task. If the two signals are independent, as is the case here, then the transition between robust control in two one-dimensional tasks and robust control in one two-dimensional task is straightforward. The combination of hand and tongue linked features is good (as in (C)), because they are well demarcated on the pre-central gyrus, but the pair chosen in any particular instance will be dependent on the coverage of the electrode array. The example shown in (C), with the frequency range 80-90Hz demonstrates how robust, screened, features (left) can be used for robust control in one-dimensional tasks (center). The electrode for up-down control in both the one- and two-dimensional tasks was from the classic tongue area. The electrode for left-right control in both the one- and two-dimensional tasks was from the classic hand area. The one- and two-dimensional control tasks were successful (100% Left/Right 1D, 97% Up/Down 1D, and 84% 2D).

A.7 End notes

Aoki, F., E. E. Fetz, et al. (1999). "Increased gamma-range activity in human sensorimotor cortex during performance of visuomotor tasks." *Clin Neurophysiol* 110(3): 524-37.

Blakeley, T., K. J. Miller, et al. (2008). "Localization and classification of phonemes using high spatial resolution ECoG grids." IN SUBMISSION.

Blakeley, T., K. J. Miller, et al. (2008). "Robust long term control of an electrocorticographic brain computer interface with fixed parameters."

Blankertz, B., G. Dornhege, et al. (2007). "The non-invasive Berlin Brain-Computer Interface: fast acquisition of effective performance in untrained subjects." *Neuroimage* 37(2): 539-50.

Crone, N. E., D. L. Miglioretti, et al. (1998). "Functional mapping of human sensorimotor cortex with electrocorticographic spectral analysis. II. Event-related synchronization in the gamma band." *Brain* 121 (Pt 12): 2301-15.

Crone, N. E., D. L. Miglioretti, et al. (1998). "Functional mapping of human sensorimotor cortex with electrocorticographic spectral analysis. I. Alpha and beta event-related desynchronization." *Brain* 121 (Pt 12): 2271-99.

Felton, E. A., J. A. Wilson, et al. (2007). "Electrocorticographically controlled brain-computer interfaces using motor and sensory imagery in patients with temporary subdural electrode implants. Report of four cases." *J Neurosurg* 106(3): 495-500.

Graimann, B., J. E. Huggins, et al. (2002). "Visualization of significant ERD/ERS patterns in multichannel EEG and ECoG data." *Clin Neurophysiol* 113(1): 43-7.

Hochberg, L. R., M. D. Serruya, et al. (2006). "Neuronal ensemble control of prosthetic devices by a human with tetraplegia." *Nature* 442(7099): 164-71.

Kennedy, P. R. and R. A. Bakay (1998). "Restoration of neural output from a paralyzed patient by a direct brain connection." *Neuroreport* 9(8): 1707-11.

Lemm, S., B. Blankertz, et al. (2005). "Spatio-spectral filters for improving the classification of single trial EEG." *IEEE Trans Biomed Eng* 52(9): 1541-8.

Leuthardt, E. C., K. J. Miller, et al. (2006). "Electrocorticography-based brain computer interface—the Seattle experience." *IEEE Trans Neural Syst Rehabil Eng* 14(2): 194-8.

Leuthardt, E. C., G. Schalk, et al. (2004). "A brain-computer interface using electrocorticographic signals in humans." *J Neural Eng* 1(2): 63-71.

Miller, K. J., T. Blakeley, et al. (2008). "Three Cases of Feature Correlation in an Electrocor-

ticographic BCI." IN SUBMISSION.

Miller, K. J., E. C. Leuthardt, et al. (2007). "Spectral changes in cortical surface potentials during motor movement." *J Neurosci* 27(9): 2424-32.

Miller, K. J., S. Makeig, et al. (2007). "Cortical electrode localization from X-rays and simple mapping for electrocorticographic research: The "Location on Cortex" (LOC) package for MATLAB." *J Neurosci Methods* 162(1-2): 303-8.

Miller, K. J., J. G. Ojemann, et al. (2008). "The Cortical Bluff: Changes in the Neocortical Power Spectrum during Motor Movement, Motor Imagery, and Imagery-Based Feedback." IN SUBMISSION.

Miller, K. J., P. Shenoy, et al. (2008). "Beyond the Gamma Band: The Role of High-Frequency Features in Movement Classification." *IEEE Trans Biomed Eng* 55(5): 1634-1637.

Miller, K. J., L. B. Sorensen, et al. (2008). "ECoG observations of power-law scaling in the human cortex." IN SUBMISSION - see <http://arxiv.org/abs/0712.0846>.

Miller, K. J., S. Zanos, et al. (2008). "Decoupling the Cortical Power Spectrum Reveals Individual Finger Representation in Humans." IN SUBMISSION.

Muller, K. R., M. Tangermann, et al. (2008). "Machine learning for real-time single-trial EEG-analysis: from brain-computer interfacing to mental state monitoring." *J Neurosci Methods* 167(1): 82-90.

Neuper, C., R. Scherer, et al. (2005). "Imagery of motor actions: differential effects of kinesthetic and visual-motor mode of imagery in single-trial EEG." *Brain Res Cogn Brain Res* 25(3): 668-77.

Nunez, P. L. and B. A. Cuttillo (1995). *Neocortical dynamics and human EEG rhythms*. New York, Oxford University Press.

Ojemann, J. G., E. C. Leuthardt, et al. (2007). "Brain-Machine Interface: Restoring Neurological Function through Bioengineering." *Clin Neurosurg* 54(28).

Pfurtscheller, G. (1999). *Event-Related Desynchronization (ERD) and Event Related Synchronization (ERS)*. Baltimore, Williams and Wilkins.

Pfurtscheller, G., B. Graimann, et al. (2003). "Spatiotemporal patterns of beta desynchronization and gamma synchronization in corticographic data during self-paced movement." *Clin Neurophysiol* 114(7): 1226-36.

Schalk, G., D. J. McFarland, et al. (2004). "BCI2000: a general-purpose brain-computer interface (BCI) system." *IEEE Trans Biomed Eng* 51(6): 1034-43.

Schalk, G., K. J. Miller, et al. (2008). "Two-dimensional movement control using electrocortico-

graphic signals in humans." *J Neural Eng* 5(1): 75-84.

Scherer, R., B. Graimann, et al. (2003). "Frequency component selection for an ECoG-based brain-computer interface." *Biomed Tech (Berl)* 48(1-2): 31-6.

Shenoy, P., K. J. Miller, et al. (2008). "Generalized features for electrocorticographic BCIs." *IEEE Trans Biomed Eng* 55(1): 273-80.

Wilson, J. A., E. A. Felton, et al. (2006). "ECoG factors underlying multimodal control of a brain-computer interface." *IEEE Trans Neural Syst Rehabil Eng* 14(2): 246-50.

Wolpaw, J. R., N. Birbaumer, et al. (2002). "Brain-computer interfaces for communication and control." *Clin Neurophysiol* 113(6): 767-91.

Wolpaw, J. R. and D. J. McFarland (2004). "Control of a two-dimensional movement signal by a noninvasive brain-computer interface in humans." *Proc Natl Acad Sci U S A* 101(51): 17849-54.

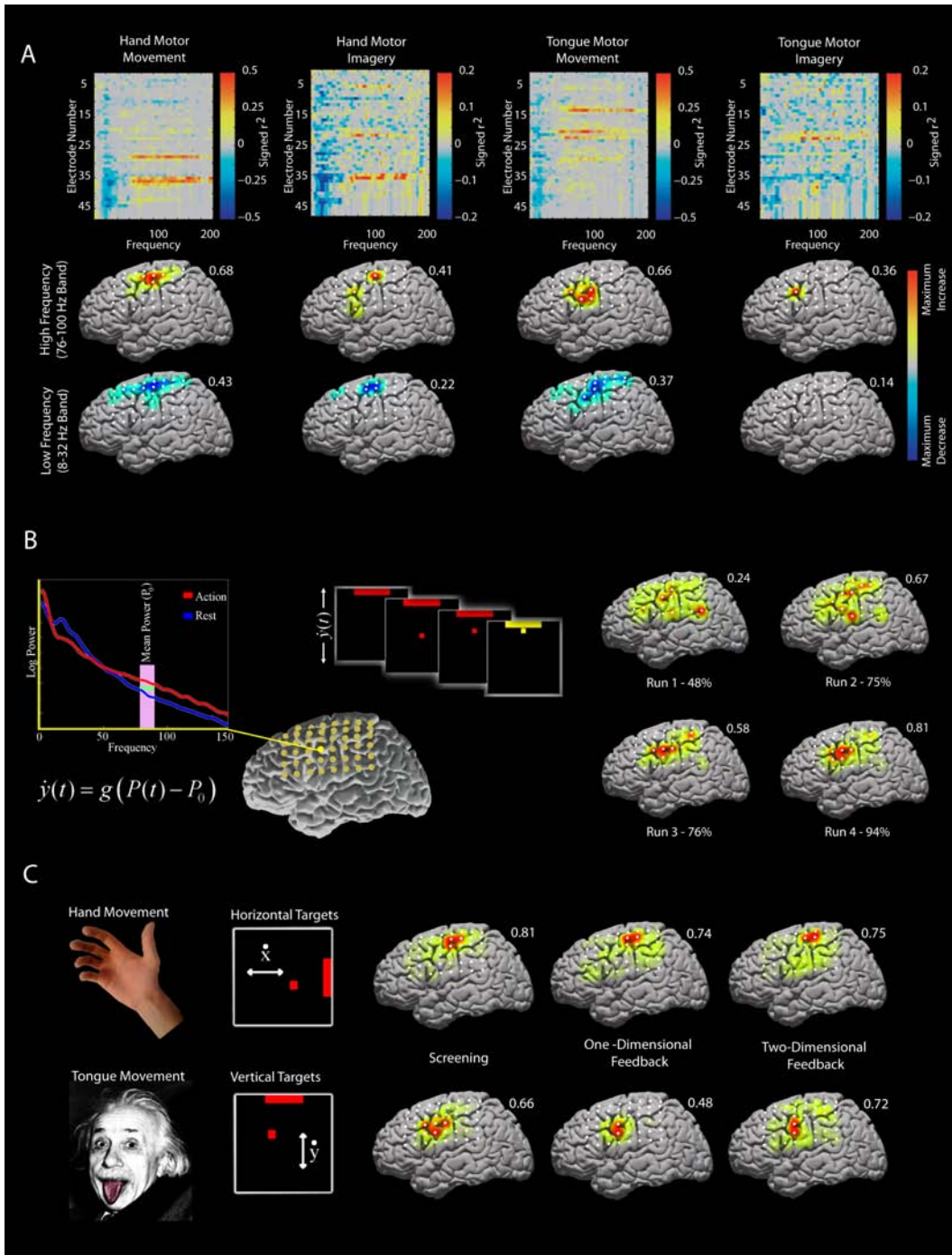


Figure A.7: A single case demonstration of the entire BCI process.

Appendix B

CORTICAL ELECTRODE LOCALIZATION FROM X-RAYS AND SIMPLE MAPPING FOR ELECTROCORTICOGRAPHIC RESEARCH: THE “LOCATION ON CORTEX” (LOC) PACKAGE FOR MATLAB

Medically refractory epilepsy accounts for more than 30% of the epilepsy population. Scalp EEG electrodes have limited ability to localize seizure onset from deep structures and implantation of subdural electrodes with long term monitoring provides additional information. Apart from clinical application, this patient population provides a unique opportunity for acquiring electrocorticography data in research paradigms. We present a method for rapid localization of electrodes using lateral and anterior-posterior x-rays. Skull landmarks and proportions are used for co-registration with the standardized Talairach coordinate system. This MATLAB-based “Location On Cortex” (LOC) package facilitates rapid visualization of clinical and experimental data in a user-friendly manner.

B.1 Introduction

Medically refractory epilepsy affects more than 30% of the epilepsy population (Kwan and Brodie, 2000). One significant clinical challenge is the accurate localization of seizure onset. Scalp EEG electrodes are limited in their ability to localize seizure onset from deep structures, and implantation of subdural electrodes with long term monitoring provides additional seizure localization information (Lesser, Gordon et al., 1991). In addition to the clinical application of subdural electrodes, long term electrocorticographic monitoring provides a unique opportunity for acquiring data in research paradigms. In order to accurately interpret the seizure onset and to interpret electrocorticography data for research paradigms, the three-dimensional location of the electrodes must be known. Although intra-operative photographs of subdural grids provide locations for electrodes on exposed cortex (see supplemental figure), they do not provide information for electrodes passed beyond the limits of the cranial exposure. These electrodes may be located with post-operative CT or MRI (Wellmer, von Oertzen et al., 2002; Kovalev, Spreer et al., 2005), but this process requires sophisticated image acquisition preoperatively and postoperatively and these image studies are often

unavailable. Post-operative x-rays, however, are ubiquitous and readily accessible. The method and the associated package presented here address the need for a fast, reliable co-localization technique to locate and standardize radio-opaque electrodes from anterior-posterior (AP, also called ‘coronal’) and lateral x-rays.

This MATLAB (The MathWorks, Inc.) based “Location On Cortex” (LOC) package uses skull landmarks and proportions for co-registration with the standardized Talairach coordinate system. The Talairach coordinate system defines the origin as the anterior commissure (AC) and the anterior-posterior (y) axis as the line connecting the anterior and posterior commissures (AC/PC line). The x axis is perpendicular to the y axis in the axial plane, and the z axis is normal to the x-y plane (Talairach and Tournoux, 1988).

Skull landmarks visible on the lateral x-ray may be used to approximate the Talairach axes. The line segment drawn from the glabella to the inion (GI line) is parallel to the AC/PC line (Fox, Perlmutter et al., 1985; Friston, Passingham et al., 1989). The y axis is defined as the AC/PC line. The x axis is the direction of left-right symmetry and the z axis is perpendicular to the GI line, and thus normal to the x-y plane. The origin is defined in the x direction as the center of the skull on AP x-rays. In the z direction, it is defined as 21% along the perpendicular line segment corresponding to the maximum distance between the GI line and the inner table of the superior surface of the skull. In the y direction, the distance from the posterior inner table of the skull to the anterior inner table along the y axis is normalized to 173mm, and the origin is taken at 115mm anterior to the midpoint of this line. The y axis is positive anterior to the origin, the x axis is positive on the patient’s right, and the z axis is positive superior to the origin.

To interpret the location of subdural electrodes for clinical analysis and inter-patient comparison, the patient’s brain is normalized to standard dimensions. By making the assumption that the inner table of the skull matches the brain surface, the maximum x, y, and z coordinates of the inner table of the skull can be normalized to a template brain volume. Furthermore, the position of any radio-opaque objects within this volume can also be normalized to the template brain. The AFNI template brain is routinely used in imaging research and is available in Talairach coordinates (Collins, Neelin et al., 1994; Brett, Johnsrude et al., 2002; Holmes, Hoge et al., 1998; <http://afni.nimh.nih.gov>). Its maximum x, y, and z dimensions are 138 mm, 173 mm, and 116 mm, respectively. Normalization to this template brain allows clinicians and researchers to interpret electrocorticographic data with reference to this standardized brain atlas.

B.2 Methods

This technique was implemented on patients enrolled in an electrocorticographic research study at the University of Washington Regional Epilepsy Center. As part of standard clinical practice, subdural platinum electrode arrays with 1 cm center-to-center separation were implanted for seizure localization (AdTech, Racine, WI). Digital skull x-rays were obtained for clinical purposes to localize the subdural electrodes. These x-rays were stored and analyzed as part of a pre-approved research protocol supervised by the University of Washington Institutional Review Board.

The x-ray images were converted to JPEG or BMP format and used with the Location on Cortex (LOC) package for MATLAB, freely downloadable from the EEGLAB site (Swartz Center for Computational Neuroscience, 2006, see <http://sccn.ucsd.edu/eeglab/plugins.html>).

The orthogonal axes in Talairach space were calculated using skull landmarks. The user identifies the glabella and inion, and the inner table of the skull. Complementary bilateral structures on the AP x-ray (for example, the mandibular condyles) are used to define the x origin.

Using the inner table of the skull to approximate the dimensions of the surface of the brain, the axes are linearly scaled to match the MNI template brain in Talairach coordinates. This is done by resizing the width of the brain to 138 mm, the anterior-posterior length of the brain to 173 mm and the positive z axis to a length of 75 mm.

Radio-opaque electrodes present on the patient's skull x-rays are co-registered to the template brain surface. Interpolation to a cortical shell template may be used to simplify this process (Lancaster, Fox et al., 1999), facilitating the localization of positions off of the cortical surface by telescoping. A convex shell template is generated from the model brain by radially smearing each point, both in the polar direction and the azimuthal direction (see Figure 1E where the shell is shown in cross section). Cortical surface locations in regions of low curvature from the lateral perspective require localization only the lateral x-ray, since a given y and z coordinate uniquely determine an x coordinate on the surface of the template shell (Fox, Perlmutter, and Raichle, 1985). In regions of high curvature (e.g. orbitofrontal, occipital, and subtemporal locations), small changes in y and z position produce large changes in the estimated x coordinate. In these cases, the user must also define each electrode location on the AP x-ray to calculate the set of x-coordinates.

By our assumption that the inner table of the skull matches the brain surface, the coordinate triplets may not be precisely on the surface of the template brain. By representing these locations using polar coordinates, they may be radially telescoped to the surface of the convex hemispheric

template with the same solid angle. This is illustrated in cross-section in Figure 1, inset (E).

The LOC package includes graphical rendering functions to present the electrode locations on the surface of the AFNI template brain. Unrestricted three dimensional rotation is possible to visualize the electrode locations.

An interleaved face and house picture presentation paradigm was used in conjunction with the LOC package to identify subtemporal face processing areas (figure 2). An interleaved movement and rest task where subjects performed 3 second blocks of hand or tongue movement followed by 3 seconds of rest was used with the LOC package to identify hand and tongue rolandic cortex. Maps of the cross-correlation strength of power changes (between movement and rest) at each electrode in a cortical ensemble are shown in figure 3.

To assess the precision of resulting locations and inter-user reproducibility of this method, two of the authors independently calculated the subdural electrode positions using the LOC package.

B.3 Results

This technique was used on 17 patients enrolled in an electrocorticographic research study at the University of Washington Regional Epilepsy Center. We present the results for 4 patients as a demonstration of the technique. Figures 1, 2, and 3 demonstrate how the LOC program may be used to localize electrodes and visualize electrocorticographic data.

To examine how reproducible the calculation of electrode positions was with this method, two of the authors independently calculated positions in 4 subjects. For two subjects, the lateral x-ray was used to calculate the location of a 64-electrode grid array. The mean distance between calculated positions was 1.3 mm (SD: 2.1 mm) for the first subject and 1.2 mm (SD: 0.7 mm) for the second subject. Two other subjects had a total of 36 electrodes each in frontal, sub-temporal, and occipital sites. Electrode locations were calculated from a combination of the lateral and AP x-rays. The mean distance between calculated positions was 3.5 mm for the third subject (SD: 2.5 mm) and 3.6 mm (SD: 2.4 mm) for the fourth subject. The diameter of each electrode was 4 mm. These results suggest that the method is highly reproducible, with a standard error smaller than the width of each electrode.

The plotting functions of the LOC package may be used to present electrode locations and render electrocorticographic data onto the template brain surface. For example, electrodes found to be significant for some effect may be highlighted, as shown in Figure 2 where face-specific and visually responsive electrode locations are identified. Simple enumeration of electrode number for

identification of relevant areas may be used to compare electrode locations with known functional areas in standardized coordinates. Alternatively, superposition of weighted kernels at each electrode locus presents continuous spatial distributions of electrocorticographic change with a particular task. When the changes in cortical potential with movement are examined both in a single case and in a large cohort, spatial normalization tightly localizes these changes to coordinates in sensorimotor cortex (Figure 3). Discussion This Location on Cortex (LOC) package facilitates the rapid localization of subdural electrode arrays onto a standardized template brain volume. Once familiar with the procedure, the average time to localize a 64-contact grid using lateral x-ray only, or a 20 contact subtemporal strip array using AP and lateral x-ray is 5 to 10 minutes. Co-registration of electrode locations by individual calculation takes an hour or more for a 64-contact grid using a lateral x-ray. Calculation of Talaraich axes using both AP and lateral x-rays may take considerably longer, and 3-D telescopic interpolation is not feasible by hand.

The major limitations of this technique are the quality of the skull x-rays and the assumptions made based on these x-rays. Differences in x-ray technique may affect the differential magnification of electrodes and skull landmarks. Also, the electrode location calculations assumes the x-rays are directly lateral and AP (i.e., without rotation). Deviations from this assumption may be corrected by rotating all measurements appropriately if the axis and magnitude of rotation is known. Furthermore, the angle of the AP x-ray may affect the amount of superposition of subtemporal electrodes, creating challenges for identifying individual electrodes.

Scaling of the patient's x-ray to match the template brain is limited to the three cardinal directions without oblique correction. This linear transformation limits the accuracy of electrode localization, but the functional results in our patients agree well with known cortical organization, as demonstrated in Figures 1 and 2.

Cross-subject variability and postoperative brain shift also limit the accuracy of this technique. The inner table of the skull is used as a surrogate for the cortical surface in calculations; this does not take into account the possible shift in brain shape after implantation of subdural electrode arrays that may result in the electrode locations being mapped to subcortical locations on the template brain. Telescopic projection onto the surface of the template brain is required to reduce this error. Co-registration onto a template may ultimately be limited by cross-subject cortical variability, such as regional differences in cortical cytoarchitecture (Rajkowska and Goldman-Rakic, 1995), or functional variability in, for example, the location of language cortex (Ojemann, Ojemann et al., 1989).

If specialized pre-operative MRI imaging sequences are available, the patient's own brain can be

used for the volumetric template using brain extraction algorithms (Dale, Fischl et al., 1999; Kovalev, Spreer, Honegger, Zentner, Schulze-Bonhage, and Huppertz, 2005). This requires normalization of the brain volume to Talairach dimensions. A custom shell can be generated from this, and cortical locations calculated accordingly. These cortical locations plotted on this particular brain will be displayed as biologically precise cortical phenomena, with associated Talairach coordinates to compare with known functional areas.

B.4 Conclusion

The Location on Cortex (LOC) package implements a rapid and reliable method of estimating the coordinates of radio-opaque markers such as subdural electrocorticography electrodes. The open source LOC package can also be used to visualize clinical and experimental data in a quantitative fashion with reference to a standardized brain template. This tool can be readily implemented in clinical research settings in which invasive electrophysiology is recorded during the treatment of patients with medically refractory seizures or other brain pathologies.

Acknowledgements KJM is funded by the Poncin award, the NIH MSTP grant, a Neurosurgical Training Grant through the University of Washington and the Packard award via RPNR. AOH is funded by the Epilepsy Foundation through the generous support of Abbott Laboratories. JGO is funded by NS41272. SM is funded in part by the Swartz Foundation. The National Institute for Mental Health (RO1-NS497293) supports the continued development of the open source EEGLAB environment.

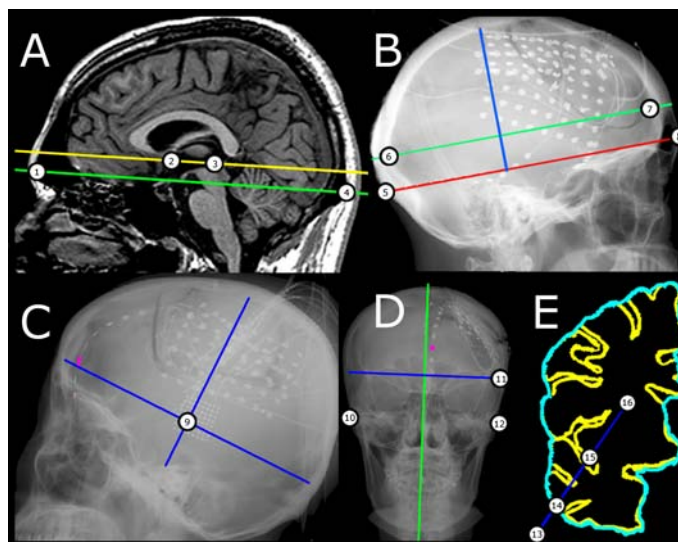


Figure B.1:

(A) The anterior commissure - posterior commissure (AC-PC) line (2 to 3) defines the Talairach y axis, shown in yellow on a patient MRI. The glabella-inion (GI) line (1 to 4) is parallel to AC-PC line and the glabella (1,8) and inion (4,5) are therefore used to approximate the AC-PC line. (B) X-ray image of the same patient. The y-axis (6 to 7, teal) is positioned parallel and superior to the GI line (5 to 8, red), 21% along the length of the longest perpendicular line segment joining the GI line to the skull's inner table (perpendicular line - blue). The distance between posterior and anterior inner tables of the skull (6 to 7) along the y axis is scaled to template dimensions. (C) The y-z origin, the estimated position of the AC, is defined 115mm anterior of the midpoint (9) of the line segment between the two skull tables. (D) A vertical line segment is drawn that perpendicularly bisects a user-defined line segment joining two symmetric structures (10 and 12). The x,y,z origin is defined as the intersection of this line segment with the y-z origin defined on the lateral projection. The maximal biparietal distance measured on the AP x-ray (11) is scaled to the template brain. (E) Points that do not fall on the cortex after identification using the AP and Lateral x-rays (e.g. 13 and 15) may be projected to the surface of cortex by switching to spherical coordinates, with the center of mass of the surface template (shown in light blue / white in BW figure) as the origin (16). The point on the surface template (14) for this solid angle (dark blue line / white line in BW figure) defines the replacement location, which is converted to standard Talairach coordinates.

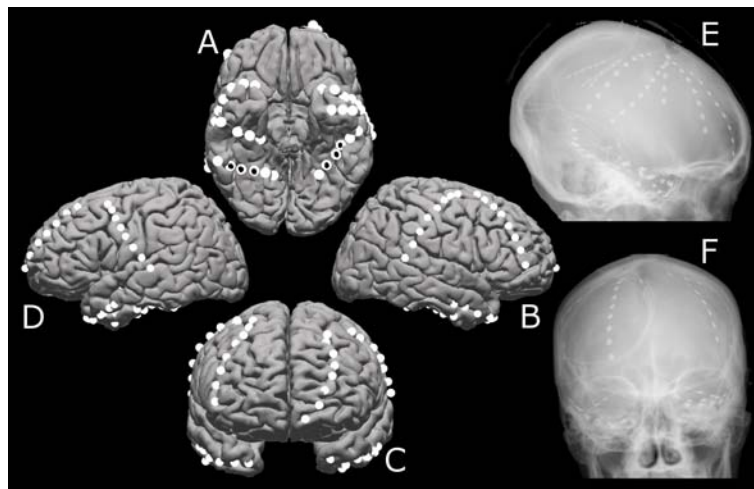


Figure B.2:

(A-D) Localization of strip electrodes calculated from lateral (E) and AP (F) x-rays. (A) The functional localization of fusiform gyrus face recognition area in a patient with bitemporal electrode strips. The patient was shown pictures of faces or houses, and areas showing a selective N170 response for face stimuli were identified. Bilateral changes were observed in the electrodes shown with black dots (located at $(-41, -27, -22)$ $(-37, -35, -23)$ $(-30, -43, -17)$ on the left and $(28, -48, -16)$, $(38, -47, -21)$, $(47, -44, -24)$ on the right). These locations correspond with previously published data for the fusiform face area (Kanwisher, McDermott et al., 1997).

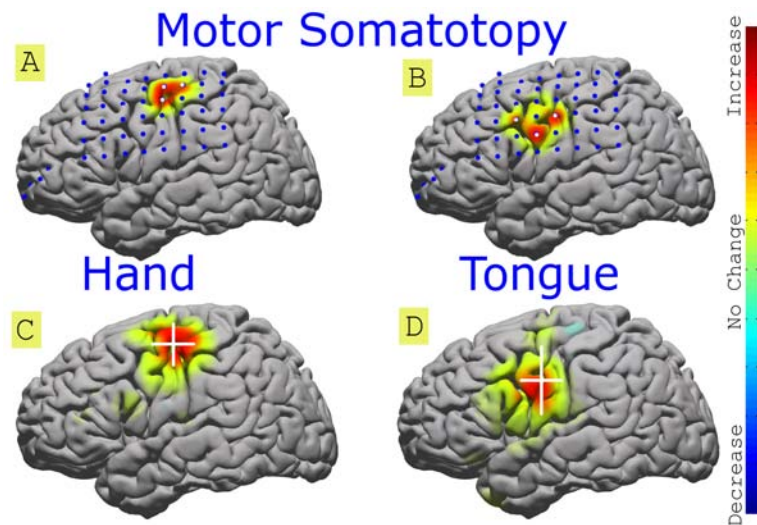


Figure B.3:

Gaussian interpolated maps for hand (A, C) and tongue (B, D) changes associated with a movement task in a single patient (A, B) and cohort average (C, D). Yellow and red surface colors indicate power increases in the 76-100Hz frequency band during this task. Blue dots indicate electrode locations and white dots highlight electrodes with a statistically significant response after Bonferroni correction ($p_{ij} < 0.01$). All highlighted motor electrodes are located within the primary motor area, Brodmann area 4 (Fox and Uecker, 2005). (A) The highlighted electrode coordinates for the hand movement task are $(-47, -25, 57)$, $(-44, -14, 56)$, and $(-42, -3, 55)$. (B) The highlighted electrode coordinates for the tongue movement task are $(-60, -3, 30)$, $(-57, -13, 40)$, $(-53, 8, 38)$. Published coordinates of the activation area center-of-mass based on fMRI data are $(-36 \pm 3, -22 \pm 4, 58 \pm 3)$ for hand and $(-52 \pm 3, -5 \pm 3, 29 \pm 6)$ for tongue (Alkadhi, Crelier et al., 2002). Thus, the observed activation areas in these patients flank the center-of-mass area reported from fMRI data. Insets C and D illustrate the results of hand and tongue area mapping averaged across a large cohort (C, hand, $n=17$ and D, tongue, $n=14$) and projected to the left hemisphere for all patients. The mean electrode positions were $y=-15 \pm 11\text{mm}$, $z=52 \pm 11\text{mm}$ for hand movement, and $y=-9 \pm 11\text{mm}$, $z=31 \pm 18\text{mm}$ for tongue movement. The white cross represents the mean position and variance along each axis.

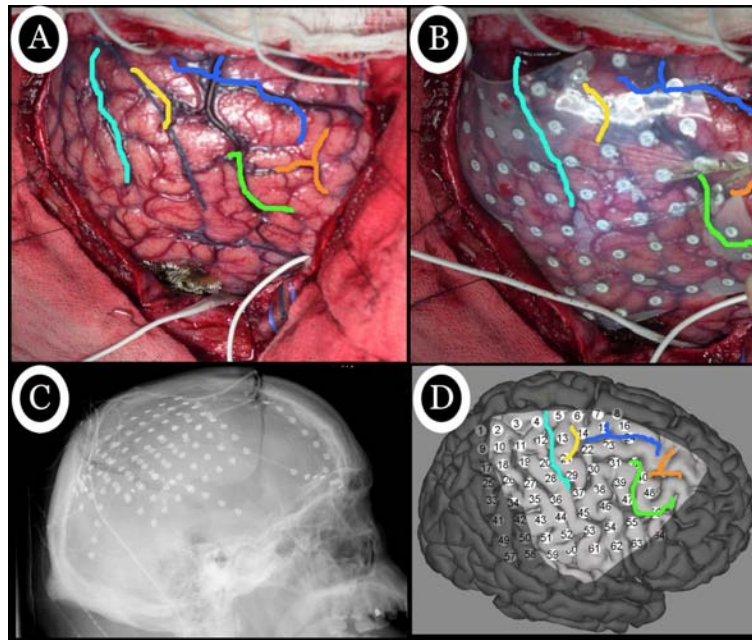


Figure B.4: Supplemental figure - We performed a comparison of the LOC method with intra-operative figures to show correspondence.

(A) A photograph taken before placement of a subdural grid array is used to identify brain sulcal landmarks. (B) The same sulci are identified after electrode placement. (C) The lateral x-ray used to identify the positions of cortical electrodes using the LOC package. (D) The identified electrode positions with the exposed craniotomy unshaded, and the sulci corresponding to those identified in A and B are shown. The cortical schematic in D has been rotated so that its orientation is closer to that of A and B. Comparison of B with D reveals agreement between intra-operative findings and the LOC localization results. Particularly, the central sulcus (shown in light blue) is flanked anteriorly and posteriorly by the same electrodes in both B and D. This type of correspondence between identified electrodes locations on the AFNI template brain and subject specific cortical structures is clear in this example, but this may not be a generalized phenomenon. Any interpretation of cortical location in a standardized coordinate space must take into account that there is considerable variation in cortical structure across individuals (Van Essen, 2005; NeuroImage; 28(3):635-62), and a single template or normalized coordinate system will not reflect this.

B.5 End notes

1. Alkadhi H, Crelier GR, Boendermaker SH, Golay X, Hepp-Reymond MC, Kollias SS. Reproducibility of primary motor cortex somatotopy under controlled conditions. *AJNR Am.J.Neuroradiol.*, 2002; 23: 1524-1532.
2. Brett M, Johnsrude IS, Owen AM. The problem of functional localization in the human brain. *Nat.Rev.Neurosci.*, 2002; 3: 243-249.
3. Collins DL, Neelin P, Peters TM, Evans AC. Automatic 3D intersubject registration of MR volumetric data in standardized Talairach space. *J.Comput.Assist.Tomogr.*, 1994; 18: 192-205.
4. Dale AM, Fischl B, Sereno MI. Cortical surface-based analysis. I. Segmentation and surface reconstruction. *Neuroimage.*, 1999; 9: 179-194.
5. Fox, Mick and Uecker, Angela. Talairach Daemon Client. (2.0). 2005. <http://ric.uthscsa.edu/projects/talairachdaemon.html>.
6. Fox PT, Perlmutter JS, Raichle ME. A stereotactic method of anatomical localization for positron emission tomography. *J.Comput.Assist.Tomogr.*, 1985; 9: 141-153.
7. Friston KJ, Passingham RE, Nutt JG, Heather JD, Sawle GV, Frackowiak RS. Localisation in PET images: direct fitting of the intercommissural (AC-PC) line. *J.Cereb.Blood Flow Metab*, 1989; 9: 690-695.
8. Holmes, C.J., Hoge, R., Collins, L., Woods, R., Toga, A.W. and Evans, A.C. Enhancement of Magnetic Resonance Images Using Registration for Signal Averaging. *J. Comp. Asst. Tomograph*, 1998; 22(2):324-333.
9. Kanwisher N, McDermott J, Chun MM. The fusiform face area: a module in human extrastriate cortex specialized for face perception. *J.Neurosci.*, 1997; 17: 4302-4311.
10. Kovalev D, Spreer J, Honegger J, Zentner J, Schulze-Bonhage A, Huppertz HJ. Rapid and fully automated visualization of subdural electrodes in the presurgical evaluation of epilepsy patients. *AJNR Am.J.Neuroradiol.*, 2005; 26: 1078-1083.
11. Kwan P, Brodie MJ. Early identification of refractory epilepsy. *N.Engl.J.Med.*, 2000; 342: 314-319.
12. Lancaster JL, Fox PT, Downs H, Nickerson DS, Hander TA, El Mallah M, Kochunov PV, Zamarripa F. Global spatial normalization of human brain using convex hulls. *J.Nucl.Med.*, 1999; 40: 942-955.
13. Lesser R, Gordon B, Fisher R, Hart J, Uematsu S. Subdural grid electrodes in surgery of

epilepsy. In Luders HO, editor. *Epilepsy Surgery*. Raven Press: New York, 1991; 399-408.

14. Ojemann G, Ojemann J, Lettich E, Berger M. Cortical language localization in left, dominant hemisphere. An electrical stimulation mapping investigation in 117 patients. *J.Neurosurg.*, 1989; 71: 316-326.

15. Rajkowska G, Goldman-Rakic PS. Cytoarchitectonic definition of prefrontal areas in the normal human cortex: II. Variability in locations of areas 9 and 46 and relationship to the Talairach Coordinate System. *Cereb.Cortex*, 1995; 5: 323-337.

16. Swartz Center for Computational Neuroscience. EEGLAB - Open Source Matlab Toolbox for Electrophysiological Research. <http://www.sccn.ucsd.edu/eeglab/> . 2006.

17. Talairach J, Tournoux P. *Co-Planar Stereotaxic Atlas of the Human Brain*. Thieme: 1988.

18. Wellmer J, von Oertzen J, Schaller C, Urbach H, Konig R, Widman G, Van Roost D, Elger CE. Digital photography and 3D MRI-based multimodal imaging for individualized planning of resective neocortical epilepsy surgery. *Epilepsia*, 2002; 43: 1543-1550.

VITA

Kai Joshua Miller is a native of California. He attended the University of California, San Diego as an undergraduate, where he graduated in 2000. He earned a Doctorate of Philosophy in Physics at the University of Washington in 2008.